A Hybrid Continuum-Rarefied Hypersonics Methodology with Automatic Mesh Optimization

Shrutakeerti Mallikarjun Vagishwari

Department of Mechanical Engineering

McGill University, Montréal

May 2022

A thesis submitted to McGill University

in partial fulfillment of the requirements for the degree of

DOCTOR OF PHILOSOPHY

Abstract

HALO3D (High-Altitude Low-Orbit, 3D) is a multidisciplinary all-Mach CFD system developed by the McGill CFD Lab to simulate flow fields around hypersonic aircraft whose flight path spans low (continuum) to high (rarefied) altitudes. HALO3D uses an unstructured edge-based finite-element Navier-Stokes (NS) flow solver (HALO3D-NS) for the continuum regime that includes complex thermochemistry. This thesis extends the applicability of HALO3D to the rarefied regime through three significant efforts.

First, a rarefied flow solver, **HALO3D-DSMC** (Direct Simulation Monte Carlo), is developed to tackle the high-altitude flow field. It is a 3D unstructured DSMC code capable of simulating thermochemical non-equilibrium and volume chemistry with sub-cell features for collision pair selection. Validation simulations for HALO3D-DSMC are presented.

Second, a **HALO3D-HYBRID** infrastructure is developed to simulate moderate Knudsen number flows. In a domain consisting of continuum and rarefied patches, the hybrid routine transparently steps between NS and DSMC techniques to calculate a global solution with no user intervention. Delineating the DSMC and NS regions is accomplished by using the gradient length local Knudsen number (Kn_{GLL}) as a continuum breakdown detector. Cell and node masks based on the Kn_{GLL} distribution are inputs for mesh population, particle insertion, buffer zone creation, and NS-DSMC boundary condition routines. Bird's leading-edge and 2D cylinder cases are used to demonstrate that a finite-element NS-DSMC hybrid algorithm can be successfully built to address high-Mach flows. Consistent treatment of thermochemical non-equilibrium by both continuum and rarefied modules is found to be necessary to accurately simulate complex flows.

Third, is the coupling of HALO3D-DSMC and HALO3D-HYBRID with a powerful in-house solution-driven automatic mesh optimizer, OptiGrid, heavily used in the NS context. A thorough investigation is carried out on scalars and constraints needed to optimize DSMC and hybrid meshes, an aspect that is currently lacking in the literature. Three optimization constraints: the minimum and maximum edge lengths, and a target number of node/cells are studied and applied to the leading-edge case and flows over 2D and 3D cylinder geometries for freestream Knudsen numbers ranging from 0.01 to 0.047. It is shown that an adaptation scalar combination of flow variables such as density, velocities, temperatures, pressure, and Mach number automatically converges to

a final optimized mesh through a series of mesh iterations. The adapted meshes gradually improve the solution's quality without necessarily increasing the number of mesh points or cells, even reducing them sometimes. The solutions represented by the final adapted mesh are smooth and free of irregularities. The solutions and meshes of adapted full DSMC simulations and adapted hybrid simulations are seen to match, thus validating the hybrid solver and showcasing the solver-independence aspect of OptiGrid. Further, the optimized hybrid mesh generates buffers with smooth boundaries and consists of coarse NS cells and refined DSMC cells. The cell sizes from NS to DSMC are seen to reduce organically in the shock and boundary layer. This coupled DSMC/hybrid-OptiGrid system can thus simulate complex 3D geometries and multiscale flow features while drastically reducing mesh preparation time as these are automatically adapted to the emerging physics during the iterative solutions.

Taken altogether, the DSMC, hybrid NS-DSMC, and mesh optimization efforts form an advanced system to simulate hypersonic flows over complex geometries with controlled precision and at a much lower expense both in the pre-processing and solution phases. These contributions are the essential components of a seamless hybrid solution approach within HALO3D, upon which other functionalities could be easily built in the future.

Résumé

HALO3D (High-Altitude Low-Orbit, 3D) est un logiciel CFD développé par le Laboratoire CFD de McGill pour simuler les écoulements chevauchant les basses vitesses de Mach jusqu'aux vitesses hypersoniques, donc depuis les écoulements en milieux continus jusqu'aux gaz raréfiés. En régime continu HALO3D est un solveur Navier-Stokes (NS) à éléments finis basé sur les arêtes (HALO3D-NS) qui tient compte de la thermochimie complexe. Cette thèse étend l'applicabilité de HALO3D au régime raréfié à travers trois efforts principaux.

En premier, un solveur d'écoulement raréfié, **HALO3D-DSMC** (Direct Simulation Monte Carlo), est développé pour simuler le champ d'écoulement à haute altitude. Il s'agit d'un code DSMC 3D à maillage non-structuré capable de simuler le non-équilibre thermochimique et la chimie de volume et possédant également des caractéristiques de sous-cellules pour la sélection de paires de collisions. Des simulations de validation pour HALO3D-DSMC sont présentées.

Deuxièmement, l'infrastructure **HALO3D-HYBRID** est développée pour créer un algorithme de solution hybride pour simuler les écoulements à nombre de Knudsen modéré. Lorsque le domaine est constitué à la fois de zones continues et raréfiées, la routine hybride passe de manière transparente entre ces zones sans intervention de l'utilisateur, la délimitation se basant sur un nombre de Knudsen à gradient de longueur locale (Kn_{GLL}) comme détecteur de rupture de continuum. Les masques de cellules et de nœuds basés sur la distribution Kn_{GLL} sont utilisés comme entrées pour la population de mailles, l'insertion de particules, la création de zones tampons et les routines de conditions limites NS-DSMC. Trois couches de tampon externe où les particules sont générées dans le domaine et trois couches de tampon interne où les particules sont libres d'évoluer sont employées pour toutes les simulations de cette étude. Les cas du bord d'attaque et du cylindre 2D démontrent les capabilités de ce code hybride pour traiter les écoulements à très haut nombres de Mach. Le traitement cohérent du non-équilibre thermochimique par les modules continuum et raréfié s'avère nécessaire pour simuler avec précision de tels écoulements complexes.

Troisièmement, HALO3D-DSMC et HALO3D-HYBRID sont interfacés avec un puissant optimiseur de maillage automatique axé sur les solutions, OptiGrid, développé au CFD Lab et très utilisé dans le contexte NS. Une étude est entreprise sur les scalaires et les contraintes d'optimisation des maillages DSMC et hybrides, un aspect qui fait actuellement défaut dans la

littérature. Trois contraintes d'optimisation sont analysées soit les longueurs minimales et maximales des bords et le nombre cible de nœuds/cellules. L'adaptation du maillage est démontrée pour le cas du bord d'attaque de Bird et des géométries cylindriques 2D et 3D pour des nombres de Knudsen du flux libre allant de 0,01 à 0,047. On conclut qu'un ensemble de scalaires d'adaptation combinant des variables telles que la densité, les vitesses, les températures, la pression et le nombre de Mach produit un maillage d'échantillonnage collisionnel non-structuré améliorant considérablement la qualité de la solution sans pour autant augmenter le nombre de nœuds ou de cellules, parfois même les réduisant. Les solutions représentées par les maillages adaptés sont lisses et exemptes d'irrégularités et les caractéristiques saillantes de l'écoulement sont bien capturées sans aucune intervention de l'utilisateur. Les solutions et les maillages des simulations DSMC complètes adaptées et des simulations hybrides adaptées correspondent, ce qui valide le solveur hybride et met en évidence l'indépendance d'OptiGrid vis-à-vis du solveur. En outre, le maillage hybride optimisé génère des tampons aux frontières lisses et se compose de cellules NS grossières et de cellules DSMC raffinées. On constate que la taille des cellules de NS à DSMC diminue organiquement dans la couche de choc et la couche limite. Ce système couplé DSMC/hybride-OptiGrid peut donc simuler les caractéristiques d'écoulements à multi-échelles autour de géométries complexes tout en minimisant l'effort initial de maillage étant donné son adaptation automatique lors de la solution itérative du système.

Dans leur ensemble, les développements de DSMC, de NS-DSMC hybride et d'optimisation du maillage permettent de simuler les écoulements hypersoniques sur des géométries complexes avec une précision contrôlée et à bien moindre coût tant dans les phases de prétraitement que de solution. Ces contributions forment les composantes essentielles d'une approche de solution hybride transparente dans HALO3D sur laquelle d'autres fonctionnalités pourraient être facilement ajoutées dans le futur.

Acknowledgements

I would like to express my gratitude to my supervisor Prof. Wagdi G. Habashi, for his expertise, guidance, and support throughout my studies.

I am also grateful to Dr. Abolfazl Karchani (Ansys) for numerous technical discussions and advice at crucial junctures during the research.

I would like to thank Dr. Vincent Casseau (CFD Lab) for technical discussions, code development, debugging, and editorial assistance.

I acknowledge with thanks the discussions with Dr. Song Gao (Ansys, formerly with the CFD Lab) regarding several features of the continuum regime solver and his general advice regarding the mesh optimization code.

The dynamic environment of the CFD Lab allowed me to interact with Wenbo Zhang, John Huang, Gan Yang, Guangwei Liu, Xiangda Cui, Adam Targui, and Daniela Caraeni, with whom I took common coursework and discussed many technical problems.

I would like to also thank my family and friends for their continued support, companionship, and interest in my work.

Supercomputing time provided by the Digital Research Alliance of Canada is gratefully acknowledged.

Finally, I would like to express my gratitude to the Lockheed Martin Corporation, Ansys Canada, and MITACS for the MITACS Accelerate grant that supported the current project.

Table of Contents

List of Figures

List of Tables

List of Symbols

Latin Alphabet

A_r^f	Pre-exponential Arrhenius parameter
$\boldsymbol{c}'$	Peculiar velocity
C_{CM}	Centre of mass velocity of two particles
c_r	Relative velocity between two particles
$C_{p,s}^t$	Translational constant pressure specific heat
$C_{p,s}^{tr}$	Trans-rotational constant pressure specific heat
$C_{v,s}^t$	Translational constant volume specific heat
$C_{v,s}^r$	Rotational constant volume specific heat
$C_{v,s}^v$	Vibrational constant volume specific heat
D	Mass diffusion coefficient
d_s	Reference diameter of species
E	Total energy
e_{coll}	Collision energy
e_t	Translational energy
e_r	Rotational energy
e_v	Vibrational energy
f_o	Maxwellian velocity distribution function
$\boldsymbol{F}$	Flux vector
g_v	Vibrational degeneracy
H	Total enthalpy per unit mass
$\boldsymbol{H}$	Hessian of adaptation scalar
i_v	Vibrational energy level
k	Boltzmann constant
Kn	Knudsen number
K_r^{eq}	Equilibrium constant for a chemical reaction
k_r^b	Backward reaction rate
k_r^f	Forward reaction rate

$\mathbf{J}$	Mass diffusion vector
m	Molecular/atomic mass
N_j	Finite element shape function
N_{coll}	Number of collisions to be performed
P	Pressure
$\boldsymbol{q}$	Heat flux vector
R	Random number
R_s	Species gas constant
R_u	Universal gas constant
S_S^c	Chemical source term
S^v	Vibrational source term
T_r	Rotational temperature
T_t	Translational temperature
T_{tr}	Trans-rotational temperature
T_v	Vibrational temperature
$\mathbf{V}$	Velocity vector
W_f	Number of real molecules approximated by one particle
$\boldsymbol{x}$	Particle/node position in physical space
X	Molar fraction
Y	Mass fraction
Z_r	Rotational collision number
Z_v	Vibrational collision number

Greek Alphabet

α, β	Post-collision scattering angles
α_{ij}	Distance based weight for data interpolation
λ	Mean free path
ϕ	Macroscopic variable
ρ	Density
$\boldsymbol{\tau}$	Shear stress vector

μ	Viscosity coefficient
κ	Thermal conductivity
κ_{tr}	Trans-rotational thermal conductivity
κ_v	Vibrational thermal conductivity
θ_v	Characteristic vibrational temperature
θ_d	Characteristic dissociation temperature
σ_s	Collision cross-section
$\nu'_{s,r}$	Reactant stoichiometric coefficient
$\nu''_{s,r}$	Product stoichiometric coefficient
η_r^f	Arrhenius temperature exponent
ω	Power law exponent
γ	Ratio of specific heats
$\boldsymbol{\xi}$	Particle position in primitive space
ζ	Degrees of freedom

Abbreviations

DAC	DSMC Analysis Code
DPLR	Data Parallel Line Relaxation
DSMC	Direct Simulation Monte Carlo
dsmcFoam	DSMC Field Operation And Manipulation
GLL	Gradient Length Local
HALO3D	High-Altitude Low-Orbit 3D
JAXA	Japan Aerospace Exploration Agency
LB	Larsen-Borgnakke
LeMANS	Michigan Aerothermodynamic Navier-Stokes Solver
mcs	mean collision separation
mfp	mean free path
NASA	National Aeronautics and Space Administration
NEQ	Non-equilibrium
NN	Nearest Neighbour

NS	Navier-Stokes
NTC	No-Time-Counter
QK	Quantum-Kinetic
RANS	Reynolds Averaged Navier-Stokes
SMILE	Statistical Modeling In Low-Density Environment
SPARTA	Stochastic PArallel Rarefied-gas Time-accurate Analyzer
TAS	Transient Adaptive Sub-cell
TCE	Total Collision Energy
UGKP	Unified Gas-Kinetic Particle method
UGKS	Unified Gas-Kinetic Scheme
UGKWP	Unified Gas-Kinetic Wave-Particle method
VHS	Variable Hard Sphere
VSS	Variable Soft Sphere

Chapter 1
Introduction

1.1 Motivation

A several-fold increase in air-space transportation speed would enable a new ecosystem to develop around the idea that distance and time are no longer constraining factors for point-to-point travel. This is the prospect brought by the re-emergence of higher-speed technology programs with space agencies and companies strenuously pushing boundaries to be leaders in this billion-dollar market. Defined as travel at speeds greater than Mach 5 below the Kármán line, hypersonic flight benefits space exploration, tourism, and civilian and cargo transportation, whose economic sustainability heavily relies upon the pillars of reliability, operational efficiency, and re-usability [1]. These three pillars are now part of most planned launch vehicles and spaceplanes as exemplified by Space X's Starship, Blue Origin's New Glenn, Hermeus' Quarterhorse Mach 5 jet, NASA-Lockheed Martin's X-59 QueSST demonstrator, JAXA's Sky Frontier hypersonic research program, and supersonic vehicles from Aerion, Boom Supersonic, Spike Aerospace, and Virgin Galactic, to name a few. Space X's Falcon 9 rocket is the first of such transportation systems to be profitable – although being only partially reusable.

Hypersonic flows present complex aero-chemical-magneto dynamics such as finite-rate chemistry, non-equilibrium effects, flow, and magnetic field interactions, radiative effects, and ablation of the heat shield, as illustrated in Fig. 1.1 [2]. The development of computational methods for hypersonic vehicle analysis and design is rapidly growing since experimental campaigns are expensive, not always feasible, and only provide a limited amount of data compared to numerical solutions. This thesis documents the development of fundamental modules of a code to monolithically simulate the widely different stages of a hypersonic flight from take-off to ascent, cruise, descent and landing, covering the subsonic, supersonic, hypersonic, and rarefied flow regimes. Such a flight path spans a range of altitudes where the freestream density changes significantly. Design tools for hypersonic aircraft should account for these changes in density and apply the appropriate computational techniques to each flow regime. The Knudsen number, defined as the ratio of the local mean free path (mfp) to a characteristic length scale, is commonly used to categorize the flow regimes, as shown in Fig. 1.2.

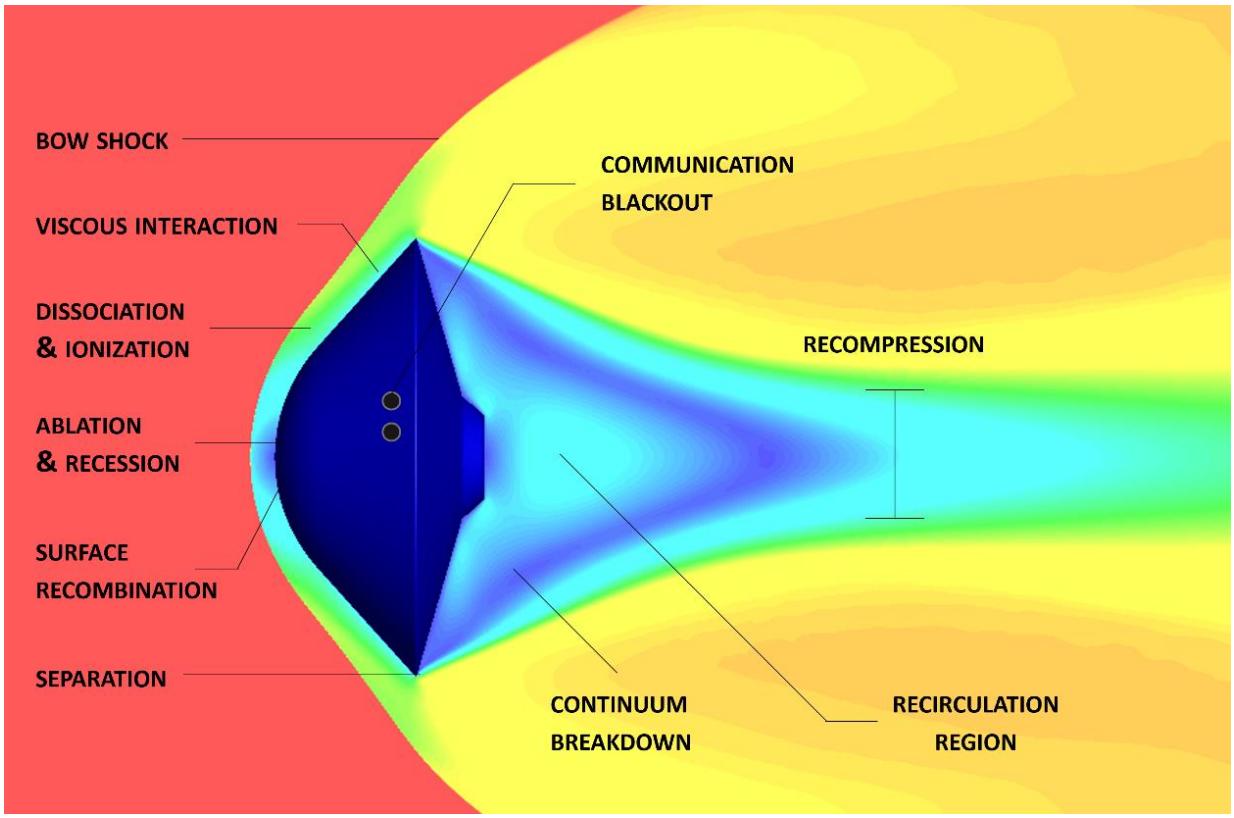

Fig. 1.1 The complex physics of hypersonic flight

The Reynolds Averaged Navier-Stokes (RANS) equations are only applicable in the continuum regime and become increasingly invalid as the Knudsen number increases. Particle-based methods such as the Direct Simulation Monte Carlo (DSMC) method are more appropriate for the large Knudsen numbers typifying the rarefied regime. Another alternative for the simulation of high-speed flows is the Unified Gas-Kinetic Wave-Particle (UGKWP) method [3] which derives from the Unified Gas-Kinetic Scheme (UGKS) [4] and the Unified Gas-Kinetic Particle (UGKP) [3] method. The UGKS considers the conservation of the flow field variables and the microscopic distribution functions, thus enabling a unified simulation of all Knudsen regimes. It proves less expensive than RANS in the continuum regime but more expensive than DSMC in the rarefied regime. The not insignificant extra cost for the rarefied regime and significant memory requirements are recovered in the UGKWP method, which has also seen development in photon transport [5], multispecies mixtures, and plasma transport [6], among other areas.

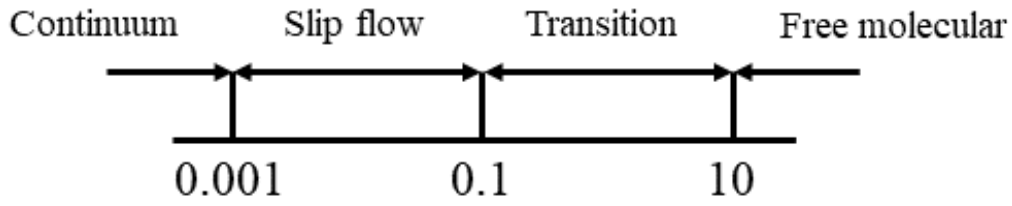

Fig. 1.2 Regimes of flow based on the freestream Knudsen number

The UGKS was first introduced in 2010 and extended to the UGKWP methods in 2020. The development of rarefied flow modules for the present work began in 2018 when a proper consideration of the UGKWP methods was not yet possible. The DSMC method, which has undergone development since 1963, and has since been extended to solve multispecies reacting flows, is considered in this thesis instead. Various DSMC implementations are available for study and comparison, making the development process less error-prone. Developed by Bird [7-9], DSMC is a stochastic method that uses mesoscale particles to model rarefied gas flows and is widely used to solve non-equilibrium problems from the nano- to the meter-scale [10-14]. Each particle in DSMC represents a large number of real molecules, with the dilute gas assumption allowing particle motion and collision to be decoupled. At each time step, particles are first moved deterministically throughout the domain based on their current velocities, and then binary collision pairs are selected through an acceptance-rejection routine. Following this, inter-particle collisions occur between the selected particle pairs, and their velocities and modal energies are updated. Finally, macroscopic quantities are sampled after the simulation reaches steady-state.

Despite its stochastic nature, it has been mathematically proven by Wagner [15] that the DSMC method converges to the solution of the Boltzmann transport equation if an infinite number of particles and infinitesimal cell sizes and time steps are used. Nevertheless, these conditions, similar to the Navier-Stokes (NS) equations for the continuum part of any hypersonic flow, cannot be satisfied for practical flows. Sensitivity to the time step size can be minimized by using automatically adaptive variable time steps [16,17], while the effect of the number of particles on solution accuracy can be controlled by using enough particles in the domain [8,18,19]. Also, the cell size should be smaller than the local mean free path (mfp) throughout the domain to avoid unphysical collisions [8,20]. Controlling cell size is not an easy task since the flow features and local mfp are not known *a priori*, and it is usually done through successive mesh refinements. For

static meshes, one would instead estimate the cell size based on known freestream information and predict the locations of non-equilibrium regions (e.g., singularities such as shocks, vacuum regions, boundary layers) to cluster the domain accordingly. However, these approaches are not accurate nor practical for arbitrary unstructured or structured meshes and complex geometries. Therefore, the application of automatic mesh refinement techniques is desired not only for resolving multiscale flow features while using the least number of particles but also for reducing the error in DSMC simulations.

At moderate Knudsen numbers, only certain regions of the domain can begin to exhibit continuum breakdown, and only these regions need to be solved using DSMC. The interest in solving only the rarefied portions of the domain using DSMC instead of a full DSMC simulation is because the DSMC method is by nature more expensive than continuum methods. Hybrid NS-DSMC algorithms thus partition the domain into NS and DSMC regions and run the two solvers in their respective regions. By doing this, they reduce the overall cost of the simulation while preserving accuracy.

1.2 Existing Hybrid NS-DSMC Approaches

Continuum breakdown can be best observed by comparing NS and DSMC results of the same test problems [21-24], where the DSMC solution acts as the benchmark since DSMC is accurate everywhere in the domain, albeit more expensive. For flows across 1D and 2D shocks [21], it was observed that the comparisons between NS and DSMC solutions deteriorate as the Mach number increases because an increase in Mach number comes with a slight increase in continuum breakdown [22]. Continuum breakdown is recorded inside the shock and boundary layer because of large gradients in the flow properties and the wake due to increased rarefaction. Comparisons of the predicted NS and DSMC surface heat flux, drag, and shear stress deteriorate when the freestream Knudsen number is increased [22,23]. The surface heat flux seems to depend on the continuum breakdown in the shock and the size of the thermal boundary layer. The drag is influenced by the continuum breakdown in the wake region, and the shear stress is the most sensitive wall quantity to changes in the degree of rarefaction. NS surface pressure agrees with DSMC computations until a Knudsen number of 0.25, after which the agreement deteriorates. The NS methods are also observed to predict much thinner shocks than DSMC, with DSMC methods agreeing with experimental results on shock thickness while the shock locations are seen to match

[21,23]. For the NS calculations, a single trans-rotational temperature [22] and separate translational and rotational temperatures [21] have been employed for modeling the rotational energy. Since DSMC generally employs separate translational, rotational, and vibrational temperatures, a DSMC trans-rotational temperature is calculated to compare against the NS trans-rotational temperature. Good agreement is observed for both temperature representations at low Mach and Knudsen numbers, but that deteriorates as the Mach and Knudsen numbers increase. These comparisons illustrate the need to account for the deficiency of the NS equations at increased Knudsen numbers which is done through a hybrid coupling with the DSMC method.

A hybrid algorithm requires modules and functions apart from the NS and DSMC codes necessary for the hybrid coupling. Firstly, a means of distinguishing NS and DSMC regions on a mesh is required where the boundary between the two zones has to be positioned such that a globally physically accurate solution is obtained, and the computational time of the simulation is reduced. In the year following the introduction of the first DSMC code, DSMC94, a continuum breakdown detector, the gradient length local Knudsen number (Kn_{GLL}), was introduced by Boyd *et al.* [21] to delineate NS and DSMC regions. The definition of Kn_{GLL} was slightly modified in [25], and this definition is

$$Kn_{\mathrm{GLL}-Q} = \lambda \left| \frac{\nabla Q}{Q} \right| \tag{1.1}$$

where Q is any flow quantity such as density, temperature, and pressure and λ is the local mfp. The breakdown parameter $Kn_{\max}$ is obtained by calculating the maximum $Kn_{\mathrm{GLL}-Q}$ among different scalars as

$$Kn_{\max} = \max\left(Kn_{\mathrm{GLL}-\rho}, Kn_{\mathrm{GLL}-T_{\mathrm{tr}}}, Kn_{\mathrm{GLL}-T_{\mathrm{v}}}, Kn_{\mathrm{GLL}-\boldsymbol{U}}\right) \tag{1.2}$$

where the scalars used in the present study are listed here: density (ρ), trans-rotational temperature (T_{tr}), vibrational temperature (T_{v}), and the velocity components ($\boldsymbol{U}$). Along with $Kn_{\max}$, a thermal non-equilibrium detector [26] given by

$$Kn_{\mathrm{ROT-NEQ}} = \left| \frac{T_{\mathrm{t}} - T_{\mathrm{r}}}{2T_{\mathrm{r}}} \right| \tag{1.3}$$

is sometimes used to assign regions of the domain that exhibit rotational non-equilibrium as DSMC regions. Here T_t is the translational temperature and T_r is the rotational temperature. The denominator in Equation 1.3 is replaced in [27] with the translational temperature.

Secondly, particles should be generated in the outer buffer regions with properties consistent with the NS solution in this region. Once the outer buffer is populated, the particles have to be allowed to collide several times, which happens in the inner buffer regions where particles collide before entering the DSMC region (particles are refreshed at each time step in the outer buffer). For an equilibrium monoatomic gas, particles can be initialized with a Maxwellian distribution which also provides a reasonable approximation for an equilibrium polyatomic gas mixture. For weak non-equilibrium conditions and equilibrium polyatomic gases, particles might require the Chapman-Enskog distribution for initialization. For polyatomic gas mixtures and thermal non-equilibrium, the generalized Chapman-Enskog distribution may be required.

Thirdly, a means of transferring information between the NS and DSMC regions is needed. Two methods have been used in the literature to transfer such information: a flux-based coupling method [28,29,30] and a state-based coupling [27,31,32] method. For flux-based coupling, mass, momentum, and energy fluxes have to be computed at the interface, and since these fluxes are usually different between the NS and DSMC modules, a correction factor is required. For state-based coupling, the NS and DSMC domains are extended into each other's regions to form buffer zones where macroscopic solutions are imposed. The present study employs state-based coupling with the construction of buffer layers of cells described in Section 2.3. Some hybrid codes are described in the following paragraphs.

One of the earliest hybrid codes developed in 1996 by Hash and Hassan [28] is a decoupled NS-DSMC hybrid code. First, an NS solution of the entire domain is computed based on which the NS and DSMC regions are distinguished using the $Kn_{\max}$ breakdown parameter, after which the interface is frozen. The NS-DSMC boundary is treated as an inflow patch with flux-based coupling for particles entering the DSMC domain. Gupta's [33] model is used for transport property calculations, and Park's [34] reaction rates are used for modeling chemical reactions in the NS solver. The NS solver also assumes a constant rotational relaxation number of 5 and employs the Millikan and White [35] model for vibrational relaxation. The DSMC solver uses the VHS collision model where the parameters for the model are obtained from curve fits to Gupta's data.

The DSMC solver also uses Evans's [36] reaction rates which are slightly different from Park's coefficients. Parker's model [37] is applied to model rotational and vibrational relaxation in the DSMC module instead of using constant collision numbers. Flows around a blunted cone are simulated and compared with experimental results where the wake and boundary layer regions are simulated using DSMC. The shock region is excluded from the DSMC zone in the interest of computational time. The hybrid solution is more accurate than the full NS solution in the forebody region. Results from the use of Maxwellian and Chapman-Enskog distributions to initialize particles at the hybrid interface are compared. While surface pressure and skin friction agree between the two cases, the surface heat flux compares best with experimental data when the Chapman-Enskog distribution is used.

Wu *et al*. report [27] the coupling between the unstructured mesh finite volume NS code, HYB3D [38], with the unstructured mesh variable time step DSMC code, PDSC [39], through simulations of the flow over a wedge geometry and two parallel jets flowing into near vacuum conditions. The findings indicate that the value of the breakdown parameter is high at the shock and near the wall due to large gradients in flow properties. HYB3D employs a single trans-rotational temperature, while PDSC uses a separate rotational temperature. This coupling, therefore, benefits from the rotational energy non-equilibrium detector from Equation 1.3, alongside the gradient length local Knudsen number, to delineate NS and DSMC zones. A constant rotational collision number of 5 is employed in the DSMC code. The rotational energy non-equilibrium detector delineates a larger region around the shock as DSMC than is predicted by $Kn_{\max}$, thus validating their use of a thermal non-equilibrium detector. A Maxwellian distribution function is used to initialize particles at the buffer regions since using a Chapman-Enskog distribution was deemed to be computationally expensive. The buffer zone consists of two sets of cell layers that extend from the DSMC region into the NS region, where the number of layers in each set can be adjusted by the user. Both DSMC and NS calculations are performed in the buffers, and Dirichlet-type boundary conditions are imposed at the nodes of the buffers. A moving hybrid interface setup is used where the final converged interface locations are different from the initial locations predicted by the first NS simulation, with the DSMC regions expanding outwards from the initial interface locations until convergence. Further, it is stated that unstructured meshes are preferred for hybrid simulations since the hybrid interfaces are highly irregular and can be better represented by unstructured meshes.

The LeMANS [40] finite volume NS code has been loosely coupled with the MONACO [41] DSMC code to produce the Modular Particle Continuum (MPC) hybrid algorithm and simulate 1D shock waves, flows over 2D cylinders, and re-entry flows [42]. LeMANS started with a two-temperature model and has since evolved to solve a separate rotational energy equation, with Parker's model [37] being used for calculating the rotational collision number taken to be a function of the translational temperature. LeMANS uses the Millikan and White data [35] and Park's correction [43] to account for translational-vibrational relaxation. The MPC algorithm uses $Kn_{\max}$ to delineate the NS and DSMC regions and is capable of accounting for rotational [26] and vibrational non-equilibrium [44] and can simulate multispecies flows [45] by consistently modeling the modal energy relaxation between NS and DSMC modules. Initial efforts involved the use of the same mesh for NS, DSMC, and hybrid simulations [46], but the approach has evolved to the use of two separate meshes for NS and DSMC regions [47]. Mesh refinement is conducted on the initial mesh with the local mean free path providing a size estimate for the refinement of the NS mesh to generate a DSMC mesh comprised of refined NS cells. The refined mesh results differ from coarse mesh results in the bow shock region. The use of two meshes reduces scatter since averaging is conducted over multiple DSMC cells found within a larger NS cell in the buffer regions for information transfer. The addition of buffer regions mitigates the error arising from mislocated NS-DSMC boundaries [48]. A moving hybrid interface setup is considered where gradients that evolve in the overlap regions as the DSMC computation progresses are accounted for by a change in the interface location. A smoothing algorithm is also employed to remove isolated patches of NS or DSMC regions. During a hybrid routine, if the NS computation results in a significant change in the boundary conditions supplied to DSMC, the hybrid cycle continues. Once the hybrid boundary conditions converge, the interfaces are frozen, and the simulation runs till acceptable results have been obtained. State-based coupling is utilized, and statistical scatter in the solution vectors of the DSMC region is further minimized by using a sub-relaxation technique that combines elements of spatial and temporal averaging [49]. The time average of a macroscopic variable $\overline{\phi_n}$ at iteration n can be written as

$$\overline{\phi_n} = (1-\theta)\overline{\phi_{n-1}} + \theta\phi_n \tag{1.4}$$

where ϕ_n is the instantaneous value of the variable. This relaxation formula is said to be "sub-relaxed" when θ is less than 1 and is "over-relaxed" when θ is larger than 1.

Verhoff *et al.* [45] extend this setup to accommodate gas mixtures where continuum methods without advanced chemistry models fail to accurately capture the species concentrations in the shock and boundary layer regions at increased Knudsen numbers. The hybrid code, however, compares well with the DSMC species concentrations throughout the stagnation line. While the NS module cannot capture species concentrations well by itself, it succeeds when accurate boundary conditions are supplied by the DSMC regions of the flow. The power law model [9] is used for calculating species viscosity in LeMANS with the Gupta mixing rule [33] utilized for computing mixture transport properties. Correspondingly, the parameters of the VHS model in DSMC are calculated to match the results of the viscosity from NS. A new parameter for rotational non-equilibrium given by

$$Kn_{\mathrm{rot}} = Z_{\mathrm{r}}\lambda\left|\frac{\nabla T_{\mathrm{r}}}{T_{\mathrm{r}}}\right| \tag{1.5}$$

is also introduced, and it is found that hybrid results obtained by using $Kn_{\mathrm{ROT-NEQ}}$ deviate further from DSMC results than hybrid results obtained by using the Kn_{rot} parameter [50] along the stagnation line in the bow shock and boundary layer regions.

The DSMC Analysis Code (DAC) [51] and the Data Parallel Line Relaxation (DPLR) [52] finite volume NS solver have been employed to create a decoupled hybrid solver by Stephani *et al.* [30] to compute the solution over a patch of surface roughness used to trip the flow on the Orbiter vehicle for a 5-species air mixture [53]. A flux-based coupling between the NS and DSMC regions is employed alongside a Chapman-Enskog distribution function to initialize particles at the hybrid interface. Further, the Chapman-Enskog boundary condition is extended to accommodate mixtures and internal energies under the generalized Chapman-Enskog theory. The Variable Hard Sphere (VHS) [9] and the Variable Soft Sphere (VSS) [9] models are used to model binary collisions. Consistency in modeling transport properties, thermodynamics, and reaction models between the NS and DSMC solvers is discussed. Diffusion coefficients in DPLR are computed according to the self-consistent effective binary diffusion (SCEBD) model [54], and the viscosity and thermal conductivity are computed according to the Gupta mixing rules [33]. To fit the calculated DSMC transport coefficients with the NS solver, the Nelder-Mead Simplex Method [55] is used to find the set of VHS/VSS parameters that result in a good comparison of transport coefficients with NS values. The simplex method performs the fitting process by first starting with an initial guess of

the VHS/VSS parameters that are then perturbed. If the perturbation results in a better comparison of transport properties, the perturbation is extended in the same direction. Otherwise, the direction is reversed, and the search continues until an acceptable error level is reached in the transport property computations. The VSS model performs better than the VHS model during the fitting process by producing transport properties that compare well with NS models. When the parameters of the VHS/VSS models are specified for each collision pair rather than calculating an average set of parameters, the comparisons between the NS and DSMC transport properties improve. Rotational and vibrational conductivities in DPLR are calculated according to Eucken's model [56]. For modeling thermal non-equilibrium, DAC uses a constant rotational collision number of 5. For consistency with the NS solver, the vibrational collision number in DAC is modeled according to Gimelshein *et al.* [57]. DPLR uses a three-temperature model with separate translational, rotational, and vibrational temperatures for which the translational-rotational relaxation is modeled according to Parker [37] and the translational-vibrational relaxation is modeled according to the data of Millikan and White [35] with Park's [43] high-temperature correction.

The open-source two-temperature finite volume NS solver hy2Foam [58] and DSMC solver dsmcFoam[59] have been coupled by Espinoza *et al.* [32], and the hybrid code tested through a heat transfer flow, a Couette flow for Argon and Nitrogen with and without vibrational energy modeling and the flow over a 2D cylinder [60]. The vibrationless Nitrogen flow shows a good comparison between the single trans-rotational temperature predicted by hy2Foam with the computed trans-rotational temperature from dsmcFoam. When vibrational energy is considered, it is found to compare well between the NS, DSMC, and hybrid results. $Kn_{\max}$ and the rotational energy non-equilibrium detector are used for delineating DSMC and NS zones with state-based coupling employed for NS-DSMC communication at the hybrid interface. A Maxwellian distribution, the Chapman-Enskog distribution, and the generalized Chapman-Enskog distribution function have been used to initialize particles at the hybrid interface, and the results between the three are compared. The generalized Chapman-Enskog distribution produces the most accurate results in all the cases considered, especially for the vibrational Nitrogen flow. Translational-vibrational relaxation in hy2Foam is modeled using the Landau-Teller [56,61] formula, wherein the relaxation time is evaluated with the Millikan and White data [35] along with Park's high-temperature correction factor [62]. In dsmcFoam, the rotational collision number is taken as a

constant of 5, and the vibrational collision number is modeled to have temperature dependence [63]. The power law model [9] is used to calculate species viscosity, and Wilke's mixing rule [64] is used to model mixture transport properties in hy2Foam which is matched by the use of the VHS model in dsmcFoam.

Table 1.1 summarises the capabilities of the listed hybrid formulations. As shown, most of the NS solvers used in the hybrid algorithms are finite volume solvers. A loosely coupled strategy seems to be suitable for coupling the NS and DSMC solvers. Reliable results have been obtained with the use of a trans-rotational temperature for NS. However, it seems that temperature dependent vibrational collision numbers are necessary for the DSMC module to match the Landau-Teller, Millikan and White model in the NS module. Several studies have obtained accurate results by employing $Kn_{\max}$ to delineate NS and DSMC regions. For NS, the power law model along with mixing rules should provide a good approximation for viscosity that can be matched by the VHS model in DSMC. Importantly, there are few unstructured mesh hybrid codes and even fewer hybrid codes with mesh adaptation.

Table 1.1 List of surveyed hybrid NS-DSMC codes

Hybrid code	NS solver	Coupling	NS Rotational energy	Mesh / Adaptation?
Hash and Hassan [28]	-	Decoupled	Separate rotational temperature	- / no
Wu *et al* [27]	finite volume	Loosely coupled	Trans-rotational temperature	unstructured / no
MPC [42]	finite volume	Loosely coupled	Separate rotational temperature	structured / no
Stephani *et al* [30]	finite volume	Decoupled	Separate rotational temperature	structured / no
Espinoza *et al* [32]	finite volume	Loosely coupled	Trans-rotational temperature	structured / no

1.3 Existing DSMC Mesh Adaptation Work

The two ways of tessellating and refining the domain for DSMC methods are through structured meshes consisting of hexahedra [51,59,65-70] and unstructured meshes [41,71-73] consisting of a combination of tetrahedra, prisms, pyramids, and hexahedra. Structured mesh methods generally need a triangulated surface mesh [51,65-67] to represent surfaces where cut-cell algorithms manage the intersection of the surface mesh and the volume mesh. Such methods are grouped into hierarchical two/three level mesh [51,65,66,68] and hierarchical recursive any-level mesh [59,67,69,70] methods. Any-level mesh adaptation methods extend the mesh over several levels,

distributed in a tree-based data structure from root cells to leaf cells [67]. Mapping particles into leaf cells is a computationally expensive task that approaches a similar expense as ray tracing algorithms for unstructured meshes. In contrast, unstructured mesh approaches naturally accommodate the surface geometry and align better with singular flow features, yielding a higher resolution of gradients in regions of interest and higher flexibility [41,71] than structured mesh methods. Further, adapted unstructured meshes can rectify irregularities in the flow solutions from un-adapted meshes and produce globally smooth results. Refinement for structured and unstructured meshes requires an increase in particle count since refined volume patches and surface triangulations register lower particles and particle-surface interactions when compared against coarser meshes.

DSMC94 is the first DSMC solver developed by Bird using structured mesh technology and made freely available in 1994 [9]. It allows domain clustering by distributing node positions unevenly in the *i*, *j*, and *k* directions. Garcia *et al*. [29] developed the Adaptive Mesh and Algorithm Refinement (AMAR) method in 1999, which is the first use of mesh adaptation techniques in DSMC. In that study, a hybrid NS-DSMC algorithm is coupled to a mesh optimization routine that uses a structured hierarchical refinement strategy and an adaptive time step method. Since then, several DSMC solvers with unique features have been developed [41,51,59,68,70,74], and the few notable ones incorporating mesh adaptation are shortly discussed hereafter.

The Statistical Modeling In Low-Density Environment (SMILE) package [68, 74] provides tools to conduct the entire lifecycle of a DSMC simulation with the help of a graphical user interface: geometric modeling, preprocessing, running the DSMC algorithm, and post-processing. SMILE uses an adaptive two-layer structured mesh for collision modeling. The level-one cells store parameters required for the majorant collision frequency scheme, and the level-two cells are used to group collision candidates. The collisional mesh is adapted based on density gradients and local mfp. A separate mesh is used for the sampling routine, which may also be adapted. This multigrid approach allows SMILE to have an extremely fine mesh for collision selection and an appropriate resolution for macroscopic averaging. SMILE has been validated by analyzing the flow around the Progress spacecraft, a blunted cone, a wedge, and a space capsule [68].

The DSMC Analysis Code (DAC) [51], developed by NASA, started with a target application for a space shuttle/station plume impingement problem and was later enhanced to serve as a general-purpose tool. It has been used to capture the aerodynamic loads on the Mir space station caused by the space shuttle, simulate the flow field over NASA's X-38 re-entry vehicle, calculate the aerothermodynamics coefficients of the Mars Global Surveyor space probe and analyze the effects of the flow generated by an airlock vent on the Hubble Space Telescope. The DAC preprocessor creates an initial uniform structured mesh with cells sized to the freestream mfp on which an initial solution is computed. The gradients of the solution and the distribution of the mfp drive the adaptation of a two-level Cartesian mesh, and the body surface is captured with a triangulated surface mesh. Based on the flow field information from the previous solution, the preprocessor also sets appropriate time steps and particle weights for each cell of the adapted mesh at each iteration.

Bird's DS2V/3V suite [75] discretizes the domain with rectangular divisions that are in turn divided into rectangular elements. The number of divisions controls the visual resolution of the flow field, and the number of elements approximates the number of particles. Irregular cells are built by grouping elements closest to the cell node. The cell node is initially placed at the center of the divisions, and the node distribution throughout the domain can be adapted based on the local number density. Separate collision and sampling cells are used where the cells are adapted to have 8 particles per collision cell and 27 particles per sampling cell.

The open-source solver dsmcFoam [59] (now dsmcFoam+) can handle both structured and unstructured meshes. However, mesh adaptation is performed on structured meshes only. Gradients of density and mfp are used as adaptation scalars in an Adaptive Mesh Refinement (AMR) setup where any number of refinement levels can be created. Mesh adaptation for cube and wedge geometries has been conducted with this solver [59].

The open-source Stochastic PArallel Rarefied-gas Time-accurate Analyzer (SPARTA) DSMC code [70] built by the Sandia National Labs embeds triangulated surface geometries in a hierarchical any-level structured mesh. Here, the root level cell is the size of the domain, and each level can have as many lower-level cells in any direction as needed. SPARTA has been employed to study flows over a planetary probe geometry and a 25 – 55-degree biconic, among others.

The MONACO code [41] is the first DSMC solver to use an unstructured mesh. It has been in development by Boyd's research group since 1994 [76-78] and features several advanced techniques to accelerate a DSMC simulation. Unstructured mesh refinement is an important capability of MONACO since it allows mesh refinement based on flow features to ensure that collision cells are smaller than the local mfp and improves parallel communication. During a grid refinement cycle, cells that need to be refined are divided into smaller cells using new nodes inserted at their centroids. Then, an edge swapping operation is conducted to improve cell quality [17]. MONACO has been used for simulating various problems, including a diverging channel flow, a planetary probe, and a neutral contactor [41, 78].

Another DSMC solver that uses unstructured meshes is the unsteady, parallel DSMC code, PDSC, developed by Wu *et al*. [17, 71]. PDSC is equipped with a variable time step scheme, transient adaptive sub-cells (TAS), adaptive mesh refinement technology, and dynamic domain decomposition. During the mesh refinement procedure, adaptation scalars, such as a cell-based Knudsen number and non-dimensional density, ρ / ρ_∞, are computed and compared against threshold values. If the computed local Knudsen number is lower than the threshold value and the density ratio greater than the threshold value, the cell is marked for refinement. PDSC uses an h-refinement technique where isotropic mesh refinement is first performed on marked cells creating hanging nodes, and anisotropic refinement is then carried out to remove these nodes. Isotropic refinement is also utilized to improve the quality of the mesh cells. Some of the applications of PDSC [17, 71] are a cavity flow, a flow over a cylinder and sphere, and the interaction of twin jets in near vacuum.

One of the key parameters of mesh adaptation methods, whether structured or unstructured, is the choice of the adaptation scalar(s). A suitable adaptation scalar is generally selected, and mesh manipulation is performed based on the distribution of this scalar over the domain. Local mfp is a common choice [41,65,68,73], where the cell is refined if its characteristic dimension is greater than the local mfp. Both structured and unstructured methods advocate gradients of flow variables [59,68,69,72], such as density and velocity. Density is a natural choice since local mfp is inversely proportional to the local number density [71]. Moreover, density gradients effectively capture shocks, while the velocity gradient captures boundary layers and flow separation regions with less statistical fluctuations [72]. Some methods introduce additional criteria to disable the refinement

of cells presenting a low number of simulated particles [67,72]. From this summary of mesh adaptation techniques for DSMC, few unstructured mesh methods exist even though they present several advantages over structured mesh methods. For the choice of adaptation scalars, other flow variables such as temperatures, pressure, and Mach number have not been considered. Convergence studies involving different initial meshes that converge to the same final mesh have also not been presented in the literature. A mesh adaptation algorithm that showcases such mesh-independence capabilities will not stall when encountering poorly discretized regions (over-refined/over-coarsened) and can recover the mesh and solution quality in these regions. The present work conducts such studies.

1.4 Thesis Objectives

The CFD Lab at McGill University, in collaboration with Ansys and Lockheed Martin, is developing a monolithic software system – HALO3D (High-Altitude Low-Orbit 3D) – capable of simulating flow regimes around hypersonic aircraft from subsonic take-off speeds, acceleration to supersonic speeds, high-velocity entry into low-Earth-orbit, atmospheric re-entry at hypersonic speeds, aerobraking and landing [2,79-81]. This thesis focuses on the development and testing of the infrastructure necessary to generate the high-altitude solution in the flight path of a hypersonic transport vehicle. Along with the developments of the rarefied flow modules, the present work aims to showcase the benefits of automatic mesh optimization for rarefied flow solvers. The thesis presents computationally efficient, accurate, and robust techniques through test cases of varying complexity. Developments on adaptive hybrid interfaces, consistent hybrid thermal non-equilibrium modeling, generalized Chapman-Enskog distribution functions for particle initialization, and collision-specific collisional model parameterization are not considered and instead allocated for parallel efforts at the CFD Lab.

1.5 Thesis Contributions

The current work produces a series of Fortran modules within the HALO3D ensemble to extend its reach into the rarefied regime. After having been reviewed by experts from Ansys and Lockheed Martin, these modules have been committed into the repositories of these organizations for use in the design of hypersonic transport aircraft. The author's contributions are summarized below:

1. Development of an unstructured mesh DSMC solver – HALO3D-DSMC – to simulate high Knudsen number flows.
2. Development of a hybrid finite-element NS-DSMC architecture – HALO3D-HYBRID – to account for moderate Knudsen number flows.
3. Study of automatic mesh optimization for DSMC and hybrid NS-DSMC methods.

The thesis consists of a few novel features, which are listed below:

1. There are few works on finite element NS-DSMC solvers for hypersonic flows. This thesis employs a Finite Element NS solver in the continuum regions of the hybrid simulations. (Section 2.1, Page 17)
2. The thesis contributes to the limited body of unstructured mesh hybrid NS-DSMC and DSMC literature by investigating the generation of optimized unstructured meshes for these solvers. (Section 3.3, Page 129)
3. HALO3D-DSMC features a novel technique to generate particles in an unstructured mesh through finite element shape functions. (Section 2.2.3, Page 32)
4. An error estimate based on the Hessian of flow variables is used for the first time to evaluate both DSMC and hybrid NS-DSMC solution quality. (Section 2.4, Page 54)
5. The thesis illustrates the effect of different adaption scalars and constraints in the generation of the adapted mesh. A scalar set that has not been considered previously in the literature is used for DSMC and hybrid NS-DSMC simulations. (Section 3.3.1, Page 130)
6. Mesh convergence studies examining the effect of different initial meshes have not been seen in the literature. This thesis presents convergence studies for coarse, refined, and arbitrarily refined initial meshes. (Section 3.3.1, Page 133,134)

1.6 Thesis Outline

The thesis is organized as follows: Chapter 2 provides the methodologies employed in the HALO3D-NS, HALO3D-DSMC, and HALO3D-HYBRID routines. Governing equations, thermochemical non-equilibrium models, numerical techniques, and solution algorithms are presented. Chapter 3 discusses validation results and mesh optimization simulations for HALO3D-DSMC and HALO3D-HYBRID through hypersonic flow test cases. Chapter 4 discusses the conclusions of the study and provides directions for future work.

Chapter 2

Methodologies

This section provides details on the mathematical formulations and methodologies employed by the NS, DSMC, and hybrid modules of HALO3D and the mesh optimizer, OptiGrid. Fig. 2.1 shows the various functionalities available within HALO3D: a compressible Navier-Stokes flow solver, a magnetohydrodynamics solver, ablation and surface reaction solvers, rarefied regime DSMC, and hybrid solvers, and all of these can be coupled with OptiGrid.

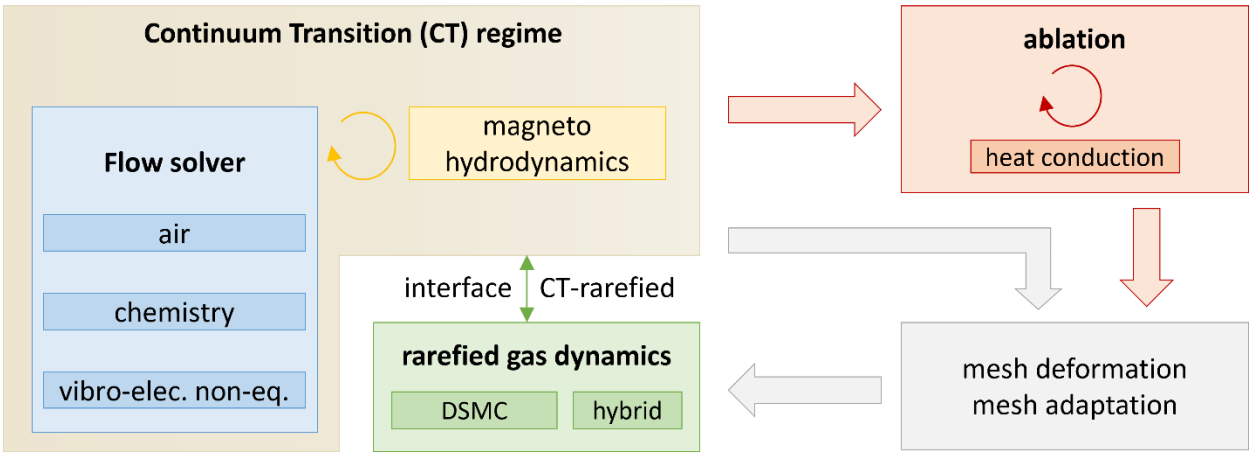

Fig. 2.1 Main modules of HALO3D

2.1 HALO3D-NS

The continuum regime thermo-chemical non-equilibrium hypersonic flow algorithm in HALO3D is composed of a compressible RANS solver, a finite-rate chemistry solver, and a two-temperature thermal non-equilibrium solver. An edge-based Finite Element formulation is employed for spatial discretization, and the Roe scheme contributes to flow stabilization due to a numerical dissipation term. In edge-based methods, the global stiffness matrix is constructed using a loop over the edges of the mesh, in contrast with element-based methods where a loop over the elements is used. The van Albada slope limiter is used to prevent oscillations near shock regions. The steady-state solution is computed by using an implicit time integration scheme. The flow equations for the conservation of mixture mass, momentum, and total energy, along with the mass conservation equations for chemical species and the conservation of vibrational energy, are solved

in a loosely coupled manner, as shown in Fig. 2.2. This Section provides details on some of the key aspects of HALO3D-NS.

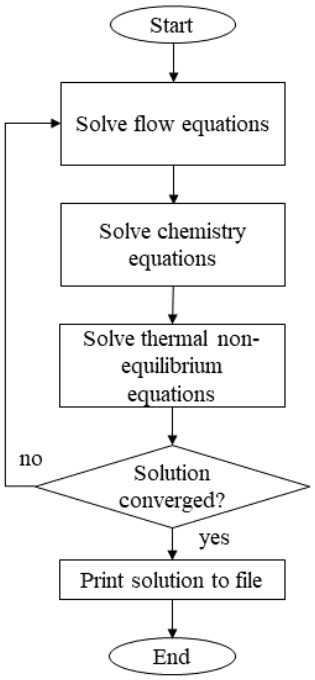

Fig. 2.2 Loosely coupled strategy of HALO3D-NS

2.1.1 Governing Equations

HALO3D-NS solves the governing equations for hypersonic flows in thermo-chemical non-equilibrium given in [61]. To account for thermal non-equilibrium, a two-temperature model is used with the translational and rotational modes represented by one temperature and the vibrational energy mode represented by another temperature. The governing equations can be written as

$$\frac{\partial \rho}{\partial t} + \nabla \cdot (\rho \boldsymbol{V}) = 0 \tag{2.1}$$

$$\frac{\partial \rho Y_s}{\partial t} + \nabla \cdot (\rho Y_s \boldsymbol{V}) = -\nabla \cdot \boldsymbol{J}_s + S_S^c \tag{2.2}$$

$$\frac{\partial \rho \boldsymbol{V}}{\partial t} + \nabla \cdot (\rho \boldsymbol{V}\boldsymbol{V}) = -\nabla P + \nabla \cdot \boldsymbol{\tau} \tag{2.3}$$

$$\frac{\partial \rho E}{\partial t} + \nabla \cdot (\rho H \boldsymbol{V}) = -\nabla \cdot \boldsymbol{q} + \nabla \cdot (\boldsymbol{\tau} \boldsymbol{V}) \tag{2.4}$$

$$\frac{\partial \rho e_v}{\partial t} + \nabla \cdot (\rho e_v \boldsymbol{V}) = -\nabla \cdot (\boldsymbol{q}_v + \boldsymbol{q}_{D,v}) + S^v \tag{2.5}$$

where t is time, ρ is mixture density, $\boldsymbol{V}$ is the velocity vector, Y_s is the mass fraction of species s, $\boldsymbol{J}_\mathrm{s}$ is the mass diffusion vector of species s, P is pressure, E is the total energy per unit mass, H is the total enthalpy per unit mass, $\boldsymbol{\tau}$ is the shear stress vector, $\boldsymbol{q}$ is the heat flux vector, S_S^c and S^v are source terms that will be elaborated in the following Sections, and e_v is the vibrational energy per unit mass. The total energy per unit volume is calculated as a sum of the kinetic and internal energies and is expressed by

$$E = \frac{1}{2}(\boldsymbol{V}\cdot\boldsymbol{V}) + \sum_{\mathrm{s}=1}^{\mathrm{N_s}} Y_\mathrm{s} e_\mathrm{s} \tag{2.6}$$

where e_s is the internal energy of species s. The gas is treated as a Newtonian fluid, and, along with the Stokes hypothesis, the viscous stress tensor is defined as

$$\boldsymbol{\tau} = \mu(\nabla\boldsymbol{V} + \nabla\boldsymbol{V}^T) - \frac{2}{3}\mu(\nabla\cdot\boldsymbol{V})\boldsymbol{I} \tag{2.7}$$

where μ is the coefficient of viscosity. The mixture components are treated as ideal gases, and the mixture equation of state links the partial pressure, trans-rotational temperature, and partial densities. Mass diffusion is modeled after Fick's law which ensures that species move from areas of higher concentration to areas of lower concentration, and the expression for the diffusion flux of species s, $\boldsymbol{J}_\mathrm{s}$**,** is given by

$$\boldsymbol{J}_\mathrm{s} = -\rho D\nabla Y_\mathrm{s} \tag{2.8}$$

where D is the mass diffusion coefficient. This is expressed as

$$D = \frac{Le\kappa_\mathrm{tr}}{\rho C_\mathrm{p}^\mathrm{tr}} \tag{2.9}$$

where the Lewis number, Le, is generally set to 1.4, κ_tr is the mixture thermal conductivity, and C_p^tr is the mixture constant pressure specific heat of the trans-rotational mode. A single diffusion coefficient is assumed for all species, ensuring that the sum of the mass diffusion fluxes is zero in the domain.

The total heat flux $\boldsymbol{q}$ from Equation 2.4 is calculated from the summation shown below

$$\boldsymbol{q} = \boldsymbol{q}_{\mathrm{tr}} + \boldsymbol{q}_{\mathrm{v}} + \boldsymbol{q}_{\mathrm{D,E}} \tag{2.10}$$

where the trans-rotational and vibrational contributions are calculated using Fourier's law. The expressions for the contributions and the inter-diffusional vibrational heat flux $\boldsymbol{q}_{\mathrm{D,v}}$ are given by

$$\boldsymbol{q}_{\mathrm{tr}} = -\kappa_{\mathrm{tr}} \boldsymbol{\nabla} T_{\mathrm{tr}} \;\; ; \;\; \boldsymbol{q}_{\mathrm{v}} = -\kappa_{\mathrm{v}} \boldsymbol{\nabla} T_{\mathrm{v}} \tag{2.11}$$

$$\boldsymbol{q}_{\mathrm{D,E}} = \sum_{\mathrm{s}=1}^{\mathrm{N_s}} \boldsymbol{J}_{\mathrm{s}} h_{\mathrm{s}} \;\; ; \;\; \boldsymbol{q}_{\mathrm{D,v}} = \sum_{\mathrm{s}=1}^{\mathrm{N_s}} \boldsymbol{J}_{\mathrm{s}} e_{\mathrm{v,s}} \tag{2.12}$$

where κ_{tr} and κ_{v} are the mixture's thermal conductivities for the respective modes.

2.1.2 Thermal Non-Equilibrium Modeling

The rigid-rotator-harmonic-oscillator model describes the rotational and vibrational energy modes where each energy mode is independent of the other. The internal energy is calculated as a sum of the energies in each mode and the zero-point energy $e_{s,f}^{0}$ of the species s, which is simply the enthalpy of formation of the species, given in Appendix A. At 298.15 K, the enthalpy of formation of molecular species is taken to be zero [82]. The two-temperature model used in the present study assumes that the translational and rotational energies are in equilibrium and are described by the trans-rotational temperature T_{tr}. The vibrational energy is described by the vibrational temperature T_{v} and the expression for internal energy is given by

$$e_{\mathrm{s}}(T_{\mathrm{tr}}, T_{\mathrm{v}}) = e_{\mathrm{s,tr}}(T_{\mathrm{tr}}) + e_{\mathrm{s,v}}(T_{\mathrm{v}}) + e_{\mathrm{s,f}}^{0} \tag{2.13}$$

where $e_{\mathrm{s,tr}}(T_{\mathrm{tr}}) = \frac{5}{2} R_{\mathrm{s}} T_{\mathrm{tr}}$ for molecules and $e_{\mathrm{s,tr}}(T_{\mathrm{tr}}) = \frac{3}{2} R_{\mathrm{s}} T_{\mathrm{tr}}$ for atoms, and R_{s} is the gas constant for species s. The vibrational energy's contribution is expressed as

$$e_{\mathrm{s,v}}(T_{\mathrm{v}}) = \frac{R_{\mathrm{s}} \theta_{\mathrm{v,s}}}{\exp\left(\frac{\theta_{\mathrm{v,s}}}{T_{\mathrm{v}}}\right) - 1} \tag{2.14}$$

where $\theta_{\mathrm{v,s}}$ is the characteristic vibrational temperature provided in Appendix A. The vibrational source term S^{v} is comprised of the contributions from the translational-vibrational energy exchange and chemical reactions, as shown below,

$$S^{\mathrm{v}} = \omega_{\mathrm{T-V}} + \omega_{\mathrm{V-D}} \tag{2.15}$$

where $\omega_{\mathrm{T-V}}$ models the energy relaxation between the translational and vibrational modes [56,61] and $\omega_{\mathrm{V-D}}$ is the vibrational energy produced or dissipated by chemical reactions assuming non-preferential dissociation. $\omega_{\mathrm{T-V}}$ is modeled using the Landau-Teller relaxation time and the expressions for both components are given by

$$\omega_{\mathrm{T-V}} = \sum_{\mathrm{s}=1}^{\mathrm{N_s}} \rho_{\mathrm{s}} \frac{e_{\mathrm{s,v}}(T_{\mathrm{tr}}) - e_{\mathrm{s,v}}(T_{\mathrm{v}})}{\tau_{\mathrm{s}}^{\mathrm{LT}}} \tag{2.16}$$

$$\omega_{\mathrm{V-D}} = \sum_{\mathrm{s}=1}^{\mathrm{N_s}} S_{\mathrm{s}}^{c} e_{\mathrm{s,v}} \tag{2.17}$$

The Landau-Teller relaxation time, $\tau_{\mathrm{s}}^{\mathrm{LT}}$, is calculated using the inter-species relaxation time τ_{si} as

$$\tau_{\mathrm{s}}^{\mathrm{LT}} = \frac{\sum_{\mathrm{i}=1}^{\mathrm{N_s}} X_{\mathrm{i}}}{\sum_{\mathrm{i}=1}^{\mathrm{N_s}} X_{\mathrm{i}}/\tau_{\mathrm{si}}} \tag{2.18}$$

τ_{si} is calculated based on the curve fits of Millikan and White [35] for vibrational relaxation using the expressions below.

$$\tau_{\mathrm{si}} = \frac{101325}{p} \exp\left[A_{\mathrm{si}}\left(T_{\mathrm{tr}}^{-\frac{1}{3}} - B_{\mathrm{si}}\right) - 18.42\right] \tag{2.19}$$

$$A_{\mathrm{si}} = (1.16 \times 10^{-3}) m_{\mathrm{si}}^{\frac{1}{2}} \theta_{\mathrm{vs}}^{\frac{4}{3}} \tag{2.20}$$

$$B_{\mathrm{si}} = 0.015 m_{\mathrm{si}}^{\frac{1}{4}} \tag{2.21}$$

$$m_{\mathrm{si}} = \frac{m_{\mathrm{s}} m_{\mathrm{i}}}{m_{\mathrm{s}} + m_{\mathrm{i}}} \tag{2.22}$$

The curve fits of Millikan and White underpredict the vibrational relaxation time at high temperatures, which necessitates the addition of Park's high-temperature correction term, $\tau_{\mathrm{p,s}}$, to τ_{si} [62]. The expression for $\tau_{\mathrm{p,s}}$ is

$$\tau_{\mathrm{p,s}} = \frac{1}{\sigma_{\mathrm{s}} c_{\mathrm{s}} N} \tag{2.23}$$

$$\sigma_{\mathrm{s}} = 10^{-21}\left(\frac{50000}{T_{\mathrm{tr}}}\right)^2 \tag{2.24}$$

$$c_{\mathrm{s}} = \sqrt{\frac{8R_{\mathrm{s}}T_{\mathrm{tr}}}{\pi}} \tag{2.25}$$

where σ_{s} is the limited collision cross-section, c_{s} is the average molecular speed, and N is the mixture number density.

2.1.3 Chemical Non-Equilibrium Modeling

Chemical non-equilibrium is accounted for by a laminar finite-rate chemistry model [83], which uses the Arrhenius equation to describe the chemical kinetics. The equilibrium constant for a reaction is calculated from the following expression:

$$K_{\mathrm{r}}^{\mathrm{eq}}(T) = \left(\frac{101325}{R_{\mathrm{u}}T}\right)^{\nu_{\mathrm{r}}} \exp\left(-\sum_{\mathrm{s}=1}^{\mathrm{N_s}}\left(\nu''_{\mathrm{s,r}} - \nu'_{\mathrm{s,r}}\right)(H_{\mathrm{s}} - TS_{\mathrm{s}})\right) \tag{2.26}$$

where $\nu'_{\mathrm{s,r}}$ and $\nu''_{\mathrm{s,r}}$ are the stoichiometric coefficients of the reactant and product for species s and reaction r, R_{u} is the universal gas constant, H_{s} and S_{s} are the enthalpy and entropy calculated from Boltzmannian theory. The forward reaction rate coefficient is calculated using the modified Arrhenius equation expressed by

$$k_{\mathrm{r}}^{\mathrm{f}}\left(\overline{T}\right) = A_{\mathrm{r}}^{\mathrm{f}}\overline{T}^{\eta_{\mathrm{r}}^{\mathrm{f}}} \exp\left(-\frac{E_{\mathrm{a,r}}}{R_{\mathrm{u}}\overline{T}}\right) \tag{2.27}$$

where for a reaction r, $A_{\mathrm{r}}^{\mathrm{f}}$is the pre-exponential factor, $\eta_{\mathrm{r}}^{\mathrm{f}}$ is the temperature exponent and $E_{\mathrm{a,r}}$ is the activation energy which can all be found in the literature. $\overline{T}$ is the rate controlling temperature defined according to Park's model as

$$\overline{T} = T_{\mathrm{tr}}^{\mathrm{q}}\, T_{\mathrm{v}}^{\mathrm{q-1}} \tag{2.28}$$

with the exponent q set to be 0.7. The backward reaction rate coefficient can be calculated from the forward rate coefficient and the equilibrium constant as shown below.

$$k_{\mathrm{r}}^{\mathrm{b}}(T) = \frac{k_{\mathrm{r}}^{\mathrm{f}}(T)}{K_{\mathrm{r}}^{\mathrm{eq}}(T)} \tag{2.29}$$

The chemical source term in Equation 2.2 for a species s is given by

$$S_{\mathrm{S}}^{\mathrm{c}} = m_{\mathrm{s}} \sum_{\mathrm{r}=1}^{\mathrm{N_r}} \left(\nu''_{\mathrm{s,r}} - \nu'_{\mathrm{s,r}}\right)\left(R_{\mathrm{r}}^{\mathrm{f}} - R_{\mathrm{r}}^{\mathrm{b}}\right) \tag{2.30}$$

where m_{s} is the species molar mass, $R_{\mathrm{r}}^{\mathrm{f}}$ is forward reaction rate and $R_{\mathrm{r}}^{\mathrm{b}}$ is the backward reaction rate of reaction r. The reaction rates are calculated from the rate coefficients, species mole fractions, and stoichiometric coefficients as shown below.

$$R_{\mathrm{r}}^{\mathrm{f}} = k_{\mathrm{r}}^{\mathrm{f}} \prod_{\mathrm{s}=1}^{\mathrm{N_s}} [X_{\mathrm{s}}]^{\nu'_{\mathrm{s,r}}} \tag{2.31}$$

$$R_{\mathrm{r}}^{\mathrm{b}} = k_{\mathrm{r}}^{\mathrm{b}} \prod_{\mathrm{p}=1}^{\mathrm{N_s}} [X_{\mathrm{p}}]^{\nu''_{\mathrm{p,r}}} \tag{2.32}$$

2.1.4 Viscosity and Thermal Conductivity

The species viscosities are calculated according to the Power law model, which is compatible with the use of the VHS collision model in the DSMC zones of the hybrid computation. The expression for the species viscosity is

$$\mu_{\mathrm{s}} = \mu_{\mathrm{s,ref}} \left(\frac{T}{T_{\mathrm{s,ref}}}\right)^{\omega} \tag{2.33}$$

$$\mu_{\mathrm{s,ref}} = \frac{15\sqrt{\pi m_{\mathrm{s}} k T_{\mathrm{s,ref}}}}{2\pi d_{\mathrm{s,ref}}^2 (5-2\omega)(7-2\omega)} \tag{2.34}$$

where $\mu_{\mathrm{s,ref}}$ is the reference viscosity, $T_{\mathrm{s,ref}}$ is the reference temperature, ω is the power law exponent, m_{s} is the molecular/atomic mass and $d_{\mathrm{s,ref}}$ is the reference diameter of species s.

The evaluation of the species thermal conductivities requires the separate calculation of the trans-rotational and vibrational contributions from Eucken's relation [56] using the following expressions

$$\kappa_{\mathrm{s,tr}} = \mu_{\mathrm{s}} \left(\frac{5}{2} C_{\mathrm{v,s}}^{\mathrm{t}} + C_{\mathrm{v,s}}^{\mathrm{r}}\right) \tag{2.35}$$

$$\kappa_{\mathrm{s,v}} = \mu_{\mathrm{s}} C_{\mathrm{v,s}}^{\mathrm{v}} \tag{2.36}$$

where $C_{v,s}^{t}$, $C_{v,s}^{r}$, $C_{v,s}^{v}$ are the species translational, rotational, and vibrational specific heats at constant volume. These specific heats are given by the following relations

$$C_{v,s}^{t} = \frac{3}{2} R_s \tag{2.37}$$

$$C_{v,s}^{r} = R_s \tag{2.38}$$

$$C_{v,s}^{v} = R_s \frac{\left(\frac{\theta_{v,s}}{T_{v,s}}\right)^2 \exp\left(\frac{\theta_{v,s}}{T_{v,s}}\right)}{\left(\exp\left(\frac{\theta_{v,s}}{T_{v,s}}\right) - 1\right)^2} \tag{2.39}$$

The species constant pressure specific heats are calculated from the constant volume specific heats for the translational mode $C_{p,s}^{t}$ and the trans-rotational mode $C_{p,s}^{tr}$ as

$$C_{p,s}^{t} = C_{v,s}^{t} + R_s \tag{2.40}$$

$$C_{p,s}^{tr} = C_{p,s}^{t} + C_{v,s}^{r} \tag{2.41}$$

The mixture viscosity is calculated using Wilke's mixing rule [64], and the mixture thermal conductivity is calculated using Mason's mixing rule [84]. The expressions for the mixture viscosity and thermal conductivity are given by

$$\mu = \sum_{s=1}^{N_s} \frac{X_s \mu_s}{\phi_s} \tag{2.42}$$

$$\kappa = \sum_{s=1}^{N_s} \frac{X_s \kappa_s}{\phi_s} \tag{2.43}$$

$$\phi_s = X_s + \sum_{i=1}^{N_s} X_i \left[1 + \sqrt{\frac{\mu_s}{\mu_i}} \left(\frac{M_i}{M_s}\right)^{\frac{1}{4}}\right]^2 \left[\sqrt{8\left(1 + \frac{M_s}{M_i}\right)}\right]^{-1} ; \; i \neq s \tag{2.44}$$

where μ_s is the species viscosity, κ_s is the species conductivity, X_s is the species mole fraction and ϕ_s is a scaling factor.

2.1.5 Slip and Jump Boundary Conditions

No-slip boundary conditions for temperature and velocity are no longer valid for Knudsen numbers (Kn) higher than 0.01 [9]. However, the domain of validity of the RANS equations can

be extended to Kn ~ 0.1 by using Maxwell's velocity slip and Smoluchowski's temperature jump boundary conditions [85] given by

$$\boldsymbol{V} = \boldsymbol{V}_{\mathrm{w}} - \frac{\lambda}{\mu}\frac{2-\sigma}{\sigma}\,\boldsymbol{\tau}_{\mathrm{slip}} - \frac{3}{4}\,\frac{(\gamma-1)Pr}{\gamma\, p}\,\mathbf{q}_{\mathrm{slip}} \tag{2.45}$$

$$T = T_{\mathrm{w}} + \frac{2-\alpha}{\alpha}\,\frac{2\gamma}{\gamma+1}\,\frac{\lambda}{Pr}\,\boldsymbol{\nabla} T \cdot \mathbf{n} \tag{2.46}$$

where $\boldsymbol{V}_{\mathrm{w}}$ and T_{w} are the prescribed wall velocity and temperature, $\boldsymbol{\tau}_{\mathrm{slip}}$ and $\mathbf{q}_{\mathrm{slip}}$ are the tangential components of the shear stress and heat flux vectors, respectively, $\mathbf{n}$ is wall normal vector, γ is the specific heat ratio, α and σ are the thermal and tangential momentum accommodation coefficients, respectively, with λ denoting the mean free path and Pr the Prandtl number.

2.1.6 Numerical Modeling

The governing equations can be rewritten in flux-divergence form as

$$\frac{\partial \boldsymbol{Q}}{\partial t} + \boldsymbol{\nabla} \cdot (\boldsymbol{F}^{\mathrm{A}}(\boldsymbol{Q}) - \boldsymbol{F}^{\mathrm{V}}(\boldsymbol{Q}, \boldsymbol{\nabla Q})) = \boldsymbol{S} \tag{2.47}$$

where $\boldsymbol{Q}$ is the vector of conservative variables, and $\boldsymbol{F}^{\mathrm{A}}$ and $\boldsymbol{F}^{\mathrm{V}}$ are the inviscid and viscous fluxes, respectively. The weak-Galerkin formulation of these equations can be obtained by multiplying both sides with a linear test function W_i (chosen as the shape function) at node i and integrating by parts [86]. This is expressed as

$$\int_{\Omega} W_{\mathrm{i}} \frac{\partial \boldsymbol{Q}}{\partial t} - \int_{\Omega} \boldsymbol{\nabla} W_{\mathrm{i}} \cdot (\boldsymbol{F}^{\mathrm{A}} - \boldsymbol{F}^{\mathrm{V}}) + \int_{\partial\Omega} W_{\mathrm{i}} \boldsymbol{n} \cdot (\boldsymbol{F}^{\mathrm{A}} - \boldsymbol{F}^{\mathrm{V}}) = \int_{\Omega} W_{\mathrm{i}} \boldsymbol{S} \tag{2.48}$$

where Ω represents integration over the volume of the domain and $\partial\Omega$ represents integration over the boundary surface. Linear finite element shape functions are used in this work since higher-order shape functions perform poorly when capturing discontinuities such as shocks, and anisotropic mesh adaptation is much simpler, more efficient, and easier to implement than higher-order implementations. The shape functions are constructed by first choosing an interpolation polynomial of a certain order. While a polynomial of infinite order returns the exact solution, for practical reasons, a finite order must be chosen. Then the solution within an element is expressed

as the sum of the products of the nodal solutions and purely geometric quantities, namely the shape functions. $\boldsymbol{Q}$ and $\boldsymbol{S}$ are interpolated using a linear shape function N_{j} at node j and the inviscid flux $\boldsymbol{F}^{\mathrm{A}}$ is discretized by the group representation [87]. The relation between the $\boldsymbol{Q}$, $\boldsymbol{F}^{\mathrm{A}}$, $\boldsymbol{S}$ fields, their nodal values, and shape functions N_{j} is given by

$$\boldsymbol{Q}(x,t) = \sum_{\mathrm{j}=1}^{\mathrm{N_N}} N_{\mathrm{j}}(x)\boldsymbol{Q}_{\mathrm{j}}(t) \tag{2.49}$$

$$\boldsymbol{F}^{\mathrm{A}}(x,t) = \sum_{\mathrm{j}=1}^{\mathrm{N_N}} N_{\mathrm{j}}(x)\boldsymbol{F}_{\mathrm{j}}^{\mathrm{A}}(t) \tag{2.50}$$

$$\boldsymbol{S}(x,t) = \sum_{\mathrm{j}=1}^{\mathrm{N_N}} N_{\mathrm{j}}(x)\boldsymbol{S}_{\mathrm{j}}(t) \tag{2.51}$$

where the summations are over all the nodes in the mesh.

Using Equations 2.49-2.51, the governing equations can be rewritten as

$$\sum_{\mathrm{e}\in\mathrm{E_i}}\sum_{\mathrm{j}\in\mathrm{K_e}}\int_{V^{\mathrm{e}}} W_{\mathrm{i}}N_{\mathrm{j}}\frac{dQ_{\mathrm{j}}}{\partial t}dV - \sum_{\mathrm{e}\in\mathrm{E_i}}\sum_{\mathrm{j}\in\mathrm{K_e}}\int_{V^{\mathrm{e}}} N_{\mathrm{j}}\boldsymbol{\nabla}W_{\mathrm{i}}\cdot\boldsymbol{F}_{\mathrm{j}}^{\mathrm{A}}dV + \sum_{\mathrm{e}\in\mathrm{E_i}}\int_{V}\boldsymbol{\nabla}W_{\mathrm{i}}\cdot\boldsymbol{F}^{\mathrm{V}}dV$$
$$+\sum_{\mathrm{e}\in\mathrm{F_i}}\int_{A} W_{\mathrm{i}}\mathbf{n}\cdot(\boldsymbol{F}^{\mathrm{A}}-\boldsymbol{F}^{\mathrm{V}})\,dA = \sum_{\mathrm{e}\in\mathrm{E_i}}\sum_{\mathrm{j}\in\mathrm{K_e}}\int_{V^{\mathrm{e}}} W_{\mathrm{i}}N_{\mathrm{j}}S_{\mathrm{j}}dV \tag{2.52}$$

where $\mathrm{E_i}$ and $\mathrm{F_i}$ are the sets of cells and facets connected to node i, $\mathrm{K_e}$ is the set of nodes of cell e, V is the volume of the domain, and V^{e} is the volume of the cell e.

The viscous and inviscid fluxes are discretized with an edge-based finite element formulation that is less expensive than element-based formulations [88]. Gauss-Legendre quadrature is used to evaluate volume and surface integrals. The second and third terms in Equation 2.52 can be recast in an edge-based manner [89,90] as

$$-\sum_{\mathrm{e}\in\mathrm{E_i}}\sum_{\mathrm{j}\in\mathrm{K_e}}\int_{V^{\mathrm{e}}} N_{\mathrm{j}}\boldsymbol{\nabla}W_{\mathrm{i}}\cdot\boldsymbol{F}_{\mathrm{j}}^{\mathrm{A}}dV = \sum_{\mathrm{j}\in\mathrm{K_i}}\boldsymbol{\eta}_{\mathrm{ij}}\cdot\frac{\boldsymbol{F}_{\mathrm{i}}^{\mathrm{A}}+\boldsymbol{F}_{\mathrm{j}}^{\mathrm{A}}}{2} - \sum_{\mathrm{j}\in\mathrm{K_i}}\boldsymbol{\chi}_{\mathrm{ij}}\cdot\frac{\boldsymbol{F}_{\mathrm{j}}^{\mathrm{A}}-\boldsymbol{F}_{\mathrm{i}}^{\mathrm{A}}}{2} \tag{2.53}$$

$$\boldsymbol{\eta}_{\mathrm{ij}} = \sum_{\mathrm{e}\in\mathrm{E_i}}\int_{V^{\mathrm{e}}}\left(W_{\mathrm{i}}\boldsymbol{\nabla}N_{\mathrm{j}} - N_{\mathrm{j}}\boldsymbol{\nabla}W_{\mathrm{i}}\right)dV \tag{2.54}$$

$$\boldsymbol{\chi}_{\mathrm{ij}} = \sum_{\mathrm{e}\in\mathrm{E_i}} \int_A W_{\mathrm{i}} N_{\mathrm{j}} \mathbf{n}\, dA \tag{2.55}$$

where $\mathrm{K_i}$ is the set of nodes connected to node i through a cell, and $\boldsymbol{\eta}_{\mathrm{ij}}$ and $\boldsymbol{\chi}_{\mathrm{ij}}$ are edge coefficients that have to only be computed once rather than at each iteration.

The numerical discretization of the viscous fluxes requires the formulation of the inter-diffusional mass flux, inter-diffusional heat flux in both the total energy equation and the vibrational energy equation, heat fluxes of the trans-rotational and vibrational modes, stress tensor, and the inner product of the stress tensor and velocity. The edge-based assembly of the stress tensor is given by

$$\sum_{\mathrm{e}\in\mathrm{E_i}} \int_V \boldsymbol{\nabla} W_{\mathrm{i}} \cdot \boldsymbol{\tau} dV = \sum_{\mathrm{j}\in\mathrm{K_i}} \left[\left(\mu_{\mathrm{ij}} \mathrm{tr}\left(\mathbf{d}_{\mathrm{ij}}\right)\mathbf{I} + \left(\mu_{\mathrm{ij}} + \lambda_{\mathrm{ij}}\right)\mathbf{d}^{\mathrm{S}}_{\mathrm{ij}} + \left(\lambda_{\mathrm{ij}} - \mu_{\mathrm{ij}}\right)\mathbf{d}^{\mathrm{A}}_{\mathrm{ij}}\right)\left(\boldsymbol{V}_{\mathrm{j}} - \boldsymbol{V}_{\mathrm{i}}\right) \right] \tag{2.56}$$

$$\mathbf{d}_{\mathrm{ij}} = \sum_{\mathrm{e}\in\mathrm{E_i}} \int_{V^{\mathrm{e}}} (\boldsymbol{\nabla} W_{\mathrm{i}} \boldsymbol{\nabla} N_{\mathrm{j}}) dV \tag{2.57}$$

where the edge center quantities, μ_{ij} and λ_{ij}, are the averages of the node values, tr() is the trace operator, $\mathbf{d}^{\mathrm{S}}_{\mathrm{ij}}$ and $\mathbf{d}^{\mathrm{A}}_{\mathrm{ij}}$ are the symmetric and anti-symmetric components of the edge coefficient $\mathbf{d}_{\mathrm{ij}}$. The edge-based assembly of the other components of the viscous fluxes is performed similarly and these formulations, along with further details on the numerical modeling of HALO3D-NS can be found in [91].

2.1.7 Dirichlet Boundary Conditions

Using Dirichlet boundary conditions, flow variables such as pressure, temperatures, velocities, and mass fractions are imposed at the domain boundaries. For enforcing Dirichlet boundary conditions on conservative variables, the rows in the system matrix and the RHS that belong to the variable are zeroed, and the diagonal element takes a value of one. To enforce Dirichlet boundary conditions for primitive variables such as temperature, constraints expressed for temperature should be rewritten in terms of equivalent conservative variables. The system matrix for hybrid NS-DSMC simulations consists of entries from the entire mesh, where entries for the DSMC regions of the mesh are the imposed Dirichlet boundary conditions for flow variables discussed in the following Sections. Imposing a constant pressure at any boundary or DSMC node is equivalent to imposing $\Delta p = 0$. In conservative variables form, this can be written as

$$\frac{\boldsymbol{V}\cdot\boldsymbol{V}}{2}\Delta\rho-\boldsymbol{V}\cdot\Delta(\rho\boldsymbol{V})+\Delta e\ =0 \tag{2.58}$$

and is imposed by placing this expression in the system matrix as

$$\begin{bmatrix}\frac{\boldsymbol{V}\cdot\boldsymbol{V}}{2} & -\boldsymbol{V} & 1\\ \cdot & \cdot & \cdot\\ \cdot & \cdot & \cdot\end{bmatrix}\begin{bmatrix}\Delta\rho\\ \Delta(\rho\boldsymbol{V})\\ \Delta e\end{bmatrix}=\begin{bmatrix}0\\ \cdot\\ \cdot\end{bmatrix} \tag{2.59}$$

A given trans-rotational temperature can be imposed at any node by imposing $\Delta T_{\mathrm{tr}}\ =0$ which in conservative variables form is given by

$$\left(\frac{\boldsymbol{V}\cdot\boldsymbol{V}}{2}-e_{\mathrm{int}}\right)\Delta\rho-\boldsymbol{V}\cdot\Delta(\rho\boldsymbol{V})+\Delta e\ =0 \tag{2.60}$$

Imposing the vibrational temperature is done similarly. Imposing constant mass fractions is done by imposing $\Delta Y_{\mathrm{s}}\ =0$.

$$(1-Y_{\mathrm{s}})\Delta(\rho Y_{\mathrm{s}})-Y_{\mathrm{s}}\sum_{\mathrm{i}\neq\mathrm{s}}\Delta(\rho Y_{\mathrm{i}})\ =0 \tag{2.61}$$

2.2 HALO3D-DSMC

This Section highlights the mathematical expressions used and key functionalities present in HALO3D-DSMC, which is an unstructured mesh DSMC code capable of accounting for thermochemical non-equilibrium and employing advanced sub-cell methods. Parallelization is achieved by conducting the sampling stage over a user-defined number of independent ensembles. The code is written in a modular fashion within the HALO3D ensemble, making it possible to share several existing features such as the data read/write routines, data structures, graphical user interface, convergence monitors, solution visualizers, and mesh editors. These functionalities have been developed by former CFD Lab students and experts and thanks to their efforts, the present work was accelerated. A description of a single DSMC iteration has been provided in Chapter 1, and this has been illustrated in Fig. 2.3. While this Section covers most DSMC methodologies, some DSMC features function differently during hybrid simulations, and these are also discussed here.

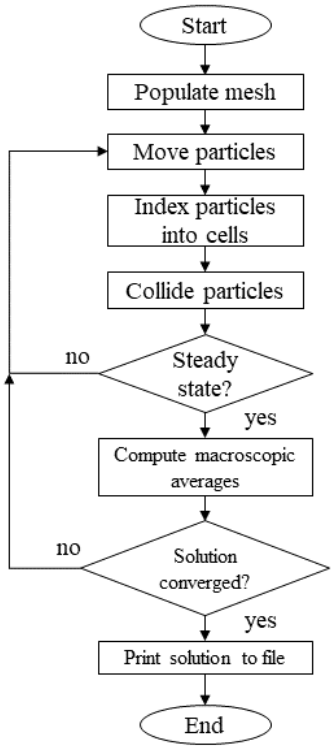

Fig. 2.3 Algorithm of HALO3D-DSMC

2.2.1 Data Structure

A combination of static and object-oriented data is chosen in such a way as to facilitate further code extensions and minimize computational cost. The DSMC particle information is stored in dynamic arrays, while each module composing the collision routine is defined as a derived type. Boundary conditions, macroscopic property estimation, mesh populators, and element occupancy are implemented like the collision routine, alongside the use of a holder as described in [92].

2.2.2 Background NS-DSMC Mesh

The grid module used by HALO3D-NS is preserved for HALO3D-DSMC and HALO3D-HYBRID, with the addition of cell-facet-node connectivity to the existing cell-node connectivity. A single unstructured background mesh is utilized in the computation for both the continuum and rarefied regions in hybrid and full DSMC simulations. The cell-facet-node connectivity information is used in particle tracking, computations at the boundaries, file output, various sub-cell methods, and buffer creation. These connectivity arrays are illustrated in Fig. 2.4 for a generic unstructured mesh where each connectivity array has an associated array of pointers. Each pointer

array element points to the initial position of the segment of nodes/cells/facets (colored differently) that are connected to the mesh object of the connectivity array. A zero in the facet-cell connectivity array implies that one out of the two cells connected to the facet does not exist, i.e., the facet is a boundary facet.

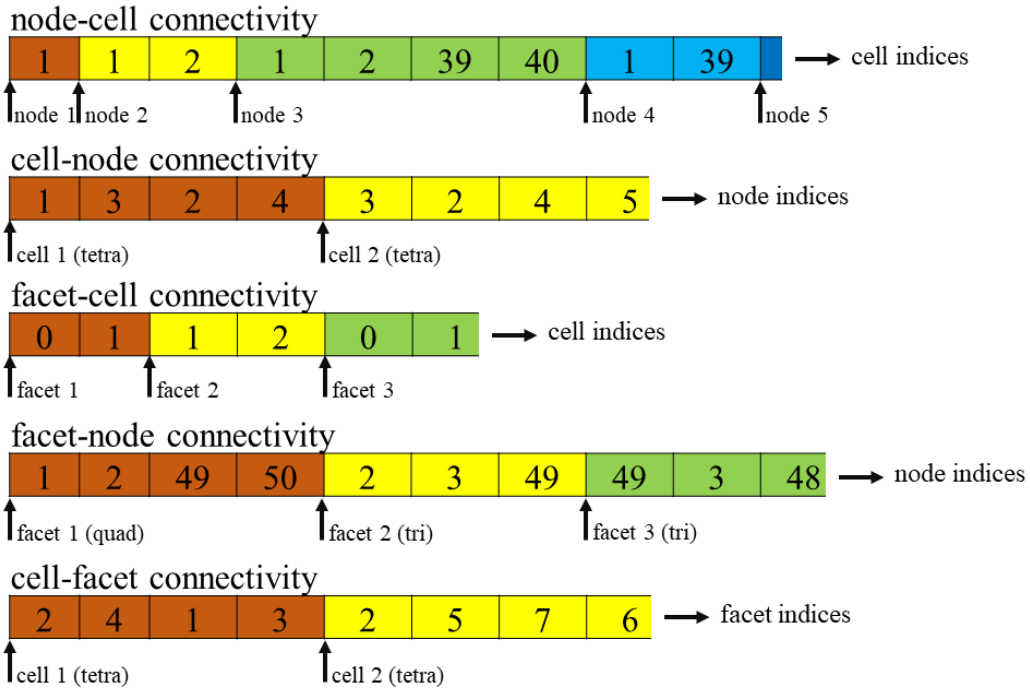

Fig. 2.4 Mesh connectivity information required by DSMC and hybrid solvers

2.2.3 Mesh Population

Particles are created in the mesh at the beginning of a DSMC simulation and are inserted into the domain at every time step through the inlet patches. During the initialization of the DSMC calculation for the first hybrid cycle, particles are created once in the DSMC and inner buffer regions. Particles in the outer buffer are created anew at every DSMC inner iteration. The particle velocities are calculated from a Maxwellian velocity distribution, shown below, offset by the local NS velocity.

$$f_o(c) = \sqrt{\left(\frac{m}{2\pi k T_t}\right)^3} \exp\left(-\frac{mc^2}{2kT_t}\right) \tag{2.62}$$

While it is not considered in the present work, the Chapman-Enskog distribution, $f_{\mathrm{CE}}(c)$, provided below may prove useful in initializing particles for complex flows [53,60].

$$f_{\mathrm{CE}}(c) = f_{\mathrm{o}}(c)\begin{bmatrix} 1 + (\hat{\boldsymbol{q}}_{\mathrm{t}} \cdot \beta \boldsymbol{c})\left(\frac{2}{5}\beta^2 c^2 - 1\right) \\ -\beta^2\left(2\left(\hat{\tau}_{\mathrm{xy}}c_{\mathrm{x}}c_{\mathrm{y}} + \hat{\tau}_{\mathrm{xz}}c_{\mathrm{x}}c_z + \hat{\tau}_{\mathrm{zy}}c_z c_{\mathrm{y}}\right) + \left(\hat{\tau}_{\mathrm{xx}}c_{\mathrm{x}}^2 + \hat{\tau}_{\mathrm{yy}}c_{\mathrm{y}}^2 + \hat{\tau}_{\mathrm{zz}}c_{\mathrm{z}}^2\right)\right) \end{bmatrix} \quad (2.63)$$

The expressions for β, the non-dimensional heat flux $\hat{\boldsymbol{q}}_{\mathrm{t}}$, and the non-dimensional shear stress $\hat{\tau}_{\mathrm{ij}}$ are

$$\beta = \sqrt{\frac{m}{2kT_{\mathrm{t}}}} \qquad \hat{\boldsymbol{q}}_{\mathrm{t}} = \frac{2\boldsymbol{q}_{\mathrm{t}}\beta}{p} \qquad \hat{\tau}_{\mathrm{ij}} = \frac{\tau_{\mathrm{ij}}}{p} \quad (2.64)$$

The rotational and vibrational energies of newly created particles are assigned based on the following expressions [75].

$$e_{\mathrm{r}} = -\ln(R)\, kT_{\mathrm{r}} \quad (2.65)$$

$$i_{\mathrm{v}} = \left|-\frac{\ln(R)\, T_{\mathrm{v}}}{\theta_{\mathrm{v}}}\right| \quad (2.66)$$

$$e_{\mathrm{v}} = i_{\mathrm{v}} k\theta_{\mathrm{v}} \quad (2.67)$$

Equations 2.66 and 2.67 state the vibrational energy level and vibrational energy for a given vibrational mode at a characteristic vibrational temperature θ_{v}, and R is a random number distributed between 0 and 1. The degeneracy g_{v} and modal vibrational energies e_{v} are needed to calculate the total vibrational energy $e_{\mathrm{v}}^{\mathrm{tot}}$ as shown below.

$$e_{\mathrm{v}}^{\mathrm{tot}} = \sum_{\mathrm{m}=1}^{\mathrm{N_m}} g_{\mathrm{v}}(m)\, e_{\mathrm{v}}\,(m) \quad (2.68)$$

To initialize particles in full DSMC simulations, the velocities and modal temperatures used are those of the freestream or obtained from a restart file.

For generating the particle positions, HALO3D-DSMC leverages the finite element functionalities of HALO3D to seed particles in primitive space and then transform their

coordinates to physical space using shape functions. The expression for the particle coordinates in physical space is

$$\boldsymbol{x} = \sum_{\mathrm{j}} \hat{\boldsymbol{x}}_{\mathrm{j}} N_{\mathrm{j}}(\boldsymbol{\xi}) \tag{2.69}$$

where $\boldsymbol{x}$ and $\boldsymbol{\xi}$ represent the position of a particle in physical and primitive spaces, respectively, $\hat{\boldsymbol{x}}_{\mathrm{j}}$ denotes the nodal coordinates of the cell in physical space, and N_{j} is the nodal shape function for node j at a position $\boldsymbol{\xi}$.

2.2.4 Particle Tracking

Unlike Cartesian meshes, where particle tracking is trivial, unstructured mesh methods require a facet-intersection algorithm. Macpherson *et al.* proposed a robust 3D algorithm valid for arbitrary polyhedral meshes [93] that has been found to be suitable for this work after a battery of tests ensuring watertightness. Here, two non-dimensional parameters called "move-fractions" that are given by the following expressions

$$\lambda_a = \frac{(\boldsymbol{C}_{\mathrm{f}} - \boldsymbol{a}) \cdot \boldsymbol{S}}{(\boldsymbol{b} - \boldsymbol{a}) \cdot \boldsymbol{S}} \tag{2.70}$$

$$\lambda_c = \frac{(\boldsymbol{C}_{\mathrm{f}} - \boldsymbol{C}_{\mathrm{c}}) \cdot \boldsymbol{S}}{(\boldsymbol{b} - \boldsymbol{C}_{\mathrm{c}}) \cdot \boldsymbol{S}} \tag{2.71}$$

are used to evaluate facets as potential intersection candidates with the particle trajectory, where $\boldsymbol{C}_{\mathrm{f}}$ is the face center, $\boldsymbol{S}$ is the face normal, $\boldsymbol{C}_{\mathrm{c}}$ is the cell center, $\boldsymbol{a}$ is the initial position and $\boldsymbol{b}$ is the final position of the particle. Snapshots of the particle cloud are presented in Fig. 2.5, where a million particles are seeded in four geometries: a hexahedron, a hexahedron with a slightly warped facet, a structured mesh of a cube geometry and an unstructured mesh of a star shaped geometry. DSMC computations are performed for 100,000 time steps, and no particle loss events are recorded in any of the cases, surprisingly, even for the slightly warped hexahedron.

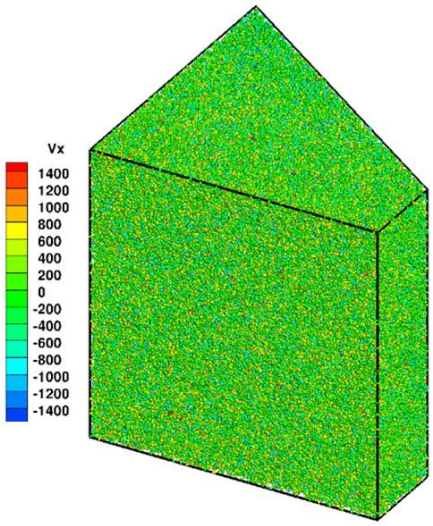

(a) Generic hexahedron

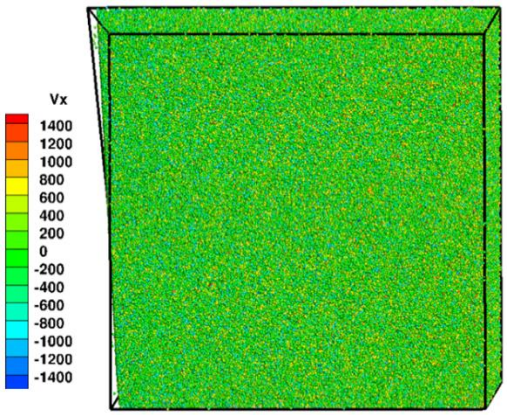

(b) Hexahedron with a warped facet

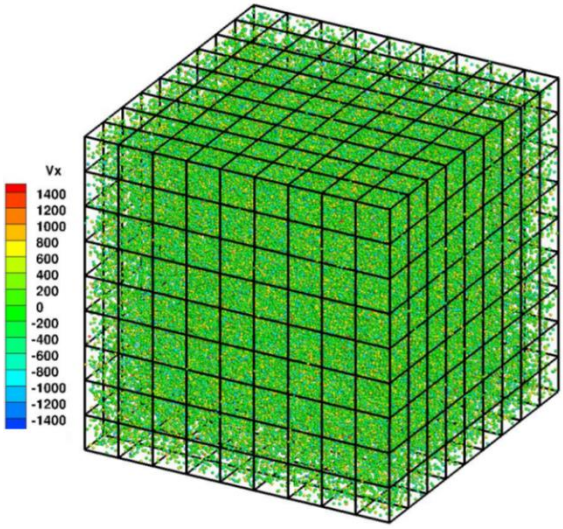

(c) Hexahedral discretization

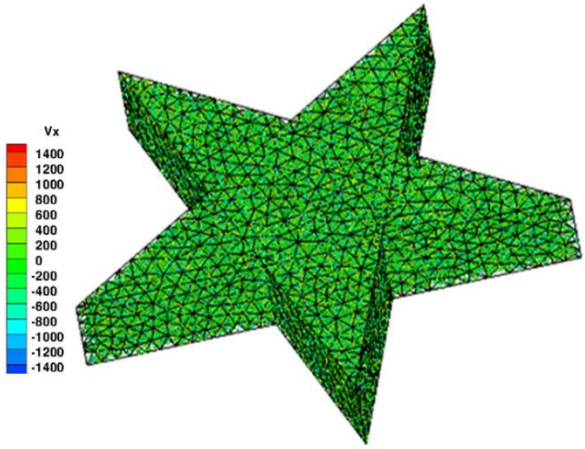

(d) Tetrahedral discretization

Fig. 2.5 Particles tracked in different meshes and colored based on their x-velocity

2.2.5 Collision Routine

Bird's No-Time-Counter (NTC) scheme [75,94], requiring a minimum of 20 particles per cell for statistical accuracy, is employed to evaluate an *a priori* number of collision candidates (N_{coll}) in each cell. This number can be calculated as

$$N_{\text{coll}} = \frac{N\bar{N}W_{\text{f}}(\sigma_{\text{T}}c_{\text{r}})_{\max}\Delta t}{2\,V_{\text{el}}} \tag{2.72}$$

where N is the number of particles in an element, $\bar{N}$ is the time averaged value of the number of particles in an element, W_{f} is the weight of each computational particle, σ_{T} is the total collision cross-section, c_{r} is the relative velocity of the particle pair, $(\sigma_{\text{T}}c_{\text{r}})_{\max}$ is the maximum value of their products, Δt is the time step, and V_{el} is the volume of the collision cell. The total collision cross-section is calculated from the following expression

$$\sigma_{\text{T}} = \pi d_{\text{ref}}^2 \left(\frac{2kT_{\text{ref}}}{m_{\text{r}}c_{\text{r}}^2}\right)^{\omega-\frac{1}{2}} \div \Gamma\left(\frac{5}{2}-\omega\right) \tag{2.73}$$

where d_{ref} is the average reference diameter of the species pair, T_{ref} is the average of the reference temperatures of the two species, m_{r} is the reduced mass of the species pair and ω is the average temperature exponent of viscosity. Once the number of particle pairs to be tested for collisions is established, particles are selected based on the sub-cell methods being employed [95] and are evaluated for elastic collisions (addressed in this Section) and inelastic collisions (explained in the following Sections). For each selected particle pair, a probability ratio given by

$$\frac{P}{P_{\max}} = \frac{\sigma_{\text{T}}c_{\text{r}}}{(\sigma_{\text{T}}c_{\text{r}})_{\max}} \tag{2.74}$$

is calculated and evaluated against a random number in an acceptance-rejection routine to determine if the particle pair is to undergo a collision or not.

Binary collision dynamics are handled by the VHS model [9] to calculate post-collision scattering angles and relative velocities. The cross-section in the VHS model is taken to be a function of the relative translational energy. First, the magnitude of the post-collision relative velocity $C_{\text{R}}^{\text{post}}$ is calculated based on the pre-collision velocities of the particles using the expression below.

$$C_{\text{R}}^{\text{post}} = \left|\boldsymbol{C}_1^{\text{post}} - \boldsymbol{C}_2^{\text{post}}\right| = \left|\boldsymbol{C}_1^{\text{pre}} - \boldsymbol{C}_2^{\text{pre}}\right| = C_{\text{R}}^{\text{pre}} \tag{2.75}$$

Following this, the three components of the velocity of the center of mass (which, along with the relative velocity, is unchanged post-collision) of the two particles, C_{CM}, is calculated from the pre-collision velocities C_1^{pre} and C_2^{pre} and species masses m_1 and m_2 as

$$C_{\mathrm{CM,x,y,z}} = \frac{m_1 C_{1,\mathrm{x,y,z}}^{\mathrm{pre}} + m_2 C_{2,\mathrm{x,y,z}}^{\mathrm{pre}}}{m_1 + m_2} \tag{2.76}$$

The scattering angles α and β are obtained using two different random numbers denoted by R in the following relations

$$\cos(\beta) = 2R - 1 \tag{2.77}$$

$$\alpha = 2\pi R \tag{2.78}$$

These angles, along with the magnitude of the post-collision relative velocity can be used to calculate the post-collision relative velocity vector, $\boldsymbol{C}_{\mathrm{R}}^{\mathrm{post}}$, given by

$$\boldsymbol{C}_{\mathrm{R}}^{\mathrm{post}} = C_{\mathrm{R}}^{\mathrm{post}} \cos(\beta)\, \hat{\boldsymbol{x}} + C_{\mathrm{R}}^{\mathrm{post}} \sin(\beta)\cos(\alpha)\, \hat{\boldsymbol{y}} + C_{\mathrm{R}}^{\mathrm{post}} \sin(\beta)\sin(\alpha)\, \hat{\boldsymbol{z}} \tag{2.79}$$

Finally, the post-collision velocities C_1^{post} and C_2^{post} can be calculated and assigned to the particle pair using the equations below.

$$C_{1,\mathrm{x,y,z}}^{\mathrm{post}} = C_{\mathrm{CM,x,y,z}} + \frac{m_2}{m_1 + m_2} C_{\mathrm{R,x,y,z}}^{\mathrm{post}} \tag{2.80}$$

$$C_{2,\mathrm{x,y,z}}^{\mathrm{post}} = C_{\mathrm{CM,x,y,z}} - \frac{m_1}{m_1 + m_2} C_{\mathrm{R,x,y,z}}^{\mathrm{post}} \tag{2.81}$$

2.2.6 Sampling Routine

Cell-based macroscopic averages are calculated for each sampling cell by utilizing the microscopic particle information of all particles within the sampling cell. Expressions for the cell-based density, velocity, pressure, shear, temperature, and heat flux as obtained from [9,96] are discussed in this Section. The cell-based quantities presented here are for one sampling time step. The quantities should then be averaged either in time or through independent ensembles. The number density n can be obtained from the number of particles N_{P} within a cell of volume V_{cell} and the number of real molecules W_{f} approximated by one computational particle using the following expression.

$$n = \frac{W_{\mathrm{f}}\, N_{\mathrm{P}}}{V_{\mathrm{cell}}} \tag{2.82}$$

The density is then computed by multiplying the number density with the molecular mass m as shown below. For a multispecies gas, each species' molecular mass is used to evaluate the mixture density.

$$\rho = nm \tag{2.83}$$

The macroscopic velocity vector $\boldsymbol{c}_0$ is obtained by averaging the instantaneous particle velocities $\boldsymbol{c}_\mathrm{i}$ of all particles found within the cell. The velocity $\boldsymbol{c}'$ of a computational particle relative to the macroscopic velocity is called the "thermal / peculiar / random" velocity. The expressions for these velocities can be written as

$$\boldsymbol{c}_0 = \frac{\sum_{\mathrm{p}=1}^{\mathrm{N_P}} \boldsymbol{c}_\mathrm{i}}{N_\mathrm{P}} \tag{2.84}$$

$$\boldsymbol{c}' = \boldsymbol{c}_\mathrm{i} - \boldsymbol{c}_0 \tag{2.85}$$

The components of the pressure tensor are defined based on the peculiar velocity components and the scalar pressure, p, is the average of the three normal components of the pressure tensor as shown in the following equations.

$$\boldsymbol{p}_\mathrm{ij} = \rho\overline{\boldsymbol{c}_\mathrm{i}'\boldsymbol{c}_\mathrm{j}'} \tag{2.86}$$

$$p = \frac{\rho\left(\overline{c_1'^2} + \overline{c_2'^2} + \overline{c_3'^2}\right)}{3} \tag{2.87}$$

The components of the viscous stress tensor are defined by

$$\tau_\mathrm{ij} = -(\rho\overline{\boldsymbol{c}_\mathrm{i}'\boldsymbol{c}_\mathrm{j}'} - \delta_\mathrm{ij}p) \tag{2.88}$$

where δ_ij is the Kronecker delta which has a value of 1 if i = j and a value of 0 if i ≠ j.

The average specific kinetic energy of the thermal velocity of a computational particle is given by

$$e_\mathrm{t} = \frac{\overline{c_1'^2} + \overline{c_2'^2} + \overline{c_3'^2}}{2} \tag{2.89}$$

Equation 2.89 can be substituted into Equation 2.87 to give the relation between pressure and the translational energy. This relation can be compared to the ideal gas law shown below.

$$p = \frac{2\rho e_\mathrm{t}}{3} \tag{2.90}$$

$$p = nkT_{\mathrm{t}} \tag{2.91}$$

When the pressure in the ideal gas law employing the translational temperature presented in Equation 2.91 is substituted into Equation 2.87, the translational temperature can be defined in terms of the other quantities through the following expression.

$$T_{\mathrm{t}} = \frac{m\left(\overline{c_1'^2} + \overline{c_2'^2} + \overline{c_3'^2}\right)}{3k} \tag{2.92}$$

Among the gases considered in this thesis, monoatomic species such as Argon possess only translational and electronic energy modes, while diatomic molecules such as N_2, O_2, and NO can store energy in rotational and vibrational modes as well. The electronic energy mode is not considered in this thesis. To calculate the rotational temperature at any cell, the relation used is

$$T_{\mathrm{r}} = \frac{2\sum_{\mathrm{i}=1}^{\mathrm{N_p}} e_{\mathrm{r,i}}}{k\sum_{\mathrm{i}=1}^{\mathrm{N_p}} \zeta_{\mathrm{r,i}}} \tag{2.93}$$

where the microscopic rotational energies, $e_{\mathrm{r,i}}$ and the degrees of freedom $\zeta_{\mathrm{r,i}}$ are required in the calculation.

The vibrational energy of any species is distributed across different vibrational energy modes, as will be discussed in the following Section on thermal non-equilibrium. Estimating the cell-based vibrational temperature requires summations over the vibrational modes and the number of species. First, a mean vibrational energy level $\bar{\iota}_{\mathrm{v,s,m}}$ is computed from the relation below by calculating a sum of the vibrational energies $e_{\mathrm{v,m,i}}$ for a given vibrational mode where N_{p} is the number of particles of the species s found in the cell while computing the summation.

$$\bar{\iota}_{\mathrm{v,s,m}} = \frac{\sum_{\mathrm{i}=1}^{N_{\mathrm{p}}} e_{\mathrm{v,m,i}}}{k\theta_{\mathrm{v}}N_{\mathrm{p}}} \tag{2.94}$$

Following this, the modal vibrational degrees of freedom, $\zeta_{\mathrm{v,s,m}}$ for species s are calculated. The modal vibrational temperatures, $T_{\mathrm{v,s,m}}$, are also calculated using the mean vibrational energy level as

$$\zeta_{\mathrm{v,s,m}} = 2\bar{\iota}_{\mathrm{v,s,m}} \ln\left(1 + \frac{1}{\bar{\iota}_{\mathrm{v,s,m}}}\right) \tag{2.95}$$

$$T_{\mathrm{v,s,m}} = \frac{\theta_{\mathrm{v,s}}}{\ln\left(1 + \frac{1}{\bar{\iota}_{\mathrm{v,s,m}}}\right)} \tag{2.96}$$

The species-based vibrational degrees of freedom, $\zeta_{\mathrm{v,s}}$, and the species-based vibrational temperature, $T_{\mathrm{v,s}}$, can now be calculated by

$$\zeta_{\mathrm{v,s}} = \sum_{\mathrm{m}=1}^{N_{\mathrm{m}}} \zeta_{\mathrm{v,s,m}} \tag{2.97}$$

$$T_{\mathrm{v,s}} = \frac{\sum_{\mathrm{m}=1}^{N_{\mathrm{m}}} \zeta_{\mathrm{v,s,m}} T_{\mathrm{v,s,m}}}{\zeta_{\mathrm{v,s}}} \tag{2.98}$$

Finally, the vibrational degrees of freedom, ζ_{v}, and vibrational temperature of the mixture, T_{v}, can be calculated as

$$\zeta_{\mathrm{v}} = \frac{\sum_{\mathrm{s}=1}^{N_{\mathrm{s}}} n_{\mathrm{s}} \zeta_{\mathrm{v,s}}}{\sum_{\mathrm{s}=1}^{N_{\mathrm{s}}} n_{\mathrm{s}}} \tag{2.99}$$

$$T_{\mathrm{v}} = \frac{\sum_{\mathrm{s}=1}^{N_{\mathrm{s}}} n_{\mathrm{s}} T_{\mathrm{v,s}}}{\sum_{\mathrm{s}=1}^{N_{\mathrm{s}}} n_{\mathrm{s}}} \tag{2.100}$$

where n_{s} is the number density of species s. The overall temperature can also be calculated from the mixture translational, rotational, vibrational temperatures and degrees of freedom as

$$T_{\mathrm{overall}} = \frac{3T_{\mathrm{t}} + \zeta_{\mathrm{r}} T_{\mathrm{r}} + \zeta_{\mathrm{v}} T_{\mathrm{v}}}{3 + \zeta_{\mathrm{r}} + \zeta_{\mathrm{v}}} \tag{2.101}$$

The heat flux and shear stress at the wall are calculated from microscopic information of the particles striking the wall. The total energy a particle possesses is the sum of its translational and internal energies as given below.

$$e_{\mathrm{tot}} = e_{\mathrm{t}} + e_{\mathrm{r}} + e_{\mathrm{v}}^{\mathrm{tot}} \tag{2.102}$$

This quantity is evaluated pre- and post-collision and is summed over all particles striking the boundary to determine the heat flux to the boundary facet of area A_{el} using the following expression.

$$q_{\mathrm{el}} = \sum_{\mathrm{i}=1}^{N_{\mathrm{p}}} \frac{W_{\mathrm{f}}\left(e_{\mathrm{tot,i}}^{\mathrm{pre}} - e_{\mathrm{tot,i}}^{\mathrm{post}}\right)}{A_{\mathrm{el}} \Delta t} \tag{2.103}$$

The particle's momentum, $\boldsymbol{p}_{\mathrm{mom}}$, is computed as a product of the mass and velocity of the particle and the pre- and post-collision values of the momentum are used to determine the shear stress $\boldsymbol{\tau}$ as

$$\boldsymbol{p}_{\mathrm{mom}} = m\boldsymbol{c} \tag{2.104}$$

$$\boldsymbol{\tau} = \left(\sum_{\mathrm{i}=1}^{N_{\mathrm{p}}} \frac{W_{\mathrm{f}} \left(\boldsymbol{p}_{\mathrm{mom}}^{\mathrm{pre}} - \boldsymbol{p}_{\mathrm{mom}}^{\mathrm{post}} \right)}{A_{\mathrm{el}} \Delta t} \right) \cdot \hat{\boldsymbol{t}} \tag{2.105}$$

In the above equation, $\hat{\boldsymbol{t}}$ is a unit vector tangential to the surface. If the facet normal vector were used instead of the tangential vector, the resulting computation would yield pressure at the surface.

HALO3D-NS and OptiGrid operate on nodal solution vectors, in contrast with the cell-based macroscopic data calculated by DSMC. To convert the cell-based DSMC data to a node-based format for information coupling between the NS and DSMC zones, an inverse distance-weighted interpolation method is used, as illustrated in Fig. 2.6. The expression for a scalar ϕ at node i is given by

$$\phi_{\mathrm{i}} = \frac{\sum_{\mathrm{j}=1}^{N_{\mathrm{c}}} \left(\phi_{\mathrm{j}} \alpha_{\mathrm{ij}} \right)}{\sum_{\mathrm{j}=1}^{N_{\mathrm{c}}} \alpha_{\mathrm{ij}}} \tag{2.106}$$

in which α_{ij} is a weight related to the reciprocal of the distance between node i and the cell-center of cell j, where j represents any of the N_{c} cells surrounding node i, and ϕ_{j} is the cell-center value of that scalar.

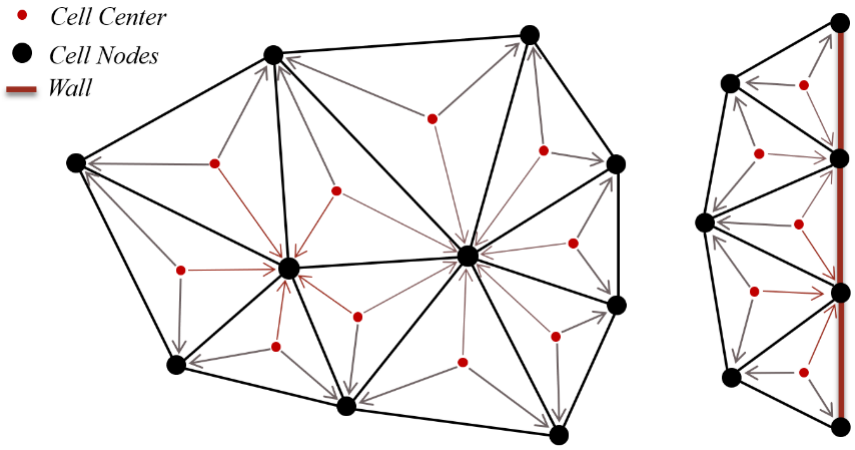

Fig. 2.6 Illustration of the inverse distance-weighted interpolation in HALO3D-DSMC's sampling routine

2.2.7 Thermal Non-Equilibrium Modeling

Post-collision rotational and vibrational energies are sampled from equilibrium distribution functions parameterized on the collision energy [9] according to the standard (rotational mode) and quantum (vibrational mode) [75] applications of the Larsen-Borgnakke (LB) procedure [97]. This thesis employs a constant rotational collision number $Z_\mathrm{r} = 5$ and a constant vibrational collision number $Z_\mathrm{v} = 50$ in all the DSMC and hybrid simulations involving thermal non-equilibrium. This means that a particle is accepted for internal energy relaxation once every 5/50 collisions on average for the rotational/vibrational modes, respectively. That is, rotational and vibrational relaxation occur if

$$\frac{1}{Z_\mathrm{r}} > R \quad ; \quad \frac{1}{Z_\mathrm{v}} > R \tag{2.107}$$

where R represents the random numbers that are generated for this evaluation. If a particle is accepted for rotational or vibrational relaxation during a collisional event, it is assigned a new rotational or vibrational energy. Then, the translational energy of the pair is decreased to accommodate this change in internal energy, thus conserving energy. From this corrected translational energy, a new post-collision relative velocity is computed as

$$C_\mathrm{R}^\mathrm{post} = \sqrt{\frac{2e_\mathrm{t}}{m_\mathrm{r}}} \tag{2.108}$$

This relative velocity is used to determine the post-collision velocity vectors of the two colliding species.

To calculate the post-collision rotational energy of the particle, first, the relative translational energy is calculated as

$$e_\mathrm{t} = \frac{m_\mathrm{r}(\boldsymbol{C}_\mathrm{R} \cdot \boldsymbol{C}_\mathrm{R})}{2} \tag{2.109}$$

Then the collision energy is calculated as a sum of the relative translational and pre-collision rotational energies.

$$e_\mathrm{coll} = e_\mathrm{t} + e_\mathrm{r} \tag{2.110}$$

The post-collision rotational energy can be calculated next by generating a random number R and using the following expression.

$$e_{\mathrm{r}}^{\mathrm{post}} = e_{\mathrm{coll}}\left(1 - R^{\frac{1}{2.5-\omega}}\right) \tag{2.111}$$

The vibrational levels of each particle are stored rather than the vibrational energy, and the total vibrational temperature of the gas is calculated during the sampling step, as discussed before. The levels are distributed according to the harmonic oscillator model, where the levels possess equal energy steps equal to $k\theta_{\mathrm{v}}$. Calculation of the post-collision vibrational energy level of each mode of a particle requires the estimation of the collision energy firstly as a sum of the relative translational and pre-collision modal vibrational energies as

$$e_{\mathrm{coll}} = e_{\mathrm{t}} + i_{\mathrm{v}} k\theta_{\mathrm{v}} \tag{2.112}$$

Next, the post-collision vibrational energy level is calculated by generating a random number R, distributed between 0 and the maximum possible energy level, $i_{\max}$ given by

$$i_{\mathrm{v}}^{\mathrm{post}} = R \tag{2.113}$$

$$i_{\max} = \left\lfloor \frac{e_{\mathrm{coll}}}{k\theta_{\mathrm{v}}} \right\rfloor \tag{2.114}$$

The Larsen-Borgnakke probability ratio is then calculated as

$$\frac{P}{P_{\max}} = \left(1 - \frac{i_{\mathrm{v}}^{\mathrm{post}} k\theta_{\mathrm{v}}}{e_{\mathrm{coll}}}\right)^{1.5-\omega} \tag{2.115}$$

An acceptance-rejection procedure is executed with this ratio against a random number while recalculating both the ratio and $i_{\mathrm{v}}^{\mathrm{post}}$ until acceptance.

2.2.8 Chemical Non-Equilibrium Modeling

The current work models dissociation and exchange reactions with the Quantum-Kinetic (QK) method [75], which relies on microscopic information such as the collision energy, vibrational levels, and molecular reaction energies to model chemical reactions. The QK model assumes that the gas is vibrationally excited. Two particles accepted for a collision are first tested to determine if any reactions could occur between them. If this fails, they are evaluated for any possible internal

energy exchange. If this too fails, they undergo an elastic collision. A generic dissociation reaction can be written as

$$AB + C \rightarrow A + B + C \tag{2.116}$$

where A and B are atomic species, AB is a molecular species and C is either an atom or a molecule. To test a particle for dissociation, the collision energy is first computed from Equation 2.112 along with a maximum possible energy level from Equation 2.114. If any vibrational mode satisfies the following condition for dissociation,

$$i_{\max} > \frac{\theta_{\mathrm{d}}}{\theta_{\mathrm{v}}} \tag{2.117}$$

$$\theta_{\mathrm{d}} = \frac{h_{\mathrm{r}}}{k} \tag{2.118}$$

then the reaction probability is set to 1 (dissociation is guaranteed to occur), and if none of the vibrational modes satisfy the condition, then no dissociation reaction is conducted. θ_{d} is the characteristic dissociation temperature and h_{r} is the heat of reaction.

Once a dissociation reaction has been selected to occur, the heat of the reaction is subtracted from the collision energy to produce an updated collision energy e^{*}_{coll} from which a post-collision relative velocity for the reactants can be determined as

$$C_{\mathrm{R,R}}^{\mathrm{post}} = \sqrt{\frac{2e^{*}_{\mathrm{coll}}}{m_{\mathrm{r.R}}}} \tag{2.119}$$

where $m_{\mathrm{r.R}}$ is the reduced mass of the reactants. The post-collision velocities of the reactants are determined with this relative velocity, in the same manner described previously.

Following this, a new particle representing one newly created product species is added to the particle cloud. The remainder of the internal energy, e_{left}, of the particle undergoing dissociation is used to calculate the post-reaction relative velocity of the products as

$$C_{\mathrm{R,P}}^{\mathrm{post}} = \sqrt{\frac{2e_{\mathrm{left}}}{m_{\mathrm{r.P}}}} \tag{2.120}$$

where $m_{\mathrm{r.P}}$ is the reduced mass of the products, thus ensuring energy conservation. Generating the other product species does not require the creation of another new particle since the particle properties of one of the reactants can be overwritten. Finally, the post-collision velocities of the new product species are calculated as discussed in Section 2.2.5 using the post-reaction relative velocities of the products and setting the center of mass velocity to be equal to the velocity of the dissociating molecule.

A generic exchange reaction can be written as

$$AB + C \rightarrow AC + B \tag{2.121}$$

where AB and AC are molecular species and A, B and C are atomic species. To test a particle pair for an exchange reaction, the "collision temperature", T_{coll}, is first calculated using the relative velocity of the colliding pair as

$$T_{\mathrm{coll}} = \frac{m_{\mathrm{r}} C_{\mathrm{R}}^2}{2k\left(\frac{5}{2} - \omega\right)} \tag{2.122}$$

Following this, the collision energy is calculated as in Equation 2.112, employing the modal vibrational energies as before. A constant, a', is required to evaluate the activation energy and is computed as

$$a' = a\left[\frac{\left(\frac{5}{2} - \omega\right)^b \Gamma\left(\frac{5}{2} - \omega\right)}{\Gamma\left(\frac{5}{2} - \omega + b\right)}\right] \tag{2.123}$$

where the two constants a and b are obtained from [63]. The modified activation energy for the exchange reaction [63] is given by

$$e_{\mathrm{act}} = a'|h_{\mathrm{r}}|\left(\frac{T_{\mathrm{coll}}}{T_{\mathrm{ref}}}\right)^b \tag{2.124}$$

where h_{r} is the heat of the reaction and if $e_{\mathrm{coll}} > e_{\mathrm{act}}$, the activation energy is used to calculate the DSMC reaction probability for an exchange reaction as

$$P_{\text{exch}} = \frac{\left(1 - \frac{e_{\text{act}}}{e_{\text{coll}}}\right)^{\frac{3}{2}-\omega}}{\sum_{i_{\text{v}}=0}^{i_{\max}} \left(1 - \frac{i_{\text{v}} k\theta_{\text{v}}}{e_{\text{coll}}}\right)^{\frac{3}{2}-\omega}} \tag{2.125}$$

$i_{\max}$ in the above expression is computed in the same manner as before, from Equation 2.114.

Once the reaction probabilities have been determined, they are evaluated against a random number to determine which reaction is accepted. When an exchange reaction is selected to occur, the heat of the reaction is subtracted from the collision energy to produce the updated collision energy, e^*_{coll}. Following this, the two reactant particles are overwritten by the product species and initialized to have zero internal energies. Then, the internal energies of the molecular product are redistributed in the same manner described in Section 2.2.7 while using e^*_{coll} as the available collision energy. The post-collision relative velocity is then calculated as

$$C_{\text{R}}^{\text{post}} = \sqrt{\frac{2e^*_{\text{coll}}}{m_{\text{r.P}}}} \tag{2.126}$$

where $m_{\text{r.P}}$ is the reduced mass of the products. The center of mass velocity is calculated as before, from Equation 2.76. These two velocities are then finally used to determine the post-collision velocities of the products in the same way as discussed in Section 2.2.5.

2.2.9 Boundaries

There are three main types of boundaries for DSMC: the inlet, wall, and outlet patches, which are usually discretized with quadrilateral or triangular facets. At inlets, particles are first generated with random positions in the primitive space of the quadrilateral or triangle. The positions are then transformed to real space using 2D finite element shape functions similar to the mesh population routine. The number of particles to be inserted is derived from the equilibrium number flux of particles passing through the inlet facet and is given by

$$N = \frac{n}{2\beta\sqrt{\pi}}\left[\exp(-C_{\text{in}}^2\beta^2\cos^2\theta) + \sqrt{\pi}C_{\text{in}}\beta\cos\theta(1 + erf(C_{\text{in}}\beta\,cos\,\theta))\right] \tag{2.127}$$

$$\beta = \sqrt{\frac{m}{2kT_{\text{in}}}} \tag{2.128}$$

where the subscript "in" refers to the values at the inlet. θ is the angle between the inlet velocity vector, C_{in}, and the inlet facet normal. Each particle inserted into the domain is assigned a velocity based on a Maxwellian velocity distribution function. The rotational and vibrational energies of the particle are set from Equations 2.65-2.67. Particles that intersect outlet facets are removed from the particle cloud.

The two types of walls available in HALO3D-DSMC are specular and diffuse walls. Specular walls reflect incoming particles at an angle of reflection equal to the angle of incidence; that is, the particle velocity component normal to the surface is reversed. For diffuse walls, all directions of reflection have an equal probability. The particle post-collision velocity magnitude is assigned from a Maxwellian velocity distribution function parameterized by the wall temperature. The rotational and vibrational energies of the particle are assigned from Equations 2.65-2.67, where the temperatures used are that of the wall. It is discussed in [96] that materials possess a complex surface structure at the micro to the nanoscale, much smaller than a DSMC surface cell, where particles undergo several collisions with the microstructure surface before returning to the bulk flow. Therefore, the assumptions of diffuse reflections of a random post-collision scattering angle and thermal accommodation to the surface temperature should be physically valid.

As the Knudsen number increases, the gas need not be equilibrated with the diffuse wall, and velocity slip and temperature jump occur. Velocity slip at a diffuse wall is given by [75]

$$V_{\text{slip}} = \frac{\sum\left(\frac{mv}{|u|}\right)}{\sum\frac{m}{|u|}} \tag{2.129}$$

where v is the velocity component tangential to the wall and u is the velocity component normal to the wall. The temperature jump can be calculated as [75]

$$T_{\text{t,jump}} = \frac{\sum\left(\frac{m\|\boldsymbol{C}\|}{|u|}\right) - \sum\left(\frac{m}{|u|}\right)V_{\text{slip}}^2}{3k\sum\frac{1}{|u|}} - T_{\text{t,wall}} \tag{2.130}$$

where the slip velocity is used in the computations. The summations in the velocity slip and temperature jump expressions are taken over the incident and reflected particles.

2.2.10 Sub-cells

Conceptually, sub-cells are divisions of collision cells into smaller volumes to further localize particles. Unless otherwise specified, the present work employs the Transient Adaptive Sub-cell (TAS) [98] technique and the Nearest Neighbour (NN) [95] method (with a switch to TAS when there are more than 30 particles in a collision cell) to accommodate cells larger than the local mfp. Various sub-cell methods have been implemented within HALO3D-DSMC and illustrations of the ones used in this thesis have been presented in Fig. 2.7. In each of the four methods illustrated, a representative pair of particles that have been accepted for a collision are also shown in green. Fig. 2.7a shows a schematic when no sub-cell methods are used, where there is a possibility of choosing two particles from opposite ends of the collision cell. As expected, this method is the least accurate. Fig. 2.7b illustrates the fixed sub-cell method with two sub-cells in each direction where the number of sub-cells in each direction can be specified by the user. All cells in the mesh are then divided into the same number of sub-cells. For this method, particle pairs are chosen from within the same sub-cell, which is more accurate than not using any sub-cells. Fig. 2.7c shows the Transient Adaptive Sub-cell method where an automatic discretization of the collision cell is performed in such a way as to guarantee a user-specified number of particles in each sub-cell. The number of sub-cells can vary from collision cell to collision cell depending on the cell volume and number of particles within the cell. This method is more sophisticated than setting a fixed number of sub-cells to every cell while being computationally more expensive. Fig. 2.7d shows the Nearest Neighbour method that scans each particle in the current collision cell and surrounding collision cells to find the nearest neighbor to a chosen collision candidate. One of the ill-effects of consistently choosing nearby particles as collision candidates is that the chances of a fast-moving, farther away particle colliding with a collision candidate are nullified, whereas in reality, these probabilities are nonzero.

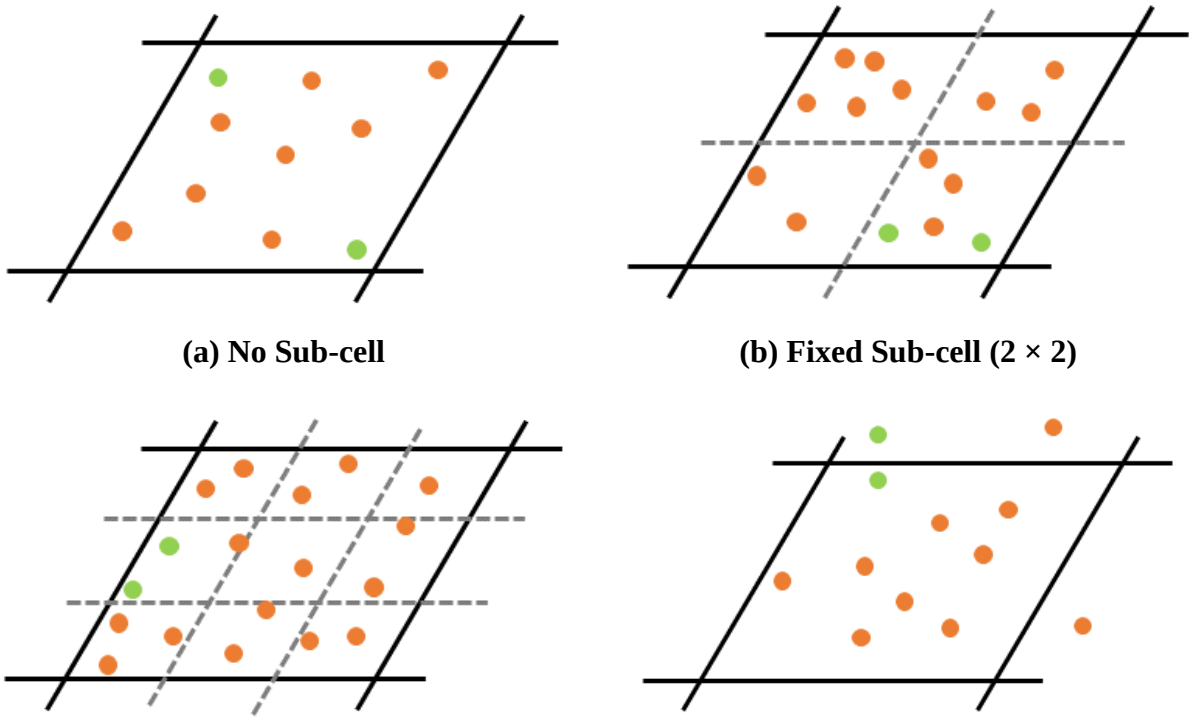

(a) No Sub-cell **(b) Fixed Sub-cell (2 × 2)**

(c) Transient Adaptive Sub-cell **(d) Nearest Neighbour**

Fig. 2.7 Sub-cell methods employed in the current work

2.3 HALO3D-HYBRID

In the present study, the coupling of the HALO3D-NS and HALO3D-DSMC solvers is performed by treating each solver as an independent module and making minor modifications to the solution algorithm of the HALO3D ensemble. The NS and DSMC solvers share some aspects of code within HALO3D, such as the same mesh modules, boundary objects, and solution assembly routines which greatly simplifies the generation of buffer regions, intercommunication between the NS and DSMC solvers, solution representation, and file input-output. The algorithm of HALO3D-HYBRID has been provided in Fig. 2.8, where a hybrid simulation begins with the calculation of a full NS solution, using which regions of continuum breakdown are identified and assigned as DSMC zones. Once particles are seeded in the buffer and DSMC regions at the beginning of the first DSMC step, they are advected for a fixed time step. Any particles that flow into the NS regions and in the outer buffer are deleted after the tracking step. The collision routine and sampling routines are then performed for DSMC cells only. The DSMC and NS solvers are then run one after the other. Each solver provides boundary conditions for the other until a

converged solution is obtained, or a user-specified number of hybrid iterations has been reached. The parameters monitored for the establishment of a statistically steady-state in DSMC computations are the total number of particles, and the total kinetic, rotational and vibrational energies. Once all these parameters reach constant values with each successive iteration, the sampling stage begins. For NS computations, the solution is considered to be converged once the residuals reach threshold values. This loosely coupled approach uses independent time steps for the NS and DSMC modules and allows the two modules to be run sequentially through multiple coupling cycles. The HALO3D-NS solver uses an implicit time integration scheme allowing much larger NS time steps than the DSMC solver. It also has less sensitivity to the statistical scatter in the DSMC regions of hybrid simulations; therefore, the statistical scatter does not affect the hybrid solution stability. Furthermore, the number of solution exchanges between the DSMC and NS solvers at the interface is significantly lesser than a fully coupled strategy. These procedures result in a hybrid framework that is faster than full DSMC simulations for flows of varying degrees of thermochemical complexity. In the following paragraphs, the main functionalities of HALO3D-HYBRID are described.

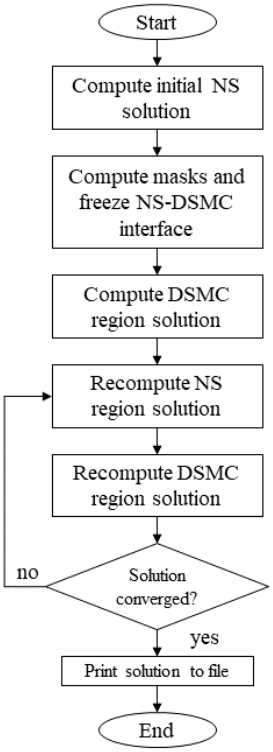

Fig. 2.8 Algorithm of HALO3D-HYBRID

2.3.1 Masks

Masks for two mesh elements: cells and nodes, are built by flagging them in Boolean arrays to demarcate DSMC, NS, and buffer regions. The breakdown parameter ($Kn_{\max}$) is computed from the distribution of $Kn_{\mathrm{GLL-Q}}$ for different scalars as explained in Section 1.2. After the initial CFD solution is computed and the breakdown parameter field is obtained, a cell mask is built based on the threshold value of the breakdown parameter. If a cell has a breakdown parameter value less than the threshold, it is flagged as an NS cell, and otherwise, it is flagged as a DSMC cell. A threshold value of 0.05 is usually selected as recommended in [21].

The cell mask is used to create other masks, buffers and during file write operations. Two other cell-based masks are computed: a mesh population mask that is true in the DSMC and inner buffer regions and an outer buffer mask that is true in the outer buffer region. The mesh population mask is supplied as an input to the particle creation routine to populate corresponding regions once at the beginning of the DSMC loop. The outer buffer mask is supplied as an input to the same particle creation routine to populate only the outer buffer region at every DSMC iteration. Node masks are built using the cell mask by flagging all the nodes of DSMC cells as DSMC nodes. The nodes that comprise the NS and DSMC interface are also flagged as DSMC nodes. These node masks are required during the assembly of the NS and DSMC solutions on global solution vectors.

2.3.2 Buffers

The inner and outer buffer regions can contain as many layers of cells as specified by the user. For all the simulations presented in this paper, both regions contain three layers unless otherwise specified. To build each layer of the buffer, “seed” locations from the previous layer are required, which can be cells/facets/nodes. Then, mesh connectivity information is used to form a layer around these seed locations. Since the buffer layers are supposed to expand outwards from the NS-DSMC boundary, this boundary can be used as the seed for the first layer. In practice, for complex 2D and 3D flows, patches of inner buffer layers might arise that are not connected to any cells belonging to the outer buffer since the patches are not big enough. These patches can have detrimental effects on the flow solution vectors and require treatment. The algorithm followed to build the buffers, and a method that cleans patches of isolated inner buffer cells is presented below.

1. Build the NS-DSMC interface
    a. Scan all facets through the facet-cell connectivity array.
    b. Use the cell mask to collect those facets that possess a DSMC cell on one side and an NS cell on the other.
2. Build the first layer
    a. Scan the list of facets in the NS-DSMC interface.
    b. Use facet-node connectivity, node-cell connectivity, and the cell mask to build the first layer of cells that surround the NS-DSMC interface on the NS side. This is the first layer of the inner buffer.
    c. Store the first layer of cells in a hashmap for easy retrieval.
3. Build the remaining layers: Loop over 2 to N layers
    a. Scan the list of cells in the layer lower than the present layer.
    b. Use cell-node and node-cell connectivity along with the information stored in the hashmap to build the current layer of cells surrounding the previous layer on the NS side.
    c. Store all cells in the current layer in the hashmap.
4. Clean the buffers: Loop over all layers in descending order
    a. Scan the list of cells in the current layer.
    b. For each cell, use cell-node and node-cell connectivity to build a list of cells surrounding the current cell.
    c. Determine if at least one of these cells belongs to the upper layer of the current layer.
    d. If no cells belong to the upper layer, the current layer loses one cell, and the lower layer gains the current cell.

An example of the buffer cleaning algorithm is presented in Fig. 2.9 for the leading-edge test case. The NS, buffer, and DSMC regions are shown where an extended inner buffer region can be observed when no cleaning algorithm is used. When the buffers are cleaned, these inner buffer cells are converted to DSMC cells.

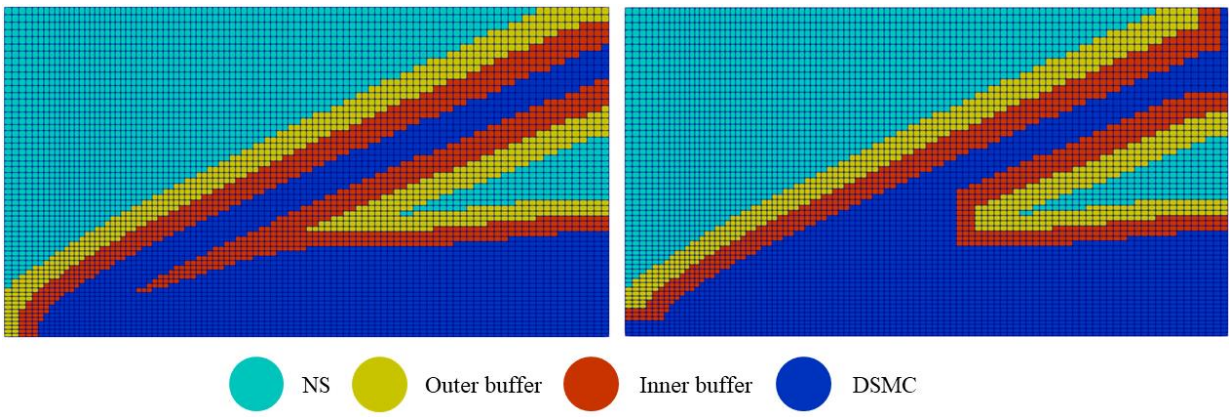

Fig. 2.9 Hybrid masks for the leading-edge case without cleaning (left) and with cleaning (right)

2.3.3 NS-DSMC Communication

As previously mentioned, the information transfer from the NS to the DSMC regions is accomplished in three regions of the mesh: during the mesh population of the DSMC and inner buffer regions (at the first DSMC step) and the mesh population of the outer buffer regions (at every DSMC inner iteration). Particle properties in these regions are initialized according to the NS solution. The node-based NS solution is interpolated at the cell centers using finite element shape functions to obtain cell-centered values that are input into the DSMC initialization routines. Information transfer from the DSMC to the NS regions first needs the cell-centered DSMC solution to be converted to a node-based solution required by HALO3D-NS. This is accomplished by the inverse distance-weighted interpolation method, as discussed before. These node-based DSMC fields are obtained for density, velocities, mass fractions of chemical species, heat flux, shear stress, and translational, rotational, and vibrational temperatures. The DSMC nodal density, velocity, mass fraction, and wall quantities are used to overwrite the NS/previous cycle solutions in the DSMC region of the global solution vectors. A DSMC trans-rotational temperature is calculated as explained in Section 3.2.1.2 from the translational and rotational temperature fields and is used to overwrite the trans-rotational temperature from the NS/previous cycles in the global solution vectors. The DSMC pressure is discarded since it follows the ideal gas law using the translational temperature instead of the trans-rotational temperature as is done for NS. A new pressure field is computed by employing the ideal gas law with the DSMC density and DSMC trans-rotational temperature. This pressure overwrites the solution in the global solution vector.

Once the DSMC solution is patched alongside the NS solution, all the DSMC region nodes are flagged as Dirichlet boundary condition nodes to be imposed on the NS solver.

2.4 OptiGrid

The present work contributes to the body of DSMC literature on unstructured mesh adaptation techniques by coupling a DSMC solver with a mesh optimizer, OptiGrid, to automatically yield a solution-driven, not just adapted, but "optimal" mesh. The hybrid algorithm can also be coupled with OptiGrid, and the benefits of an unstructured mesh hybrid solver are discussed in Chapter 3. The coupling of either the DSMC or the hybrid solvers with OptiGrid is illustrated in Fig. 2.10. A solution is first obtained on an initial mesh, which is then used to adapt the mesh, and a new solution is computed on the new mesh, and this is repeated until a converged mesh is obtained.

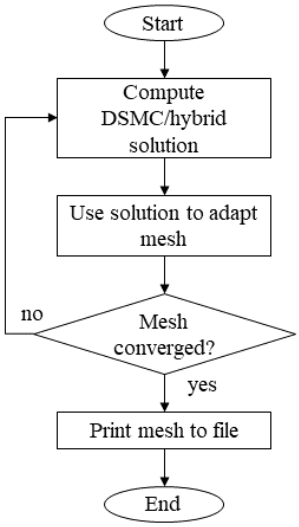

Fig. 2.10 Algorithm for the coupling of either DSMC or hybrid solvers with OptiGrid

The initial solution can be computed on a reasonably coarse mesh whose cells can be sized according to the freestream mfp [65]. The initial solution also provides useful information such as the minimum and maximum mfp values, the separation of free paths, and the minimum mean collision time to tune the optimization constraints. The target cell number decides the particle count for the simulation and is set based on computational feasibility. For the cases presented in this paper, the minimum edge lengths have been set to be a multiple of either the minimum or freestream mfp (whose approximate value is determined using the initial solution), while the maximum edge length is a case-specific input that can be equal to a fraction of the size of the computational domain. When used alongside continuum solvers, OptiGrid interpolates the solution

from the previous iteration onto the new mesh, and this interpolated solution is used as an initial condition for the computation on the new mesh. For DSMC, initializing a simulation by either populating the grid based on an interpolated macroscopic solution or loading the converged particle data from a previous mesh reduced the transient time.

OptiGrid [99], developed by the authors' group, was first introduced for the 2D continuum problems of an inviscid hypersonic flow past a double ellipse geometry, viscous transonic and supersonic flows around an airfoil, and flows over a ramp [100]. Since then, it has been shown to excel in 3D as best portrayed through the mesh adaptation for flows over complete aircraft. Mesh adaptation via OptiGrid has been shown to converge to the same final mesh irrespective of the initial mesh and often of the solver, thus demonstrating mesh- and user-independence [100]. These two features of OptiGrid enable the automatic optimization of successive meshes with no user intervention necessary between mesh iterations and only very little user input required in the creation of the initial mesh, which can be of any quality, as illustrated in Section 3.3.1. In addition, it is able, because of its directionality, to generate a final adapted mesh more accurate than any refined structured mesh and with a lesser number of nodes as demonstrated for a hypersonic continuum flow over a sphere [80]. Multiscale fluid structures and geometric features can be finely captured as exemplified by the hypersonic flow past a waverider geometry [80] exhibiting a sharp nose and leading edges. In this case, OptiGrid effectively captures a crisp shock and an extended wake region. Its capability to accommodate any new solution variable as an adaptation scalar is best highlighted by its use in magnetohydrodynamics [2], where the hypersonic continuum flow over a hemisphere is adapted based on the electric potential and flow variables to simultaneously capture steep shocks and well-resolved flow and electromagnetic quantities. Optimization constraints in the form of target node or cell count and minimum and maximum edge lengths allow for fine control of the local mesh size, and it is thus anticipated that these benefits demonstrated for the continuum regime will translate to the rarefied regime.

During an optimization cycle, OptiGrid first calculates the Hessian $\boldsymbol{H}$ of a set of optimization scalars that drive the mesh adaptation. The Hessian is then decomposed into its right eigenvectors $\boldsymbol{R}$ and eigenvalues $\boldsymbol{\Lambda}$, as

$$\boldsymbol{H} = \boldsymbol{R}\boldsymbol{\Lambda}\boldsymbol{R}^{\boldsymbol{T}} \tag{2.131}$$

The Hessian is then modified by using the absolute values of the eigenvalues.

$$\boldsymbol{M} = \boldsymbol{R}|\boldsymbol{\Lambda}|\boldsymbol{R}^{\boldsymbol{T}} \tag{2.132}$$

This modified Hessian is then used to construct the edge-based error estimator, e, of nodes i and j of an edge as

$$e(\boldsymbol{x}_{\mathrm{i}} - \boldsymbol{x}_{\mathrm{j}}) = \int_0^1 \sqrt{(\boldsymbol{x}_{\mathrm{i}} - \boldsymbol{x}_{\mathrm{j}})^{\boldsymbol{T}} \boldsymbol{M}(\boldsymbol{l})(\boldsymbol{x}_{\mathrm{i}} - \boldsymbol{x}_{\mathrm{j}})}\, dl \tag{2.133}$$

where $\boldsymbol{x}_{\mathrm{i}}$ denotes the position of node i. The eigenvalues of $\boldsymbol{H}$ provide the relative length of an edge, and the eigenvectors provide the orientation of the edge. The expression to obtain a piecewise-linear Hessian, h_{ij}, from the piecewise-linear approximation, u_{h}, and shape function, N_{I}, is [100]

$$h_{\mathrm{ij}}(\mathrm{I}) = -\left(\int_{\mathrm{E_I}} \frac{\partial u_{\mathrm{h}}}{\partial x_{\mathrm{i}}} \frac{\partial N_{\mathrm{I}}}{\partial x_{\mathrm{j}}} dx\right)\left(\int_{\mathrm{E_I}} N_{\mathrm{I}} dx\right)^{-1} \tag{2.134}$$

where $\mathrm{E_I}$ is the set of elements surrounding vertex I. In a second stage, OptiGrid utilizes a combination of four basic mesh operations to homogenize the error estimate e throughout the domain: edge refinement, edge coarsening, edge swapping, and node movement, as illustrated in Fig. 2.11.

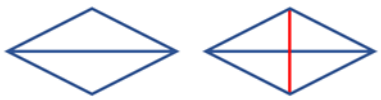

(a) Edge refinement

(b) Edge coarsening

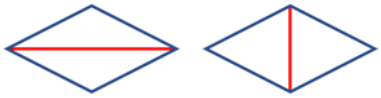

(c) Edge swapping

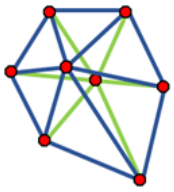

(d) Node movement

Fig. 2.11 Basic mesh operations in OptiGrid

Refinement, coarsening, and swapping are binary "on-off" or toggle operations, while node movement is a continuous operation where the edges connected to a node are modeled as springs with a stiffness proportional to the error estimate. The ideal positions of a collection of nodes to be moved are obtained by minimizing the energy of the group of edges. The sequence of mesh operations is given below [100].

1. Compute the error estimate
2. Smooth the mesh
    a. Swap all edges until convergence
    b. Move all nodes iteratively
3. Iterate over the following loop:
    a. Refine all edges above a threshold error estimate
    b. Swap edges until convergence, then apply node movement
    c. Remove all nodes whose connecting edges have an error estimate below a threshold value
    d. Repeat Step 3b
4. Repeat Step 2

A mesh generated using this algorithm and optimization constraints can progressively capture flow features at any level of accuracy. These adapted meshes can be stretched in physical space but are uniform Delaunay meshes in Riemannian space. OptiGrid's capabilities in resolving continuum regime solutions are well documented [2,80,99-101]. One of its applications with HALO3D-NS at a Knudsen number of 2.4×10^{-5} is shown in Fig. 2.12 for a flow over a re-entry capsule [101]. Here, OptiGrid generates an adapted mesh with a thin, densely populated shock region, refined boundary layer, and coarse wake region. The accuracy and degree of refinement in these regions can be controlled by increasing the target node/cell count and decreasing the minimum edge length. This is illustrated for DSMC simulations in Fig. 2.13 for a 2D hypersonic flow over a cylinder at a Knudsen number of 0.01, where two refinement levels are presented: the adapted mesh in case A has 60% more cells and half the minimum edge length than case B, resulting in refinement in the bow shock and boundary layer. Importantly, the maximum edge length is preserved between these two cases, and regions that do not require refinement, such as the freestream, and the region between the bow shock and the boundary layer, are not refined. It is

possible to force refinement in these regions by decreasing the maximum edge length, however these two meshes indicate that the freestream discretization is either over refined or adequately refined. Fig. 2.12 and 2.13 are thus a proof of concept that OptiGrid can effectively capture thin shocks as encountered in the continuum regime and the relatively thicker shocks found in the rarefied regime. This will be further demonstrated in the Chapter 3.

In prevailing DSMC literature, constraints for the sizing of collisional cells are well researched, while good definitions for the sizing and positioning of sampling cells are somewhat lacking. This study leverages OptiGrid to offer a new definition for a DSMC sampling mesh: one where the nodes of the mesh are positioned such that an error estimate of the flow field is equi-distributed throughout the domain. Any further refinement would only bring the error estimate down globally. Such a discretization of a solution positions OptiGrid in hypersonics as an additional field of research benefiting from this automatic solution-driven mesh optimization strategy.

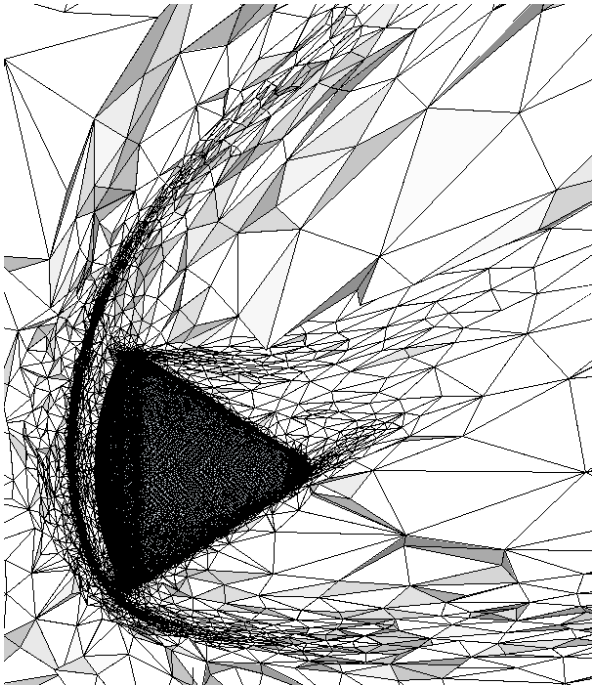

Fig. 2.12 Mesh adaptation for a re-entry capsule in the continuum regime

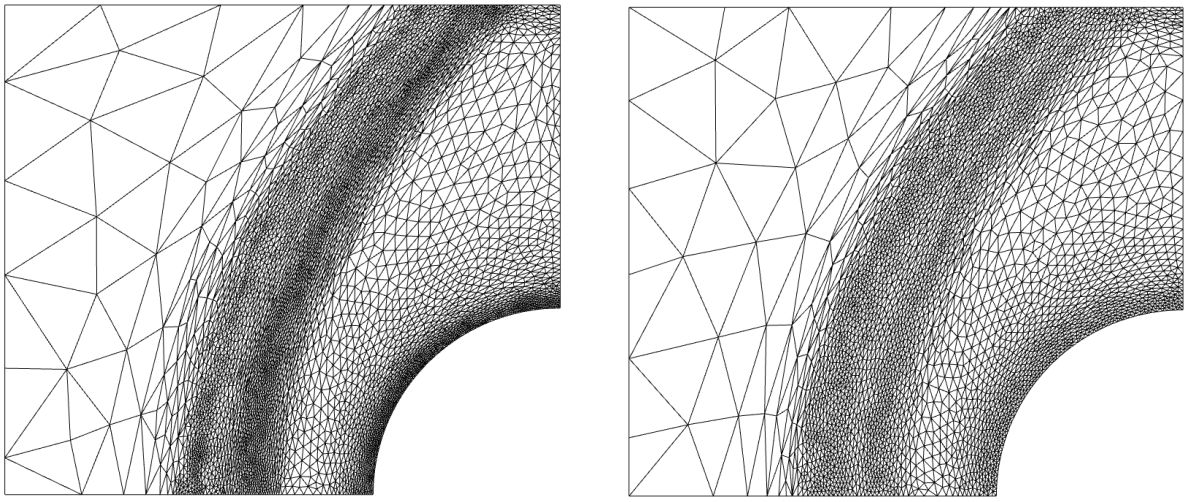

(a) Case A: 1st adapted mesh **(b) Case B: 2nd adapted mesh**

Fig. 2.13 Proof of concept for the coupling of DSMC and OptiGrid for a hypersonic flow over a 2D cylinder at two different levels of refinement

Chapter 3

Results

This Section presents several simulations to illustrate the capabilities of HALO3D-DSMC and HALO3D-HYBRID and validates the results through comparisons with literature. First, three simulations are conducted with HALO3D-DSMC and results from DS3V, MONACO, DAC, dsmcFoam, and experiment are used for validation. Next, several simulations employing all three (NS, DSMC, and hybrid) solvers are performed, and the results are compared. In all NS cases, laminar flow is assumed. Finally, the power of mesh adaptation is explored through the mesh optimization of DSMC and hybrid simulations. VHS parameters for each species modeled in the following test cases are provided in Appendix A.

3.1 DSMC Validation Simulations

This Section presents three simulations: A 3D corner flow problem with Argon, a 2D flat plate with Nitrogen, and a 2D cylinder test case with Air modeled using five chemical species. Contours of flow field quantities on slices of the domain and surface quantities are compared against results obtained from literature and discussed. These three cases test all the capabilities of HALO3D-DSMC, and through these results, HALO3D-DSMC is established as the standard for comparisons with HALO3D-HYBRID. Comparisons with literature are also made in Sections 3.2 and 3.3 and provide further strength to the validation of the hybrid and DSMC codes.

3.1.1 Bird's Corner Case (Mach 6, Knudsen 0.043)

Bird's Mach 6 corner case [9] is a 3D flow of VHS Argon gas over two perpendicular 0.25 m × 0.18 m diffuse walls maintained at a temperature of 1000 K. The freestream Knudsen number is 0.043. The domain dimensions and uniform structured mesh considered for this case are the same as in Bird's DS3V code, that is 0.3 m × 0.18 m × 0.18 m for a total of 9720 cells. Two perpendicular symmetry planes are placed upstream of the corner, and the inlet boundary extends until x = 0.3 m. The domain and boundary conditions are illustrated in Fig. 3.1. No sub-celling technique is used for this simulation, and the freestream number density, temperature, and velocity are set to 1 × 10^{20} m^3, 300 K, and 1936 m/s, respectively. The ratio of real to simulated particles is equal to 2

$\times 10^{13}$, the constant time step is 2×10^{-6} s and a total of 200,000 samples are recorded after steady-state.

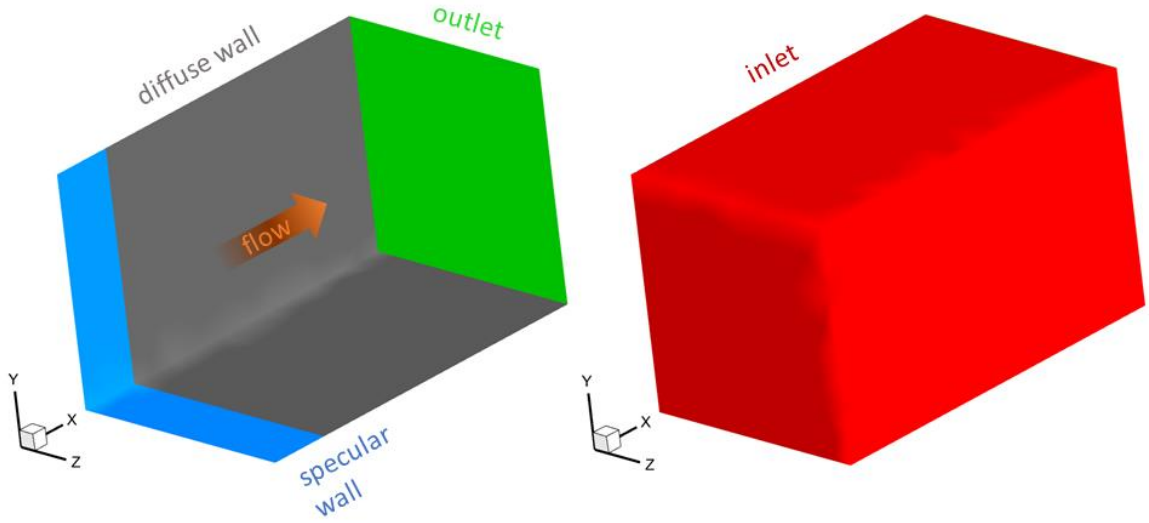

Fig. 3.1 Domain and boundary conditions for Bird's corner case

Contours of normalized density are shown in Fig. 3.2, with the solid black lines referring to HALO3D-DSMC and the solid pink lines given by DS3V. There is an excellent agreement between both solvers, and a similar observation can be made for the contours of temperature and Mach number given in Bird's book but not reproduced here for brevity. Figs. 3.3-3.5 present the skin friction and heat transfer coefficients, and a good concordance is again found between HALO3D-DSMC and DS3V.

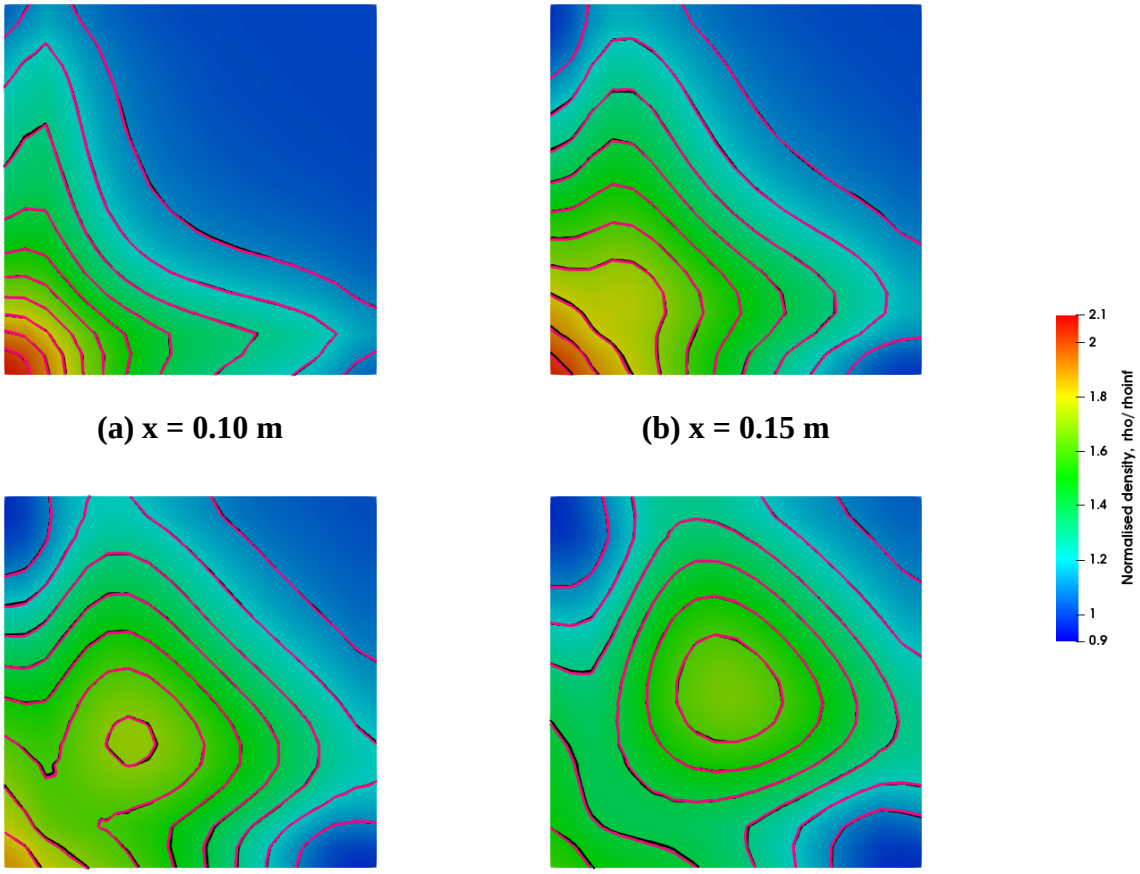

(a) x = 0.10 m **(b) x = 0.15 m**

(c) x = 0.20 m **(d) x = 0.25 m**

Fig. 3.2 Normalized density contours at various x-locations for Bird's corner case (HALO3D-DSMC: solid black lines, DS3V: solid pink lines) (Mach 6, Knudsen 0.043)

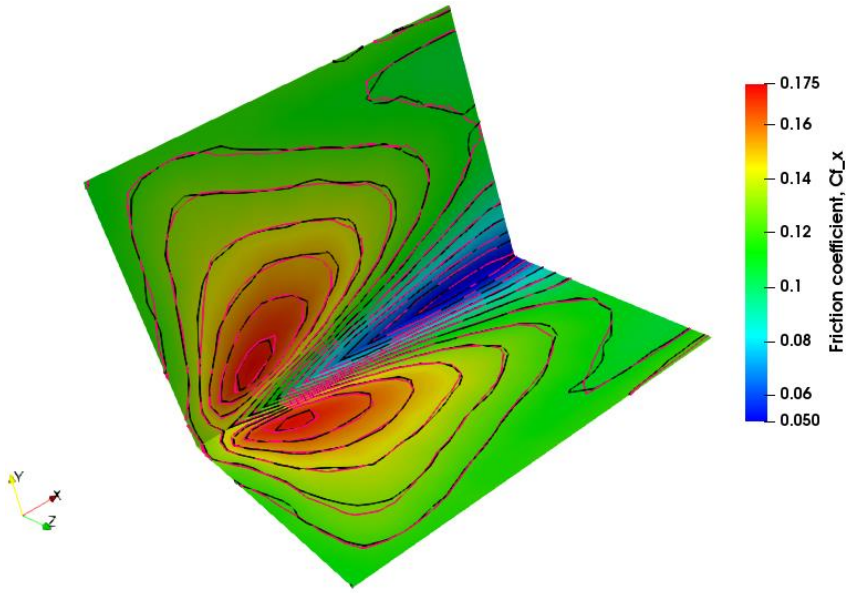

Fig. 3.3 x-component of the skin friction coefficient for Bird's corner case (HALO3D-DSMC: solid black lines, DS3V: solid pink lines) (Mach 6, Knudsen 0.043)

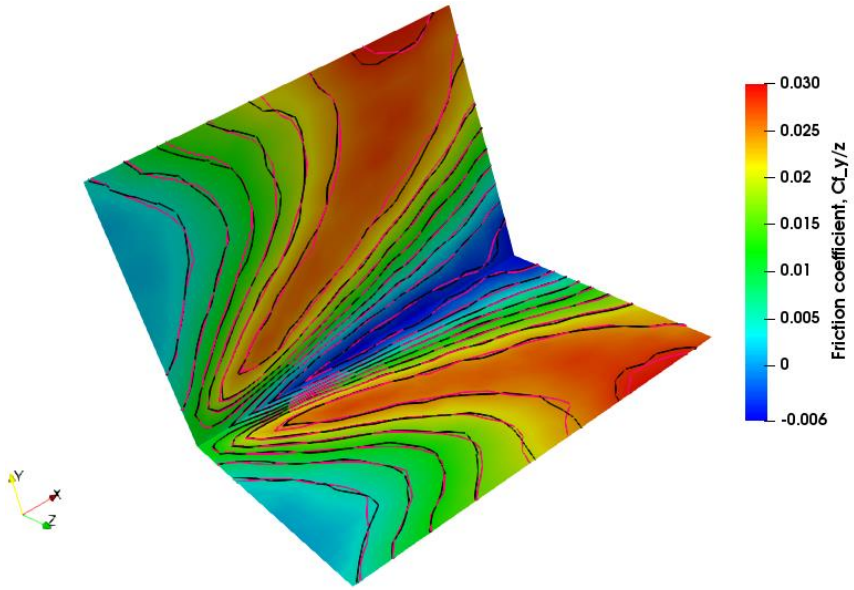

Fig. 3.4 y- and z-components of the skin friction coefficient for Bird's corner case (HALO3D-DSMC: solid black lines, DS3V: solid pink lines) (Mach 6, Knudsen 0.043)

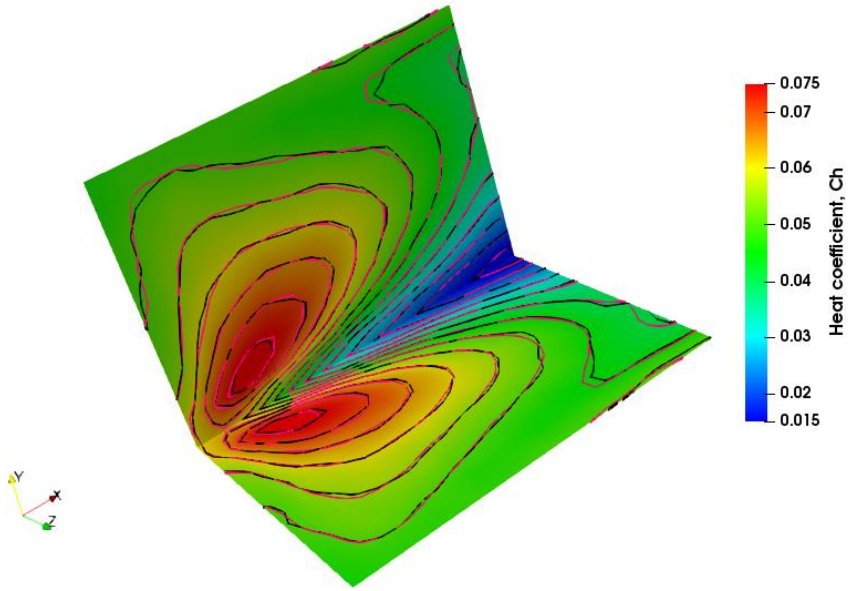

Fig. 3.5 Heat transfer coefficient for Bird's corner case
(HALO3D-DSMC: solid black lines, DS3V: solid pink lines) (Mach 6, Knudsen 0.043)

3.1.2 Nitrogen Flow over a 2D Flat Plate: DSMC and Experiment (Mach 20, Knudsen 0.017)

Allegre *et al* (1992) conducted [102] experiments on the hypersonic flow of Nitrogen over a flat plate at angles of attack of zero and ten degrees. The results from these experiments have been widely used to validate DSMC codes such as MONACO, DAC, and SPARTA. The domain, with its boundary conditions, are illustrated in Fig. 3.6 where the length of the plate is 0.1 m, and the thickness is 0.005 m. A uniformly spaced cubic mesh consisting of cells with edge lengths of 5×10^{-4} m has been used in the present work. The two z-symmetry planes (specular walls) are spaced two-cell widths apart. The flow consists of molecular Nitrogen with the following freestream conditions for pressure, temperature, x-velocity, Mach number, and Knudsen number (based on the length of the plate), respectively: 0.06834 Pa, 13.32 K, 1503 m/s, 20, 0.017. The diffuse wall temperature is kept at 290 K in the DSMC simulation, which corresponds to the experimental conditions where a cooling system within the wind tunnel model keeps the wall temperature constant. The time step is 3.102×10^{-7} s, and 16,000 iterations are used for sampling. TAS and NN methods are used for collision pair selection with a switch from TAS to NN when the cell contains fewer than 30 particles. At steady-state, the total number of particles in the domain is ~6 million. The VHS parameters for Nitrogen are provided in Appendix A. Padilla [103] compared the

performance of MONACO and DAC for this test case and found rotational energy modeling to be crucial for a good comparison with experimental results. Hence, a rotational collision number of 5 is used for the simulation, same as DAC, while MONACO uses a variable rotational collision number model.

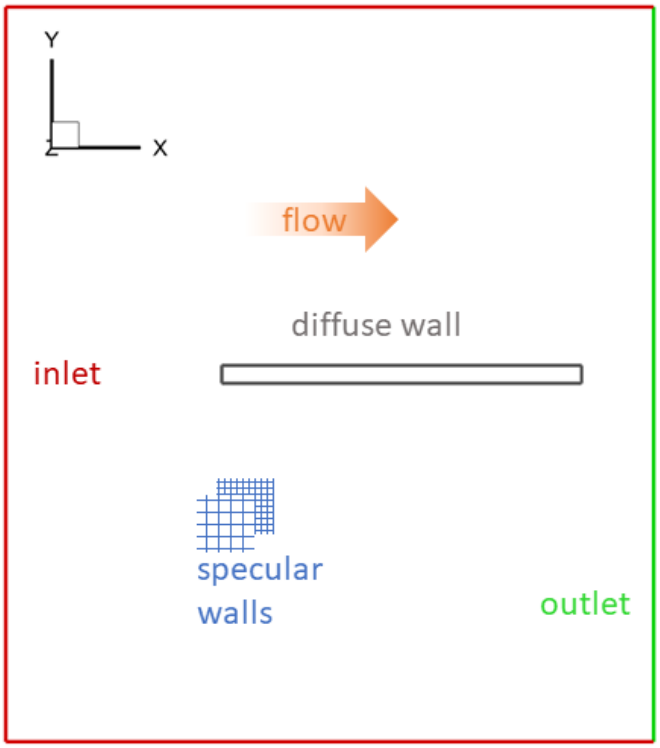

Fig. 3.6 Domain and boundary conditions for the hypersonic flow of Nitrogen over a flat plate

Contours of Mach numbers, rotational temperatures, particle counts and mfp are illustrated in Figs. 3.7 and 3.8. The Mach contours showcase a prominent bow shock upstream of the flat plate and the flow near the wall is subsonic. The rotational temperature contours indicate the presence of rotational nonequilibrium in the flow with a maximum rotational temperature of ~500 K at the stagnation point. The contours of particles/cell show large particle counts at the stagnation point, with a maximum of ~240 particles/cell, and with the wake region exhibiting lower particle counts as expected. The mfp contours show that mfp is low at the stagnation point and higher in the wake region. Surface quantities such as heat flux and surface pressure are compared in Fig. 3.9 between MONACO, DAC, HALO3D, and the experiment. The results for DAC and MONACO are obtained from [103]. All three DSMC solvers show good agreement with each other for the heat

flux and compare well with experiment. MONACO compares slightly better with experiment for the surface pressure, while DAC and HALO3D pressures are seen to match. The uncertainty in experimental measurements is ±0.1 Pa and ±0.05$\boldsymbol{q}$ W/m^2 where $\boldsymbol{q}$ is the heat flux [103].

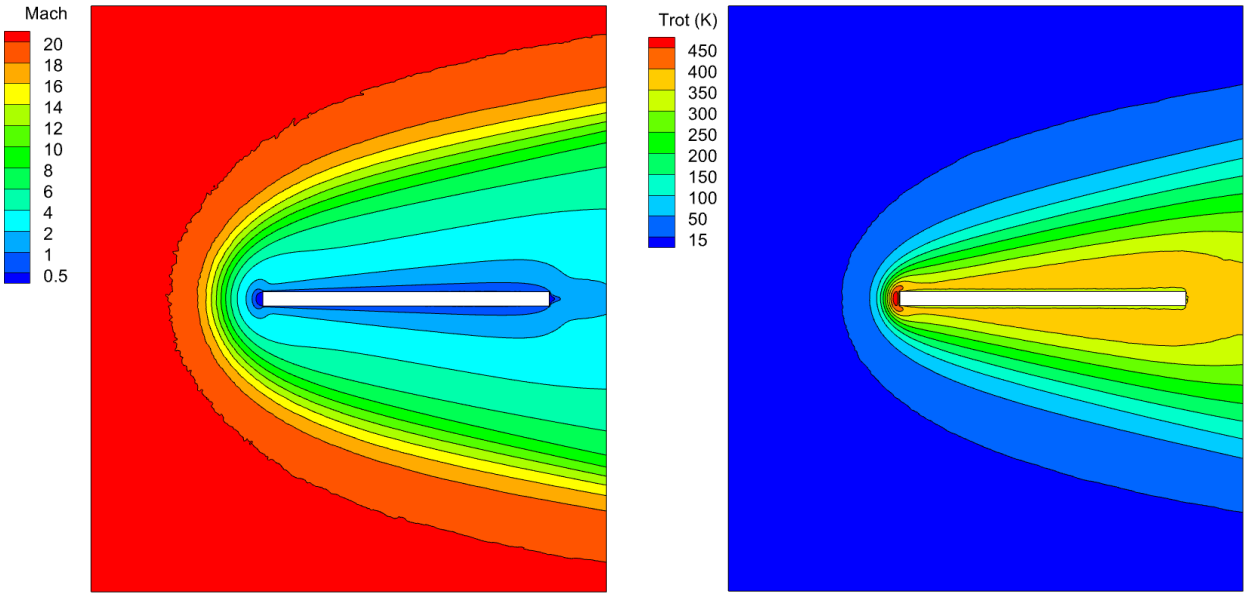

Fig. 3.7 Mach number (left) and rotational temperature (right) for the flow of Nitrogen over a flat plate (Mach 20, Knudsen 0.017)

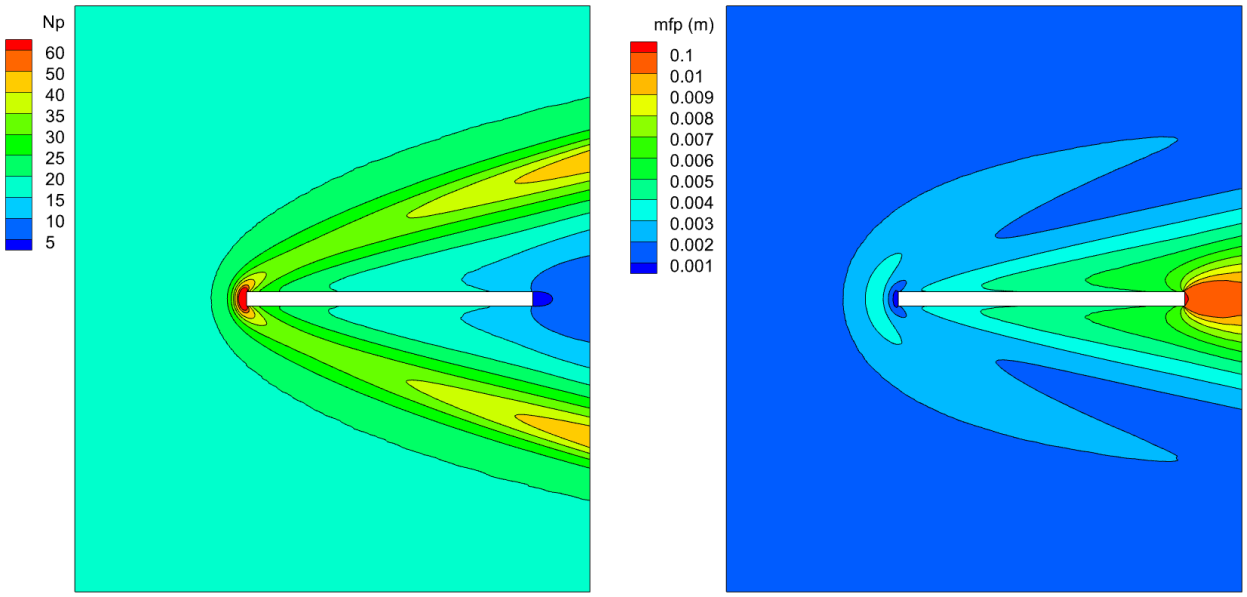

Fig. 3.8 Number of particles per cell (left) and mean free path (right) for the flow of Nitrogen over a flat plate (Mach 20, Knudsen 0.017)

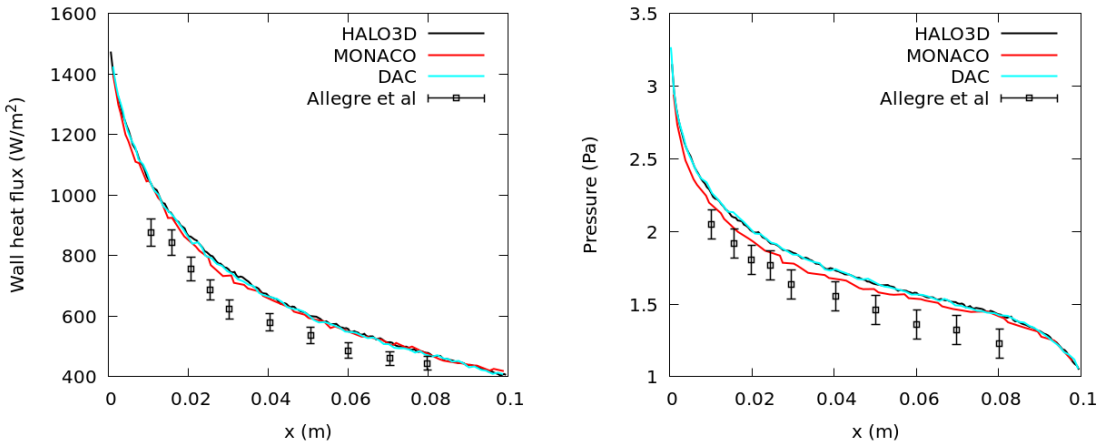

(a) Surface heat flux **(b) Surface pressure**

Fig. 3.9 Surface heat flux and pressure for the flow of Nitrogen over a flat plate (Mach 20, Knudsen 0.017)

3.1.3 Air Mixture Flow over 2D Cylinder (Mach 24.85, Knudsen 0.004)

Adiabatic heat bath simulations are presented in this Section to verify the reaction rate and post-reaction velocity, and energy computations in the Quantum-Kinetics (QK) chemistry model in HALO3D-DSMC. The set of parameters *a* and *b* used to adjust the activation energy of exchange reactions [104] is that of Bird [75] (see Appendix B), and all activation energies are taken from [63]. The heat bath is a single cell with a characteristic length equal to 1×10^{-5} m and symmetry boundaries. The mixture number density is fixed to 1×10^{23} m^3, evenly split among the 2 reactant species, and the temperature is varied between 1000 K and 40,000 K. The time step equals 1×10^{-9} s, the initial number of simulated particles is 1 M, and all collision numbers are equal to 1. In the first stage, particles are not allowed to split should they react to keep the same gas composition as time is advanced. The forward reaction rate is averaged over 100 iterations, and results for two dissociation reactions and four exchange reactions are given in Fig. 3.10a-f. The analytical QK solutions are obtained from Bird's DS0V code [75], and the dissociation reaction results given by NASA's DAC DSMC solver are taken from [105]. There is an excellent agreement for all reactions.

In a second stage, particles are allowed to split upon impact. All initial modal temperatures are set to 30,000 K, and pressure equals 6383 Pa, with a gas composition of 0.79% N_2 and 0.21% O_2 in volume. Fig. 3.11 shows the evolution of the temperature and species number density versus time for dsmcFoam and HALO3D-DSMC, and a good match can be observed.

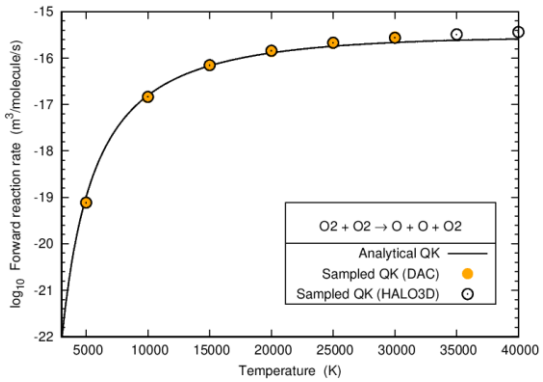

(a) Molecule-molecule dissociation

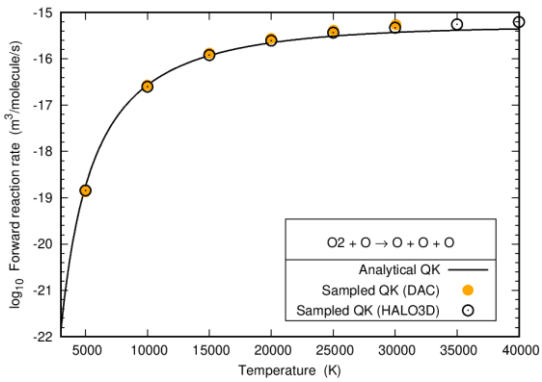

(b) Molecule-atom dissociation

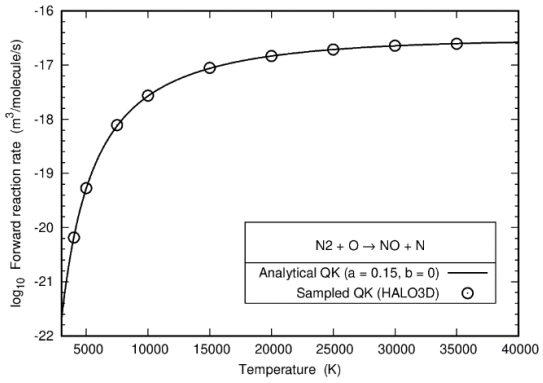

(c) First endothermic exchange reaction

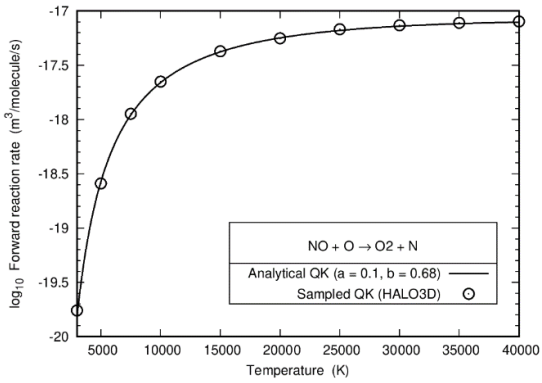

(d) Second endothermic exchange reaction

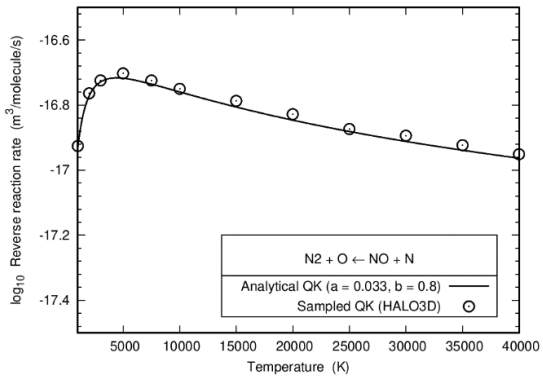

(e) First exothermic exchange reaction

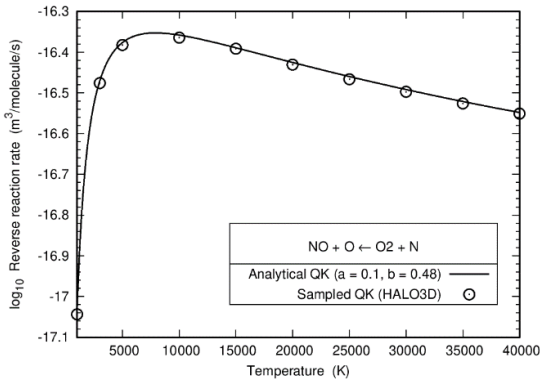

(f) Second exothermic exchange reaction

Fig. 3.10 Dissociation and exchange reaction rates using the QK model in HALO3D-DSMC

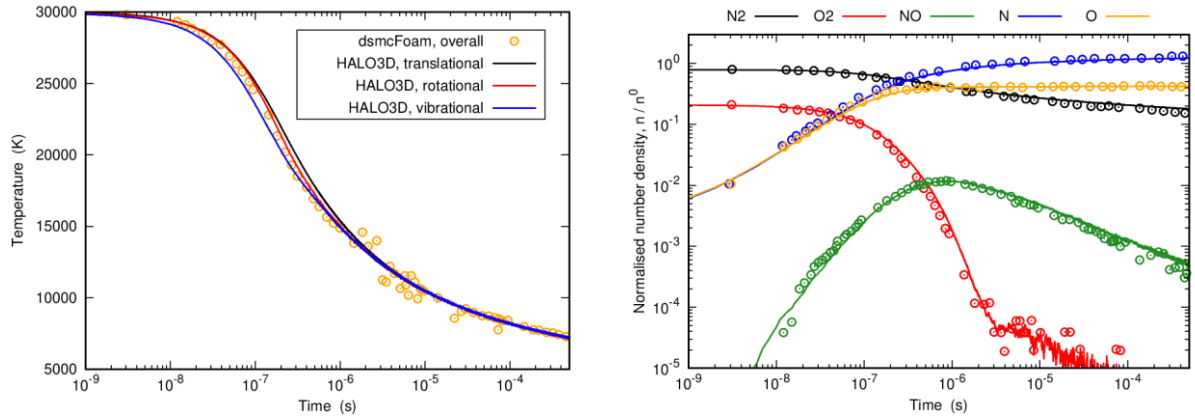

(a) Temperature **(b) Species number density**

Fig. 3.11 5-species air heat bath results versus time
(HALO3D-DSMC: solid lines, dsmcFoam: symbols)

A Mach 24.85 2-D air mixture flow past a 1-meter radius cylinder is now investigated. The domain and boundary conditions are presented in Fig. 3.12. Studied by Scanlon *et al.* [63] with simulation results provided for both non-reacting and reacting 5-species air, this continuum-transition case (overall Knudsen number 0.004) has freestream conditions corresponding to an altitude of 84 km: the freestream temperature is equal to 187 K, the freestream velocity is 6813 m/s, and the species number densities of N_2 and O_2 are set to 1.13×10^{21} m^{-3} and 3.03×10^{20} m^{-3}, respectively. The diffuse cylinder wall temperature is set to 1000 K, and the ratio of real to simulated particles equals 2×10^{12}. The time step and cell size match those given in [63]. The time step is prescribed to be 1×10^{-7} s, and the structured and uniform mesh is composed of 304 cells radially and 402 cells longitudinally, for a total of 122,208 cells. The collision scheme is NTC, and the collision partner selection technique is TAS with a target of 4 particles per sub-cell. The resulting collision grid is updated every 1000 time steps before steady-state and frozen after. Furthermore, coefficients for the VHS particles are that of Bird [9], and the constant rotational and vibrational collision numbers are set to 5 and 50, respectively. The results presented in this Section use the QK model with the same *a* and *b* coefficients and activation energies determined by Scanlon *et al.* [63].

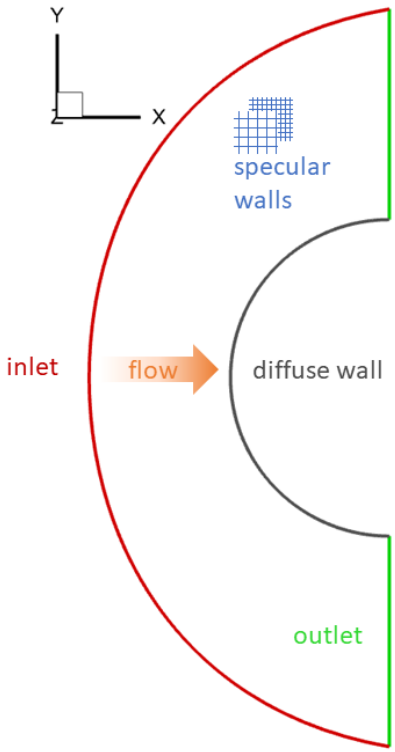

Fig. 3.12 Domain and boundary conditions for the hypersonic air mixture flow past a cylinder

Serial simulations are conducted until steady-state and ensemble averaging is then leveraged using a total of 20 statistically independent simulations for a cumulative number of 260,000 samples. There are 35.8 M particles at steady-state for the non-reacting run and 42.9 M for the reacting simulation. HALO3D-DSMC results are compared against dsmcFoam (now dsmcFoam+), which uses the QK model, and MONACO, which implements the TCE chemistry model. Figs. 3.13-3.15 show stagnation line profiles of modal temperatures, velocity magnitude, and species number densities for all three solvers. A good concordance is observed for both non-reacting and reacting simulations. Figs. 3.16-3.19 present surface quantities of surface pressure, heat flux, temperature jump, and velocity slip, and there is once more a reasonable agreement between HALO3D-DSMC, MONACO, and dsmcFoam.

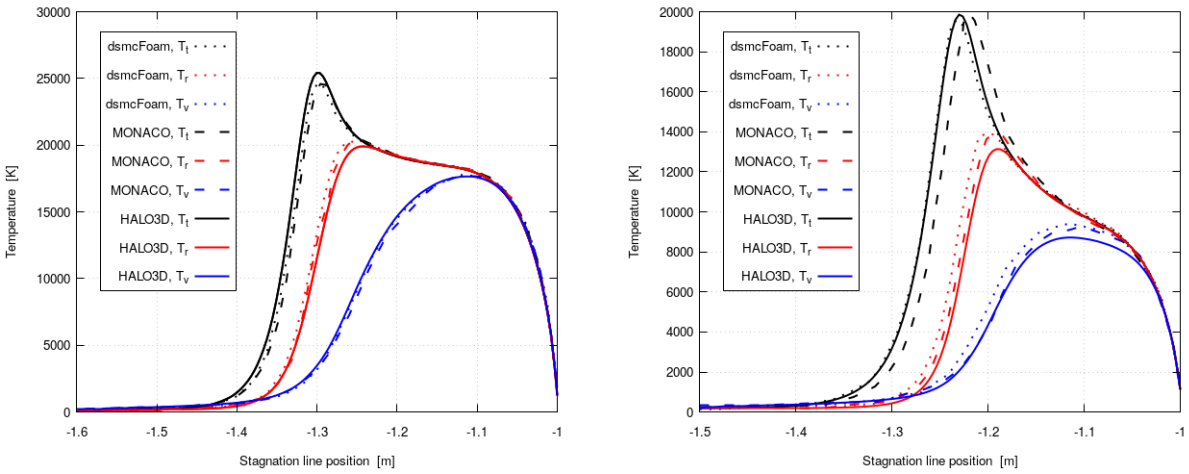

(a) Non-reacting **(b) Reacting**

Fig. 3.13 Modal temperatures profiles along the stagnation line for the air mixture flow past a cylinder (Mach 24.85, Knudsen 0.004)

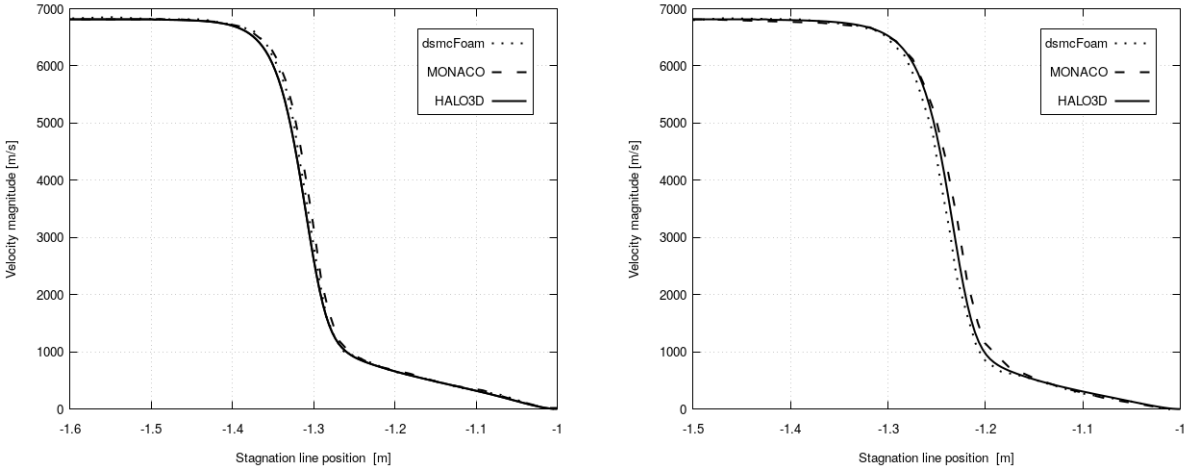

(a) Non-reacting **(b) Reacting**

Fig. 3.14 Velocity magnitude profile along the stagnation line for the air mixture flow past a cylinder (Mach 24.85, Knudsen 0.004)

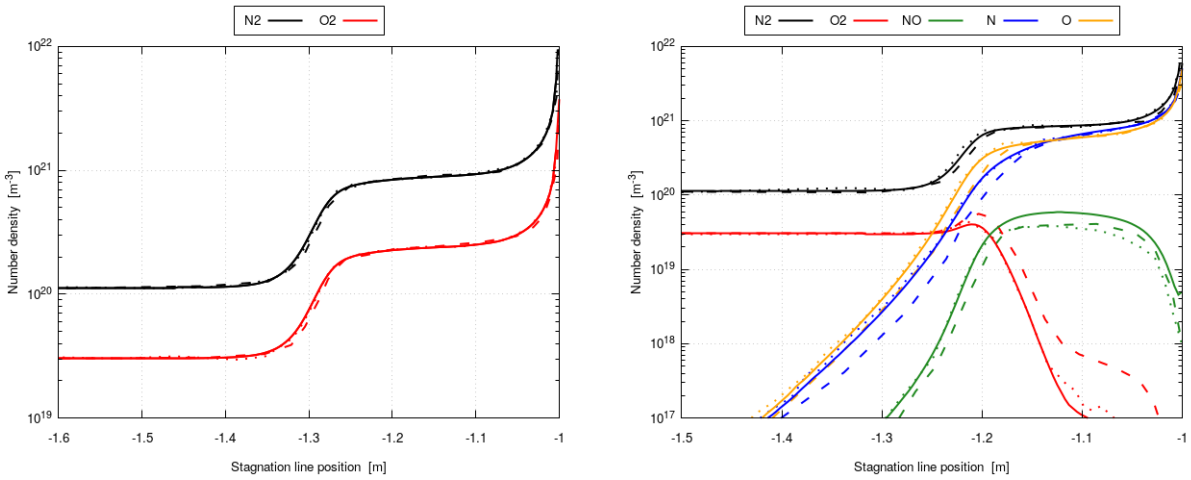

(a) Non-reacting **(b) Reacting**

Fig. 3.15 Species number density profiles along the stagnation line for the air mixture flow past a cylinder (dsmcFoam: dotted lines, MONACO: dashed lines, HALO3D-DSMC: solid lines) (Mach 24.85, Knudsen 0.004)

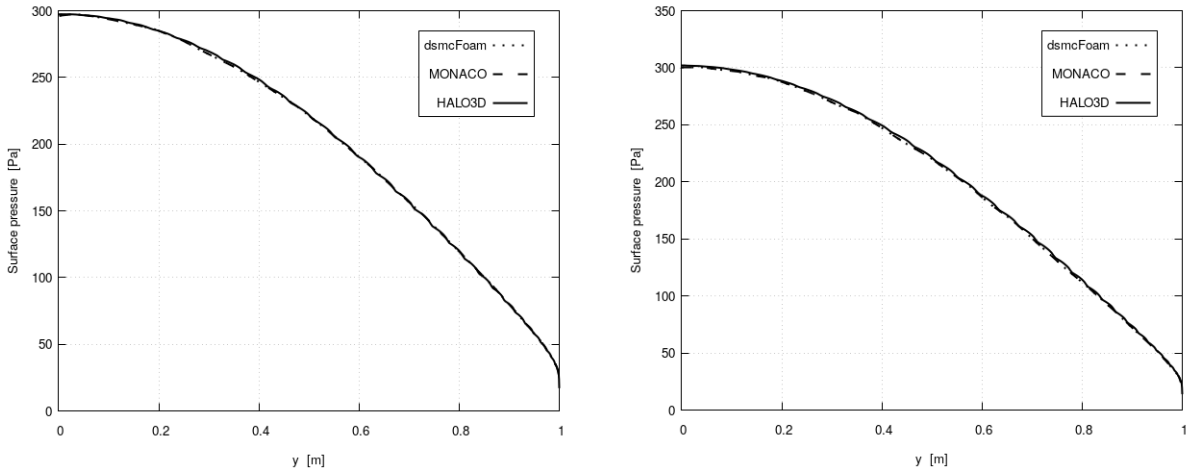

(a) Non-reacting **(b) Reacting**

Fig. 3.16 Surface pressure for the air mixture flow past a cylinder case (Mach 24.85, Knudsen 0.004)

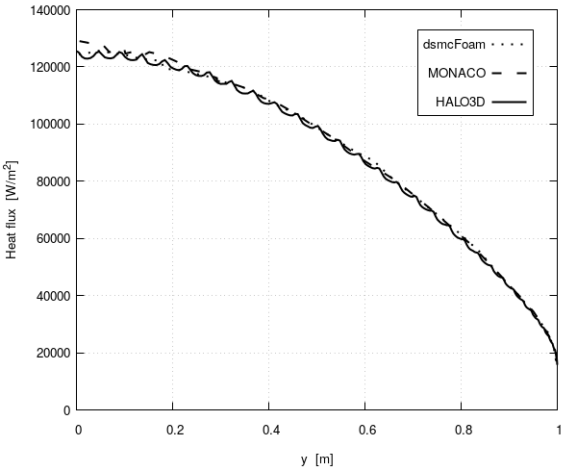

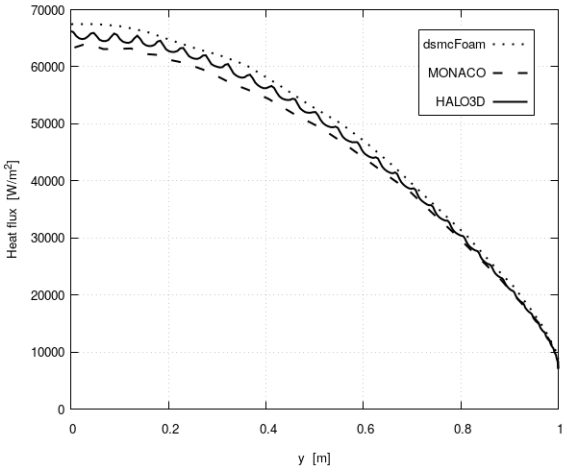

(a) Non-reacting **(b) Reacting**

Fig. 3.17 Wall heat flux for the air mixture flow past a cylinder case (Mach 24.85, Knudsen 0.004)

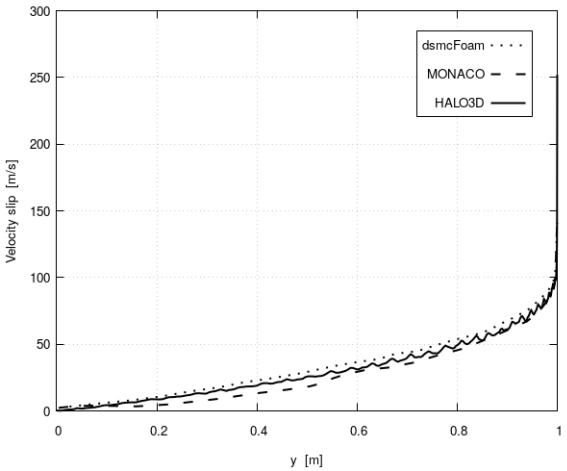

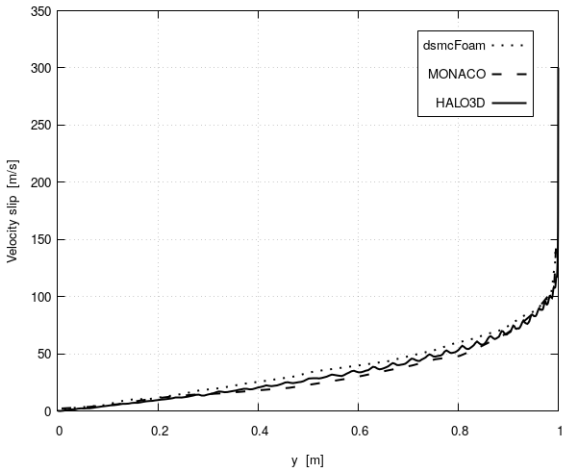

(a) Non-reacting **(b) Reacting**

Fig. 3.18 Velocity slip for the air mixture flow past a cylinder case (Mach 24.85, Knudsen 0.004)

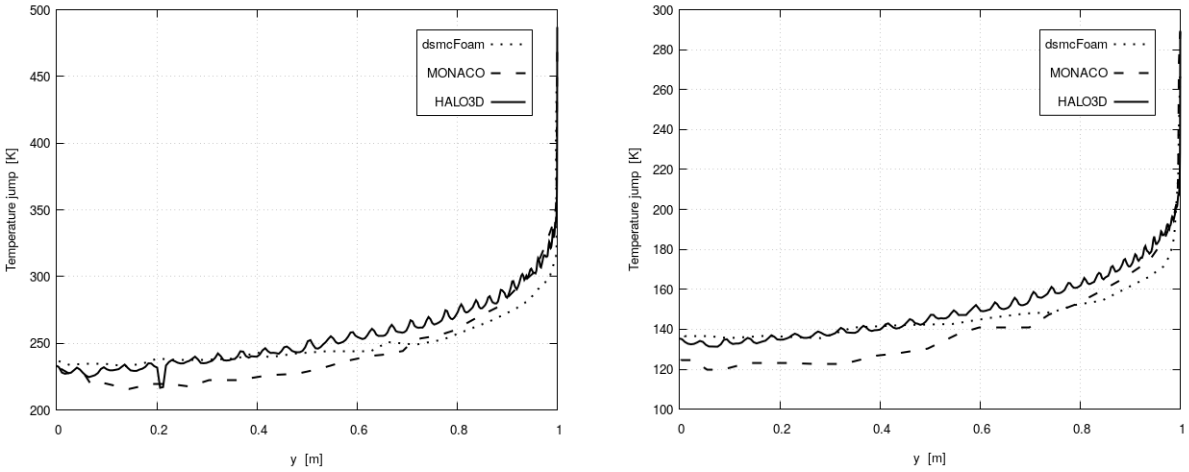

(a) Non-reacting **(b) Reacting**

Fig. 3.19 Translational temperature jump for the air mixture flow past a cylinder case (Mach 24.85, Knudsen 0.004)

Contours of translational, rotational, and vibrational temperatures are presented in Fig. 3.20 and 3.21 for HALO3D and dsmcFoam for the reacting case. A good agreement can be observed between these two codes for all three temperature contours. These verification results provide sufficient evidence of the correct implementation of the various modules in HALO3D-DSMC, and thus it can reliably be used to predict of thermo-chemical non-equilibrium flow fields at high altitudes and serve as the standard for hybrid NS-DSMC verification.

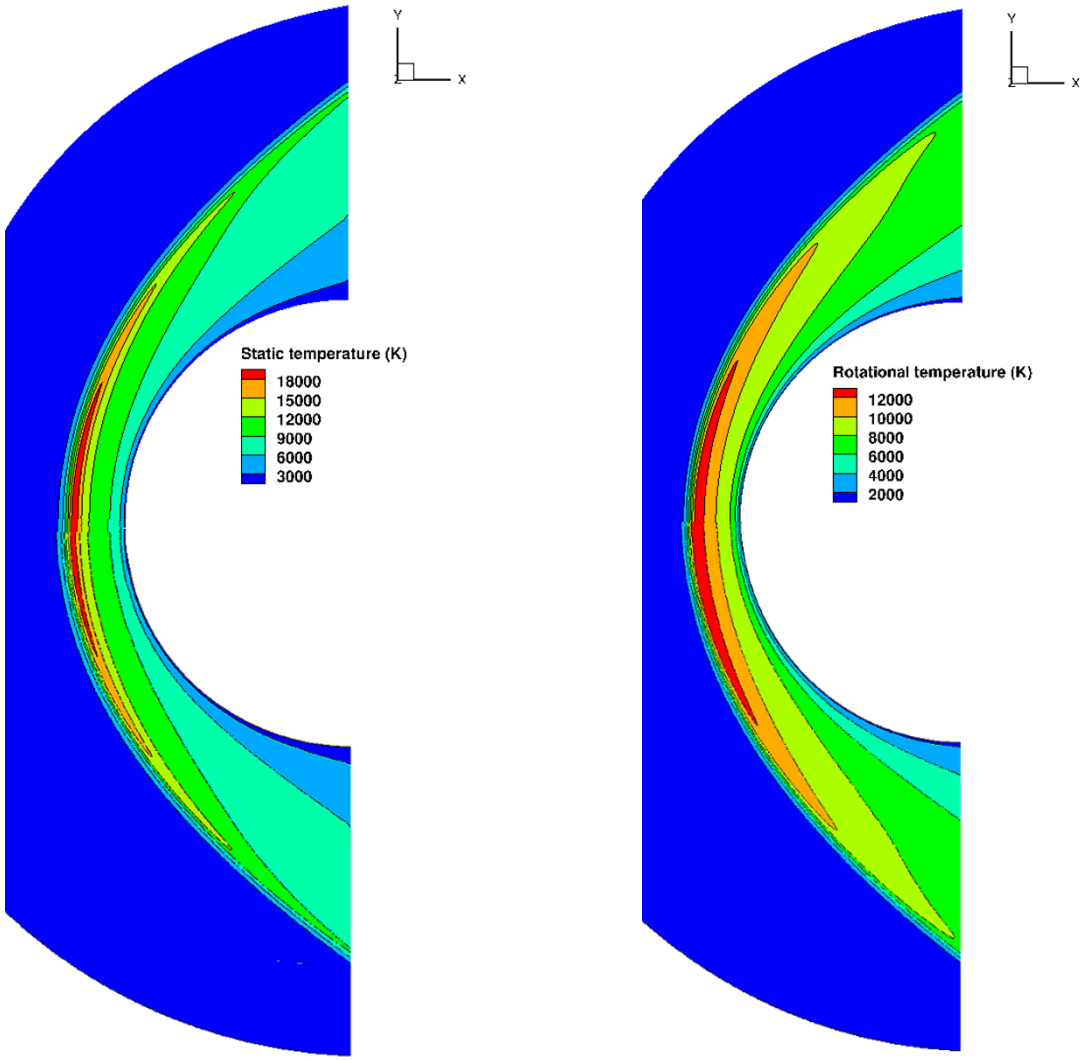

Fig. 3.20 Translational (left) and rotational (right) temperatures for the reacting air mixture flow past a cylinder. HALO3D results are presented on the top half and dsmcFoam results are on the bottom half. (Mach 24.85, Knudsen 0.004)

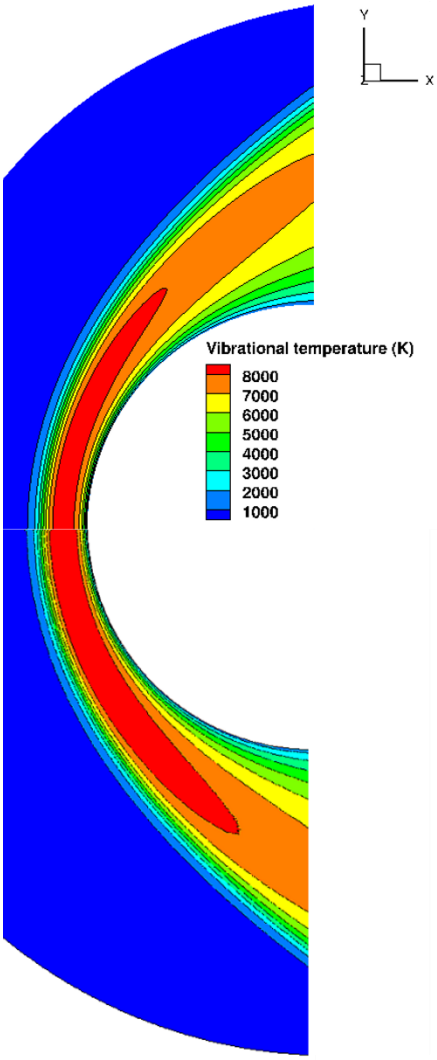

Fig. 3.21 Vibrational temperature for the reacting air mixture flow past a cylinder. HALO3D results are presented on the top half and dsmcFoam results are on the bottom half. (Mach 24.85, Knudsen 0.004)

3.2 Hybrid NS-DSMC Results

This Section presents results for the validation of HALO3D-HYBRID through comparisons with HALO3D-DSMC, HALO3D-NS, and literature. In hybrid simulations, the statistical scatter of DSMC was controlled by using a sufficient number of particles so as to not poison the NS solution. Flows over a leading-edge and a 2D cylinder are studied, and results from all three solvers are presented for each test case. Contours of the flow variables and data extracted along a line in the domain are shown for comparison. The distributions of $Kn_{\max}$ and $Kn_{\mathrm{ROT-NEQ}}$ are also presented to illustrate the degree of continuum breakdown and thermal non-equilibrium where applicable. It

should be noted that $Kn_{\mathrm{ROT-NEQ}}$ is shown as an indicator of thermal non-equilibrium only and is not used to delineate the NS and DSMC zones. The NS and DSMC regions in the hybrid solution are demarcated with vertical lines and labeled in the line plots. In this Section, structured meshes are employed for the hybrid, DSMC, and NS computations, and unstructured mesh simulations are handled in Section 3.3.

3.2.1 Leading-Edge Flows

Bird's leading-edge flow [9] is a canonical 2D analog of the 3D hypersonic corner flow where the corner effects are removed. This computationally inexpensive problem has been widely used to verify DSMC codes. In this Section, four configurations of the leading-edge problem in increasing complexity are studied to validate the HALO3D-HYBRID infrastructure. The domain and boundary conditions are shown in Fig. 3.22. The following flow conditions are kept the same for all four test cases: the freestream velocity, pressure, and temperature are 1412.5 m/s, 0.4142 Pa, and 300 K, respectively. The wall temperature is 500 K, and the DSMC time step is 2×10^{-6} s. A structured 99 × 60 × 1 mesh with some mesh clustering at the stagnation point is used in all the simulations in this Section.

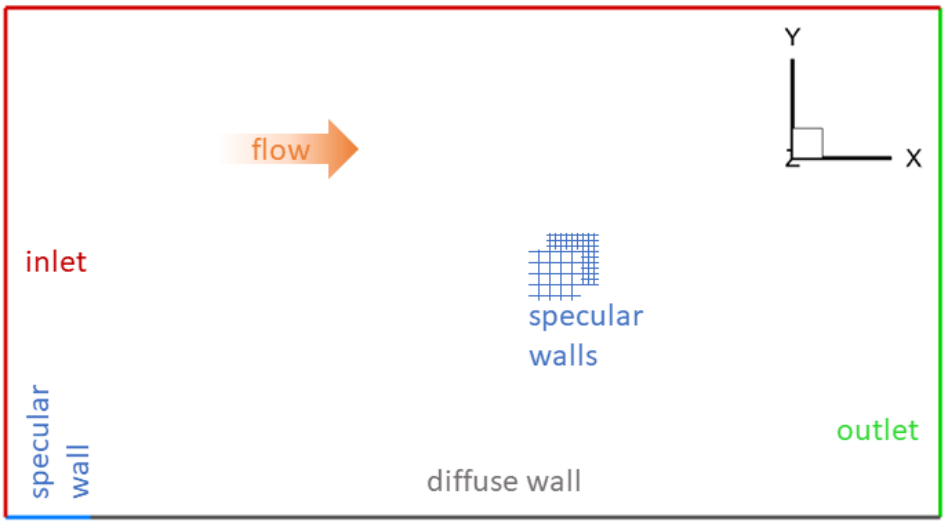

Fig. 3.22 Domain and boundary conditions for the leading-edge hypersonic flow

All the leading-edge hybrid simulations are initialized with an NS solution with no-slip boundary conditions, which performs better than initialization with a slip solution. When slip NS solutions are used to initialize the hybrid simulations, the predicted NS-DSMC boundaries are ~0.1m

downstream of the no-slip NS predictions consistently for all four leading-edge test cases. This places the upstream NS-DSMC boundary in a zone of greater non-equilibrium, which necessitates a Chapman-Enskog distribution function to generate particle velocities in the outer buffer region. Since this present study considers a Maxwellian distribution to initialize particles, the no-slip NS initial solution is ideal since it provides an upstream NS-DSMC boundary located in a zone of equilibrium. Nevertheless, for the full NS results, the slip computations compare better with DSMC, and these are presented in the contours and line plots.

3.2.1.1 Argon Flow Over Leading-Edge (Mach 4.3, Knudsen 0.013)

This first leading-edge test case considers the flow of Argon, which does not possess rotational nor vibrational modes of energy, and the VHS parameters for Argon are taken from Bird [9]. The freestream Knudsen number is 0.013, and the Mach number is 4.3. The distribution of $Kn_{\max}$ from the no-slip NS solution is presented in Fig. 3.23, with a maximum of ~1 at the stagnation point. The shock and boundary layer are both encompassed within a zone of $Kn_{\max}$ greater than 0.05, indicating that these are regions of continuum breakdown.

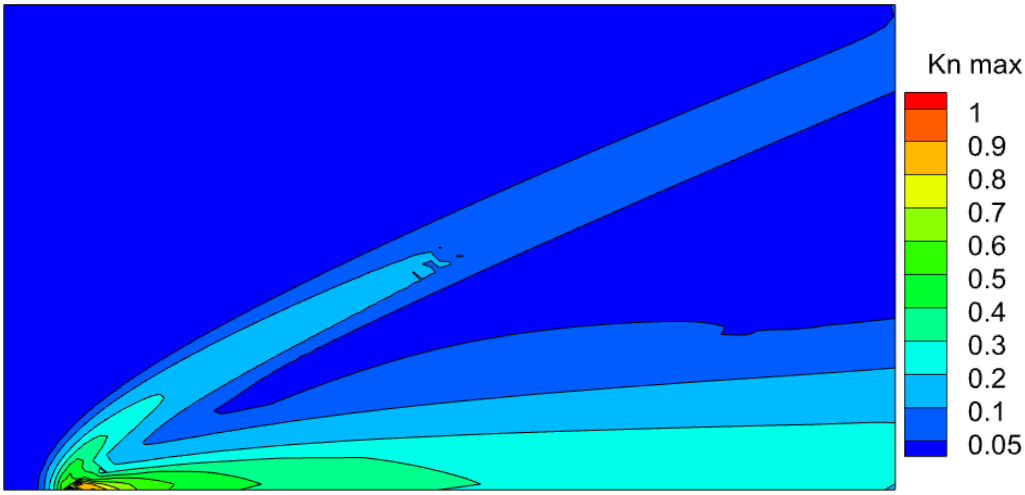

Fig. 3.23 Kn_{max} distribution for the flow of Argon over a leading-edge (Mach 4.3, Knudsen 0.013)

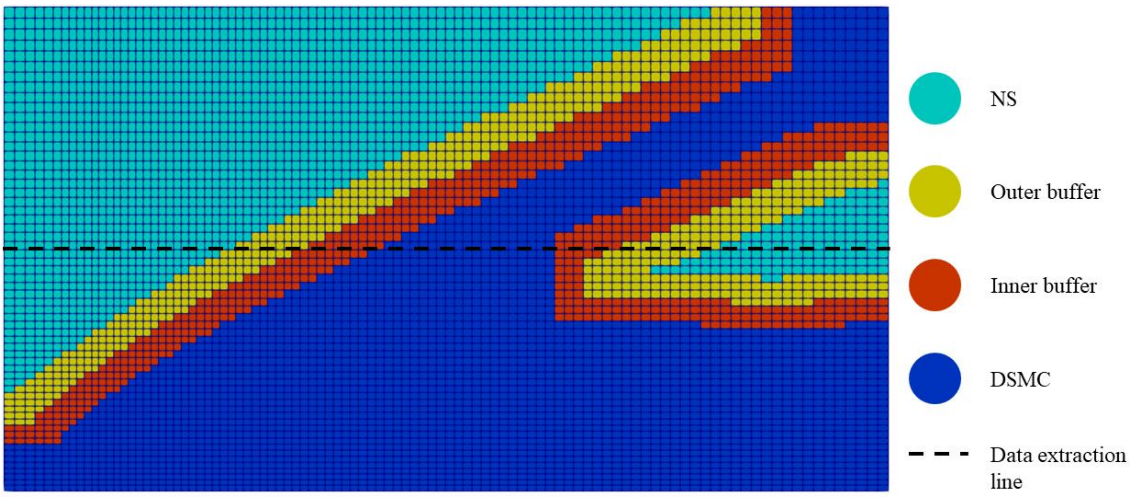

Fig. 3.24 Hybrid masks for the flow of Argon over a leading-edge (Mach 4.3, Knudsen 0.013)

The hybrid masks are shown in Fig. 3.24, where a minimum of 3 cell layers can be observed for the inner and outer buffers. The shock and boundary layer are assigned to be DSMC regions, and the freestream and a small region downstream of the shock are assigned to be NS regions. Contours of density, pressure and Mach number for the NS, DSMC, and hybrid simulations are presented in Fig. 3.25-3.27. The NS density and pressure solutions differ from the DSMC solutions, and the NS Mach number compares well with DSMC in most of the domain except near the trailing edge of the wall. The hybrid solutions for density, pressure and Mach number all agree well with DSMC contours throughout the domain.

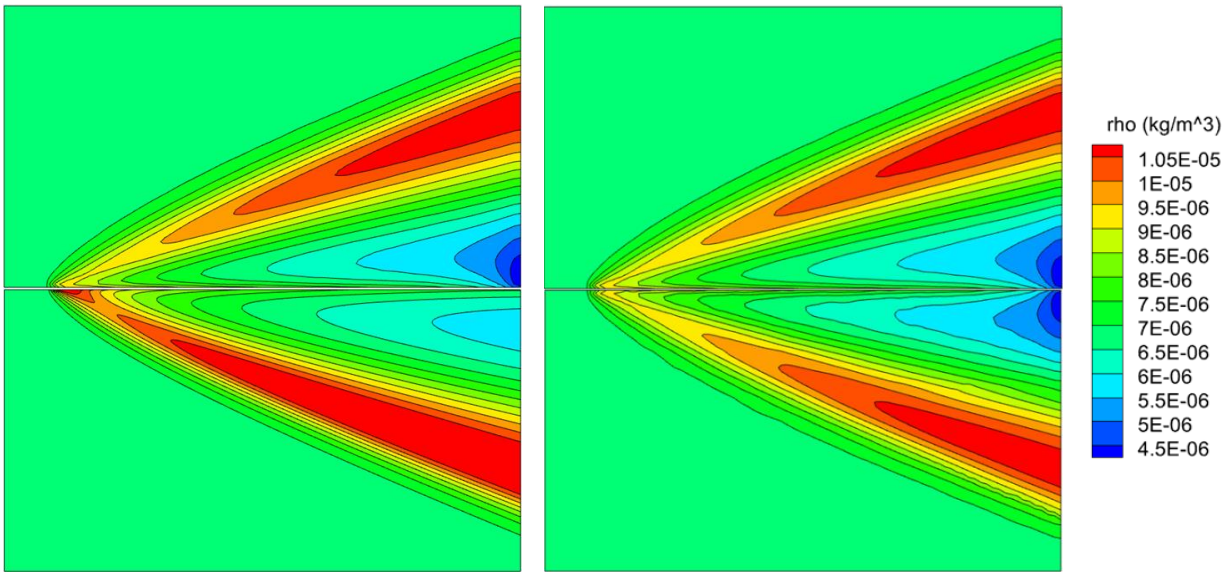

Fig. 3.25 Density contours of the NS (bottom-left) and hybrid (bottom-right) simulations compared against DSMC (top) for the flow of Argon over a leading-edge (Mach 4.3, Knudsen 0.013)

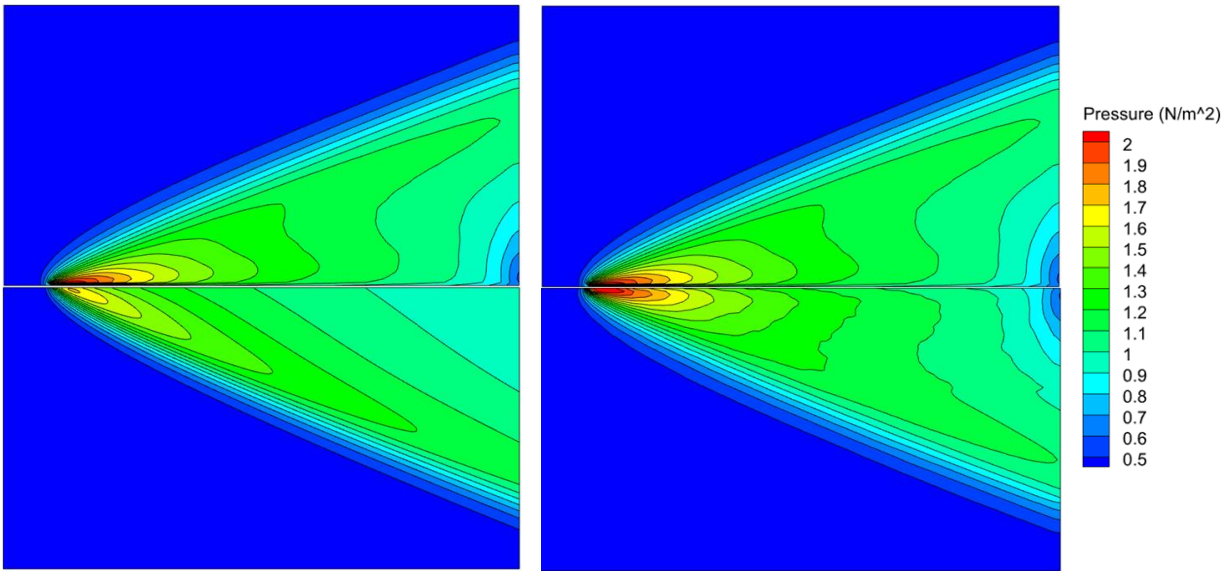

Fig. 3.26 Pressure contours of the NS (bottom-left) and hybrid (bottom-right) simulations compared against DSMC (top) for the flow of Argon over a leading-edge (Mach 4.3, Knudsen 0.013)

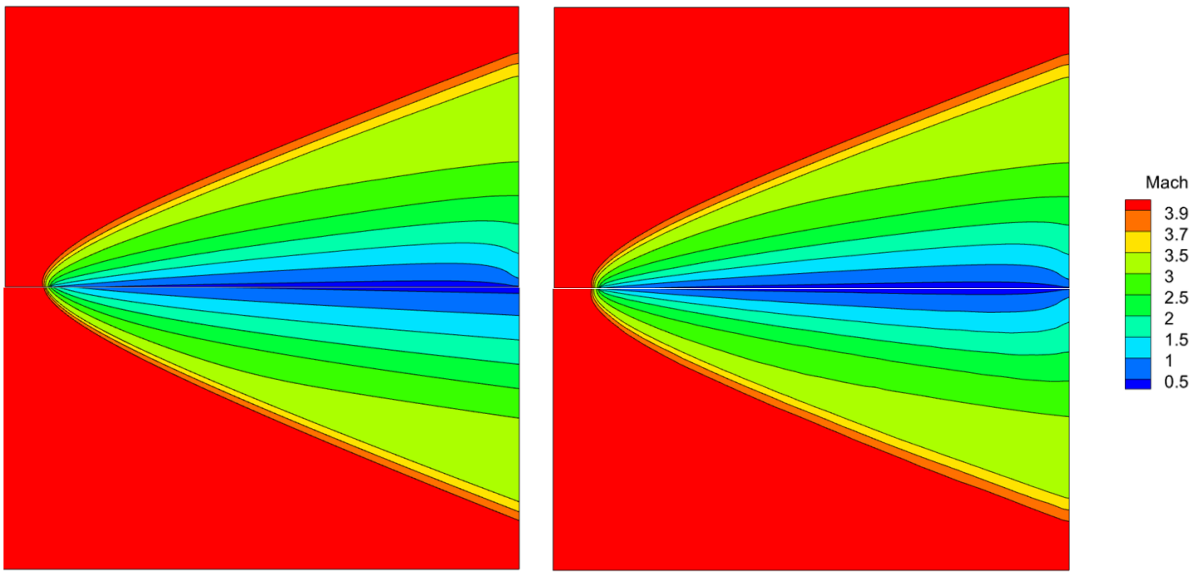

Fig. 3.27 Mach contours of the NS (bottom-left) and hybrid (bottom-right) simulations compared against DSMC (top) for the flow of Argon over a leading-edge (Mach 4.3, Knudsen 0.013)

Plots of density, pressure and translational temperature along a horizontal line at mid-height (y = 0.3 m) are shown in Fig. 3.28-3.30 for NS, DSMC, and hybrid simulations. In all three plots, the upstream NS-DSMC boundaries are located at a $Kn_{\max}$ of 0.05. However, the downstream NS-DSMC boundary is not. This is because of the smoothing algorithm used to remove disconnected patches of buffer cells. As can be seen, the algorithm tends to expand the DSMC region, which results in an NS-DSMC boundary location that is slightly farther downstream. The plots show that the full NS solution disagrees with the DSMC solution within the region of continuum breakdown for density, pressure, and temperature and downstream of this region for density and pressure. $Kn_{\max}$ is found to be greatest within the DSMC region of the hybrid solution, and correspondingly, a deviation of the NS solution from the DSMC solution can be observed here. The hybrid solutions all compare well against the DSMC solutions, with a maximum error of 1.63% for the translational temperature. These line plots illustrate that a full NS simulation cannot capture the flow field accurately. However, when augmented with a DSMC solution in the correct regions, the NS computations in this hybrid system can seamlessly reproduce full DSMC results.

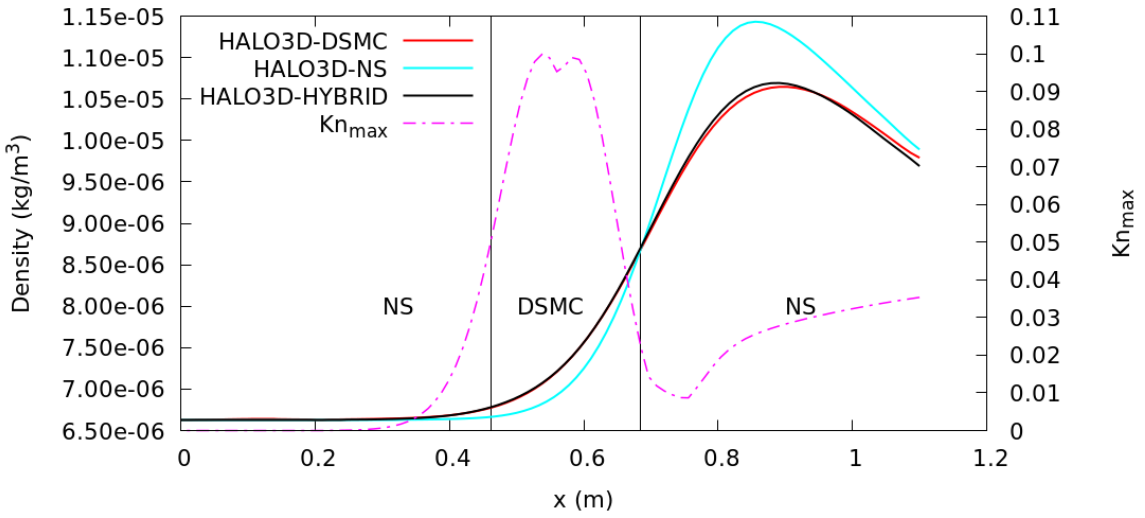

Fig. 3.28 Density along y = 0.3 m for the flow of Argon over a leading-edge (Mach 4.3, Knudsen 0.013)

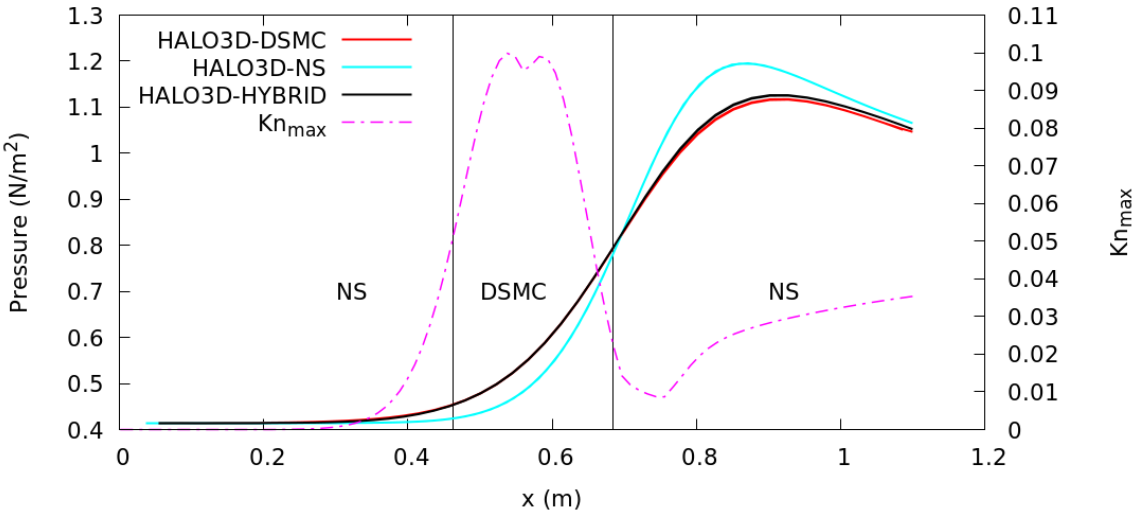

Fig. 3.29 Pressure along y = 0.3 m for the flow of Argon over a leading-edge (Mach 4.3, Knudsen 0.013)

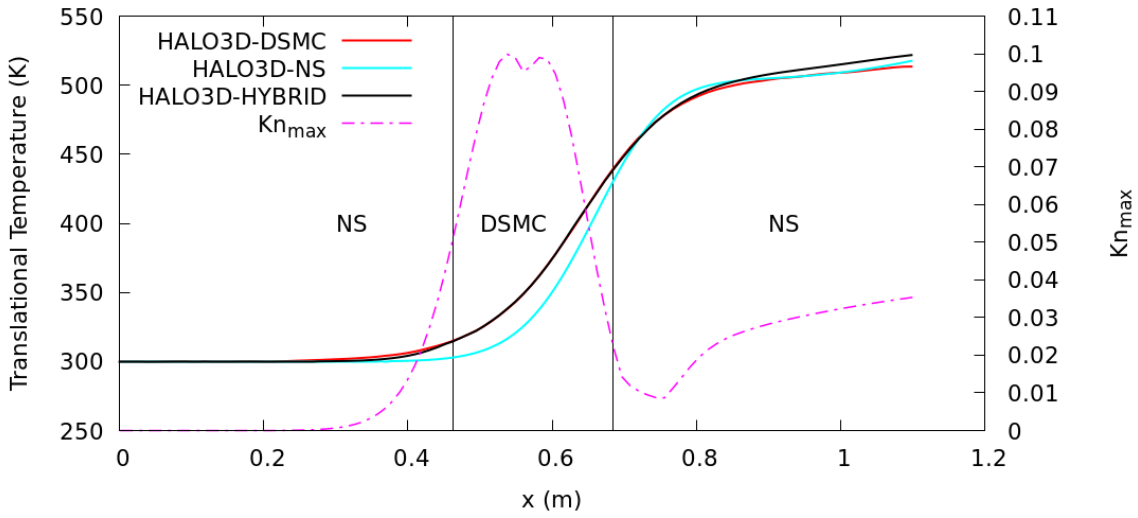

Fig. 3.30 Translational temperature along y = 0.3 m for the flow of Argon over a leading-edge (Mach 4.3, Knudsen 0.013)

The surface heat flux and shear stress for the three solvers are shown in Fig. 3.31 and 3.32. The NS computation shows a sharp increase near the stagnation point for the two surface quantities. This result is consistent with the literature [106], which mentions the presence of a leading-edge singularity in NS solutions for this problem. The peak NS heat flux is 1,372 W/m^2 and the peak NS shear stress is 2.01 N/m^2. $Kn_{\max}$ along the entire surface is greater than 0.05, ensuring that the surface is completely in a DSMC zone. The hybrid surface quantities compare well against DSMC, illustrating that while this problem is difficult for NS solvers, it can easily be tackled by hybrid and DSMC solvers. Finally, the hybrid algorithm provides significant cost benefits over the full DSMC simulation: the full DSMC solution takes 1.71 hours to compute while the hybrid solution takes only 0.73 hours.

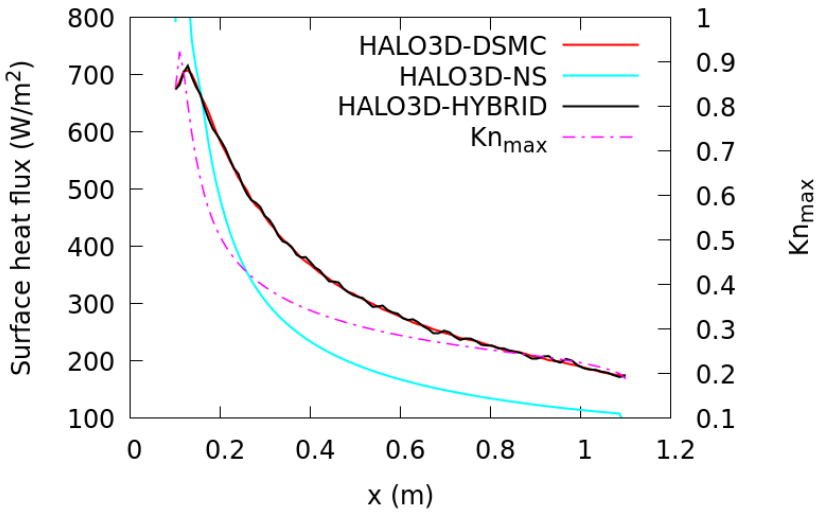

Fig. 3.31 Surface heat flux for the flow of Argon over a leading-edge (Mach 4.3, Knudsen 0.013)

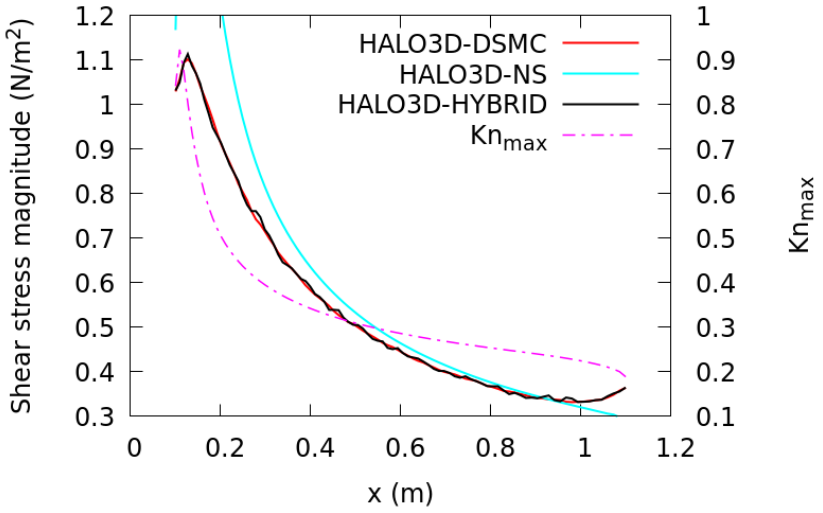

Fig. 3.32 Shear stress for the flow of Argon over a leading-edge (Mach 4.3, Knudsen 0.013)

3.2.1.2 Vibrationless N_2 Flow Over Leading-Edge (Mach 4, Knudsen 0.013)

Next, a vibrationless molecular Nitrogen flow over the diffuse wall is considered to evaluate the performance of the hybrid algorithm with the addition of rotational energy modeling. The freestream Knudsen number is 0.013, and the Mach number is 4, and this test case is identical to the leading-edge setup discussed by Bird [9]. Comparisons of HALO3D-DSMC with Bird's results are presented in Section 3.3.1. As discussed previously, the NS solver uses a single trans-rotational

temperature to describe the translational and rotational modes of energy. The DSMC solver uses a constant rotational collision number equal to 5 and calculates separate translational and rotational temperatures. To compare NS and DSMC results, a DSMC trans-rotational temperature, $T_{\mathrm{tr\ DSMC}}$, is calculated as

$$T_{\mathrm{tr\ DSMC}} = \frac{3T_{\mathrm{t}} + \zeta_{\mathrm{r}} T_{\mathrm{r}}}{3 + \zeta_{\mathrm{r}}} \tag{3.1}$$

$$\zeta_{\mathrm{r}} = \sum_{\mathrm{s}=1}^{\mathrm{N_s}} \zeta_{\mathrm{r,s}}\, X_{\mathrm{s}} \tag{3.2}$$

where T_{t} is the translational temperature, T_{r} is the rotational temperature, and ζ_{r} is the mixture rotational degrees of freedom. ζ_{r} is evaluated from the species rotational degrees of freedom $\zeta_{\mathrm{r,s}}$ and the species mole fractions X_{s}.

The contours of Kn_{max} obtained from the NS solution are presented in Fig. 3.33 where the shock and boundary layer are in a state of continuum breakdown. A maximum Kn_{max} of 0.91 is recorded at the stagnation point. Contours of $Kn_{\mathrm{ROT-NEQ}}$ shown in Fig. 3.34 indicate that, for this test case, most of the region above a $Kn_{\mathrm{ROT-NEQ}}$ of 0.05 is already encompassed by the DSMC region prediction of Kn_{max}. A $Kn_{\mathrm{ROT-NEQ}}$ of 0.05 corresponds to a difference between translational and rotational temperatures that is 10% of the rotational temperature. Thermal non-equilibrium is observed in the shock, near the wall, and at the stagnation point where the $Kn_{\mathrm{ROT-NEQ}}$ reaches a maximum of ~0.6. The hybrid masks and line for data extraction are presented in Fig. 3.35 where the line passes through NS and DSMC zones.

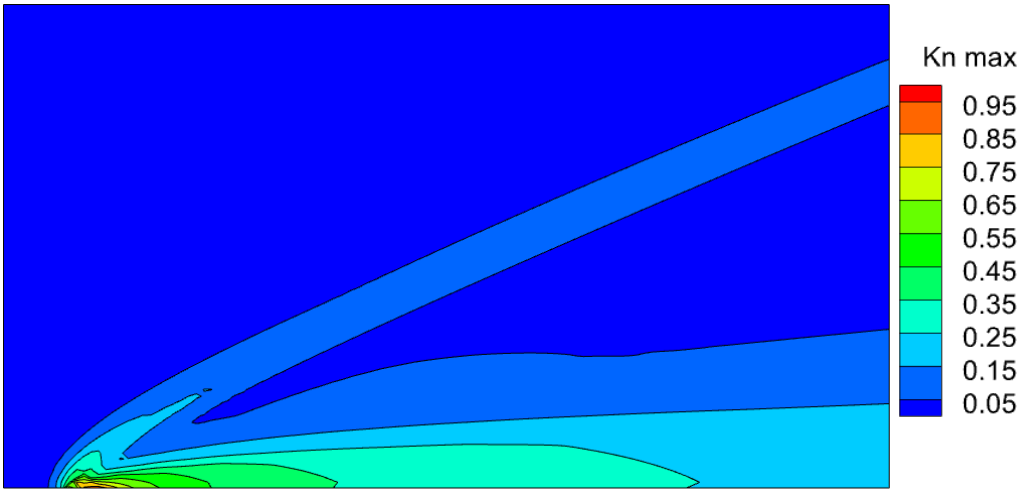

Fig. 3.33 Contours of Kn_{max} for the flow of vibrationless Nitrogen over a leading-edge. (Mach 4, Knudsen 0.013)

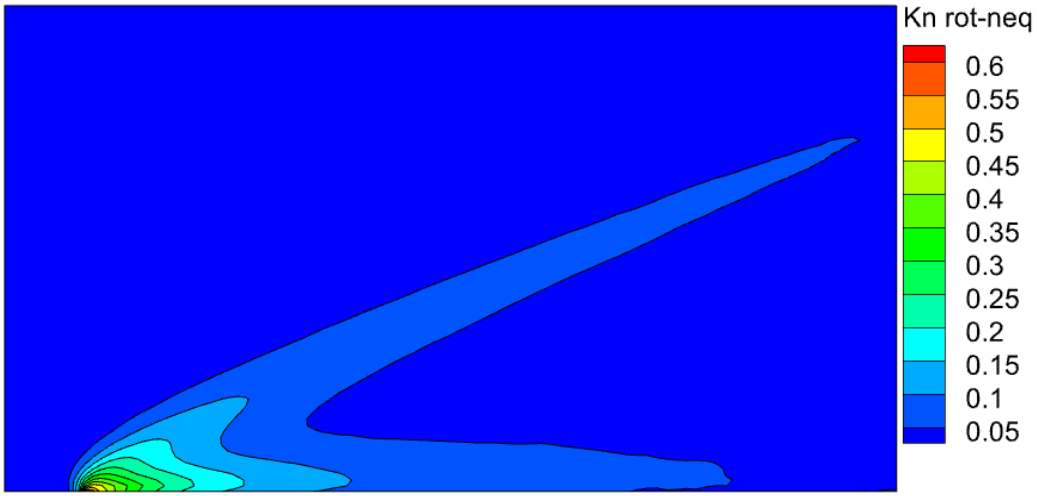

Fig. 3.34 Contours of $Kn_{ROT\text{-}NEQ}$ for the flow of vibrationless Nitrogen over a leading-edge. (Mach 4, Knudsen 0.013)

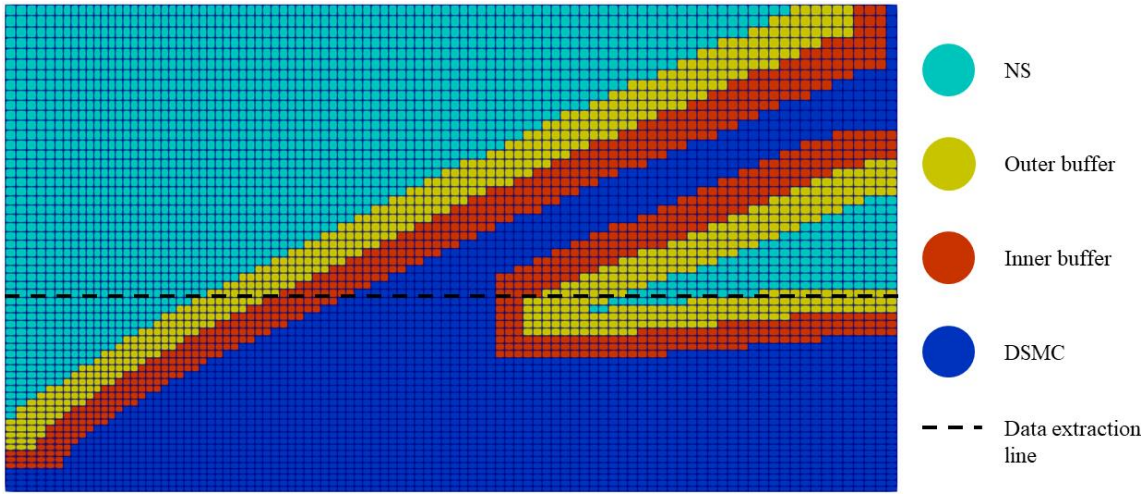

Fig. 3.35 Hybrid masks for the flow of vibrationless Nitrogen over a leading edge (Mach 4, Knudsen 0.013)

Contours of density, pressure, and Mach number for the NS, DSMC, and hybrid simulations are presented in Fig. 3.36-3.38, where the NS solutions can be seen to disagree with DSMC for the density and pressure contours. Mach number contours for NS and DSMC show better agreement, but, similar to the Argon case, discrepancies can be noted at the trailing edge. The hybrid contours all show better agreement than the NS, especially for the contours of Mach number. For the contours of the Mach number of the hybrid simulation to be smooth and continuous, the trans-rotational temperature (used to calculate the speed of sound) in the NS and DSMC regions must match each other. As can be seen, the hybrid algorithm produces seamless flow contours that match DSMC results.

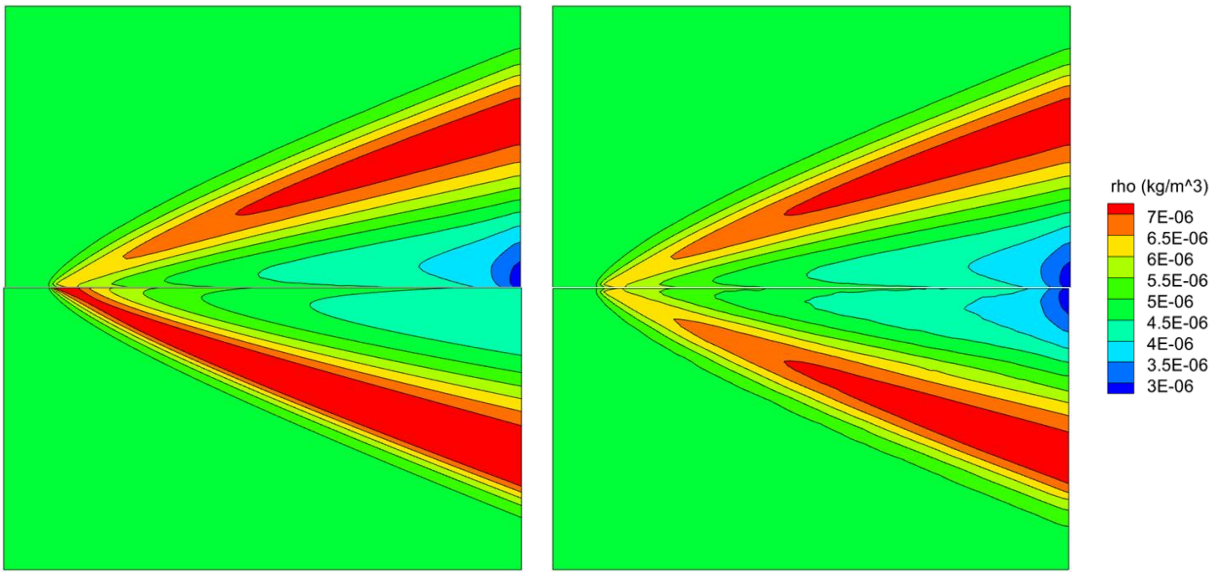

Fig. 3.36 Density contours of the NS (bottom-left) and hybrid (bottom-right) simulations compared against DSMC (top) for the flow of vibrationless Nitrogen over a leading-edge. (Mach 4, Knudsen 0.013)

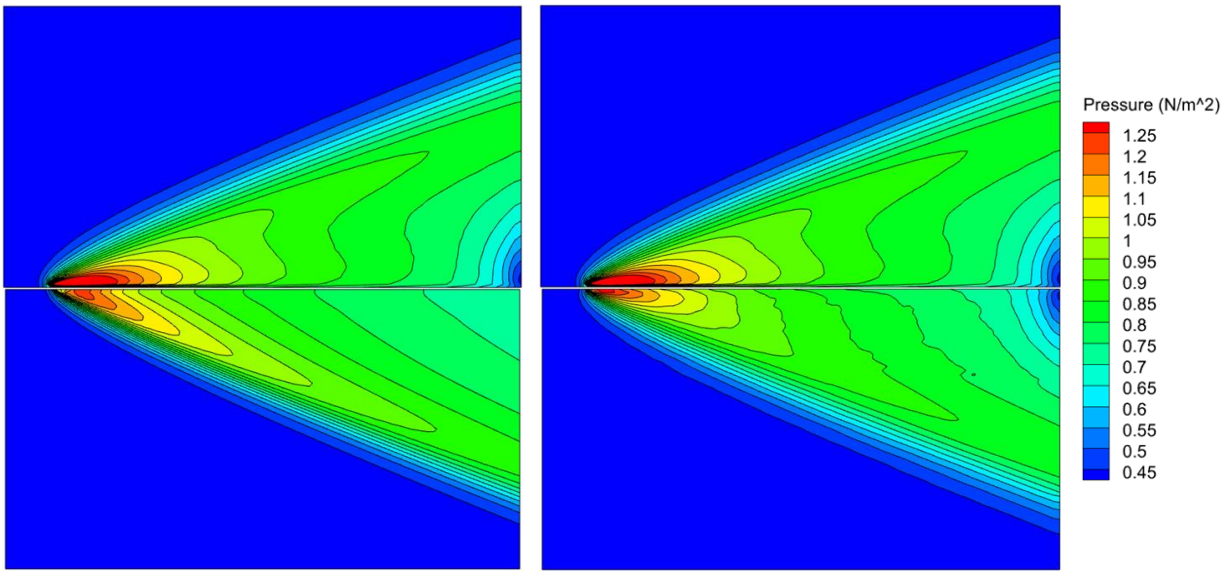

Fig. 3.37 Pressure contours of the NS (bottom-left) and hybrid (bottom-right) simulations compared against DSMC (top) for the flow of vibrationless Nitrogen over a leading-edge. (Mach 4, Knudsen 0.013)

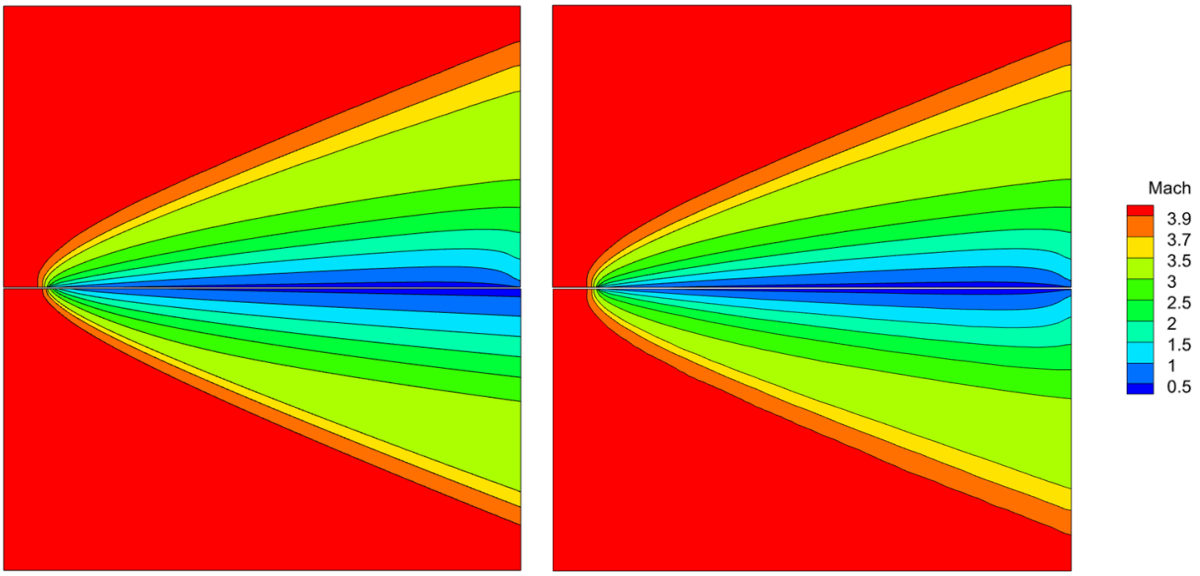

Fig. 3.38 Mach contours of the NS (bottom-left) and hybrid (bottom-right) simulations compared against DSMC (top) for the flow of vibrationless Nitrogen over a leading-edge. (Mach 4, Knudsen 0.013)

Plots of density, pressure and trans-rotational temperature along the data extraction line (y = 0.24 m) are shown in Fig. 3.39-3.41. Again, the upstream NS-DSMC boundary is located at a $Kn_{\max}$ of 0.05, while the downstream boundary is moved further downstream because of the mask smoothing algorithm. The NS solutions disagree with the DSMC solutions in the shock region and downstream of the shock. The disagreement is pronounced for the density and pressure fields, while the temperature field shows some agreement in the region downstream of the shock. The hybrid results compare better than the NS results against the full DSMC simulations for all three quantities plotted. Minor deviations for the hybrid results can be noted in the post-shock NS region for the density line plots. Similar deviations can be seen in the DSMC zone of the hybrid simulation for pressure. Indeed, pressure shows the maximum error among the three quantities, equalling 4.9%. The computed DSMC trans-rotational temperature shows good agreement with the hybrid solution despite the downstream NS-DSMC boundary not fully accommodating a small region of thermal non-equilibrium, as shown by the distribution of $Kn_{\mathrm{ROT-NEQ}}$ in Fig. 3.41.

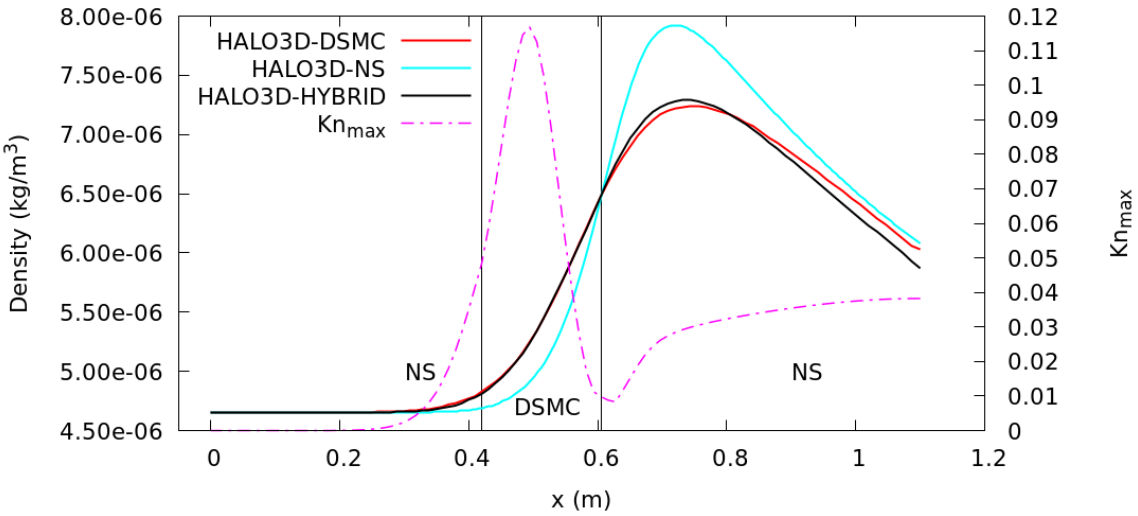

Fig. 3.39 Density along y = 0.24 m for the flow of vibrationless Nitrogen over a leading-edge. (Mach 4, Knudsen 0.013)

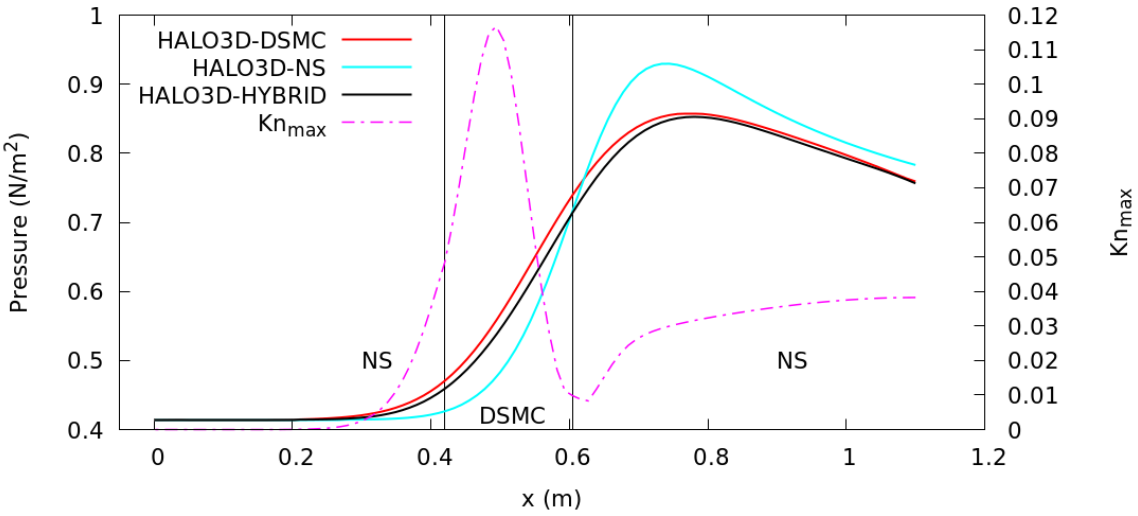

Fig. 3.40 Pressure along y = 0.24 m for the flow of vibrationless Nitrogen over a leading-edge. (Mach 4, Knudsen 0.013)

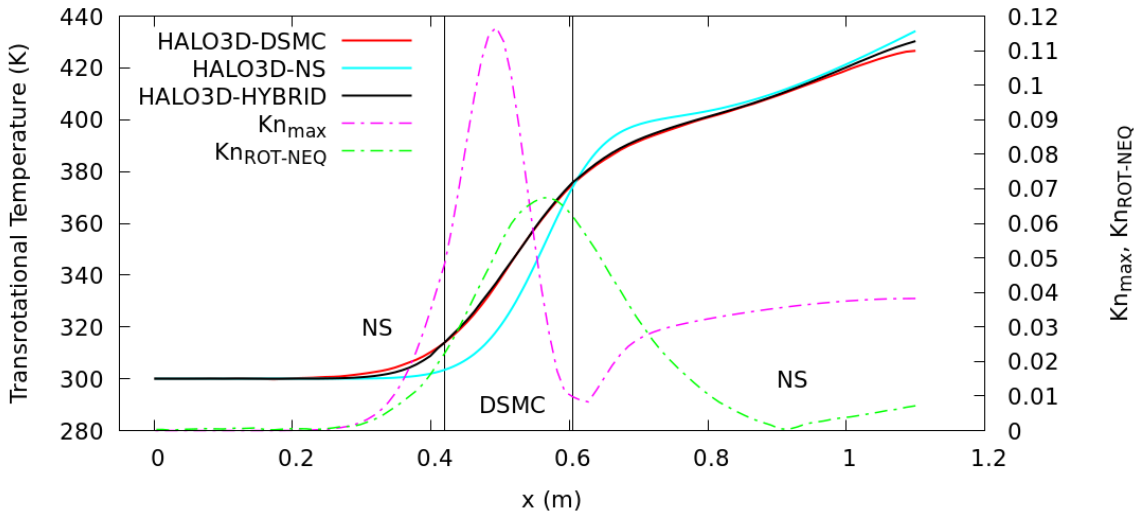

Fig. 3.41 Trans-rotational temperature along y = 0.24 m for the flow of vibrationless Nitrogen over a leading-edge. (Mach 4, Knudsen 0.013)

Plots of the surface heat flux and shear stress are provided in Fig. 3.42 and 3.43 where again, the leading-edge singularity is visible for the NS solutions. The peak heat flux predicted by the NS simulation is 909.7 W/m^2, and the peak NS shear stress is found to be 1.41 N/m^2. Again, the entire wall possesses a $Kn_{\max}$ greater than 0.05, which makes the wall a DSMC zone. Peak $Kn_{\max}$ is observed at the stagnation point, similar to the Argon flow. The hybrid results for both surface heat flux and shear stress agree well with full DSMC results, illustrating that the additional rotational energy is correctly modeled by the hybrid algorithm to produce accurate surface quantities. Cost benefits from the hybrid simulation can be seen again in this test case, with the full DSMC solution taking 1.79 hours and the hybrid computation taking only 0.73 hours.

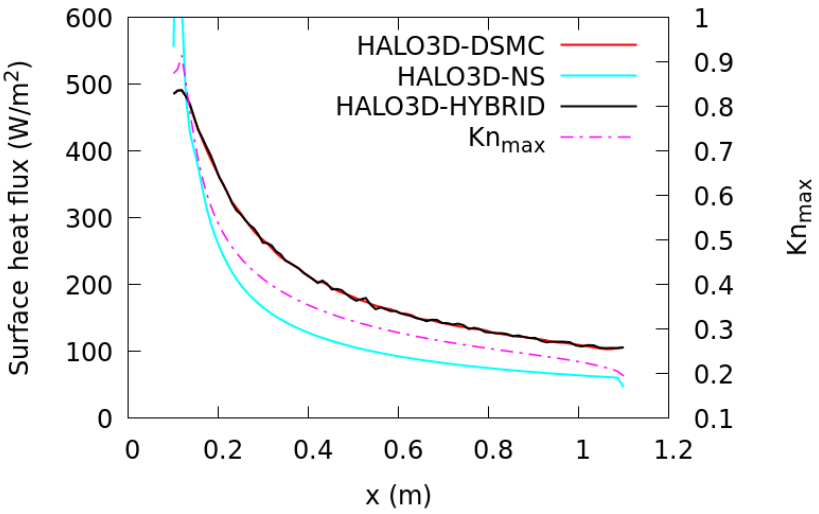

Fig. 3.42 Surface heat flux for the flow of vibrationless Nitrogen over a leading-edge. (Mach 4, Knudsen 0.013)

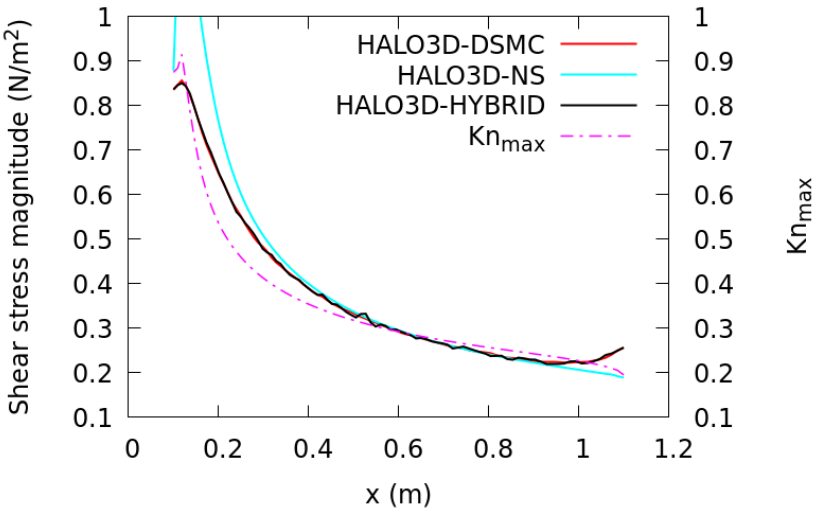

Fig. 3.43 Shear stress magnitude for the flow of vibrationless Nitrogen over a leading-edge. (Mach 4, Knudsen 0.013)

3.2.1.3 Vibrational N_2 Flow Over Leading-Edge (Mach 4, Knudsen 0.013)

This test case considers the flow of molecular Nitrogen with rotational and vibrational energy modes over a diffuse wall. The vibrational energy modeling of the hybrid algorithm is tested, where the degree of vibrational excitation is kept low. The freestream Knudsen number is 0.013,

and the Mach number is 4. The contours of $Kn_{\max}$ are presented in Fig. 3.44, which are nearly identical to the distribution from Section 3.2.1.2. The maximum $Kn_{\max}$ occurs at the stagnation point and is equal to ~0.91. Contours of $Kn_{\mathrm{ROT-NEQ}}$ are presented in Fig. 3.45 where again, most of the DSMC region predicted by $Kn_{\mathrm{ROT-NEQ}}$ is already covered within the larger region predicted by $Kn_{\max}$. The shock and boundary layer are predicted to experience continuum breakdown and thermal non-equilibrium, with a maximum $Kn_{\mathrm{ROT-NEQ}}$ of 0.6 at the stagnation point. The hybrid zones and line for data extraction are presented in Fig. 3.46.

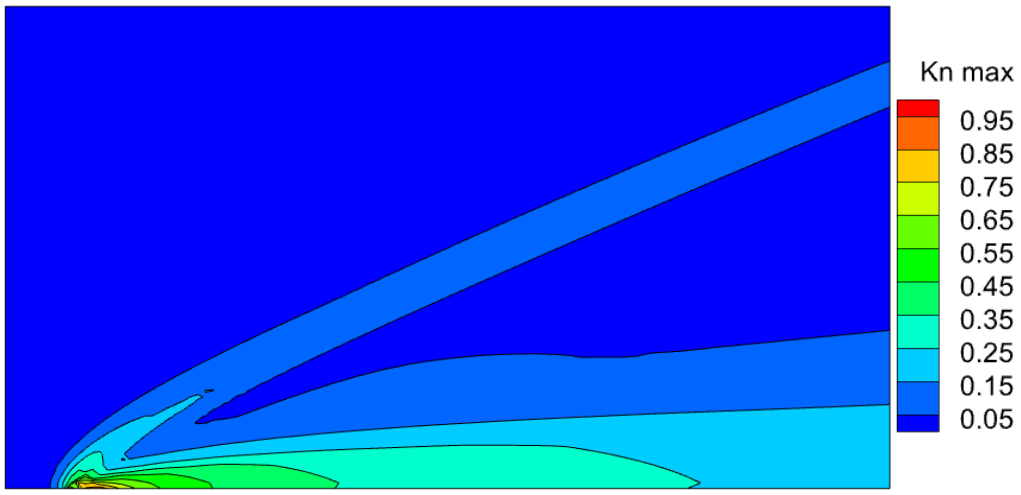

Fig. 3.44 Contours of Kn_{max} for the flow of vibrational Nitrogen over a leading-edge. (Mach 4, Knudsen 0.013)

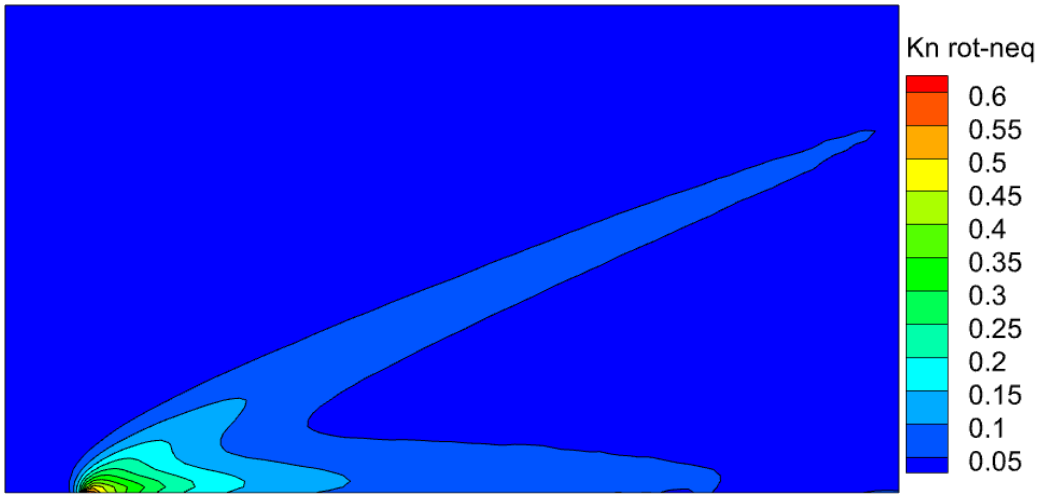

Fig. 3.45 Contours of $Kn_{ROT\text{-}NEQ}$ for the flow of vibrational Nitrogen over a leading-edge. (Mach 4, Knudsen 0.013)

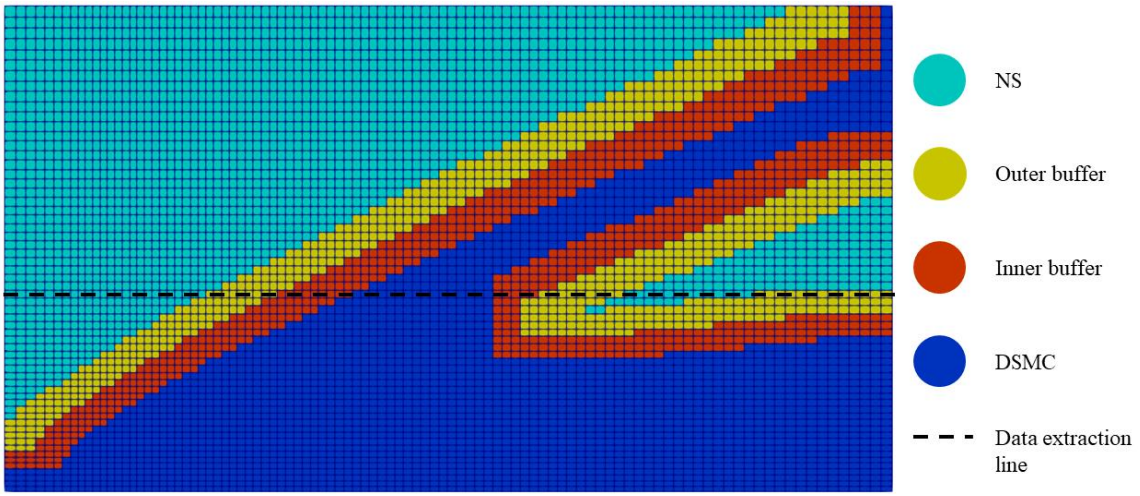

Fig. 3.46 Hybrid masks for the flow of vibrational Nitrogen over a leading-edge. (Mach 4, Knudsen 0.013)

Flowfield contours of density, pressure, Mach number, and vibrational temperature are presented in Fig. 3.47-3.50 where the NS density, pressure, and vibrational temperature all show significant differences from the DSMC solutions. The NS Mach number shows some improvement with some disagreement at the trailing edge. These differences are recovered by the hybrid simulation and the contours of all four flow variables for the hybrid simulation match the DSMC results well.

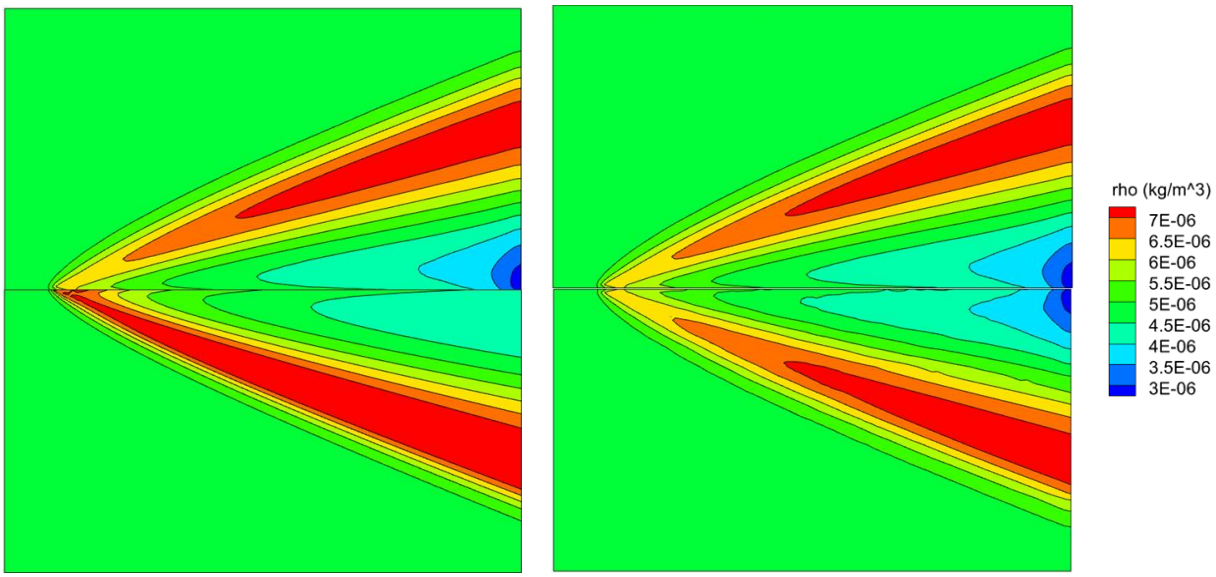

Fig. 3.47 Density contours of the NS (bottom-left) and hybrid (bottom-right) simulations compared against DSMC (top) for the flow of vibrational Nitrogen over a leading-edge. (Mach 4, Knudsen 0.013)

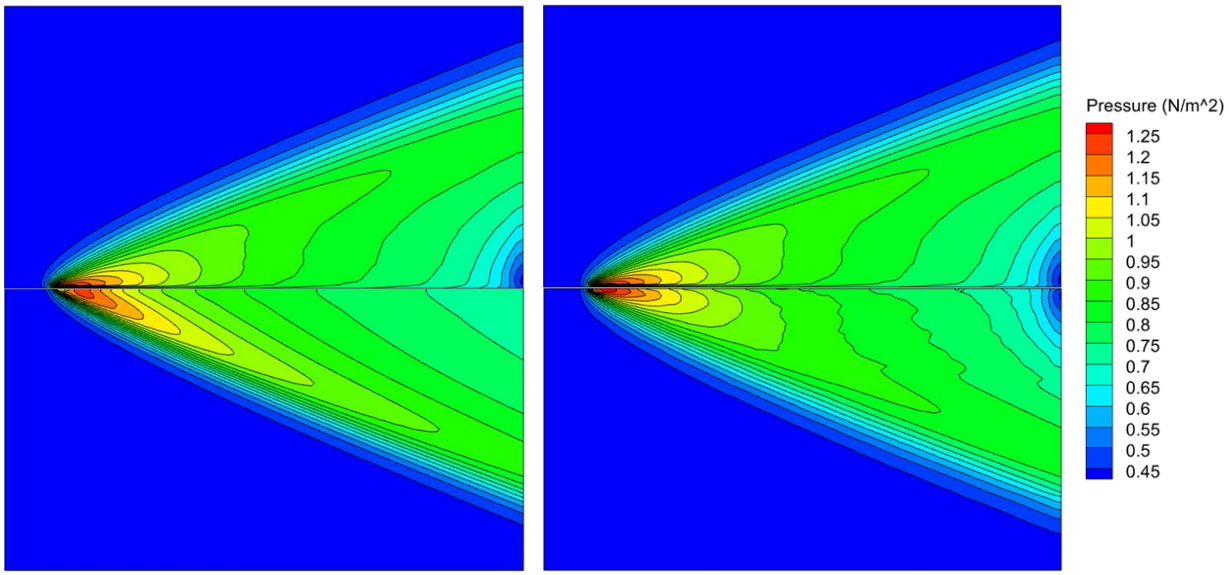

Fig. 3.48 Pressure contours of the NS (bottom-left) and hybrid (bottom-right) simulations compared against DSMC (top) for the flow of vibrational Nitrogen over a leading-edge. (Mach 4, Knudsen 0.013)

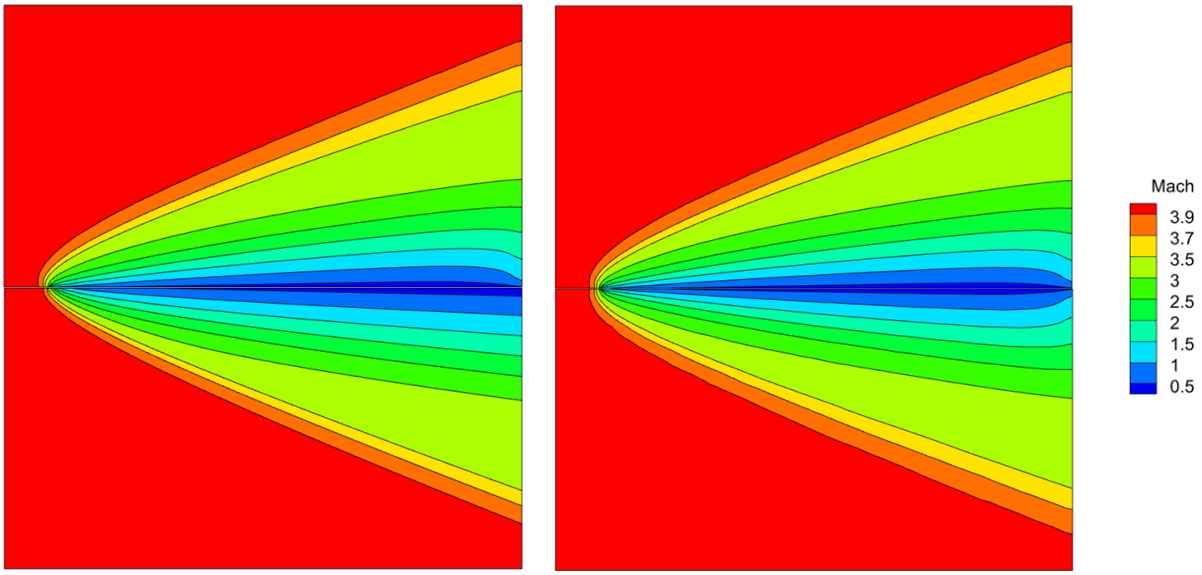

Fig. 3.49 Mach number contours of the NS (bottom-left) and hybrid (bottom-right) simulations compared against DSMC (top) for the flow of vibrational Nitrogen over a leading-edge. (Mach 4, Knudsen 0.013)

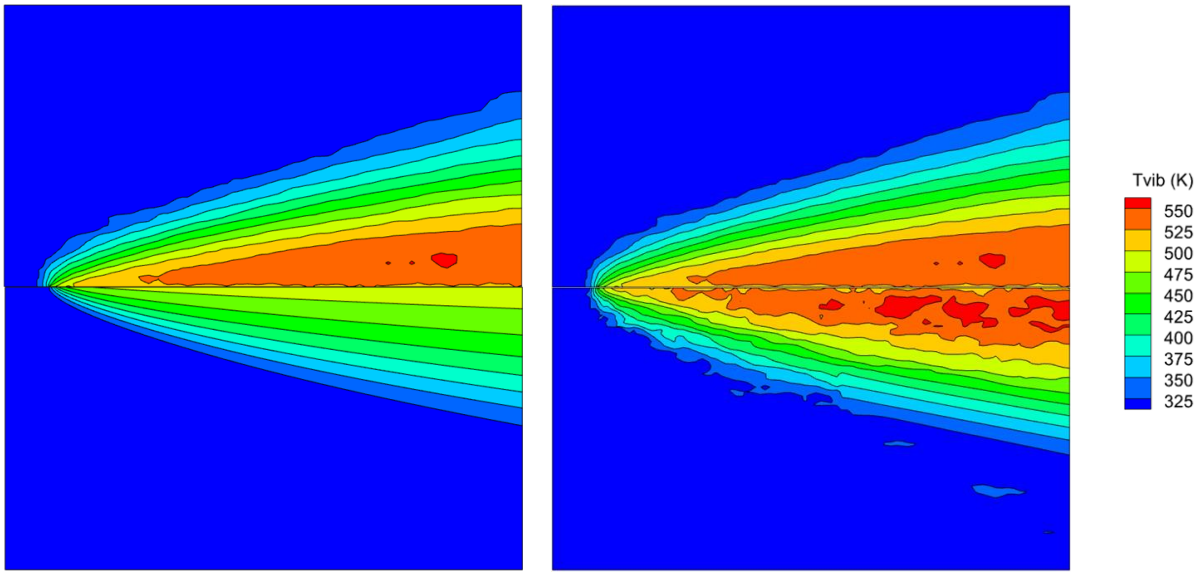

Fig. 3.50 Vibrational temperature contours of the NS (bottom-left) and hybrid (bottom-right) simulations compared against DSMC (top) for the flow of vibrational Nitrogen over a leading-edge. (Mach 4, Knudsen 0.013)

Plots of density, pressure, trans-rotational and vibrational temperatures along y = 0.243 m are provided in Fig. 3.51-3.54. The NS solutions for density, pressure and trans-rotational temperature deviate from DSMC results in the shock and post-shock regions, with the deviation starting a little upstream of the shock. For vibrational temperature, the full NS solution predicts the freestream value well into the shock, and the temperature begins to increase farther downstream of the shock. The distribution of $Kn_{\mathrm{ROT-NEQ}}$ in Fig. 3.53 shows that had $Kn_{\mathrm{ROT-NEQ}}$ been considered for establishing the NS-DSMC boundary, the DSMC region would have expanded slightly downstream. The hybrid results for density, pressure, and trans-rotational temperature all follow the DSMC solutions, with the maximum error among these three variables being 2% for the density plots. The results for vibrational temperature in Fig. 3.54 show that the hybrid algorithm predicts a vibrational temperature that agrees with DSMC better than the NS prediction while being noisy in the upstream NS and DSMC regions of the hybrid solution. The cause of this noise is attributed to the freestream temperature being cold at 300 K, due to which the probability of having a vibrationally excited particle is low. Therefore, few particles are involved in the macroscopic average calculations of vibrational temperature and employing significantly larger particle counts should rectify this issue.

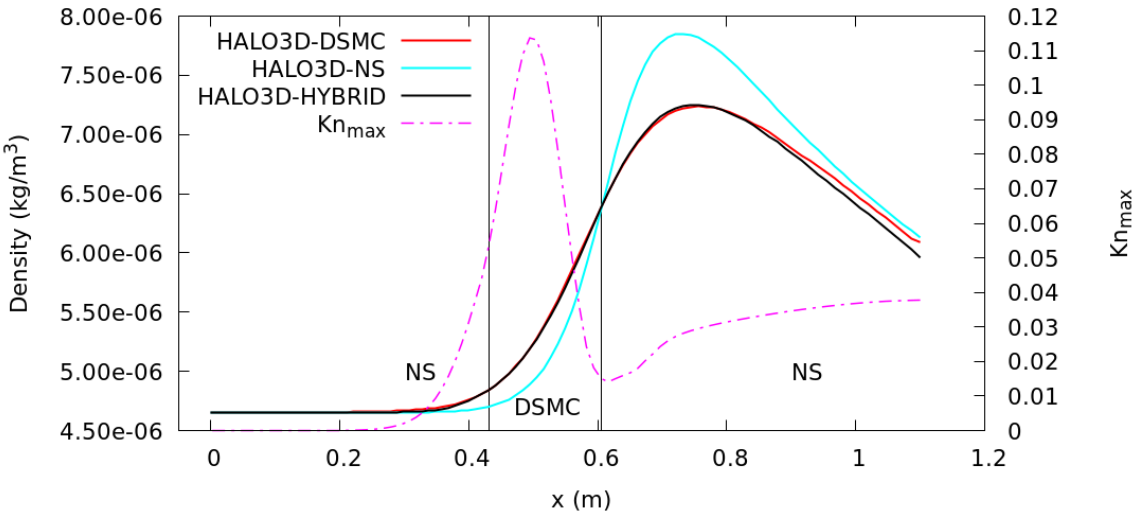

Fig. 3.51 Density along y = 0.243 m for the flow of vibrational Nitrogen over a leading-edge. (Mach 4, Knudsen 0.013)

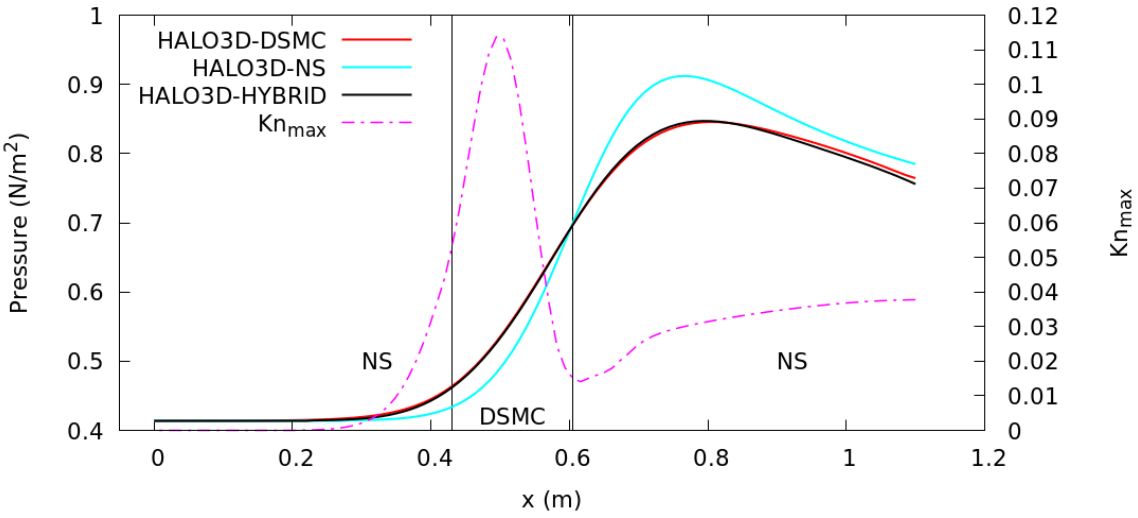

Fig. 3.52 Pressure along y = 0.243 m for the flow of vibrational Nitrogen over a leading-edge. (Mach 4, Knudsen 0.013)

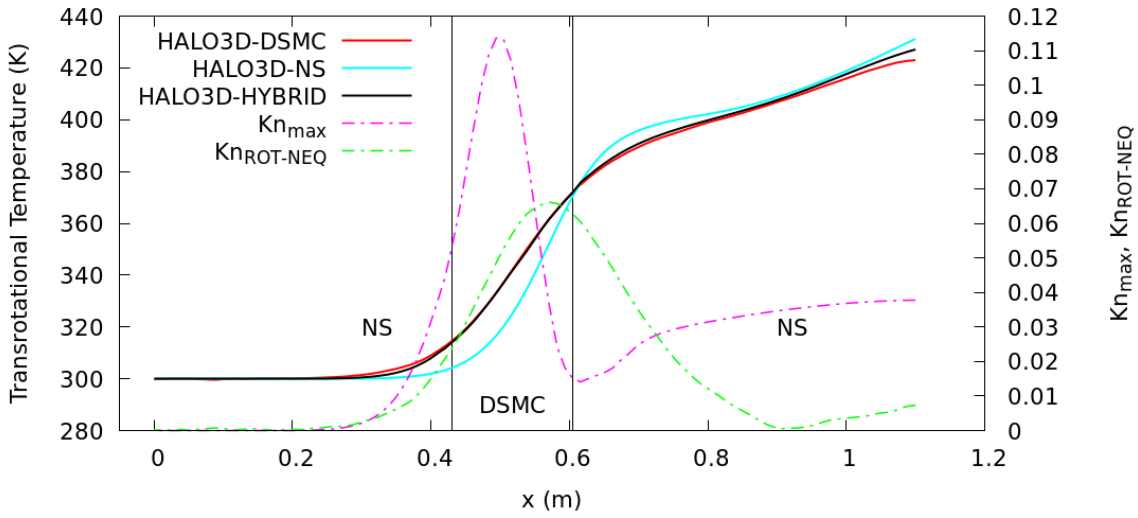

Fig. 3.53 Trans-rotational temperature along y = 0.243 m for the flow of vibrational Nitrogen over a leading-edge. (Mach 4, Knudsen 0.013)

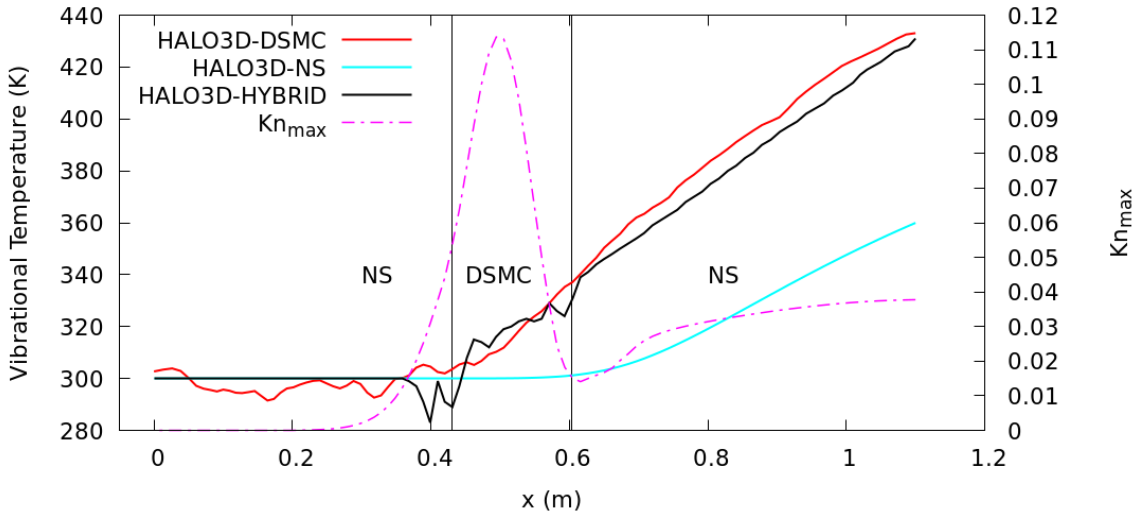

Fig. 3.54 Vibrational temperature along y = 0.243 m for the flow of vibrational Nitrogen over a leading-edge. (Mach 4, Knudsen 0.013)

Line plots of the heat flux and shear stress over the diffuse wall are provided in Fig. 3.55 and 3.56, where the leading-edge singularity in the full NS simulation presents itself through a peak surface heat flux equalling 909.4 W/m^2 and a peak shear stress of 1.41 N/m^2. The entire surface is a DSMC zone in the hybrid simulation. The hybrid heat flux and shear stress agree well with DSMC results, illustrating that the added complexity of vibrational energy is modeled accurately enough by the hybrid algorithm during the computation of surface quantities. The hybrid solution

takes 0.77 hours to compute, which is at a much lower computational cost than the full DSMC simulation, which takes 1.86 hours to compute.

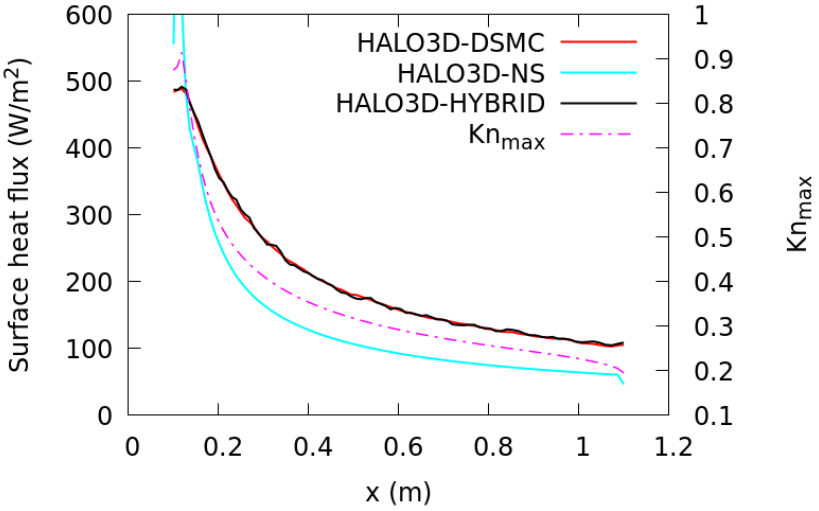

Fig. 3.55 Surface heat flux for the flow of vibrational Nitrogen over a leading-edge. (Mach 4, Knudsen 0.013)

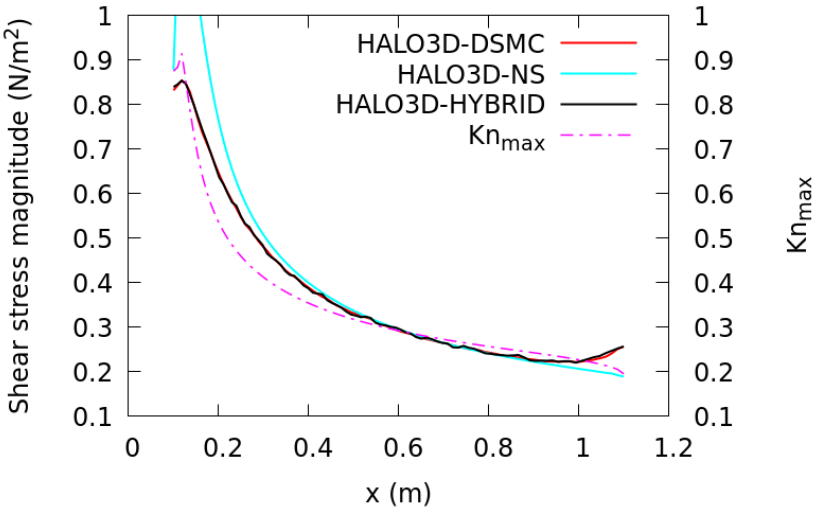

Fig. 3.56 Shear stress for the flow of vibrational Nitrogen over a leading-edge. (Mach 4, Knudsen 0.013)

3.2.1.4 Vibrationless Nitrogen Mixture Flow Over Leading-Edge (Mach 3.34, Knudsen 0.018)

This fourth leading-edge test case considers the flow of molecular and atomic Nitrogen in equal molar proportions over a diffuse wall. The mixture is non-reacting, and Fick's law of diffusion with a Lewis number of 1.4 is employed in the NS simulations and the NS regions of the hybrid simulation. The rotational energy mode is considered, and the vibrational energy mode is deactivated. The freestream Knudsen number is 0.018, and the Mach number is 3.34. Contours of $Kn_{\max}$ are presented in Fig. 3.57 where the area with a value greater than 0.05 is much larger than the previous leading-edge simulations. The maximum $Kn_{\max}$ of 2.13 at the stagnation point is larger than the previous test cases as well. Contours of $Kn_{\mathrm{ROT-NEQ}}$ are presented in Fig. 3.58 where the maximum $Kn_{\mathrm{ROT-NEQ}}$ of 0.44 is lower than the previous two test cases. Hybrid masks and the line for data extraction for this problem are shown in Fig. 3.59 where nearly the entire domain is flagged as DSMC.

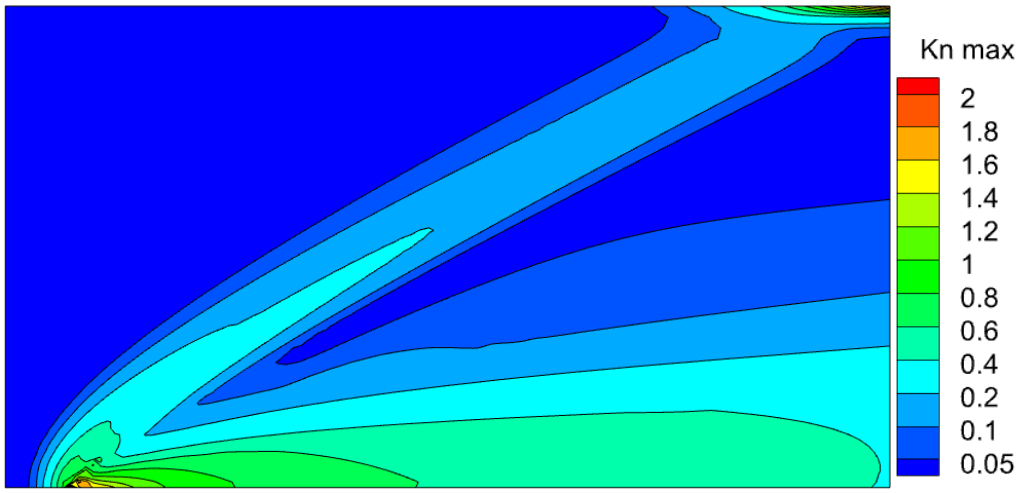

Fig. 3.57 Contours of Kn_{max} for the flow of an N_2 and N mixture over a leading-edge. (Mach 3.34, Knudsen 0.018)

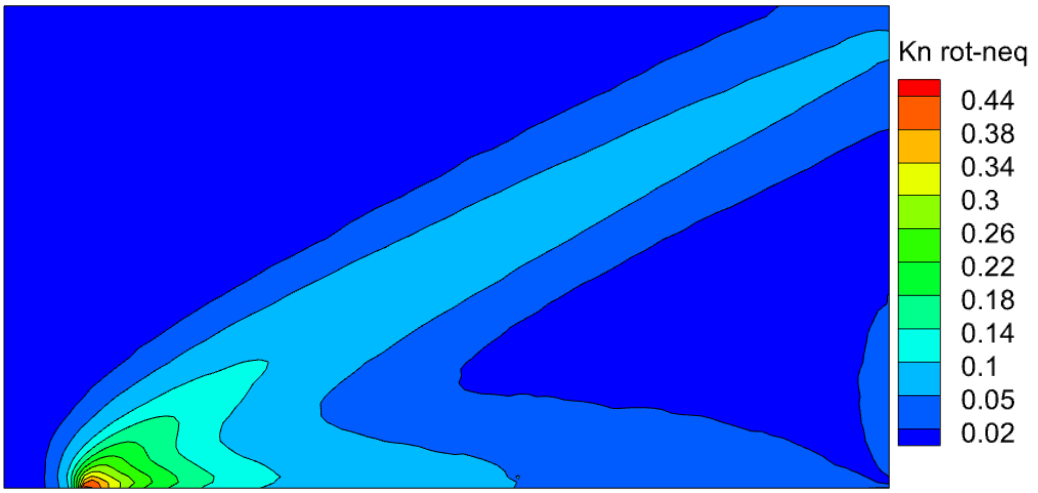

Fig. 3.58 Contours of $Kn_{ROT-NEQ}$ for the flow of an N_2 and N mixture over a leading-edge. (Mach 3.34, Knudsen 0.018)

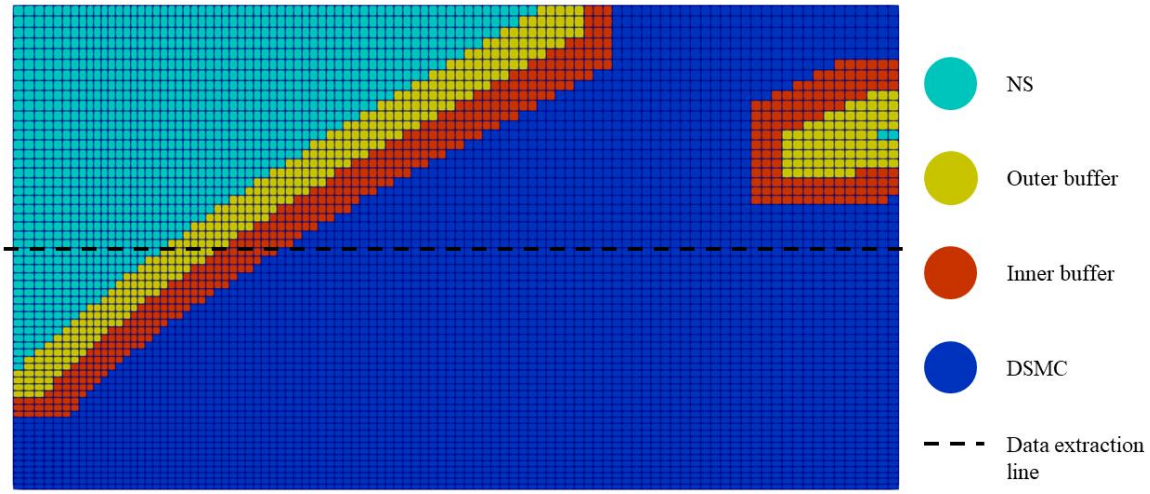

Fig. 3.59 Hybrid masks for the flow of an N_2 and N mixture over a leading-edge. (Mach 3.34, Knudsen 0.018)

Contour plots of density, pressure, Mach number, and mass fractions of N_2 and N are provided in Figs. 3.60-3.64, where the NS density and pressure continue to disagree with the DSMC contours. Again, the NS Mach field compares well in most of the domain except near the trailing edge. The hybrid density, pressure, and Mach number agree with DSMC well. The NS simulation predicts the freestream mass fractions of N_2 and N throughout the domain, while the hybrid and DSMC predictions agree and clearly outline the shock through the mass fraction contours.

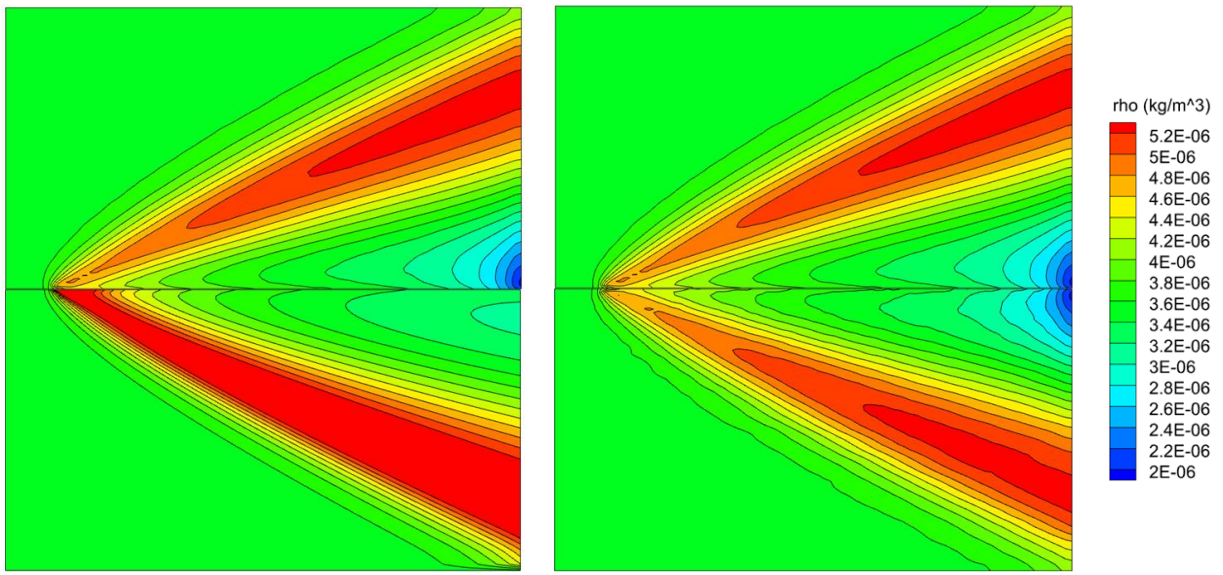

Fig. 3.60 Density contours of the NS (bottom-left) and hybrid (bottom-right) simulations compared against DSMC (top) for the flow of an N_2 and N mixture over a leading-edge. (Mach 3.34, Knudsen 0.018)

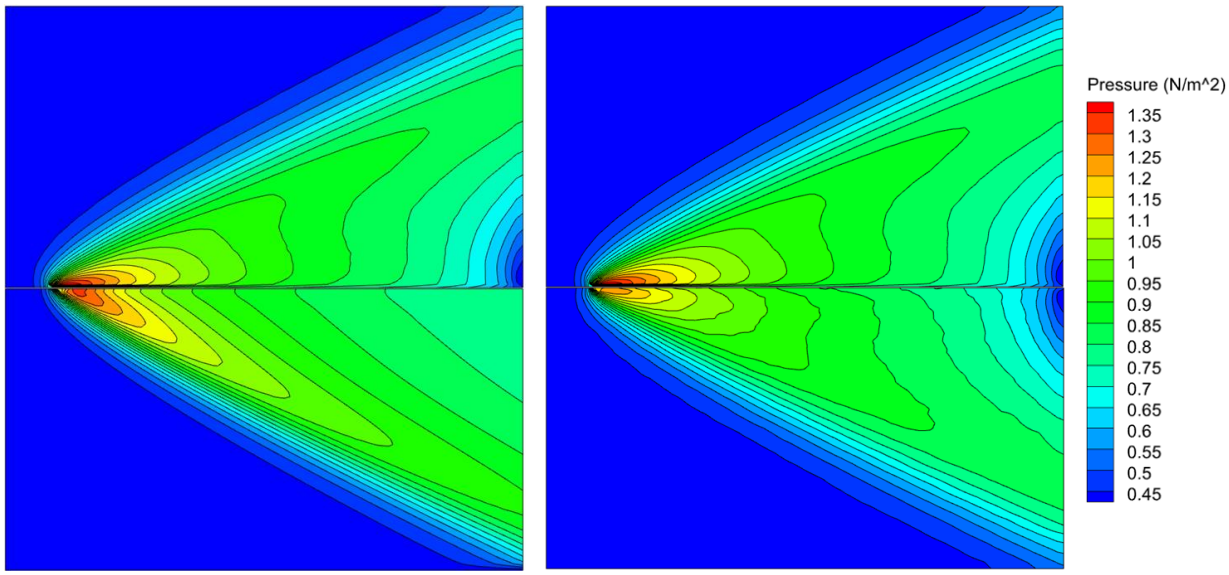

Fig. 3.61 Pressure contours of the NS (bottom-left) and hybrid (bottom-right) simulations compared against DSMC (top) for the flow of an N_2 and N mixture over a leading-edge. (Mach 3.34, Knudsen 0.018)

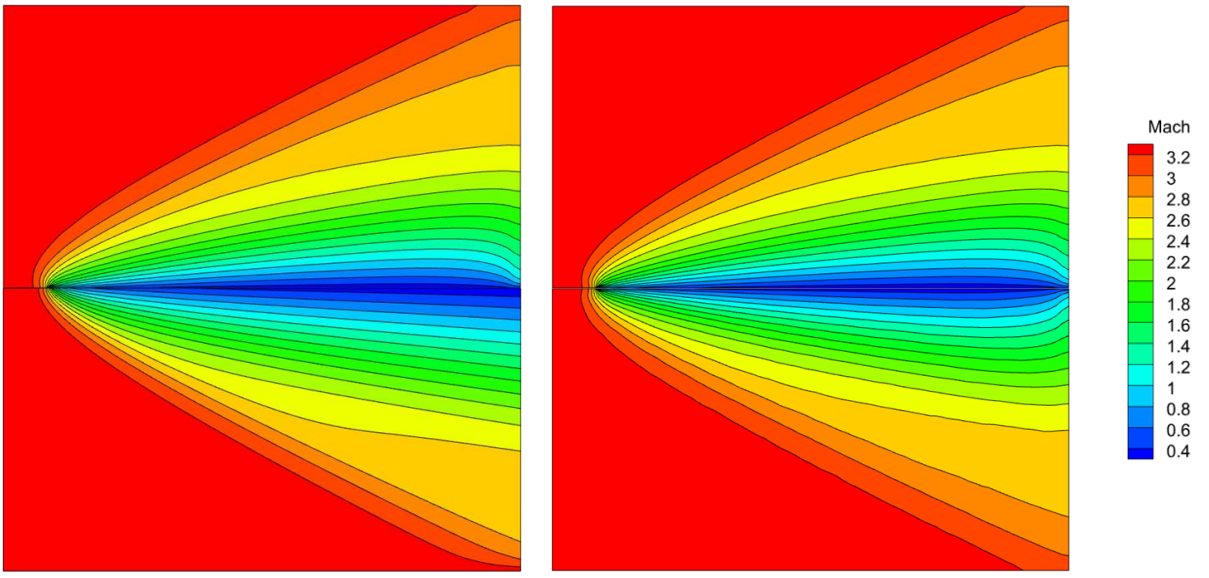

Fig. 3.62 Mach number contours of the NS (bottom-left) and hybrid (bottom-right) simulations compared against DSMC (top) for the flow of an N_2 and N mixture over a leading-edge. (Mach 3.34, Knudsen 0.018)

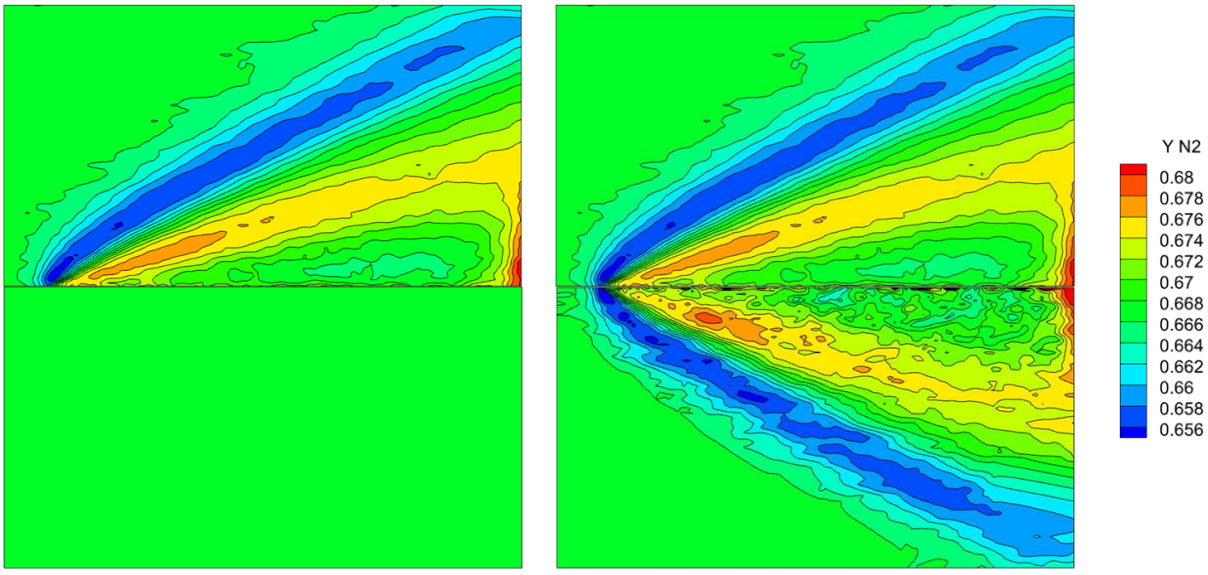

Fig. 3.63 N_2 mass fraction contours of the NS (bottom-left) and hybrid (bottom-right) simulations compared against DSMC (top) for the flow of an N_2 and N mixture over a leading-edge. (Mach 3.34, Knudsen 0.018)

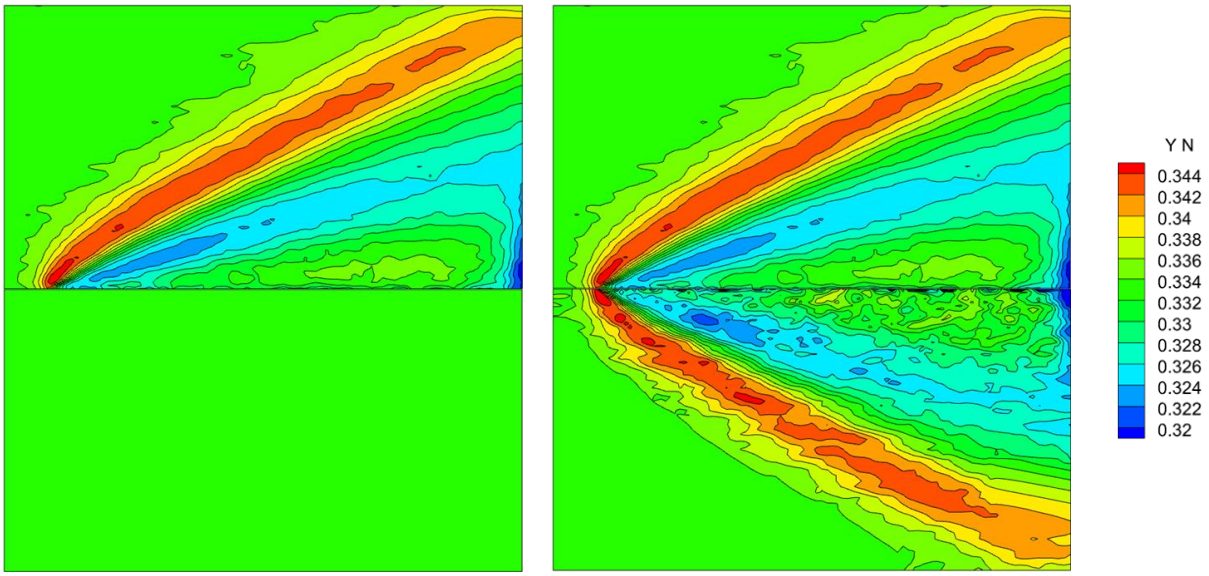

Fig. 3.64 N mass fraction contours of the NS (bottom-left) and hybrid (bottom-right) simulations compared against DSMC (top) for the flow of an N_2 and N mixture over a leading-edge. (Mach 3.34, Knudsen 0.018)

Line plots of density, pressure, trans-rotational temperature, and N_2 and N mass fractions extracted along y = 0.3 m are presented in Fig. 3.65-3.69. Differences can be observed between the NS and DSMC computations for the density, pressure, and trans-rotational temperature fields. The hybrid computation shows a good agreement for all three fields, with a maximum error of 3.0% recorded for the hybrid pressure plot. For the plots of mass fractions, as noted earlier, the full NS computation predicts the freestream values throughout the domain, while the hybrid computations agree well with DSMC, albeit with some scatter. Since most of the domain is DSMC, this case tests the ability of the hybrid mesh population routines and the ability of the NS solver to generate accurate pre-shock predictions of the flow variables when non-reacting gas mixtures are considered and, in both instances, the hybrid algorithm performs accurately.

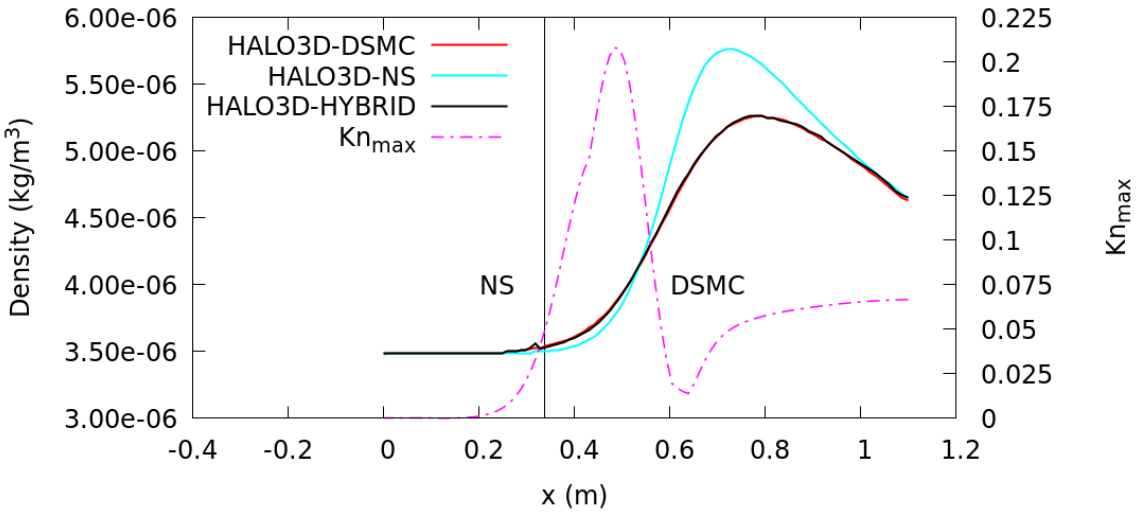

Fig. 3.65 Density along y = 0.3 m for the flow of an N_2 and N mixture over a leading-edge. (Mach 3.34, Knudsen 0.018)

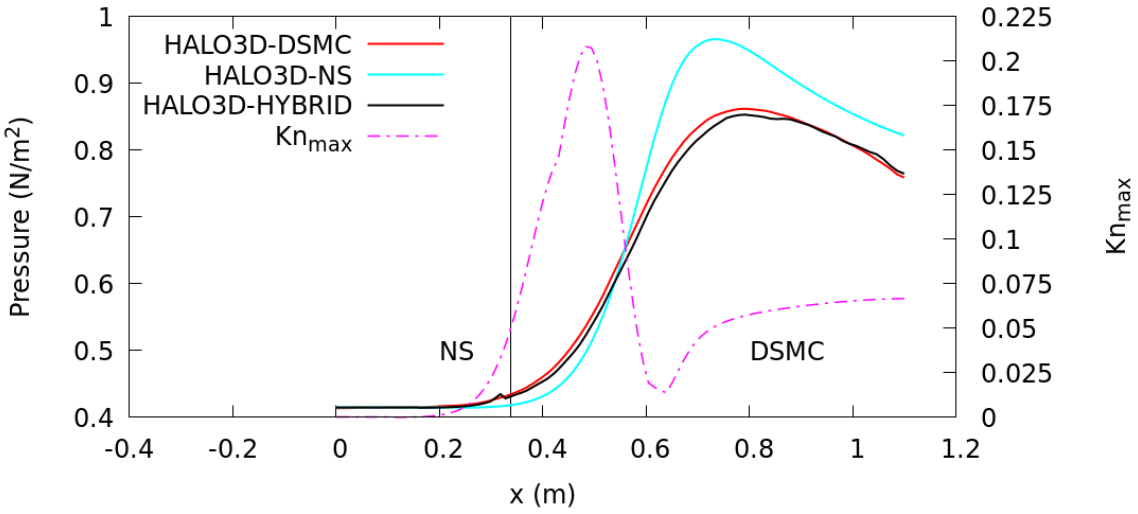

Fig. 3.66 Pressure along y = 0.3 m for the flow of an N_2 and N mixture over a leading-edge. (Mach 3.34, Knudsen 0.018)

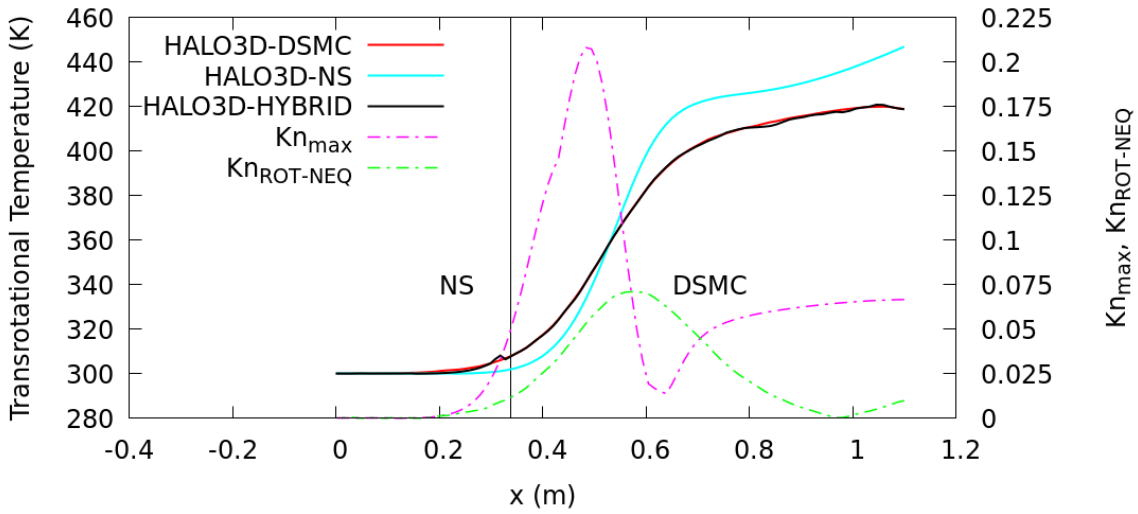

Fig. 3.67 Trans-rotational temperature along y = 0.3 m for the flow of an N_2 and N mixture over a leading-edge. (Mach 3.34, Knudsen 0.018)

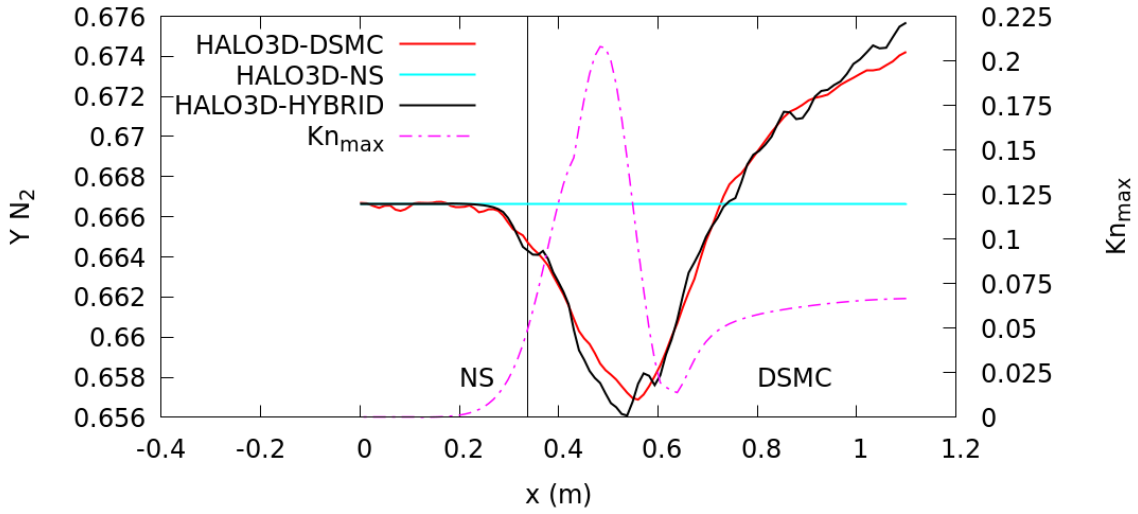

Fig. 3.68 N_2 mass fraction along y = 0.3 m for the flow of an N_2 and N mixture over a leading-edge. (Mach 3.34, Knudsen 0.018)

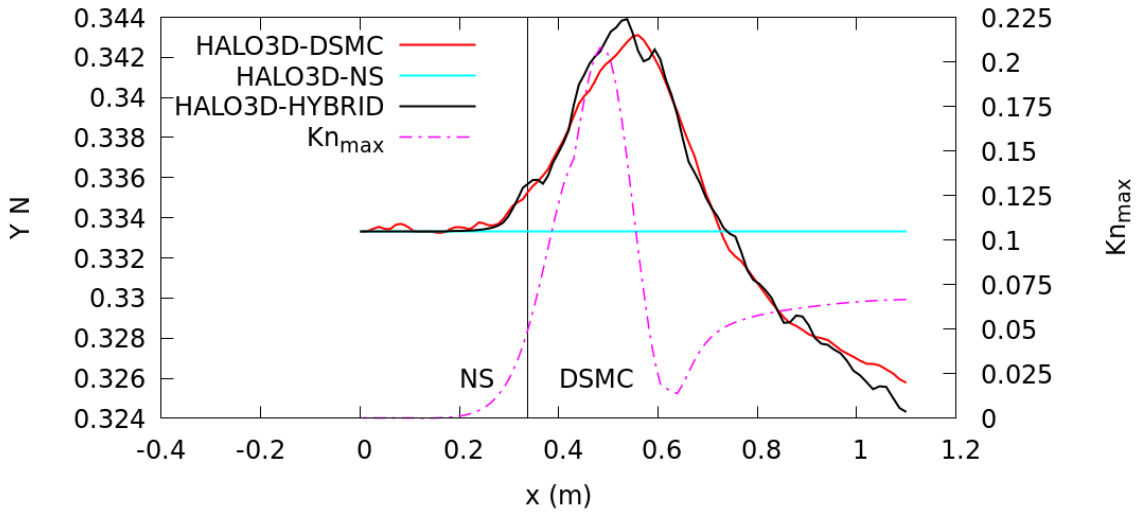

Fig. 3.69 N mass fraction along y = 0.3 m for the flow of an N_2 and N mixture over a leading-edge. (Mach 3.34, Knudsen 0.018)

Plots of surface heat flux and shear stress are presented in Fig. 3.70 and 3.71, where the peak NS heat flux is 770.24 W/m^2, and shear stress is 1.305 N/m^2. The entire surface is a DSMC region in the hybrid computation, and the hybrid predictions for both surface quantities agree well with DSMC predictions. This shows that the hybrid algorithm can successfully deal with multiple non-reacting species to generate accurate surface quantities. Again, cost benefits can be observed here, with the hybrid algorithm taking 0.9 hours to solve this problem and the full DSMC taking 1.87 hours.

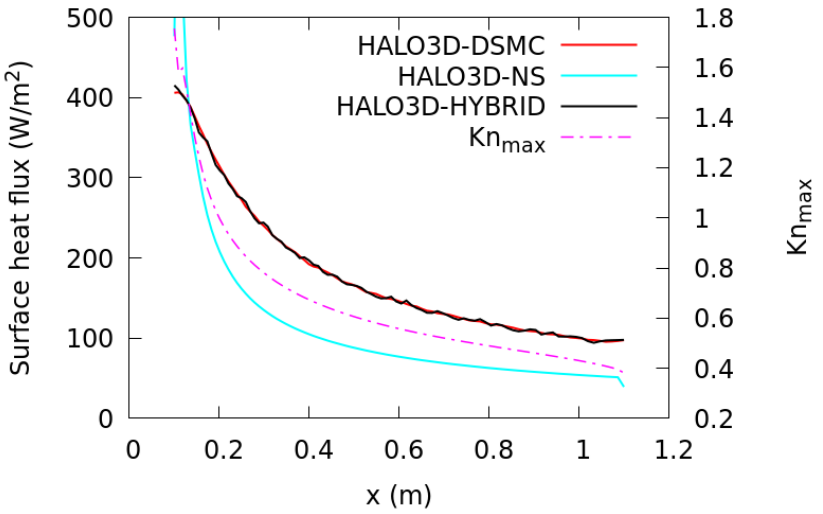

Fig. 3.70 Surface heat flux for the flow of an N_2 and N mixture over a leading-edge. (Mach 3.34, Knudsen 0.018)

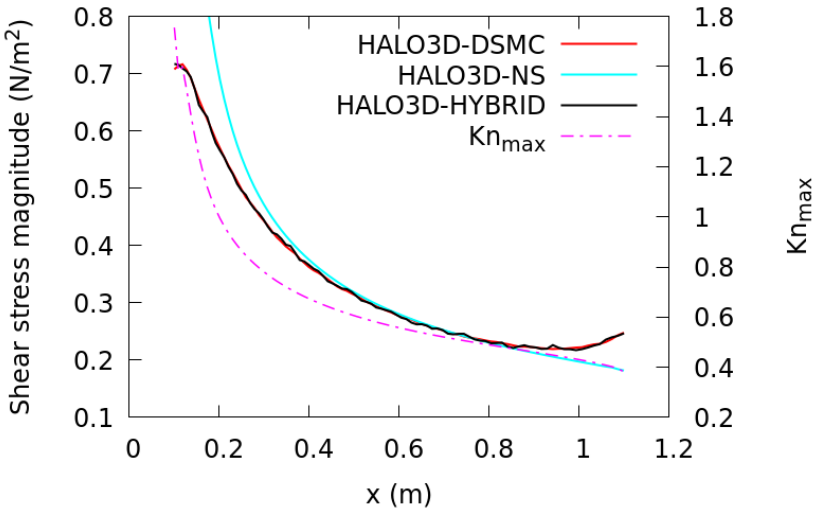

Fig. 3.71 Shear stress magnitude for the flow of an N_2 and N mixture over a leading-edge. (Mach 3.34, Knudsen 0.018)

3.2.2 Flows Over 2D Cylinders

This Section deals with three test cases of hypersonic flows over 2D cylinders with increasing thermochemical complexity. The domain and boundary conditions for all three cases is presented in Fig. 3.72. These test cases present a detached bow shock and a rarefied wake region in contrast

with the oblique shock encountered in the leading-edge case, as bow shocks form around bluff bodies while oblique shocks form at sharp leading edges. In the case of the flow over a cone, an initially attached oblique shock evolves into a detached bow shock when the cone angle is increased. From a hypersonic vehicle design standpoint, bow shocks and bluff bodies are required in re-entry vehicles such as capsules to maximize the drag, while oblique shocks and a sharp nose and leading edges are required in hypersonic aircraft to minimize the drag. In the following test cases, the cylinder diameter is the same (0.3048 m), and the angle used in the surface plots is 0˚ at the stagnation point. Focus is placed on estimating surface quantities in the absence of consistent thermodynamic modeling between the NS and DSMC modules.

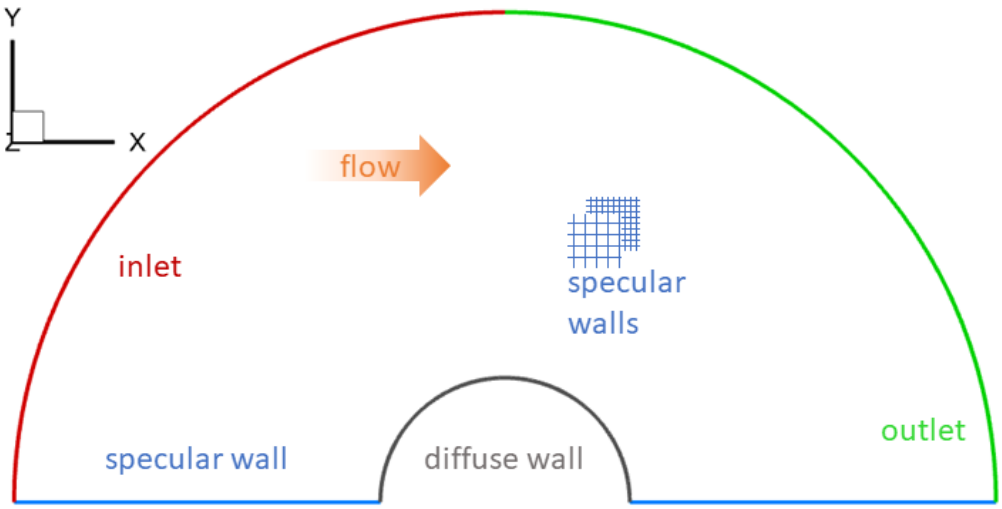

Fig. 3.72 Domain and boundary conditions for the hypersonic flow over a cylinder

3.2.2.1 Argon Flow Over 2D Cylinder (Mach 10, Knudsen 0.01)

This benchmark test case has been used to validate DSMC codes [75,107] and is a suitable candidate to test the NS, DSMC and hybrid modules of HALO3D. This test case considers a Mach 10, Knudsen 0.01 (based on the cylinder diameter) flow of Argon to evaluate the performance of the hybrid algorithm in the absence of rotational and vibrational energies and multiple reacting species. The freestream conditions for pressure, temperature, and velocity are 1.1727 Pa, 200 K, and 2624 m/s, respectively, the diffuse wall temperature is set to be 500 K, and the time step for full DSMC and the DSMC module of the hybrid computations is 1×10^{-7} seconds. An NS computation with slip boundary conditions initializes the hybrid simulation. Contours of $Kn_{\max}$ are shown in Fig. 3.73, where the maximum value of ~1.35 occurs in the bow shock region and

$Kn_{\max}$ is also large in the rarefied wake. The hybrid masks are shown in Fig. 3.74, where the shock, boundary layer, and wake regions are in a state of continuum breakdown and are hence designated as DSMC regions.

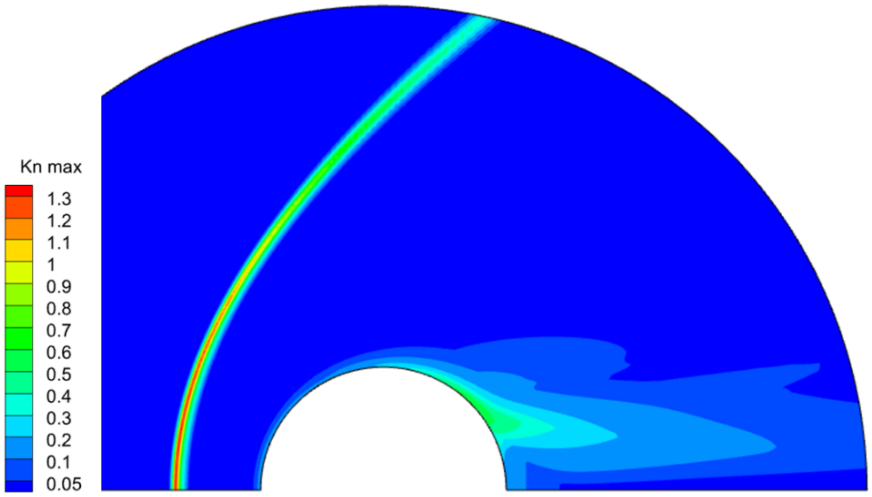

Fig. 3.73 Kn_{max} contours for the flow of Argon over a 2D cylinder. (Mach 10, Knudsen 0.01)

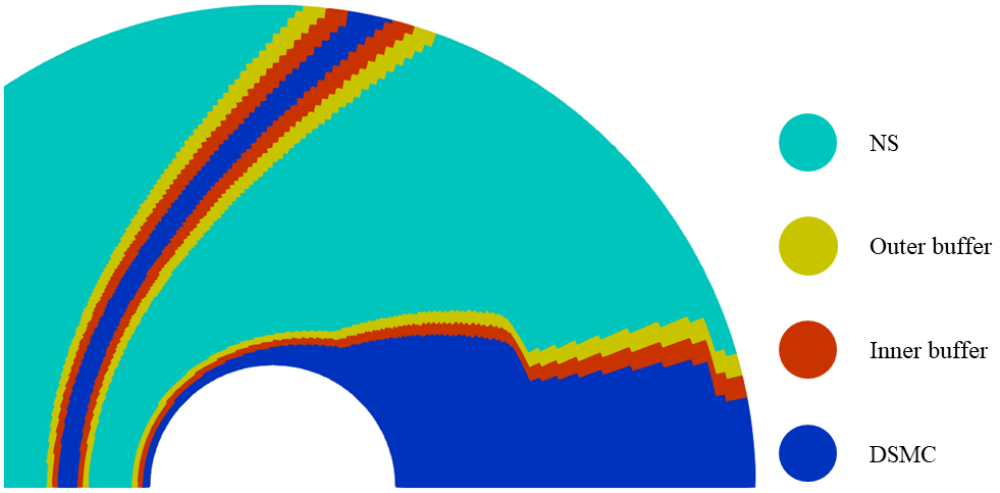

Fig. 3.74 Hybrid masks for the flow of Argon over a 2D cylinder. (Mach 10, Knudsen 0.01)

Contours of density, pressure, and Mach number of the DSMC, NS, and hybrid simulations are presented in Fig. 3.75-3.77. The NS contours show better agreement with DSMC than in the leading-edge cases, indicating that full NS calculations are unsuitable for studying the leading-edge problem. As observed in the literature [107], the NS solution predicts a thinner shock than DSMC, which is visible in the Mach contours of Fig. 3.77. While the hybrid contours all show good agreement with DSMC in most of the domain, the bow shock region in the Mach contours

seems to be replicating the NS solution and predicting a thinner shock than DSMC. The cause for this is the frozen hybrid interface method currently employed, which prevents the hybrid interface from naturally evolving to a more upstream location [45].

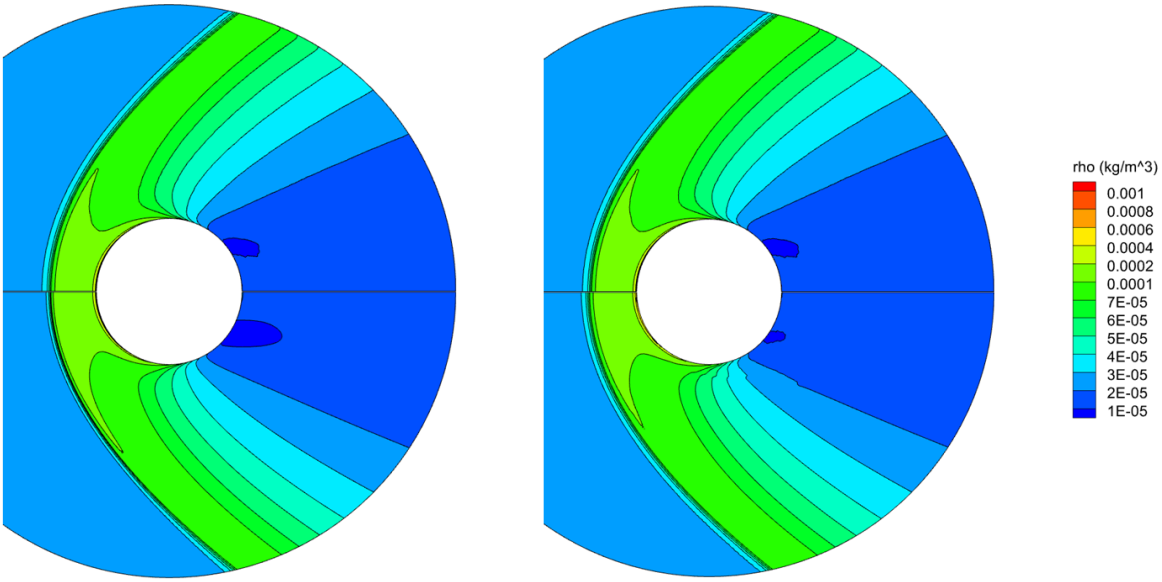

Fig. 3.75 Density contours of the NS (bottom-left) and hybrid (bottom-right) simulations compared against DSMC (top) for the flow of Argon over a 2D cylinder. (Mach 10, Knudsen 0.01)

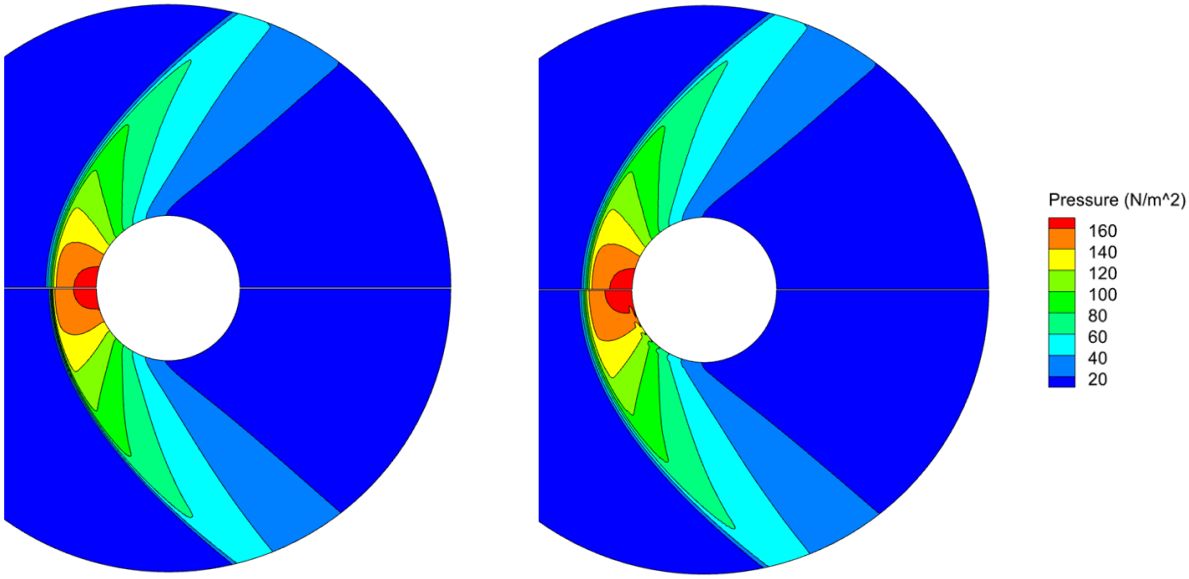

Fig. 3.76 Pressure contours of the NS (bottom-left) and hybrid (bottom-right) simulations compared against DSMC (top) for the flow of Argon over a 2D cylinder. (Mach 10, Knudsen 0.01)

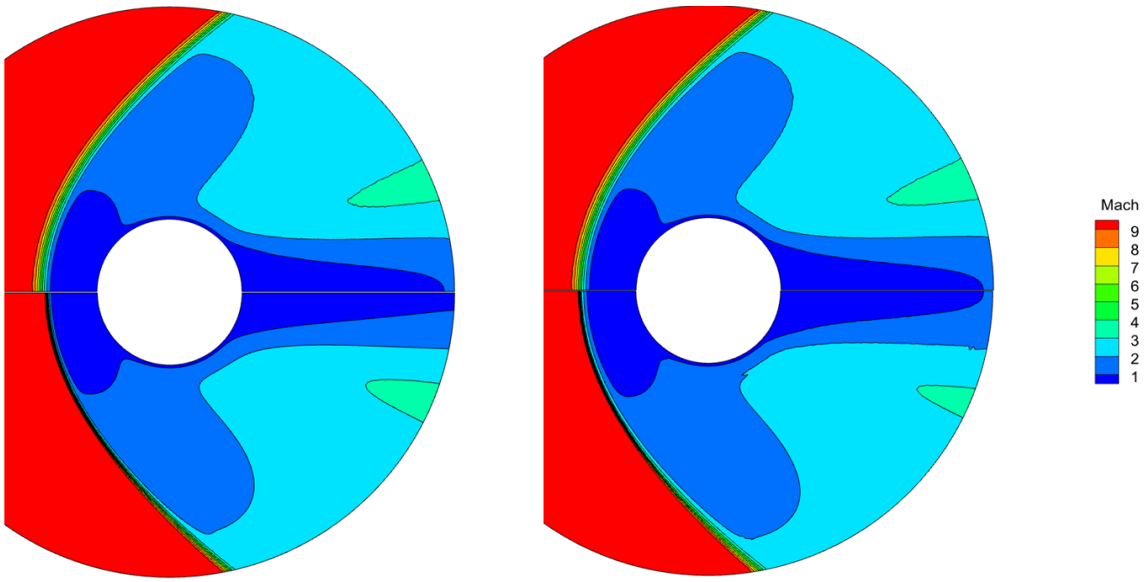

Fig. 3.77 Mach number contours of the NS (bottom-left) and hybrid (bottom-right) simulations compared against DSMC (top) for the flow of Argon over a 2D cylinder. (Mach 10, Knudsen 0.01)

Next, stagnation line plots of translational temperature and surface plots of density, pressure, heat flux, and shear stress are presented in Fig. 3.78-3.82. The NS solution for temperature in Fig. 3.78 shows deviations from the DSMC solution in areas of large $Kn_{\max}$ such as the shock and good agreement downstream of the shock. The hybrid prediction for temperature is better than the NS predictions within the shock, which is also a DSMC zone. The DSMC solution for temperature agrees well with MONACO, validating the hybrid and DSMC modules. Good agreement is observed for the surface plots of density, with the NS solution presenting a 4.7% error and the hybrid solution presenting a 3% error from DSMC results at the stagnation point. The DSMC, hybrid, and NS surface pressures all agree with MONACO, where the NS solution at the stagnation point shows an error of 0.31% and the hybrid solution an error of 3.48% when compared to DSMC results. The heat flux plots show good agreement between HALO3D-DSMC and MONACO, further validating the DSMC solver. The NS and hybrid simulations slightly underpredict the heat flux compared to the DSMC solver, which can be attributed [50] to the width of the DSMC zone next to the wall at the stagnation point. This issue is easily remedied by using evolving hybrid interfaces, which is the subject of a future study. Nevertheless, a range of peak heat fluxes is available for this problem, as shown in Table 3.1, and the error for the hybrid peak heat flux against the DS2G results is 5.3%. When the threshold $Kn_{\max}$ is set to 0.025 to make the DSMC region adjacent to the wall thicker, the heat flux prediction compares better with DSMC by presenting only a 0.73% error at the stagnation point, thus illustrating the need for an evolving hybrid interface setup. The shear stress plots show good agreement between the NS, DSMC, and hybrid codes and MONACO. The NS solution is known [107] to slightly overpredict the shear stress in the wake region, where $Kn_{\max}$ can be seen to increase. $Kn_{\max}$ is greater than 0.05 everywhere on the surface, ensuring that the entire surface is a DSMC zone. Cost benefits from the hybrid simulation are again observed, with the full DSMC computation taking 53.46 hours, whereas the hybrid simulation takes 26.92 hours.

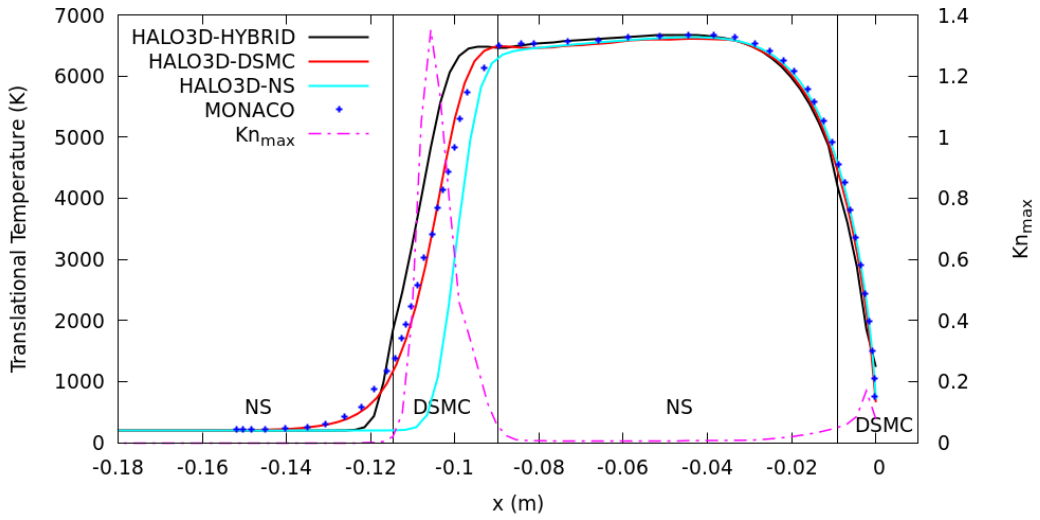

Fig. 3.78 Translational temperature along the stagnation line for the flow of Argon over a 2D cylinder. (Mach 10, Knudsen 0.01)

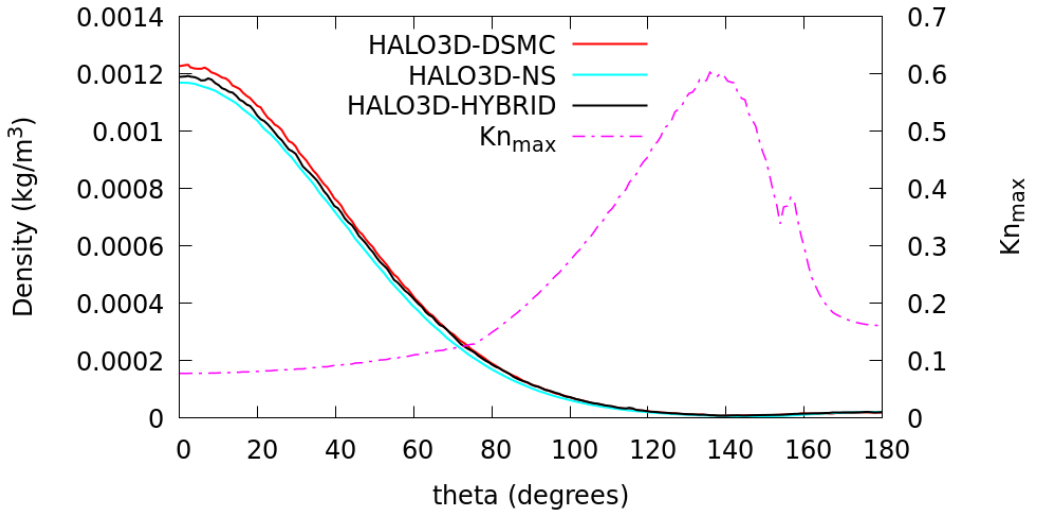

Fig. 3.79 Density along the surface for the flow of Argon over a 2D cylinder. (Mach 10, Knudsen 0.01)

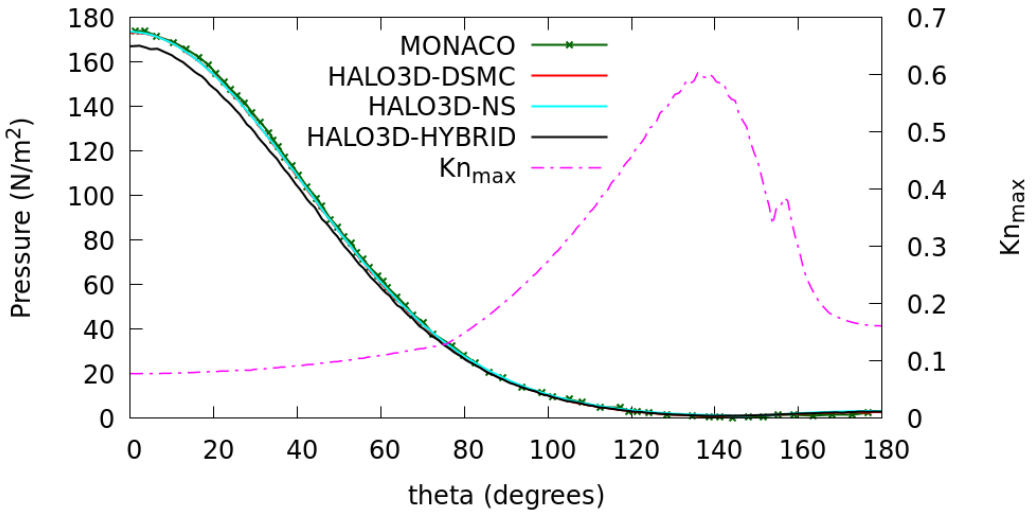

Fig. 3.80 Pressure along the surface for the flow of Argon over a 2D cylinder. (Mach 10, Knudsen 0.01)

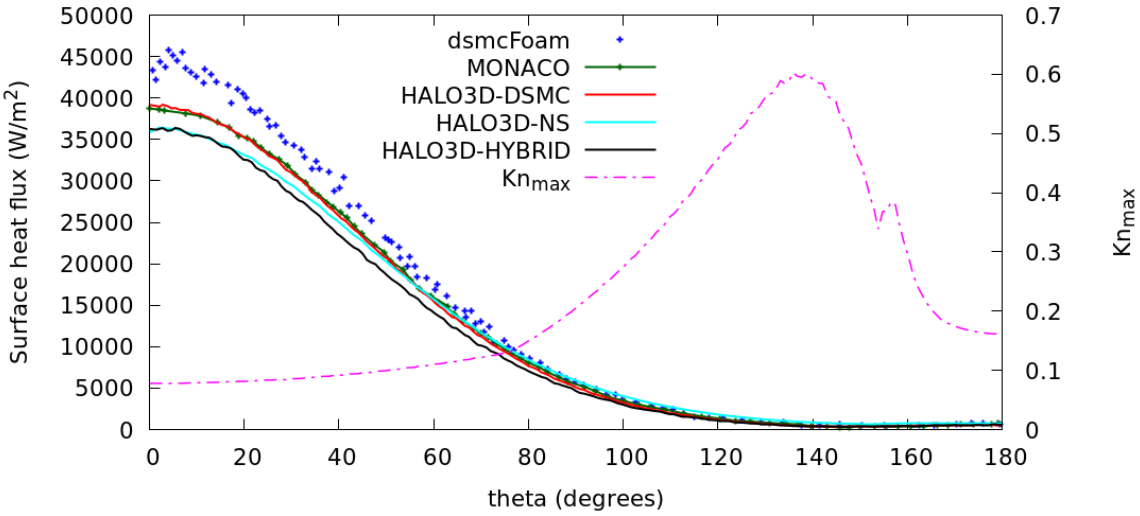

Fig. 3.81 Heat flux along the surface for the flow of Argon over a 2D cylinder. (Mach 10, Knudsen 0.01)

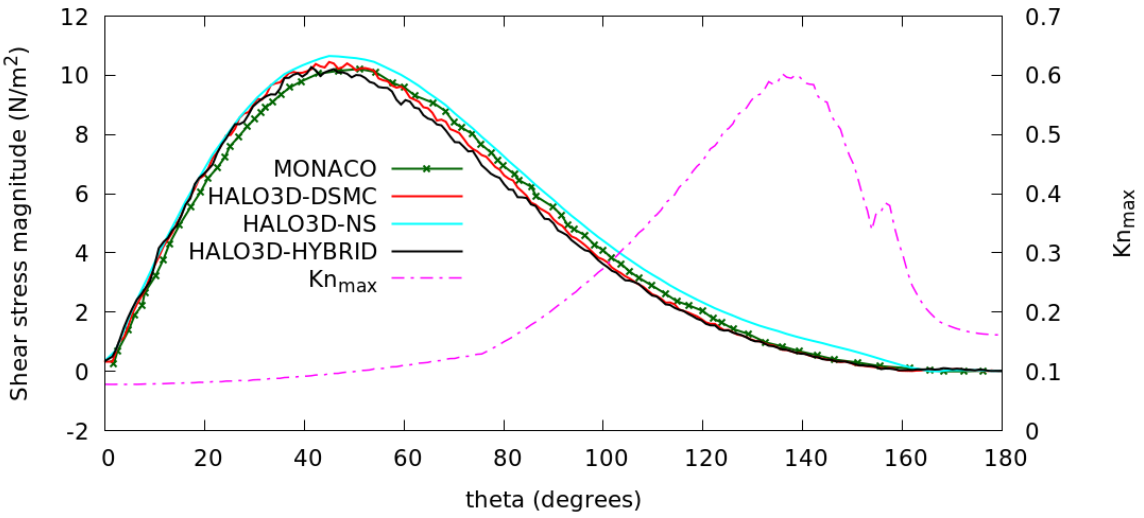

Fig. 3.82 Shear stress along the surface for the flow of Argon over a 2D cylinder. (Mach 10, Knudsen 0.01)

Table 3.1 Peak heat flux predicted by different DSMC codes for the flow of Argon over a 2D cylinder. (Mach 10, Knudsen 0.01)

DSMC solver	Peak heat flux (W/m^2)
DS2G [75]	38,300
DAC [75]	38,500
SMILE [75]	39,000
MONACO [107]	39,319
PDSC (with TAS) [98]	40,888
HALO3D-DSMC	**39,168**
dsmcFoam [108]	45,556

3.2.2.2 Vibrational N_2 Flow Over 2D Cylinder (Mach 10, Knudsen 0.006)

This test case simulates the flow of vibrational molecular Nitrogen over a 2D cylinder with the freestream Mach and Knudsen (based on the cylinder diameter) numbers being 10 and 0.006, respectively. The freestream x-velocity, pressure, and temperatures are 2883 m/s, 1.74602 N/m^2, and 200 K, respectively. The diffuse wall is set to be at 500 K, and the time step for the DSMC simulation and the DSMC module of the hybrid simulation is 6.25×10^{-8} seconds. A threshold $Kn_{\max}$ value of 0.025 is employed to increase the thickness of the DSMC zone adjacent to the

wall in a hybrid simulation. The initial NS computation applies slip boundary conditions for this problem. The prediction of surface quantities by the hybrid solver in the absence of consistent thermal non-equilibrium modeling between NS and DSMC modules is evaluated. Indeed, the rotational and vibrational temperature fields for the hybrid simulation show discrepancies such that comparisons with DSMC solutions become illogical. Hence these fields are not presented here nor in the next test case. Contours of $Kn_{\max}$ are provided in Fig. 3.83, where a maximum of ~5 is observed in the shock, which is greater than encountered in the previous test cases. Consistent with the Argon simulation, $Kn_{\max}$ is found to be large in the wake region. $Kn_{\mathrm{ROT-NEQ}}$ is shown in Fig. 3.84, which delineates the shock as a region of rotational non-equilibrium. Since the shock is well accommodated within the $Kn_{\max}$ predictions, only minor deviations from the $Kn_{\mathrm{ROT-NEQ}}$ predictions are expected. The hybrid masks resulting from a threshold $Kn_{\max}$ of 0.025 are shown in Fig. 3.85 where the shock, boundary layer and wake are all marked as DSMC zones.

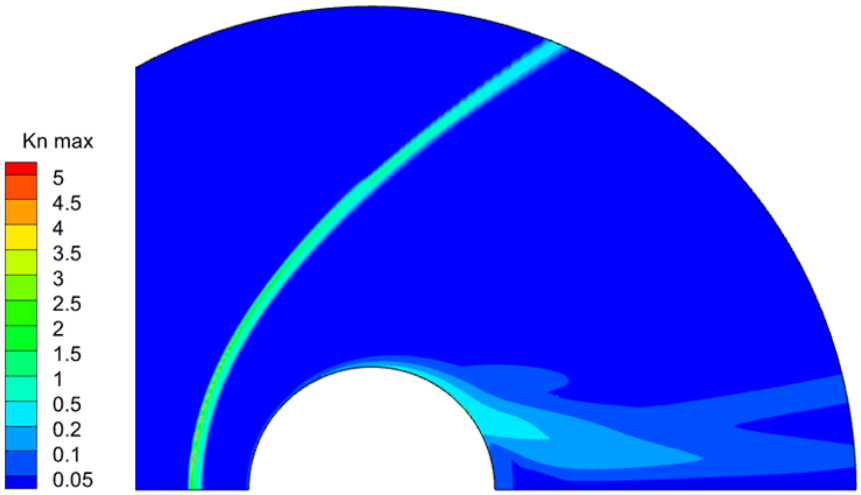

Fig. 3.83 Kn_{max} contours for the flow of vibrational Nitrogen over a 2D cylinder. (Mach 10, Knudsen 0.006)

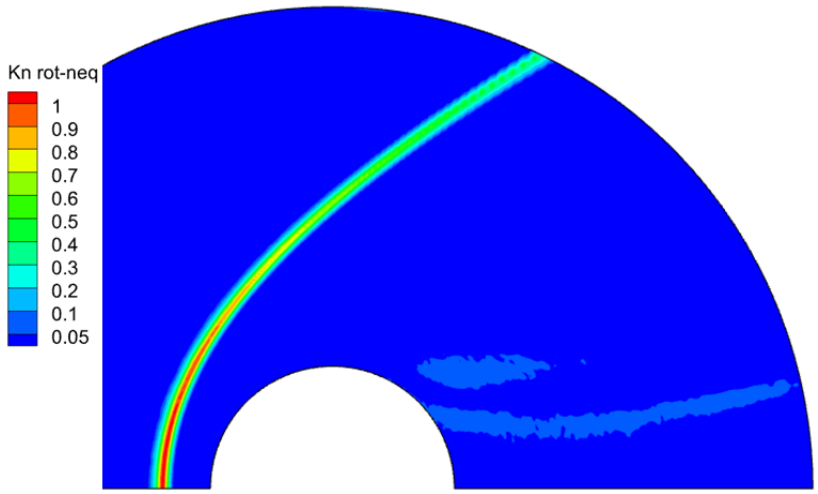

Fig. 3.84 $Kn_{ROT-NEQ}$ contours for the flow of vibrational Nitrogen over a 2D cylinder. (Mach 10, Knudsen 0.006)

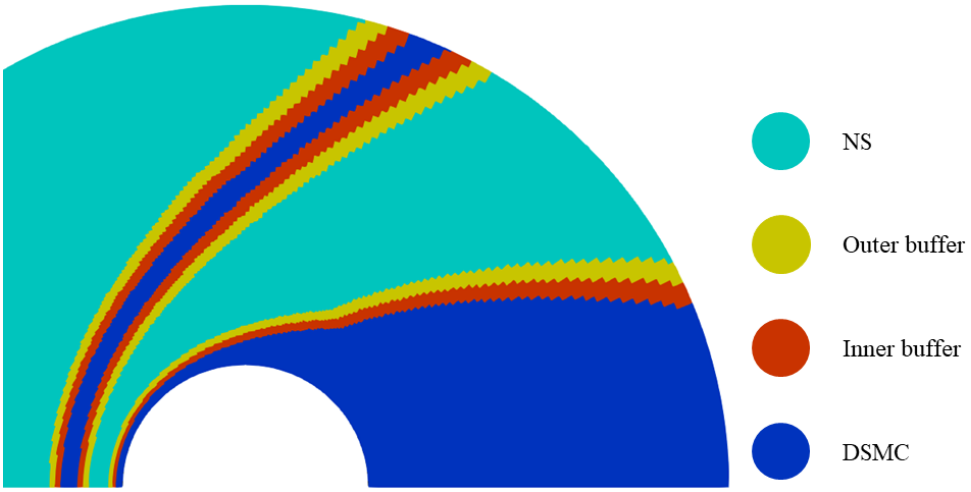

Fig. 3.85 Hybrid masks for the flow of vibrational Nitrogen over a 2D cylinder. (Mach 10, Knudsen 0.006)

Contours of density and pressure for the NS, DSMC, and hybrid simulations are shown in Fig. 3.86 and 3.87. The NS solutions again show a better comparison with DSMC than for the leading-edge simulations. The hybrid solutions also compare well against DSMC solutions. Minor discrepancies exist downstream of the bow shock, near the stagnation line for both the density and pressure contours for both NS and hybrid simulations. This is attributed to the lack of a moving

hybrid interface setup, with the help of which the NS-DSMC interfaces can be appropriately located for predicting accurate flow field results.

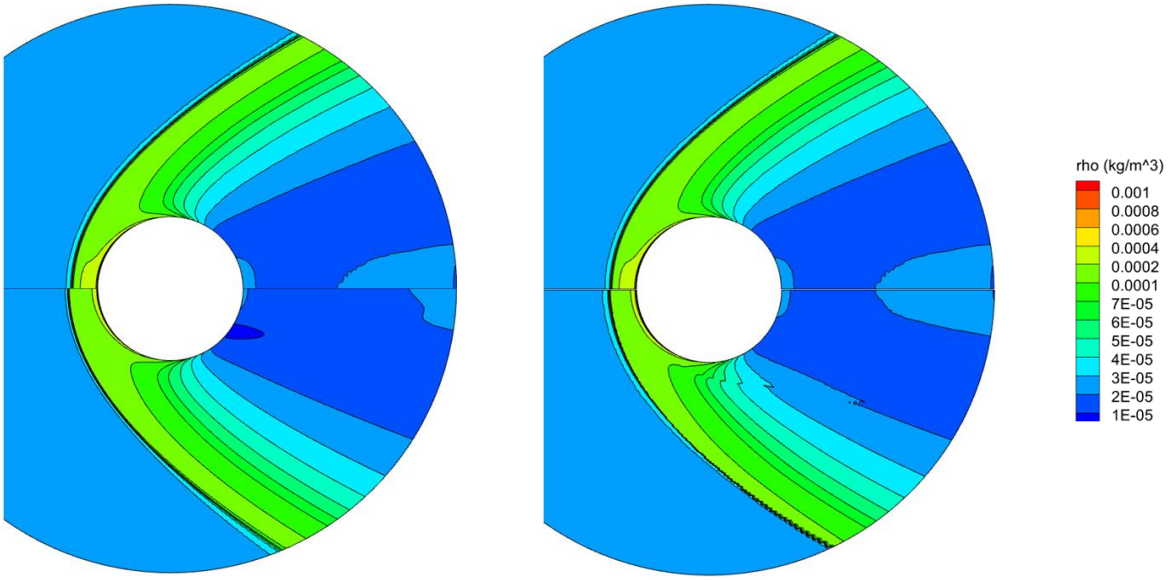

Fig. 3.86 Density contours of the NS (bottom-left) and hybrid (bottom-right) simulations compared against DSMC (top) for the flow of vibrational Nitrogen over a 2D cylinder. (Mach 10, Knudsen 0.006)

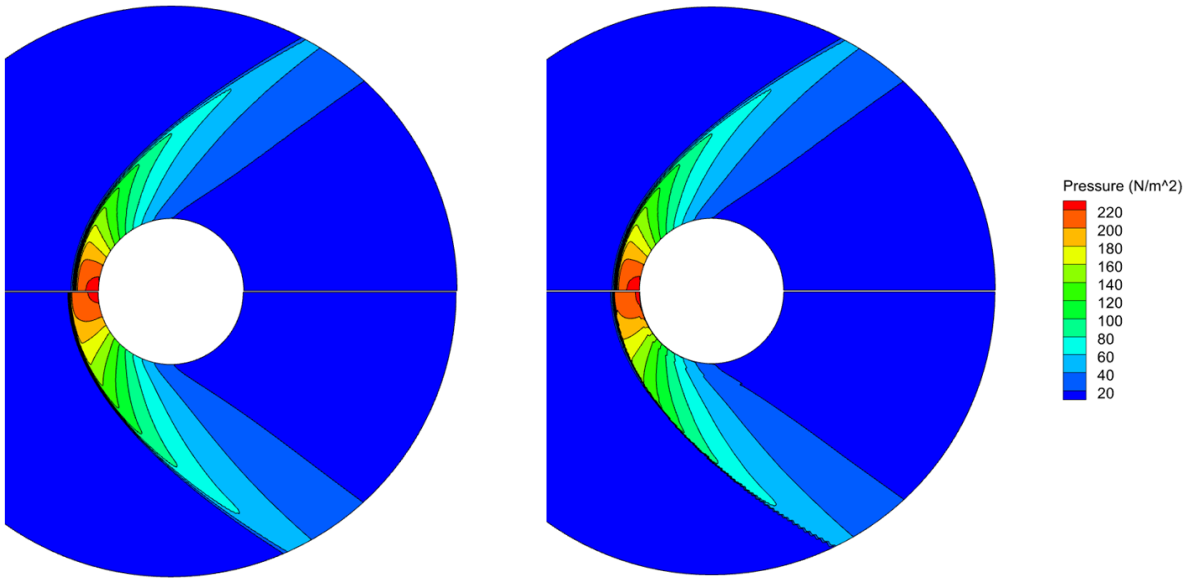

Fig. 3.87 Pressure contours of the NS (bottom-left) and hybrid (bottom-right) simulations compared against DSMC (top) for the flow of vibrational Nitrogen over a 2D cylinder. (Mach 10, Knudsen 0.006)

Surface plots of the density, pressure, heat flux and shear stress are presented in Fig. 3.88-3.91, where again, increased $Kn_{\max}$ is observed in the wake. Density along the surface shows good agreement between the NS, DSMC, and hybrid solvers, with the NS solution slightly overpredicting the density at the stagnation point, resulting in a 3.9% error. The hybrid solution compares better with a 0.95% error against DSMC. The surface pressures also show good agreement among the NS, DSMC, and hybrid solvers, with the NS solution presenting a 1% error and the hybrid solution presenting a 1.6% error against DSMC. The surface heat flux results also show NS slightly overpredicting the heat flux with an error of 4.15% compared to the hybrid prediction, which shows an error of 1.59%. The shear stress plots also show a reasonably good comparison between the three solvers where the NS solution continues to overpredict the shear stress in the wake. The hybrid solution for this problem took 27.65 hours, while the DSMC solution took 64.48 hours to compute, thus illustrating the cost benefits of the hybrid algorithm again.

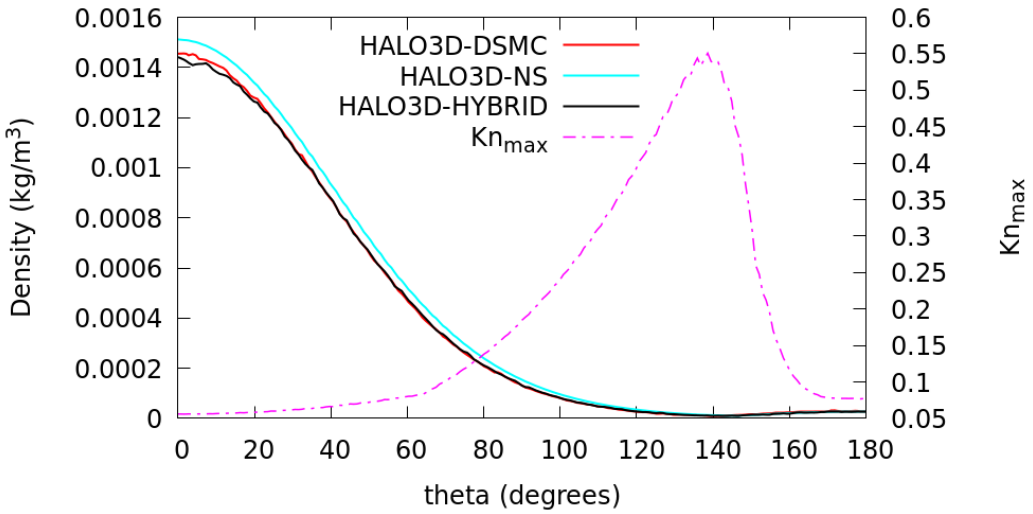

Fig. 3.88 Density along the surface for the flow of vibrational Nitrogen over a 2D cylinder. (Mach 10, Knudsen 0.006)

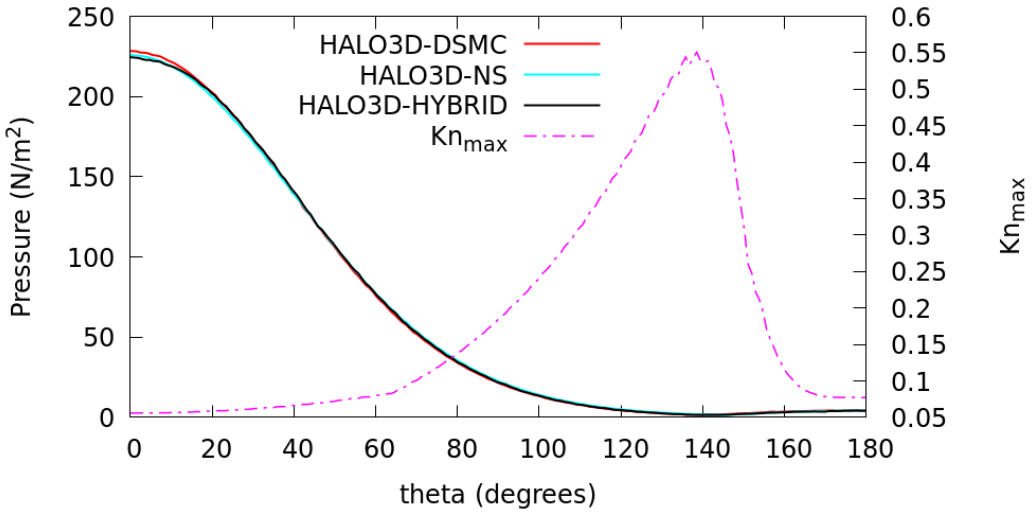

Fig. 3.89 Pressure along the surface for the flow of vibrational Nitrogen over a 2D cylinder. (Mach 10, Knudsen 0.006)

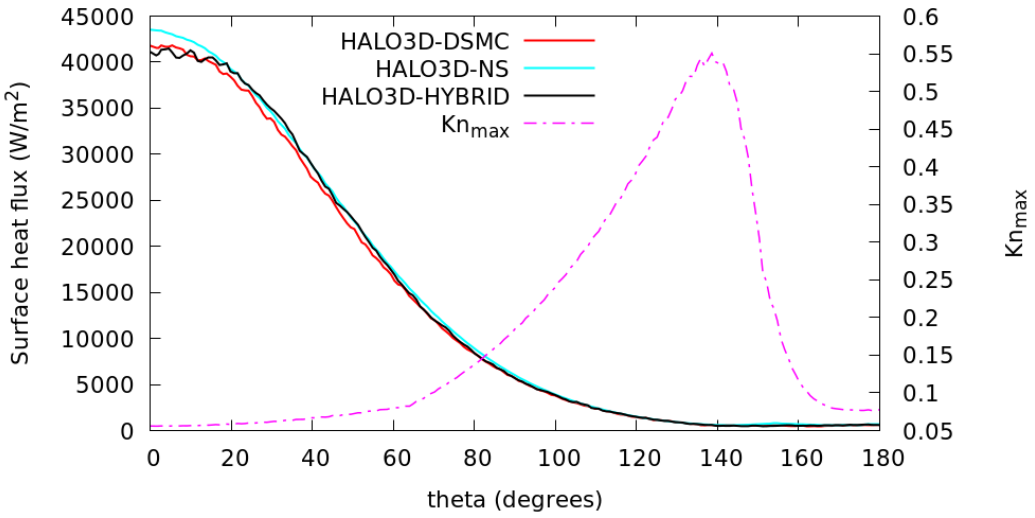

Fig. 3.90 Surface heat flux for the flow of vibrational Nitrogen over a 2D cylinder. (Mach 10, Knudsen 0.006)

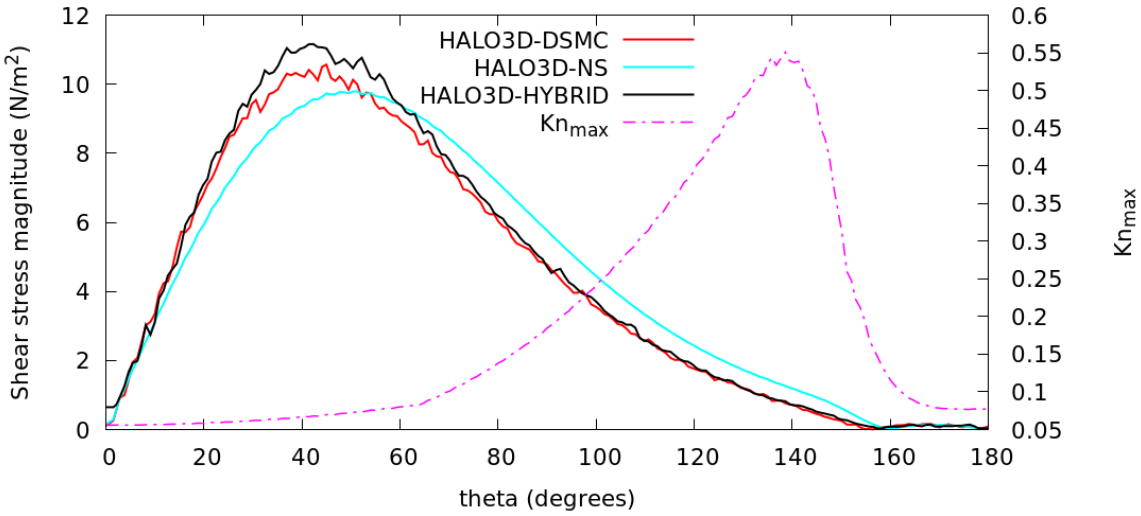

Fig. 3.91 Shear stress along the surface for the flow of vibrational Nitrogen over a 2D cylinder. (Mach 10, Knudsen 0.006)

3.2.2.3 Reacting Oxygen Mixture Flow Over 2D Cylinder (Mach 10, Knudsen 0.009)

This test case considers the flow of a mixture of chemically reacting atomic and molecular Oxygen over a 2D cylinder with the vibrational energy modeling turned on. Again, the focus is on estimating wall quantities with the addition of volume chemistry and the distribution of mass

fractions along the stagnation line. The freestream pressure, temperatures, and x-velocities are 1.746 N/m^2, 200 K, and 2883 m/s, respectively. The temperature of the diffuse wall is set to be 500 K. The freestream molar fractions of atomic and molecular Oxygen are 0.5 for both. The freestream Mach number is 10, and the Knudsen number based on the cylinder diameter is 0.009. The time step employed in the full DSMC simulation and the DSMC portion of the hybrid algorithm is 6.25×10^{-8} seconds. The reactions and parameters used for this problem are given in Appendix B. Initialization of the hybrid simulation is performed with an NS solution with no-slip boundary conditions, which results in the correct prediction of the shock location. Initialization of the hybrid algorithm with a slip NS solution results in a shock location that is slightly upstream of the full DSMC shock location. Contours of $Kn_{\max}$ for this problem are given in Fig. 3.92, where the maximum value of ~11 in the shock is the largest encountered among all the hybrid test cases. Contours of $Kn_{\mathrm{ROT-NEQ}}$ are shown in Fig. 3.93, where rotational non-equilibrium can be observed primarily in the shock. Hybrid masks obtained with a threshold $Kn_{\max}$ of 0.05 are shown in Fig. 3.94, where similar to the other cylinder cases, the shock, wake, and boundary layer regions are designated as DSMC.

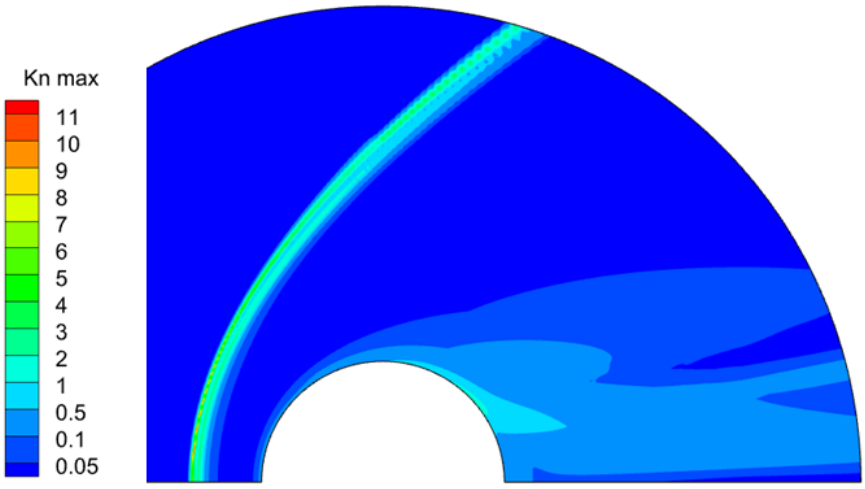

Fig. 3.92 Kn_{max} contours for the flow of an Oxygen mixture over a 2D cylinder. (Mach 10, Knudsen 0.009)

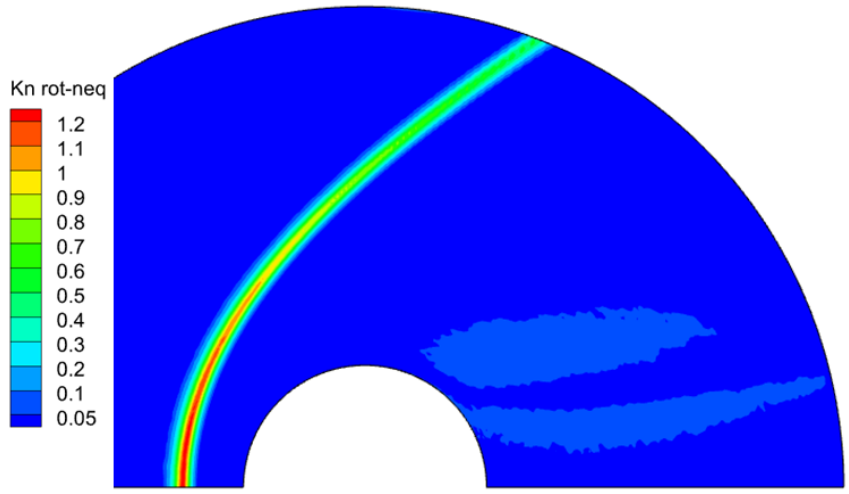

Fig. 3.93 $Kn_{ROT-NEQ}$ contours for the flow of an Oxygen mixture over a 2D cylinder. (Mach 10, Knudsen 0.009)

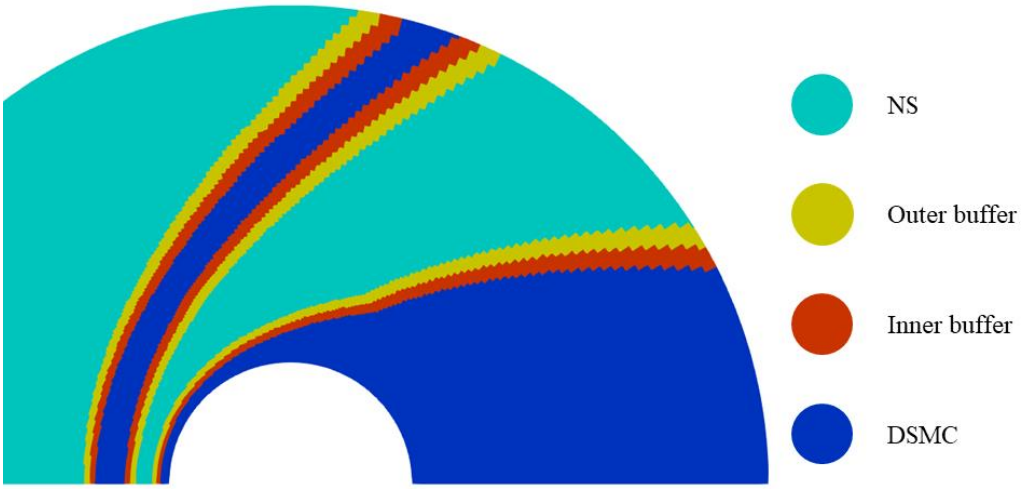

Fig. 3.94 Hybrid masks for the flow of an Oxygen mixture over a 2D cylinder. (Mach 10, Knudsen 0.009)

Contours of density, pressure, and O_2 and O mass fractions are presented in Fig. 3.95-3.98. While the NS solutions for density and pressure agree with DSMC results, the mass fractions of both O_2 and O for the NS simulations are globally the same as the freestream values. This result was previously observed in the leading-edge simulations and has also been observed in the literature [45]. The hybrid results for all four variables present smooth contours and show good agreement with the DSMC simulation. For the mass fraction contours, the hybrid algorithm successfully

recovers from the constant mass fractions initially predicted by NS, and the shock region is clearly demarcated in the final hybrid mass fractions. O_2 can be observed to be dissociating primarily in the shock region and wake.

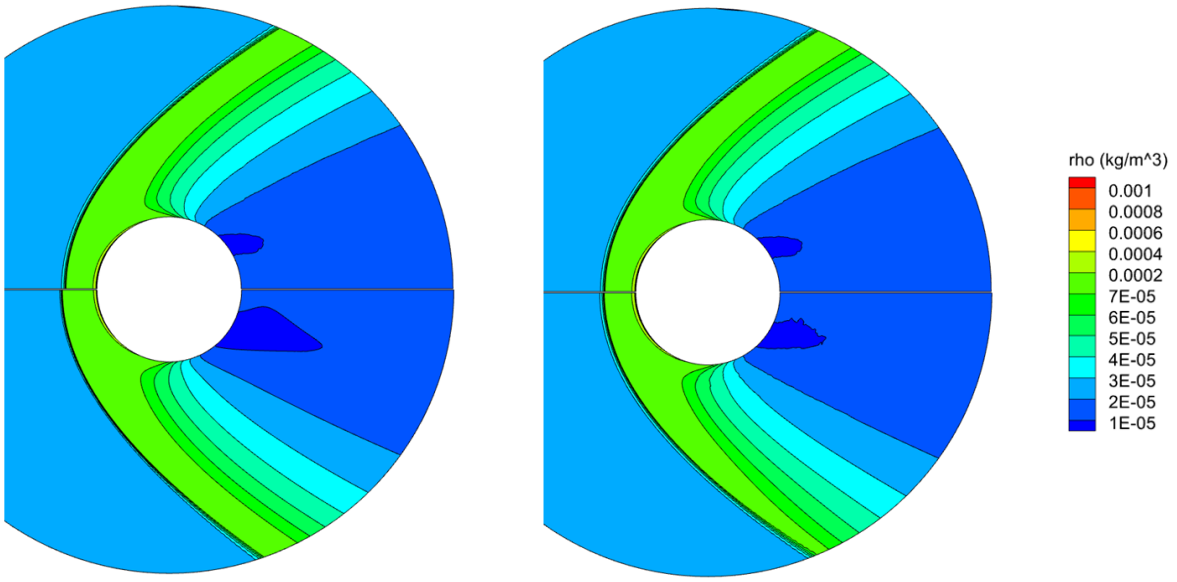

Fig. 3.95 Density contours of the NS (bottom-left) and hybrid (bottom-right) simulations compared against DSMC (top) for the flow of an Oxygen mixture over a 2D cylinder. (Mach 10, Knudsen 0.009)

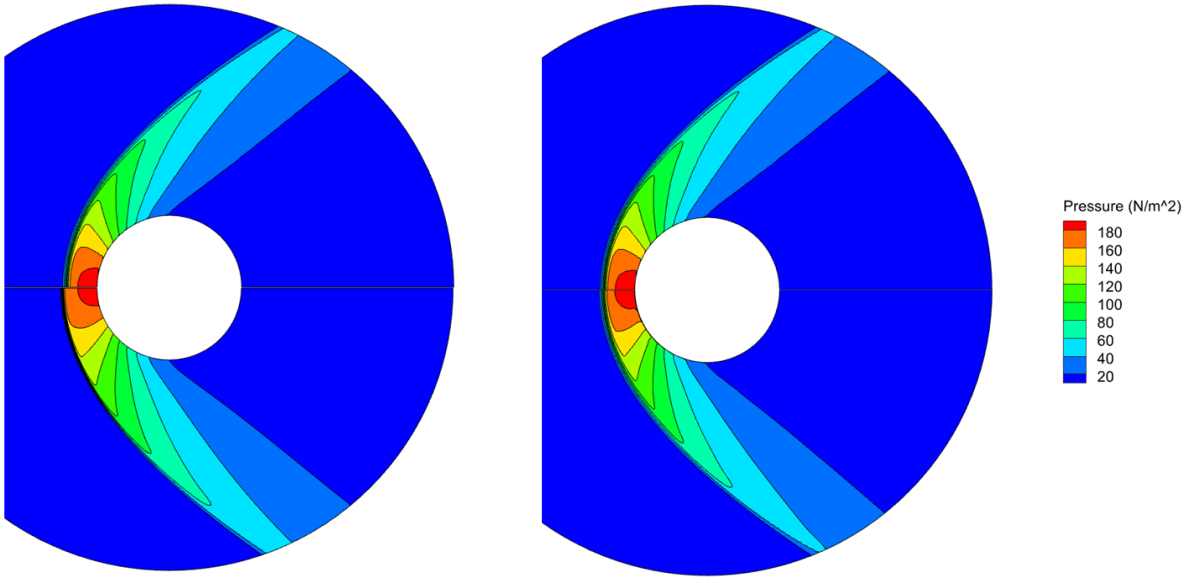

Fig. 3.96 Pressure contours of the NS (bottom-left) and hybrid (bottom-right) simulations compared against DSMC (top) for the flow of an Oxygen mixture over a 2D cylinder. (Mach 10, Knudsen 0.009)

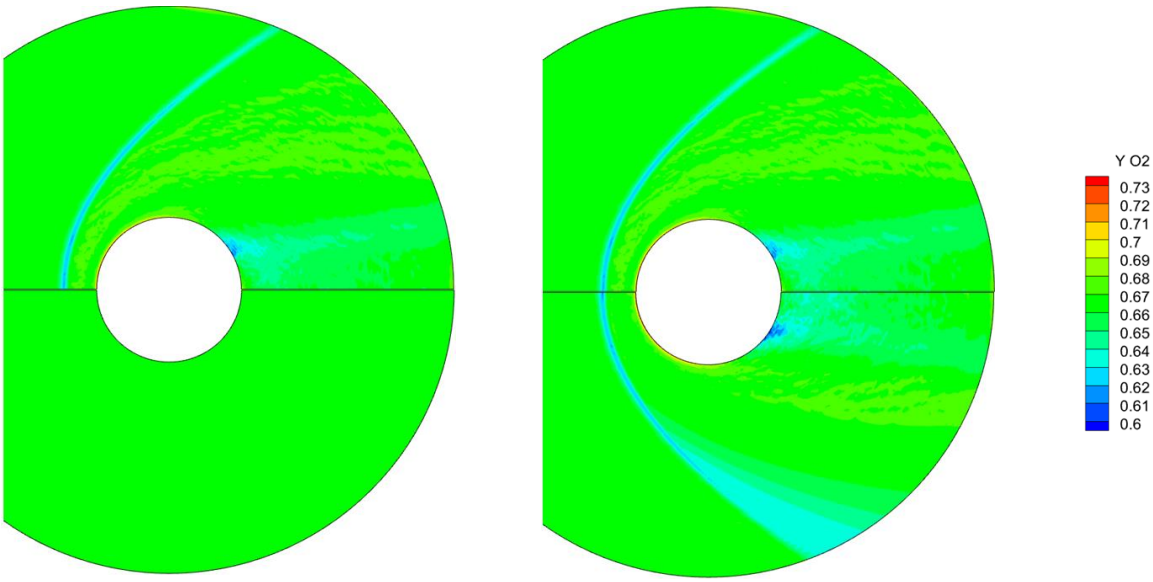

Fig. 3.97 O_2 mass fraction contours of the NS (bottom-left) and hybrid (bottom-right) simulations compared against DSMC (top) for the flow of an Oxygen mixture over a 2D cylinder. (Mach 10, Knudsen 0.009)

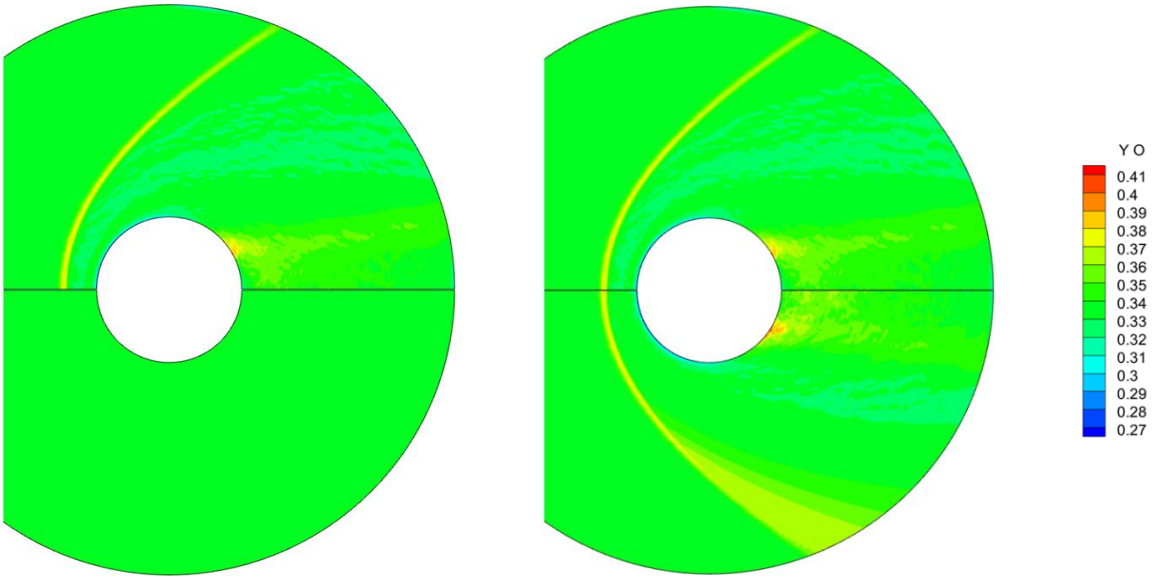

Fig. 3.98 O mass fraction contours of the NS (bottom-left) and hybrid (bottom-right) simulations compared against DSMC (top) for the flow of an Oxygen mixture over a 2D cylinder. (Mach 10, Knudsen 0.009)

Surface plots of density, pressure, heat flux and shear stress are presented in Fig. 3.99-3.102, where the NS, DSMC, and hybrid solutions compare well. The error in the hybrid solution for stagnation point density is 2.8% compared to DSMC and 7.05% for NS. NS compares better than the hybrid for the stagnation point pressure, with the hybrid solution predicting an error of 2.44% and the NS solution an error of 0.68%. The stagnation point heat flux is nearly identical between the NS, DSMC, and hybrid solutions, with the NS error being 0.51% and the hybrid solution error being 0.37%. Good agreement is found for the shear stress between the DSMC and hybrid solutions, with the NS solution again overpredicting the shear stress slightly in the wake.

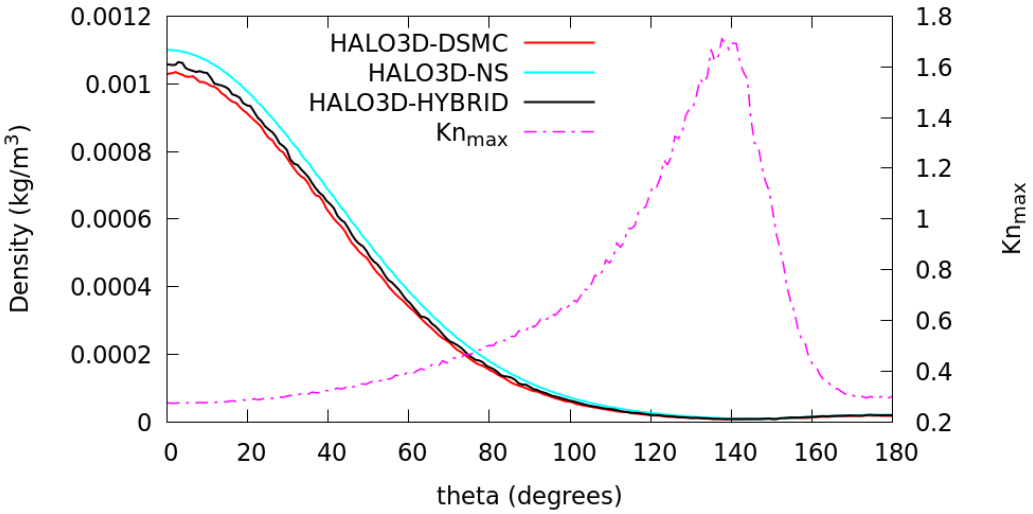

Fig. 3.99 Density along the surface for the flow of an Oxygen mixture over a 2D cylinder. (Mach 10, Knudsen 0.009)

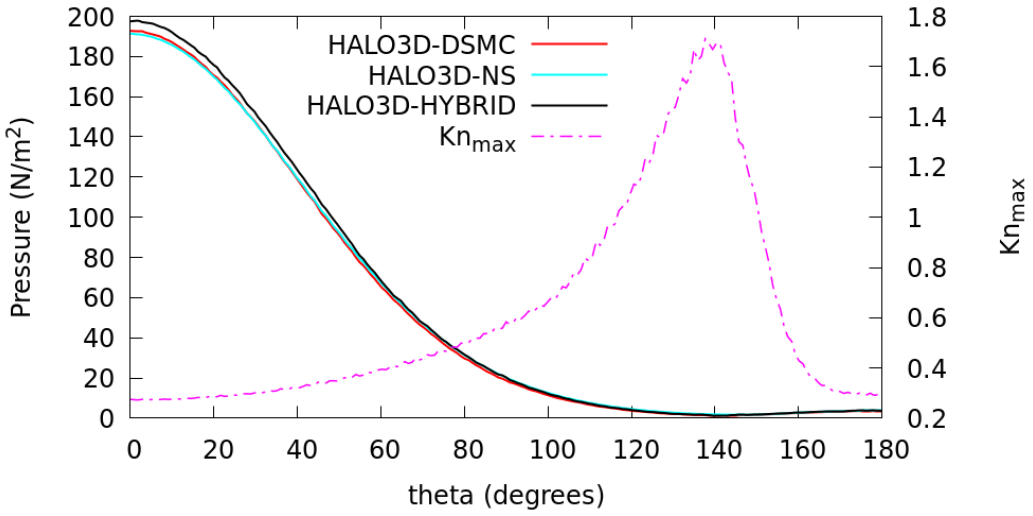

Fig. 3.100 Pressure along the surface for the flow of an Oxygen mixture over a 2D cylinder. (Mach 10, Knudsen 0.009)

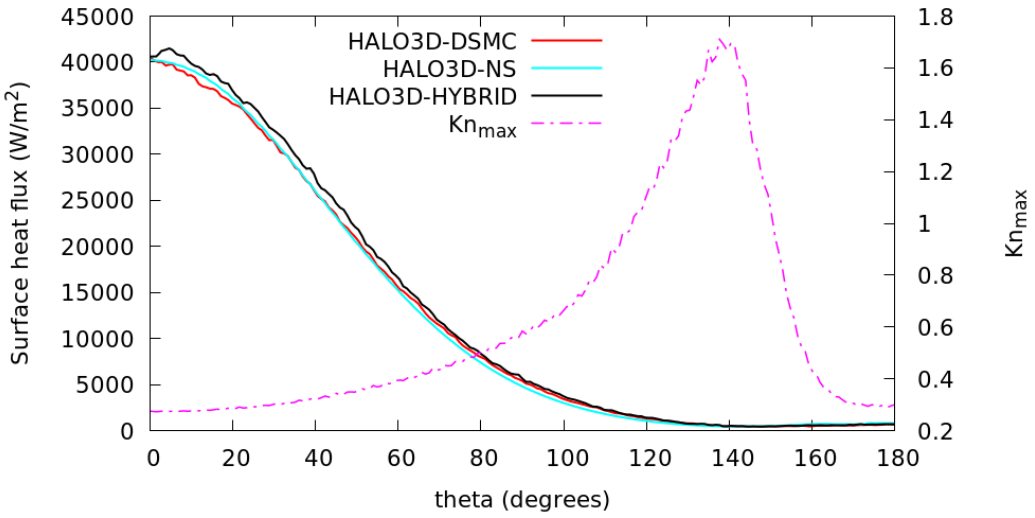

Fig. 3.101 Surface heat flux for the flow of an Oxygen mixture over a 2D cylinder. (Mach 10, Knudsen 0.009)

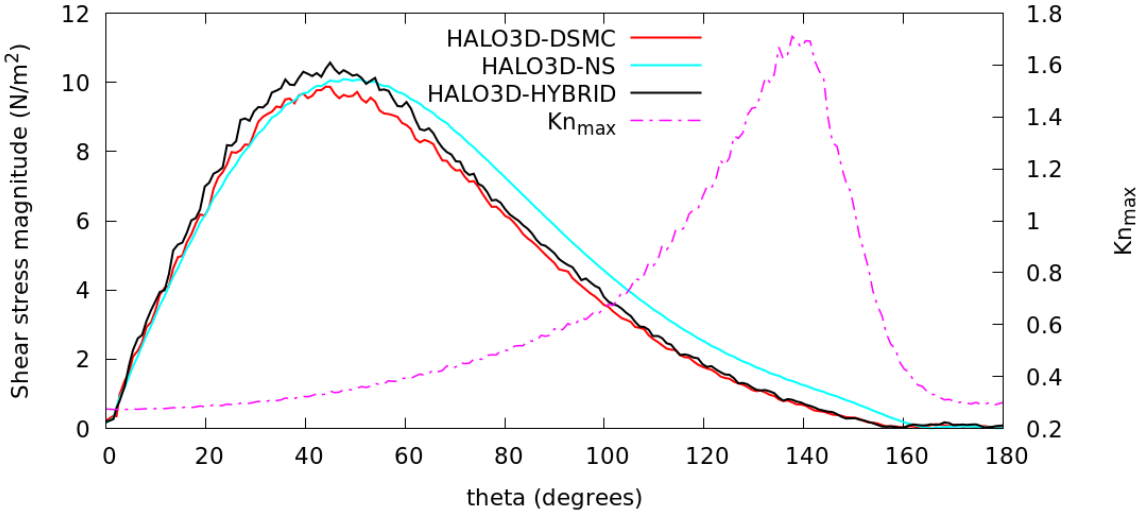

Fig. 3.102 Shear stress along the surface for the flow of an Oxygen mixture over a 2D cylinder. (Mach 10, Knudsen 0.009)

Plots of the mass fractions of O_2 and O along the stagnation line are presented in Fig. 3.103 and 3.104 where the NS and DSMC zones are demarcated. A dip in the O_2 mass fractions in the DSMC shock region (with a corresponding peak in the O mass fractions) can be observed, and the DSMC portion of the hybrid algorithm matches the full DSMC mass fractions well. Some discrepancy between the hybrid and DSMC results can be observed in the NS region downstream of the shock, and the hybrid solutions match the DSMC results again, adjacent to the wall. Smaller cost benefits

can be observed for this test case, where the time taken by the hybrid computation is 56 hours while the time taken by the DSMC computation is 61.8 hours. Better cost benefits are expected in future versions of HALO3D-HYBRID that will incorporate sophisticated hybrid procedures.

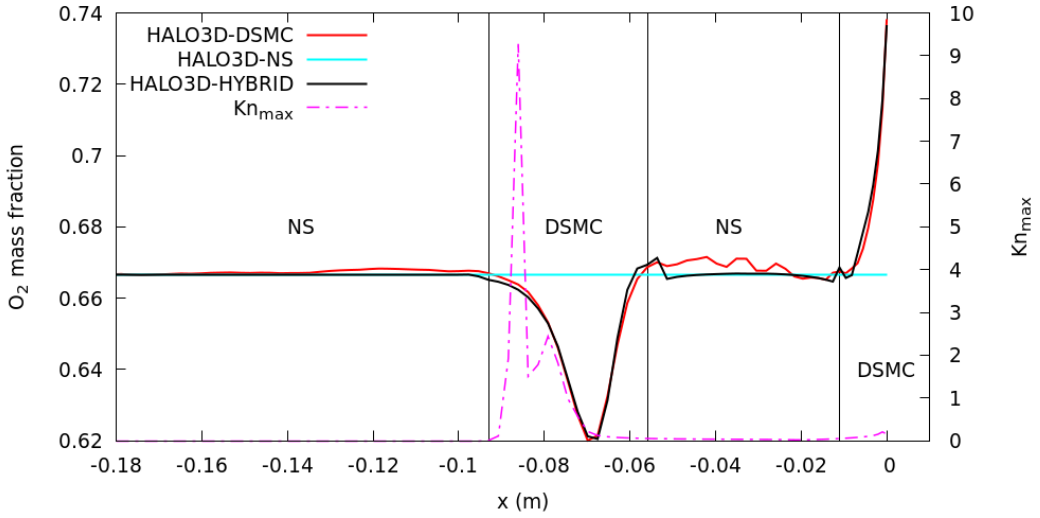

Fig. 3.103 O_2 mass fraction along the stagnation line for the flow of an Oxygen mixture over a 2D cylinder. (Mach 10, Knudsen 0.009)

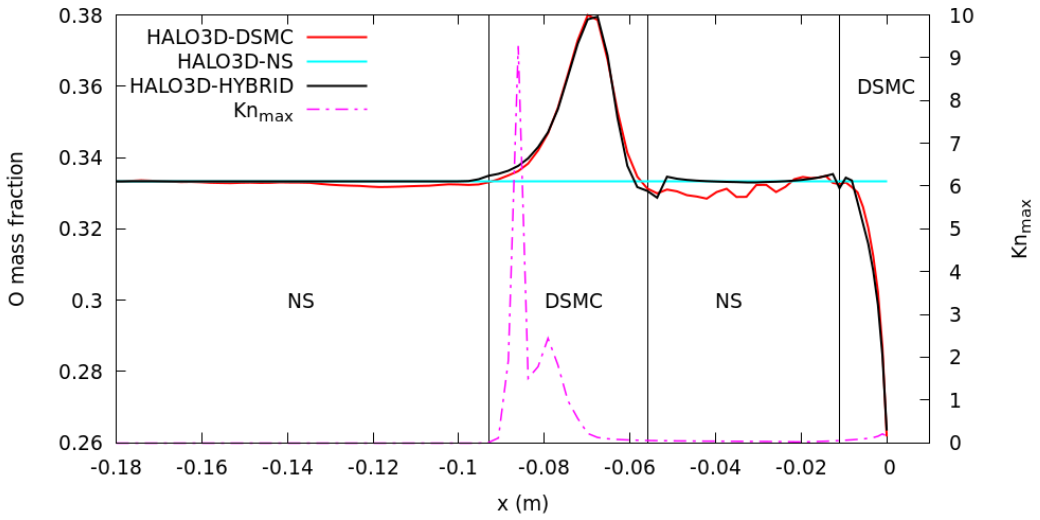

Fig. 3.104 O mass fraction along the stagnation line for the flow of an Oxygen mixture over a 2D cylinder. (Mach 10, Knudsen 0.009)

3.3 Mesh Optimization Results

This Section presents the results of mesh optimization for HALO3D-DSMC and HALO3D-HYBRID through leading-edge test cases and flows over 2D and 3D cylinders. Hybrid simulations with mesh optimization are conducted for two cases: the flow of vibrationless Nitrogen over a leading-edge and the flow of Argon over a 2D cylinder. The leading-edge runs are used to explore the parameters and initial conditions for mesh adaptation which are then applied to the cylinder simulations. Solution and mesh quality are tested with the edge-based error estimator and the separation of free paths. Comparisons with the literature are also made to validate the optimization approach.

3.3.1 Leading-Edge Flows (Mach 4, Knudsen 0.013)

The leading-edge problem is a suitable candidate for investigating the effects of OptiGrid's optimization constraints and adaptation scalars. Bird's original leading-edge setup of a Mach 4 flow of vibrationless VHS Nitrogen is considered here as in Section 3.2.1.2, with the flow conditions repeated here for convenience. The freestream Knudsen number is 0.013, and the freestream velocity, pressure, and temperature are 1412.5 m/s, 0.4142 Pa, and 300 K, respectively. The wall temperature is set to 500 K, and the time step is 2×10^{-6} s. The VHS parameters used for Nitrogen are obtained from Bird [9]. The domain and boundary conditions have been illustrated in Fig. 3.22. The dimensions of the domain are 1.1 m × 0.6 m, and a 99 × 60 × 1 uniform structured mesh is employed for code verification. The collision grid for the structured mesh employs 2 sub-cells in each direction. Around 300,000 simulated particles are present in the domain at steady-state, and 20,000 samples are subsequently accumulated. A comparison of skin friction and heat flux coefficients is shown in Fig. 3.105, and an excellent agreement exists between the HALO3D-DSMC and DS2V solvers. This non-adapted structured mesh will now serve as a reference in the remainder of this Section dealing with automatic mesh adaptation.

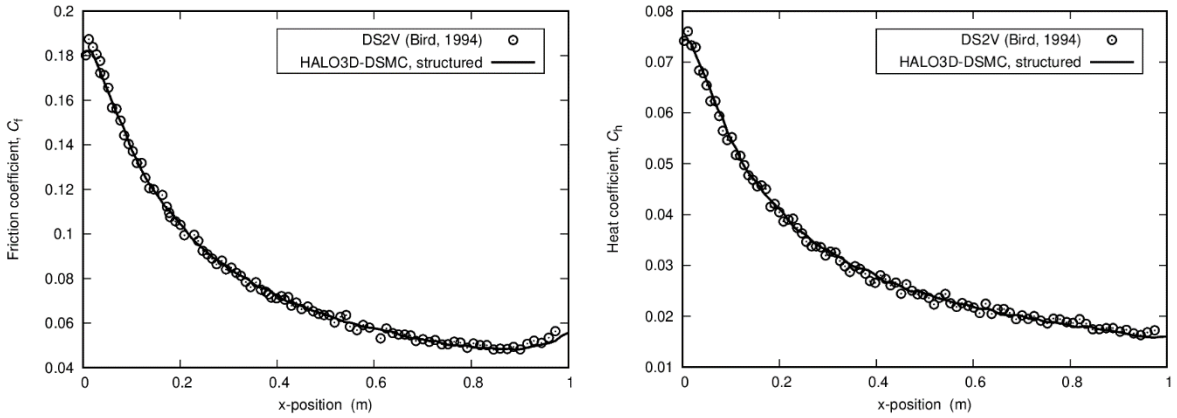

(a) Skin friction coefficient **(b) Heat flux coefficient**

Fig. 3.105 Comparison of surface coefficients given by HALO3D-DSMC and DS2V for the leading-edge simulation. (Mach 4, Knudsen 0.013)

Unstructured adapted mesh simulations share the same case setup but for the sub-celling method that is discarded in this first test case to evaluate the optimized grid quality in its absence. The sets of multiphysics adaptation scalars explored are shown in Table 3.2, where ρ is the mixture density, U_{x} and U_{y} are the x- and y-components of the velocity vector, T_{t} and T_{r} are the translational and rotational temperatures, respectively, T_{tr} is the trans-rotational temperature, Ma is the Mach number, and p is the pressure. Case C is split into three test cases: C1, C2, and C3, with three different initial meshes and the same optimization constraints and adaptation scalar set to test the convergence of the optimization algorithm further. To explore unstructured mesh hybrid simulations and confirm the solver-independence of OptiGrid in the rarefied regime, mesh optimization of HALO3D-HYBRID is performed for case D where the optimization constraints and adaptation scalar set are kept the same as for cases C1, C2, and C3.

Table 3.2 Sets of adaptation scalars retained for the leading-edge problem

Test case	Adaptation scalar set
Case A	$\{\rho\}$
Case B	$\{\rho, U_x, U_y\}$
Cases C1, C2, C3	$\{\rho, U_x, U_y, T_t, T_r, p, Ma\}$
Case D	$\{\rho, U_x, U_y, T_{tr}, p, Ma\}$

The optimization constraints given to OptiGrid are as follows: (i) a minimum edge length of 0.01 m (*i.e.*, slightly greater than the minimum mfp of 0.0089 m), (ii) a maximum edge length of 0.2 m, and (iii) a target node count equal to 4,000. The coarse initial mesh used for cases A, B, and C1 and the adapted meshes are presented in Fig. 3.106. Each final adapted mesh contains approximately 12,000 cells with cell, facet, and node counts reaching a plateau after 30 optimization cycles. The convergence of the mesh adaptation algorithm is shown in Table 3.3 for case C1 for the first 10 cycles and the last cycle. The coarse initial mesh causes the adaptation algorithm to converge to the final mesh at a much slower rate than in cases C2 and C3, where the initial meshes are more refined, and mesh counts reach a plateau after only 10 cycles. While case C1 is allowed to run to cycle 67 to compare with C2 and C3 to prove convergence, all cases begin producing successive meshes with nearly identical solutions after only the 4th cycle. This will become evident in the edge distribution plot for case C1 that follows.

Table 3.3 Convergence of the mesh adaptation algorithm for case C1 of the leading-edge flow

	Node count	**Facet count**	**Cell count**
Structured mesh (with sub-cells)	12,200	12,198	5,940
Adapted mesh case C1			
cycle 1 (initial mesh)	598	1,192	1,584
cycle 2	3,937	6,998	12,423
cycle 3	3,983	7,304	12,482
cycle 4	3,959	7,374	12,323
cycle 5	3,949	7,400	12,254
cycle 6	3,955	7,442	12,225
cycle 7	3,970	7,522	12,184
cycle 8	3,965	7,554	12,134
cycle 9	3,965	7,560	12,087
cycle 10	3,962	7,574	12,058
cycle 67 (Fig. 3.106d)	**4,194**	**8,250**	**12,466**
Adapted mesh case C2 (Fig. 3.106f)	**4,254**	**8,496**	**12,407**
Adapted mesh case C3 (Fig. 3.106h)	**4,204**	**8,346**	**12,311**

Table 3.4 Convergence of the mesh adaptation algorithm for case D of the leading-edge flow

	Node count	Facet count	Cell count
Adapted mesh case D			
cycle 1 (initial mesh)	8,684	17,364	25,218
cycle 2	3,726	7,370	10,975
cycle 3	4,112	8,158	12,126
cycle 4	4,207	8,288	12,419
cycle 5	4,158	8,170	12,279
cycle 6	4,161	8,192	12,272
cycle 7	4,160	8,202	12,285
cycle 8	4,184	8,250	12,350
cycle 9	4,169	8,244	12,272
cycle 10	4,171	8,248	12,290
cycle 14 (Fig. 3.106i)	**4,209**	**8,336**	**12,391**

Density as the sole adaptation scalar is sufficient to discern the shock (case A, Fig. 3.106b) but also results in an ill-distributed mesh in the boundary layer. Thus, the adapted mesh fails to capture the surface skin friction and heat flux coefficients compared to the baseline structured grid simulation in Fig. 3.107. To alleviate this issue, velocity components are added to the set of adaptation scalars in case B, and a more refined mesh distribution near the wall is achieved as a result in Fig. 3.106c, with skin friction and heat flux coefficients now showing only minor discrepancies in Fig. 3.107. Previous applications of OptiGrid with the HALO3D-NS flow solver for various re-entry bodies [80,100,101] highlighted the necessity of considering pressure, modal temperatures, and Mach number in conjunction with the aforementioned adaptation scalars. They are thus added to the set of case C1 to generate an optimized mesh shown in Fig. 3.106d that best represents all these flow field and surface quantities. The resulting mesh is similar to that of case B except for a smaller coarse region downstream of the shock, and it is anticipated that these additional scalars could be helpful for detached bow shock problems with steep gradients.

The capability of OptiGrid to generate the same final mesh irrespective of the initial mesh has been documented [99] for continuum regime simulations. To verify this for the rarefied regime, mesh adaptation is performed on two other initial meshes with the same optimization constraints

and scalar set as case C1. The initial meshes for these two cases (C2 and C3) are shown in Fig. 3.106e,g, where the initial mesh for case C2 is refined globally and for C3 is refined arbitrarily. Both initial meshes converge to the final meshes shown in Fig. 3.106f,h. These adapted meshes are statistically identical to the optimized mesh of case C1 shown in Fig. 3.106d, which began with the globally coarse initial mesh shown in Fig. 3.106a. The node, facet, and cell counts of all three adapted meshes of cases C1, C2 and C3 are similar, with a maximum error of 2.98% between these meshes occurring for the facet counts. The convergence of the mesh optimizer for case D, starting with the initial mesh of case C3, is presented in Table 3.4, where the mesh counts of the converged mesh are similar to the adapted DSMC meshes of cases C1, C2, and C3, with a maximum error of 1.88% for the facet counts between the adapted meshes of case D and C2. The optimized mesh for case D in Fig. 3.106i is indeed statistically identical to the adapted meshes of cases C1, C2, and C3. The skin friction and heat flux coefficients for case D agree well with the structured mesh results in Fig. 3.107, thus validating the hybrid mesh optimization approach.

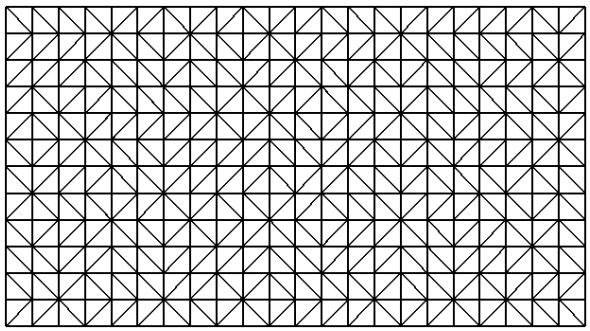

(a) Initial mesh for cases A, B, C1

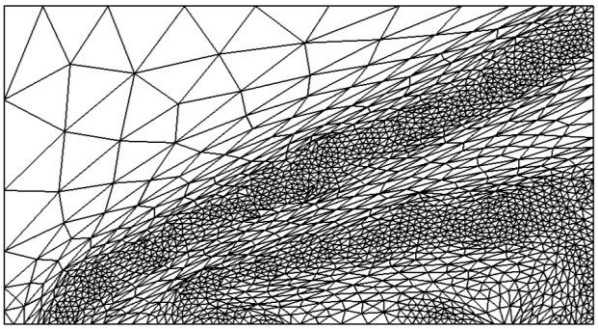

(b) Optimized mesh for case A

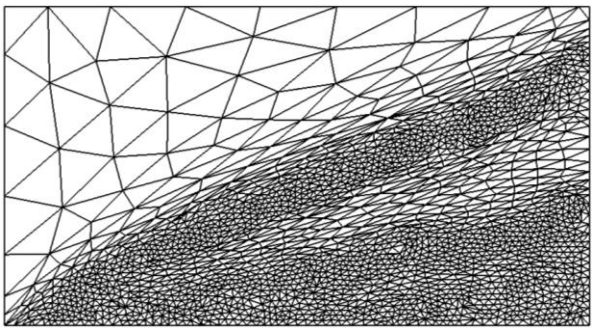

(c) Optimized mesh for case B

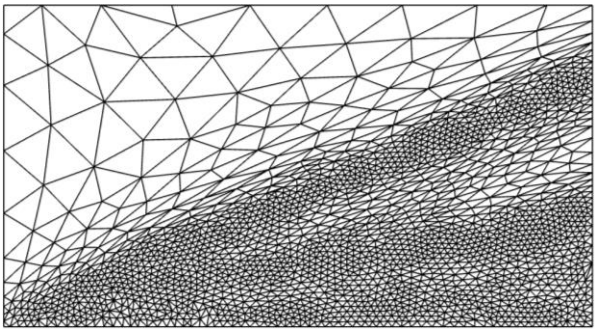

(d) Optimized mesh for case C1

Fig. 3.106 Automatic mesh optimization for the leading-edge flow. (Mach 4, Knudsen 0.013)

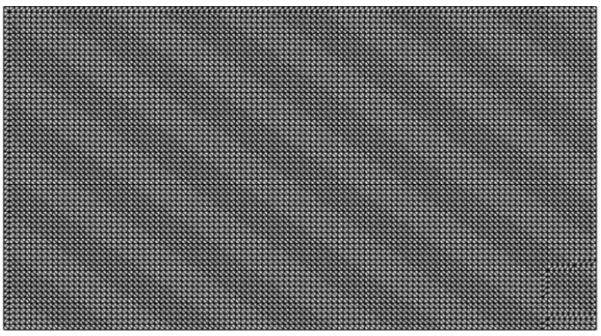

(e) Initial mesh for case C2

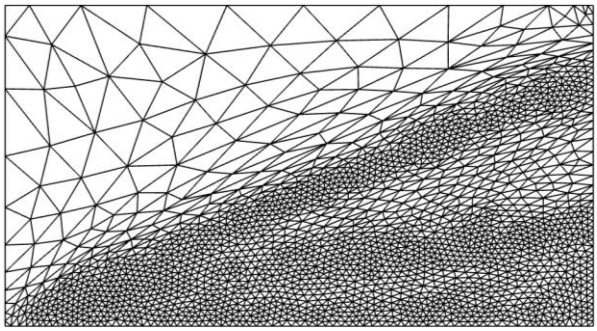

(f) Optimized mesh for case C2

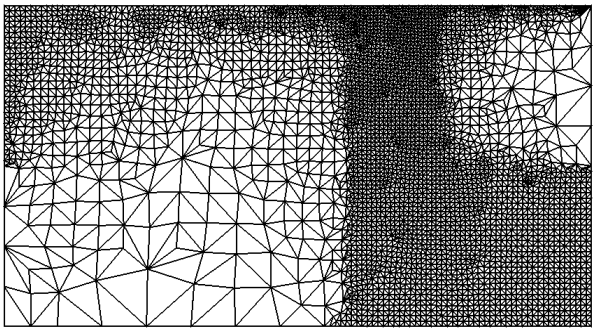

(g) Initial mesh for cases C3 and D

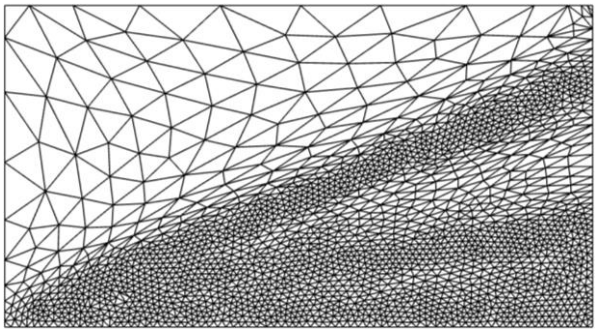

(h) Optimized mesh for case C3

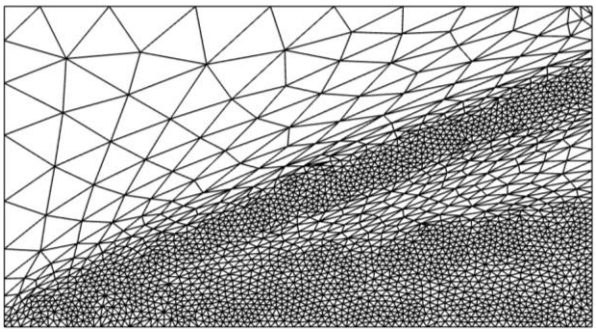

(i) Optimized mesh for case D

Fig. 3.106 Automatic mesh optimization for the leading-edge flow.

(Mach 4, Knudsen 0.013)

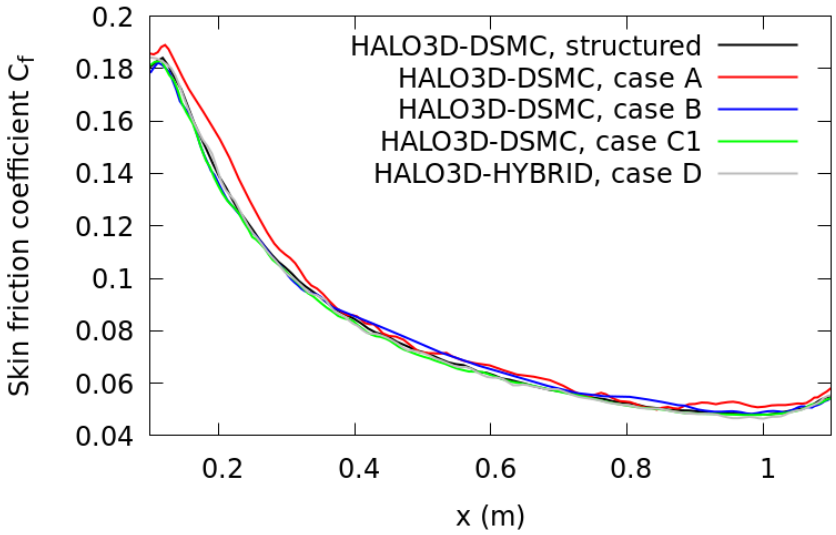

(a) Skin friction coefficient

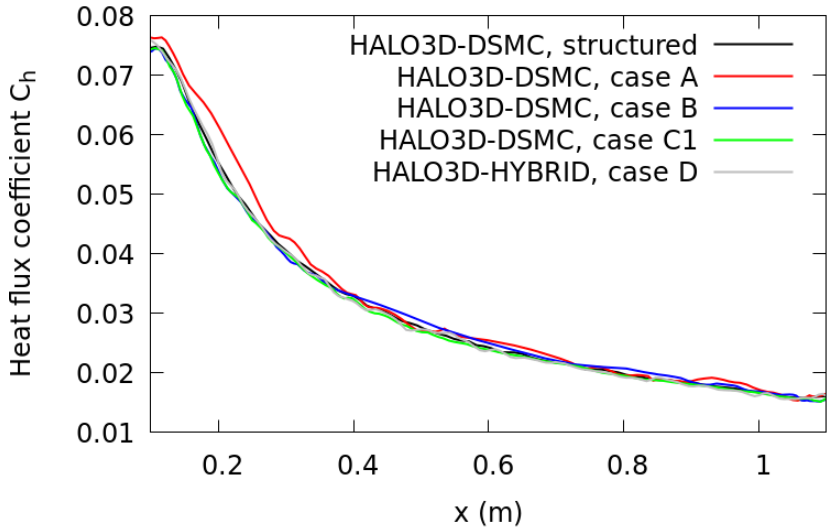

(b) Heat flux coefficient

Fig. 3.107 Comparison of surface coefficients given by HALO3D-DSMC and HALO3D-HYBRID for the structured and adapted grids for the leading-edge simulation. (Mach 4, Knudsen 0.013)

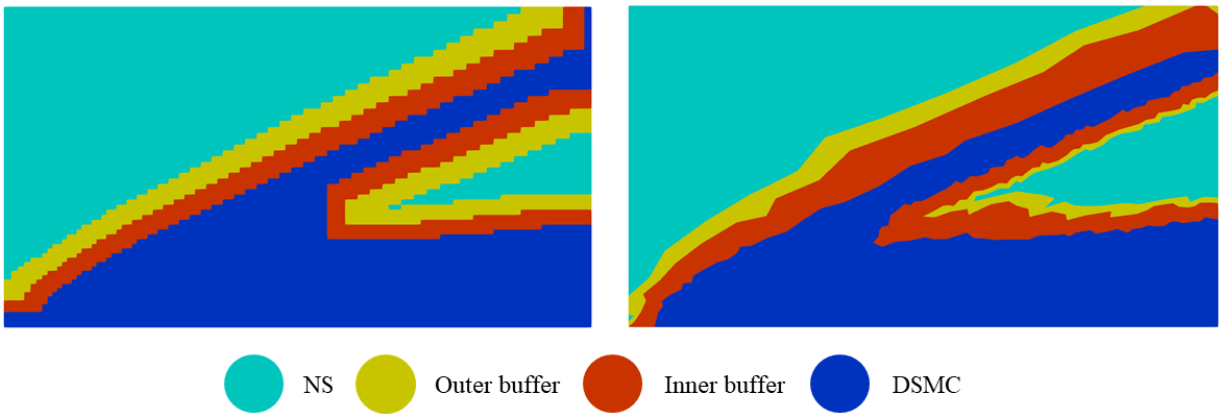

Fig. 3.108 Hybrid masks for the structured (left) and unstructured optimized (right) meshes for the leading-edge flow. (Mach 4, Knudsen 0.013)

A comparison of the hybrid masks between the structured mesh (from Section 3.2.1.2) and the optimized unstructured mesh (case D) is presented in Fig. 3.108. The structured mesh simulation employs three inner and outer buffer levels, while case D employs three inner and one outer buffer level to account for the large cells in the freestream. The structured mesh results show a castellated pattern along the shock since the hexahedra are not aligned with the shock, while the masks for case D are smoother since the optimizer comfortably aligns the tetrahedra with the shock. A comparison between the adapted mesh of case D in Fig. 3.106i and the hybrid masks from Fig. 3.108 outlines the allocation of larger cells in the adapted mesh as NS zones and smaller cells as DSMC zones. This is further discussed and illustrated for bow shocks in Section 3.3.2.

Figure. 3.109 shows the Mach number and non-dimensionalized number density contours for structured and adapted (case C1) meshes. A good agreement is found between the two meshes, proving that the unstructured adapted sampling meshes can represent the flow field with the same level of accuracy as a near-optimal structured mesh using sub-cells. In addition, the minimum edge lengths occurring in the structured and adapted meshes are similar, and while the uniform structured mesh is globally refined, the mesh adaptation algorithm can generate edges of this dimension only in areas where it is needed, as dictated by the adaptation scalars. Mach number and density contours for the structured mesh DSMC simulation and adapted mesh hybrid simulation of case D are presented in Fig. 3.110, where a good agreement between both meshes/solvers can be observed. This provides further validation to the hybrid mesh optimization approach.

Abbreviating mean collision separation as mcs, the mcs/mfp ratio (also called separation of free paths) is provided in Fig. 3.111 for the structured and adapted meshes C1 and D. A maximum cut-off value equal to 1 is chosen to highlight the shock and boundary layer regions better. The NS region mcs/mfp for case D is assigned to be zero. The maximum mcs/mfp value for the structured mesh is 0.4 (clearly benefiting from the sub-cell method) and is 3 for case C1. Some advantages of unstructured mesh optimization are visible in that the mcs/mfp ratio for the adapted meshes is lower than 1 in the shock, stagnation point, and boundary layer, with these regions being sharply defined. It is possible to further lower the mcs/mfp in these regions by changing the minimum edge length. The regions of case C1 with mcs/mfp greater than 1 in the freestream and downstream of the shock can be treated using sub-cell methods or by decreasing the maximum edge length constraint as is done in Sections 3.3.2-3.3.4. In contrast, the relatively low mcs/mfp in the freestream for the structured mesh indicates that the freestream is unnecessarily refined.

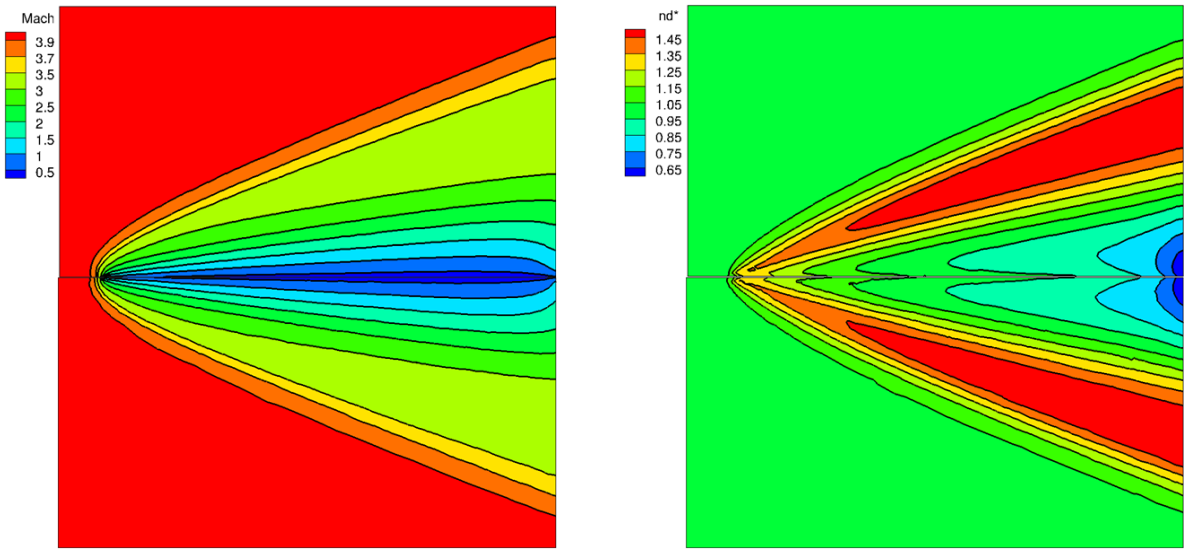

Fig. 3.109 Mach number (left) and non-dimensionalized number density (right) for the structured (top) and adapted (case C1, bottom) meshes of the leading-edge flow. (Mach 4, Knudsen 0.013)

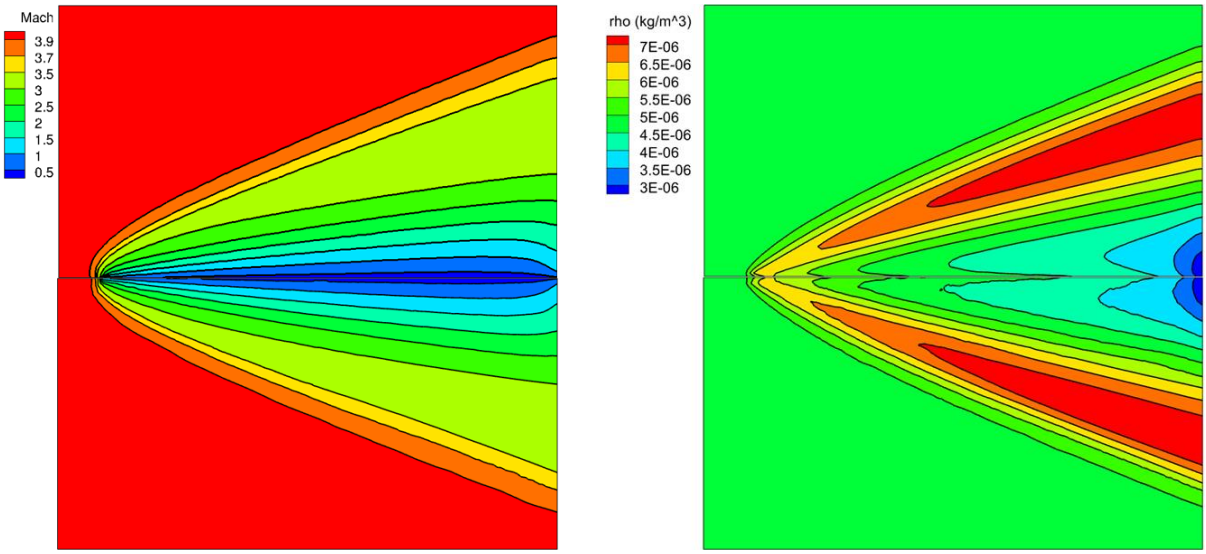

Fig. 3.110 Mach number (left) and density (right) for the structured (top) and adapted (case D, bottom) meshes of the leading-edge flow. (Mach 4, Knudsen 0.013)

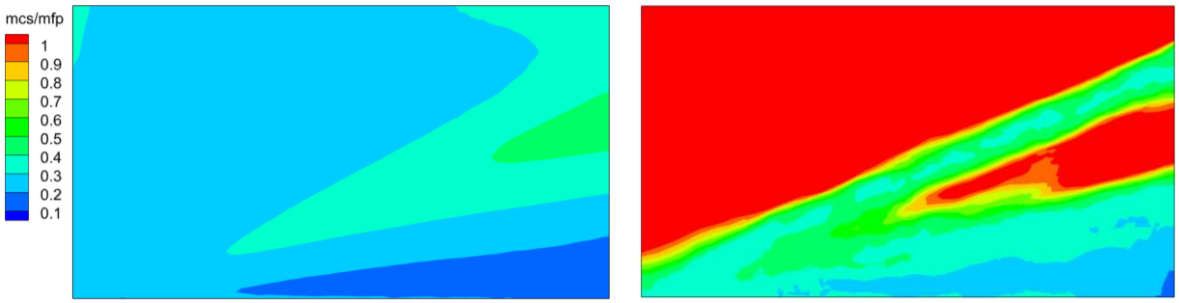

(a) Structured mesh **(b) Adapted mesh (case C1)**

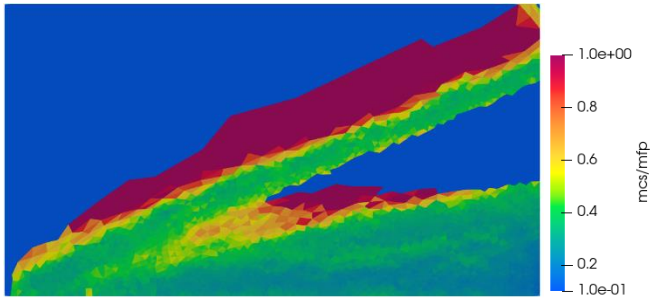

(c) Adapted mesh (case D)

Fig. 3.111 mcs/mfp ratio for the structured and adapted meshes of the leading-edge flow. (Mach 4, Knudsen 0.013)

The distribution of the mcs/mfp ratio provides information on the degree of physical accuracy of the solution and is also used to evaluate the quality of the mesh as a collisional mesh. In contrast, the distribution of the error estimate defined in Equation 2.133 provides a way to evaluate the quality of the solution that is represented on a given sampling mesh. For continuum regime mesh adaptation, the error estimate represents the discretization error of the PDE being solved, and for DSMC, it is expected that the error estimate represents the amount of deviation from a solution obtained on vanishingly small sampling cells. The distribution of the error estimate for the initial and adapted meshes of the full DSMC simulations of cases C1, C2, and C3 are shown in Fig. 3.112. All three initial meshes present their maximum errors at the stagnation point, and the error estimate distribution of initial mesh C2 is generally lower than initial meshes C1 and C3. All three adapted meshes display low error in the freestream, again showing that the flow field variables are well captured in the freestream despite the large cell size. Plots of the percentage of edges possessing different error estimate values for cases C1, C2, and C3 are shown in Fig. 3.113. For case C1, the coarse initial mesh has a much larger maximum error than the adapted mesh and the edge distribution converges within the first few iterations to a similar profile as that of the final mesh, as shown in Fig. 3.113a. The refined initial mesh of case C2 displays two peaks in the percentage of edges in Fig. 3.113b that are consolidated into a single peak around a similar error level through mesh adaptation. The peaks in the percentage of edges at very low error for the initial mesh of case C2 are due to the over-refined freestream. The distribution for case C3 plotted in Fig. 3.113c indicates that the few edges with high errors at the stagnation point in the initial mesh are refined to produce lower error regions. For cases C1, C2, and C3, multiple peaks can be observed in the plots for the initial meshes that change to a single peak for the adapted mesh. This shows that the error is getting equi-distributed across the domain. Fig 3.113e plots the edge distributions for the adapted meshes from cases C1, C2, and C3 on the same graph. The degree of similarity between these three plots is a testament to the ability of OptiGrid to converge to the same final mesh irrespective of the initial mesh or solver. Similar conclusions can be drawn from the error estimate contours for hybrid simulations from case D shown in Fig. 3.112g,h where the error is high at the stagnation point in the initial mesh and the adapted mesh results show the error being equi-distributed among the NS and DSMC regions. Edges with large error estimates in the initial mesh are treated as shown in Fig. 3.113d, and the edge distribution for the adapted mesh of case D is similar to that of the adapted meshes of cases C1, C2 and C3 in Fig. 3.113e.

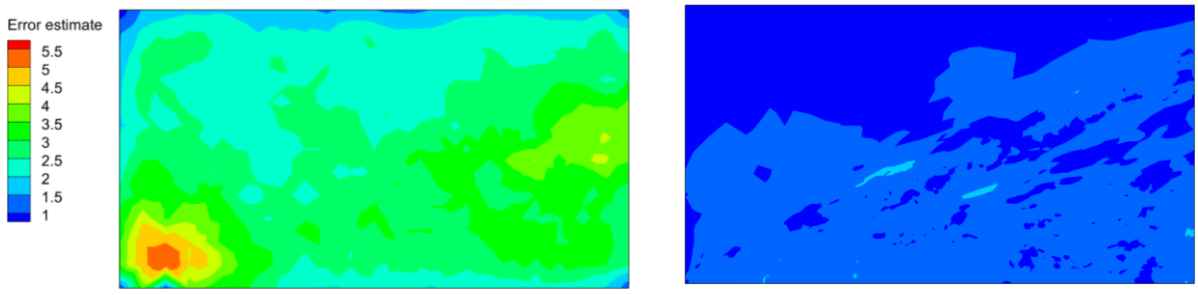

(a) Initial mesh of case C1 **(b) Optimized mesh of case C1**

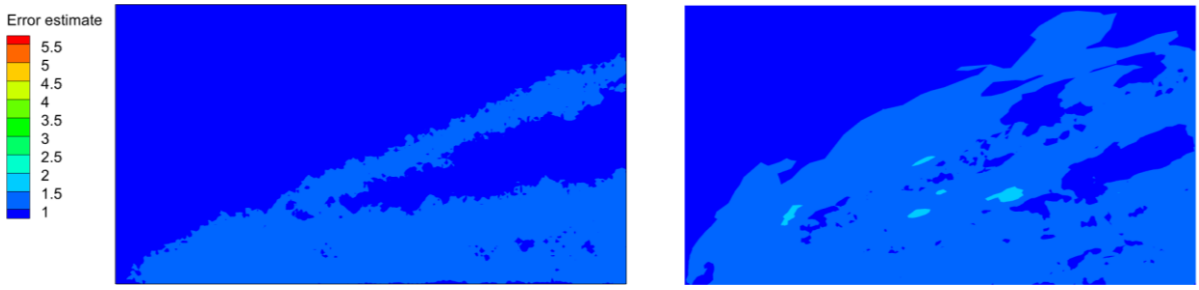

(c) Initial mesh of case C2 **(d) Optimized mesh of case C2**

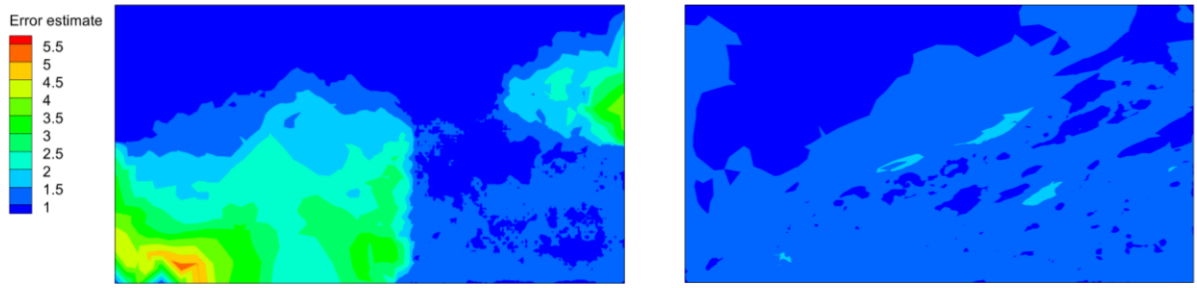

(e) Initial mesh of case C3 **(f) Optimized mesh of case C3**

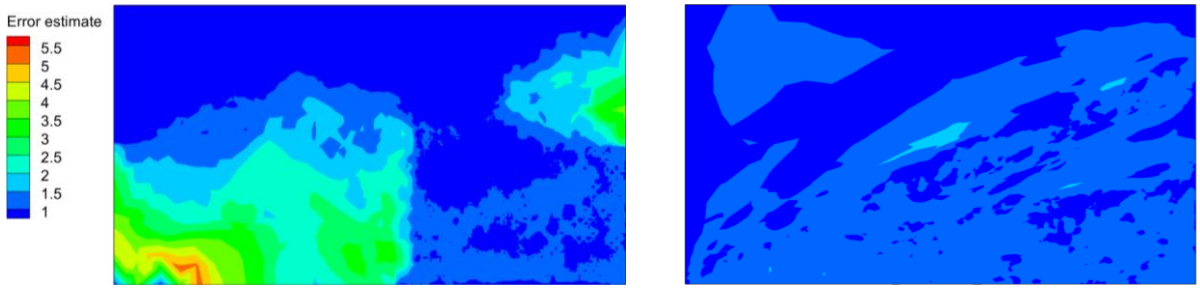

(g) Initial mesh of case D **(h) Optimized mesh of case D**

Fig. 3.112 Error estimate contours for cases C1, C2, C3 and D. (Mach 4, Knudsen 0.013)

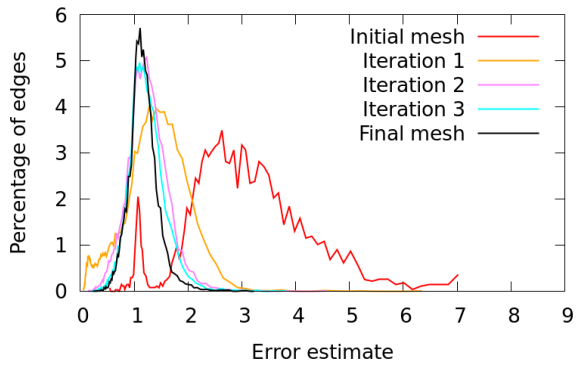

(a) Edge distribution for case C1

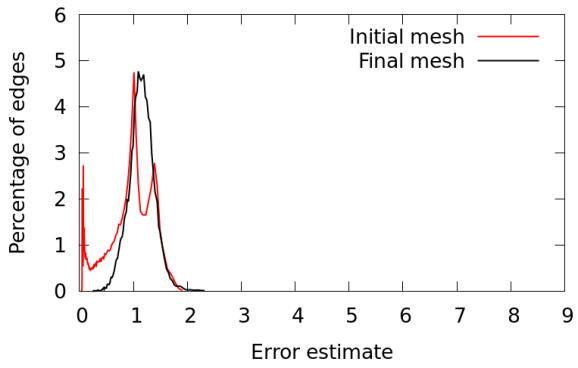

(b) Edge distribution for case C2

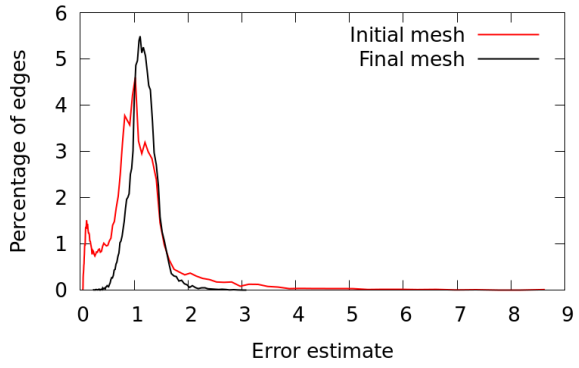

(c) Edge distribution for case C3

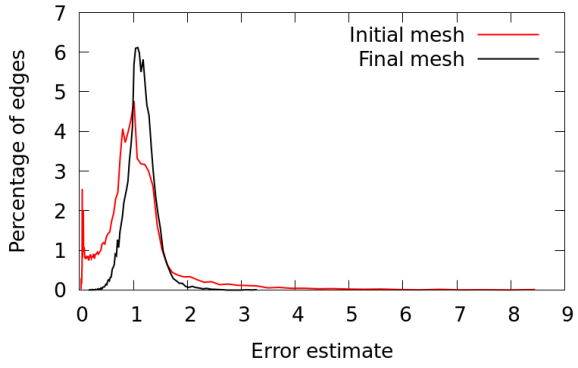

(d) Edge distribution for case D

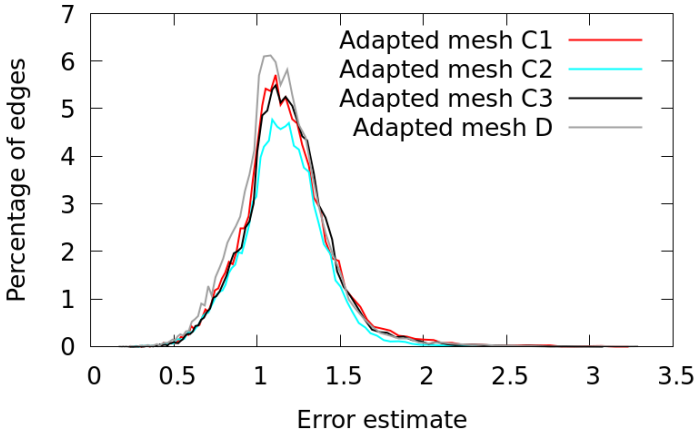

(e) Edge distribution for the adapted meshes

Fig. 3.113 Edge distributions for cases C1, C2, C3 and D. (Mach 4, Knudsen 0.013)

In summary, the leading-edge tests indicate that a suitable DSMC mesh that produces results of similar accuracy as a refined tetrahedralized uniform structured initial mesh (that has 13,542 nodes, 27,200 facets and 39,600 cells) while employing fewer node, cell and facet counts can be created

through OptiGrid for attached shock problems. They also indicate that a single error estimator built from the Hessian of the adaptation scalars can be used to examine the quality of both the NS and DSMC solutions in a hybrid algorithm. The following three cylinder cases will aim to demonstrate similar conclusions for 2D and 3D flows exhibiting a strong detached bow shock and a wake region.

3.3.2 Argon Flow over 2D Cylinder (Mach 10, Knudsen 0.01)

Lofthouse [107] and Bird [75] have used this benchmark Mach 10 Knudsen 0.01 flow of Argon over a 0.3048 m-diameter 2D cylinder to perform mesh adaptation with the MONACO and DS2V codes. This test case is the same as in Section 3.2.2.1 except for a bigger domain to accommodate the shock to a larger extent. The domain and boundary conditions are illustrated in Fig. 3.114. Two cases are considered: case A is for the mesh adaptation of a full DSMC solution, and case B is for the mesh adaptation of a hybrid solution. The freestream conditions, repeated here for convenience, for pressure, temperature, and velocity are 1.1727 Pa, 200 K, and 2634.1 m/s, respectively, the diffuse wall temperature is set to 500 K, and the time step is 1×10^{-7} s in the full DSMC and DSMC portions of the hybrid simulation. The threshold $Kn_{\max}$ for the hybrid simulations of case B is set to be 0.05. The findings of the leading-edge case led to the consideration of $\{ \rho, U_x, U_y, T_t, p, Ma \}$ as the set of multiphysics adaptation scalars for both case A and B as well.

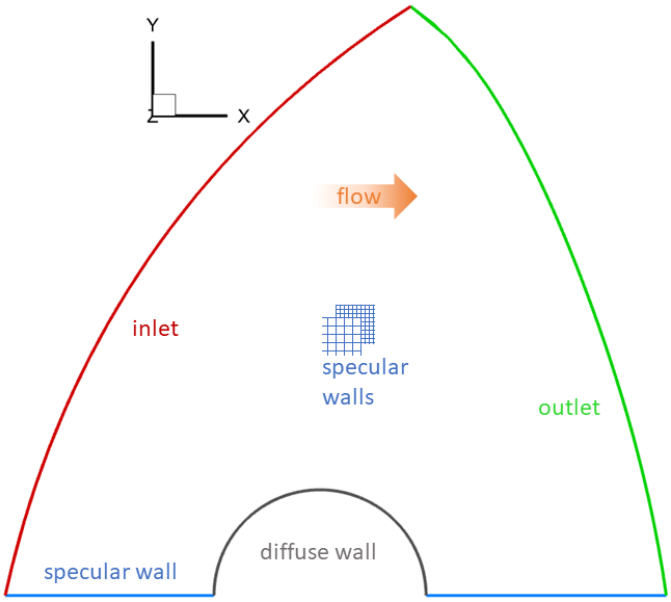

Fig. 3.114 Domain and boundary conditions for the hypersonic flow over a cylinder

The optimization constraints given to OptiGrid for both cases are as follows: (i) a minimum edge length of 0.0025 m (equal to 0.87 times the freestream mfp), (ii) a maximum edge length of 0.07 m (equal to 5 times the maximum mfp, as found from the first iteration of the adaptation algorithm), and (iii) a target cell count equal to 85,000. The convergence of the mesh adaptation algorithm for both cases is provided in Table 3.5 and 3.6, and the adapted meshes are shown in Fig. 3.115. The two adapted meshes look similar, and the maximum error for the mesh counts between the two meshes occurs for the cell count and is equal to 0.48%. This result confirms the solver-independence of OptiGrid and validates the hybrid algorithm since it has to produce the same solution as full DSMC for the two meshes to be the same. The same initial mesh is used for both cases, which is sized such that the edge length at the wall is 0.0025 m and gradually increases outward to a maximum of 0.01 m, to accelerate the convergence of the mesh adaptation algorithm. Such a large cell size is used primarily to test the capability of the background mesh to function as a sampling mesh first and as a collisional mesh second (indeed, more sub-cells are created as a result).

Preliminary mesh adaptation studies for varying minimum edge length and particle count have been conducted for this problem, as shown in Fig. 2.13. These studies highlighted the sensitivity of the surface heat flux to the cell size and particle count at the wall and the tendency of refined meshes to over-predict the peak heat flux when the particle count is insufficient. Following these studies, the minimum edge length is set to be 0.0025 m since it resulted in the least surface heat flux for the same particle cost among all the minimum edge lengths considered. The adaptation target from this case onward is changed from a node count to a cell count approach since an estimate for the total number of particles can be derived, and we can employ at least 20 particles per cell, on average, for the intermediate mesh iterations.

Table 3.5 Convergence of the mesh adaptation algorithm for the flow of Argon over a 2D cylinder (case A)

	Node count	Facet count	Cell count
Unstructured adapted mesh			
cycle 1 (initial mesh)	25,732	51,460	75,630
cycle 2	24,252	38,878	83,749
cycle 3	24,095	38,070	84,876
cycle 4	23,846	37,756	84,400
cycle 5	23,874	37,796	84,565
cycle 6 (Fig. 3.115)	**23,801**	**37,698**	**84,487**

Table 3.6 Convergence of the mesh adaptation algorithm for the flow of Argon over a 2D cylinder (case B)

	Node count	Facet count	Cell count
Unstructured adapted mesh			
cycle 1 (initial mesh)	25,732	51,460	75,630
cycle 2	24,568	39,726	84,576
cycle 3	24,081	38,052	84,805
cycle 4	23,834	37,678	84,170
cycle 5	23,767	37,530	84,166
cycle 6 (Fig. 3.115)	**23,768**	**37,634**	**84,080**

Hybrid masks for the structured mesh simulations from Fig. 3.74 are presented again, along with the masks for the unstructured mesh simulations of case B in Fig. 3.116. The structured mesh masks in Fig. 3.116a show a castellated pattern along the shock and the wake, and these boundaries are smoother in the adapted unstructured mesh results in Fig. 3.116b due to mesh adaptation. The masks for the initial unstructured mesh in Fig. 3.116a are of poor quality and are handled robustly by the hybrid solver. Similar to the leading-edge results, when the adapted mesh in Fig. 3.115 is compared against the hybrid masks in Fig. 3.116b, it would seem that refined cells occur in DSMC regions, and the cell sizes in the NS regions are coarser around the shock and boundary layer. The shock region delineated by both the Hessian of the set of multiphysics adaptation scalars and by $Kn_{\max}$ is of similar thickness. This becomes more evident when an enlarged section of the shock

is examined in Fig. 3.116b. In the literature, multigrid setups employing separate structured DSMC and NS meshes [47] have been built where the DSMC mesh is generated by refining selected cells of the coarser NS mesh and ensuring that the resulting DSMC cells have a characteristic length smaller than the local mfp. In contrast, the unstructured mesh of case B shows cell sizes reducing from NS to DSMC zones organically, indicating that a single adapted unstructured mesh can perform the functions of two structured meshes while guaranteeing good collision cell size in the DSMC regions. Better alignment of the masks and the mesh is possible by employing an evolving interface setup.

Contours of Mach number, temperature, and density from the adapted meshes of Fig. 3.115 are presented in Fig. 3.117-3.119. These contours, along with those of velocity and pressure are better captured on the adapted meshes than on the initial mesh, with a good representation of the steep gradients. The adapted hybrid contours compare well against the adapted DSMC contours. Contours of mcs/mfp for the initial and adapted meshes of cases A and B are shown in Fig. 3.120, and maximum cut-off values are chosen for better visualization. The NS region in case B is assigned an mcs/mfp of zero. The maximum mcs/mfp for the initial and adapted case A meshes is around 7 at the stagnation point, and this is due to the choice of a large minimum edge length. Overall, both the adapted meshes reduce the mcs/mfp ratio in the stagnation region due to a better distribution of cells, and a well-defined shock region is obtained (with an mcs/mfp ratio lower than that of the initial mesh). The freestream mcs/mfp for the adapted DSMC mesh (case A) is around 1, which indicates that the sub-cell method is working effectively. The larger mcs/mfp values in the wake region for the adapted meshes indicate that the mesh optimization methodology is coarsening this lower-density region as needed to balance the error across the domain. The mcs/mfp distribution of the adapted hybrid simulation in Fig. 3.120c is similar to the adapted full DSMC result in Fig. 3.120b since both the hybrid and DSMC adaptations use the same min/max edge length constraints and adaptation scalars. This shows that the DSMC region mesh of the adapted hybrid simulation is of good quality.

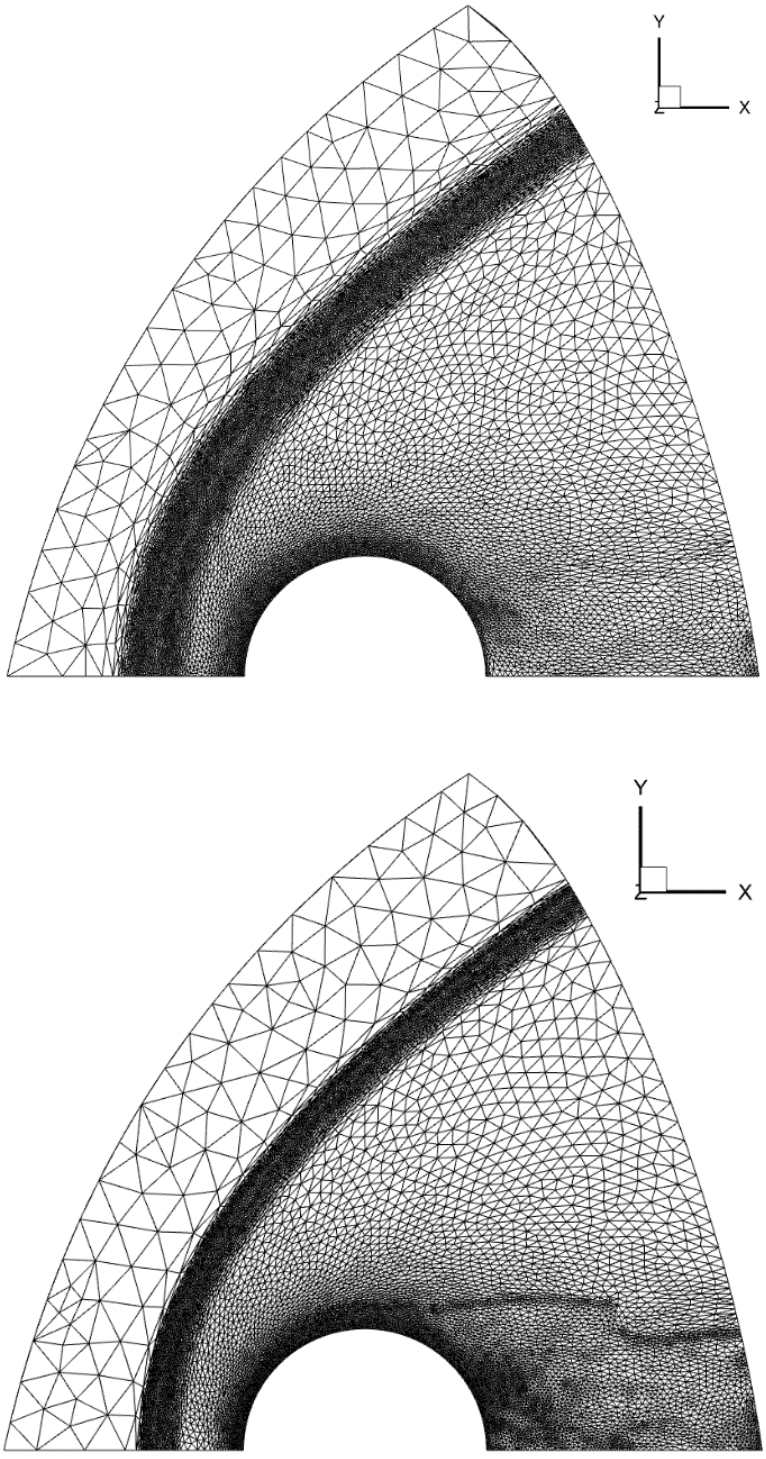

Fig. 3.115 Final adapted meshes for case A (top) and case B (bottom) after 6 optimization cycles for the flow of Argon over a 2D cylinder. (Mach 10, Knudsen 0.01)

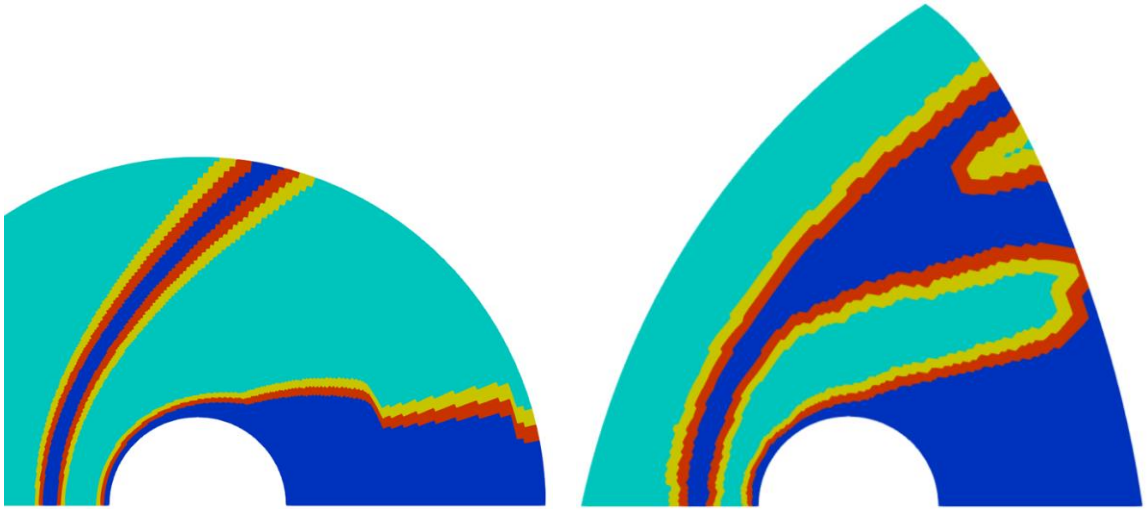

(a) Structured mesh (left) initial unstructured mesh (case B) (right)

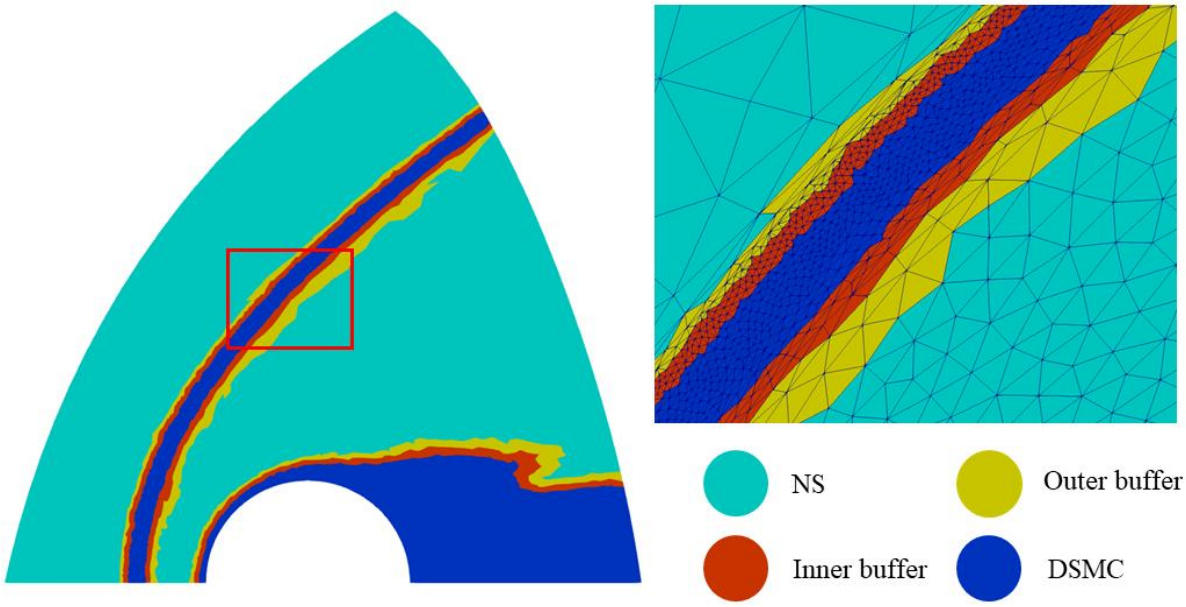

(b) Adapted unstructured mesh (case B)

Fig. 3.116 Hybrid masks for the flow of Argon over a 2D cylinder. (Mach 10, Knudsen 0.01)

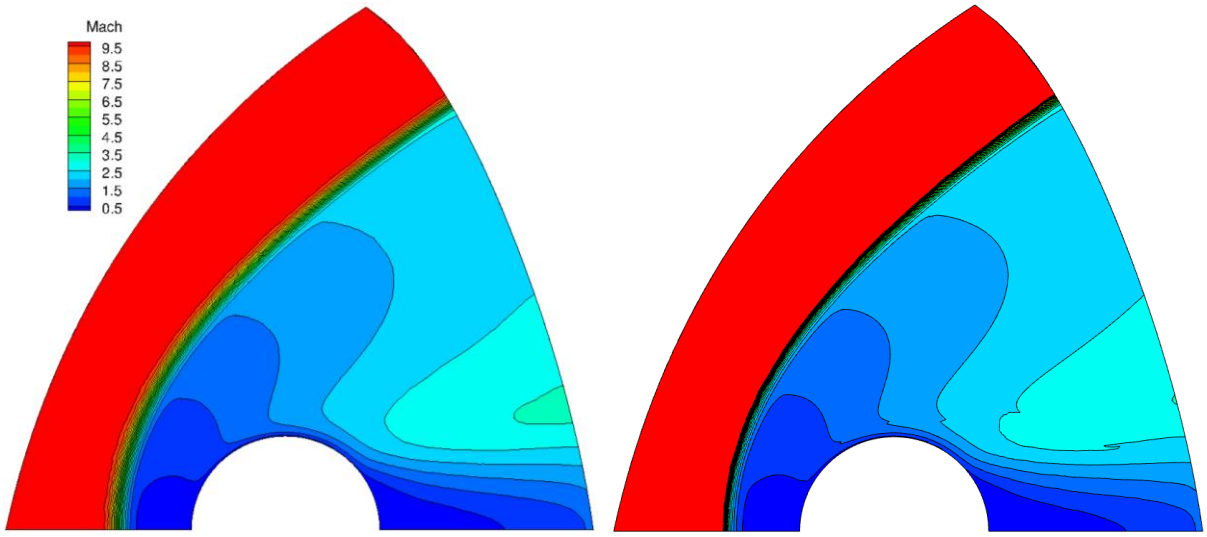

Fig. 3.117 Mach contours of the adapted meshes of case A (left) and case B (right) for the flow of Argon over a 2D cylinder. (Mach 10, Knudsen 0.01)

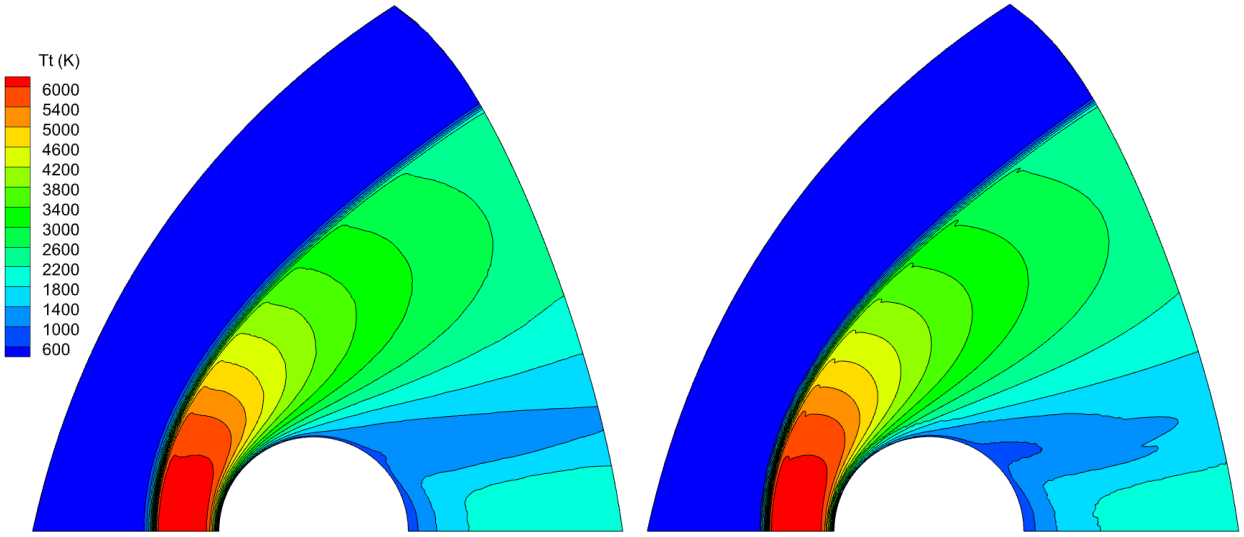

Fig. 3.118 Contours of translational temperature of the adapted meshes of case A (left) and case B (right) for the flow of Argon over a 2D cylinder. (Mach 10, Knudsen 0.01)

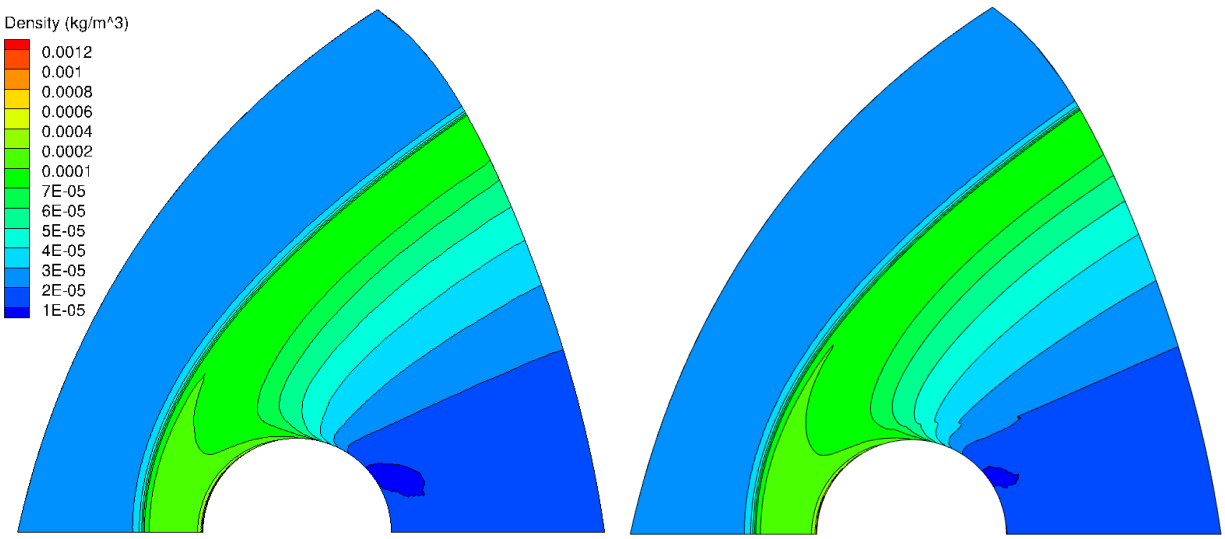

Fig. 3.119 Contours of density of the adapted meshes of case A (left) and case B (right) for the flow of Argon over a 2D cylinder. (Mach 10, Knudsen 0.01)

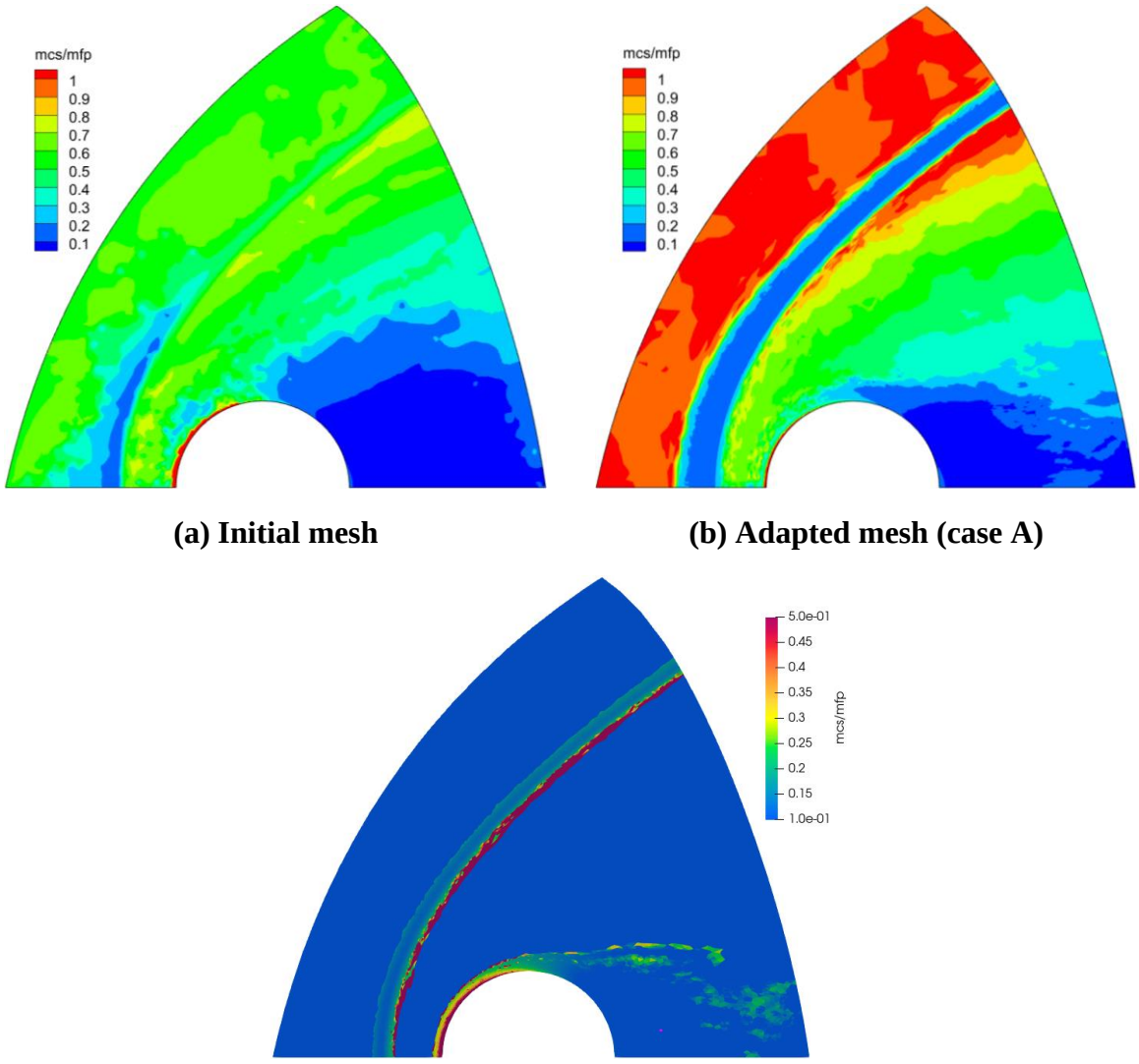

(a) Initial mesh **(b) Adapted mesh (case A)**

(c) Adapted mesh (case B)

Fig. 3.120 Contours of mcs/mfp for the flow of Argon over a 2D cylinder on the initial and adapted meshes. (Mach 10, Knudsen 0.01)

Figure. 3.121 presents the surface heat flux and shear stress distributions along the cylinder for the full DSMC solutions on the structured mesh, case A, and hybrid solutions from case B. The hybrid heat flux compares well against both DSMC simulations but underpredicts the value with an error of 5% at the stagnation point. As discussed, this is because the NS-DSMC interface near the wall is located too close to the wall, and an evolving hybrid interface setup will remedy this easily. To confirm, the threshold $Kn_{\max}$ is set to 0.025, and a hybrid simulation is run on the adapted mesh. The resulting stagnation point heat flux presents a 1.3% error when compared to the structured mesh results. The adapted full DSMC heat flux (case A) presents a 4.75% error against the

structured mesh and shows some scatter, and the shear stress compares well for all three simulations. The scatter in the heat flux and shear stress plots shown in cases A and B is due to an insufficient number of particles used by both solvers. Fig. 3.122 shows the temperature along the stagnation line for the structured mesh, case A, and case B. Good agreement is observed between all three solvers, validating the mesh optimization approach for both DSMC and hybrid NS-DSMC.

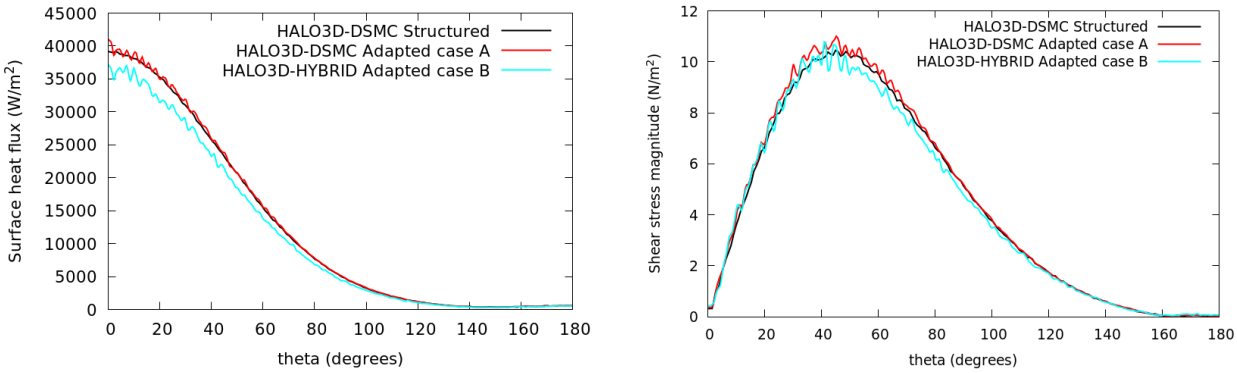

Fig. 3.121 Surface heat flux (left) and shear stress (right) for the flow of Argon over a 2D cylinder. (Mach 10, Knudsen 0.01)

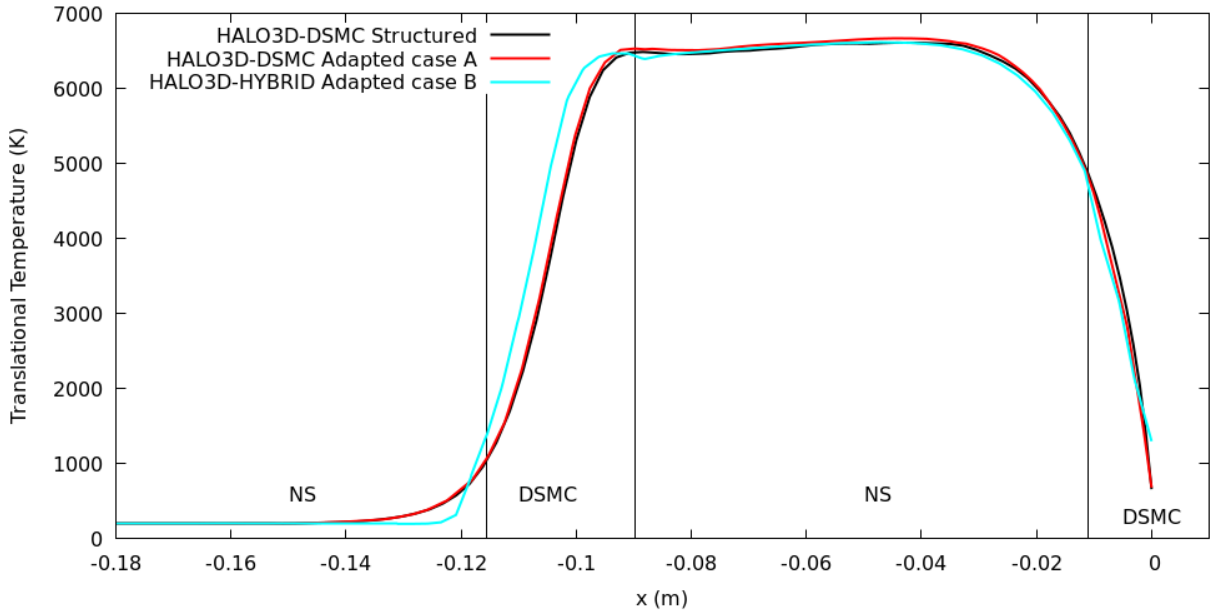

Fig. 3.122 Translational temperature along the stagnation line for the flow of Argon over a 2D cylinder. (Mach 10, Knudsen 0.01)

Contours of the error estimate for the initial and adapted meshes of cases A and B are illustrated in Fig. 3.123 and 3.124, where the error on the initial meshes is large in the shock and boundary layer regions, and the error in the shock region is maximum near the top of the domain where the irregularities in the solution fields are the greatest. The adapted meshes display a lower error distribution in the shock and boundary layer, indicating that the sampling mesh generated by OptiGrid captures the solution better than the initial mesh. Along with the leading-edge simulations, these results indicate that using a single error estimator to quantify solution error in both NS and DSMC regions is possible. This ensures that the standards for evaluating solution quality are the same, irrespective of the source of the solutions and that the conditions for mesh deformation are preserved between NS and DSMC regions. The distribution of the percentage of edges in Fig. 3.125 shows that a considerable number of edges at higher error in the initial mesh are treated to produce a lower maximum error for the adapted mesh for cases A and B. The adapted meshes collect most of the edges under a single peak, thus indicating that the error estimate is being equi-distributed.

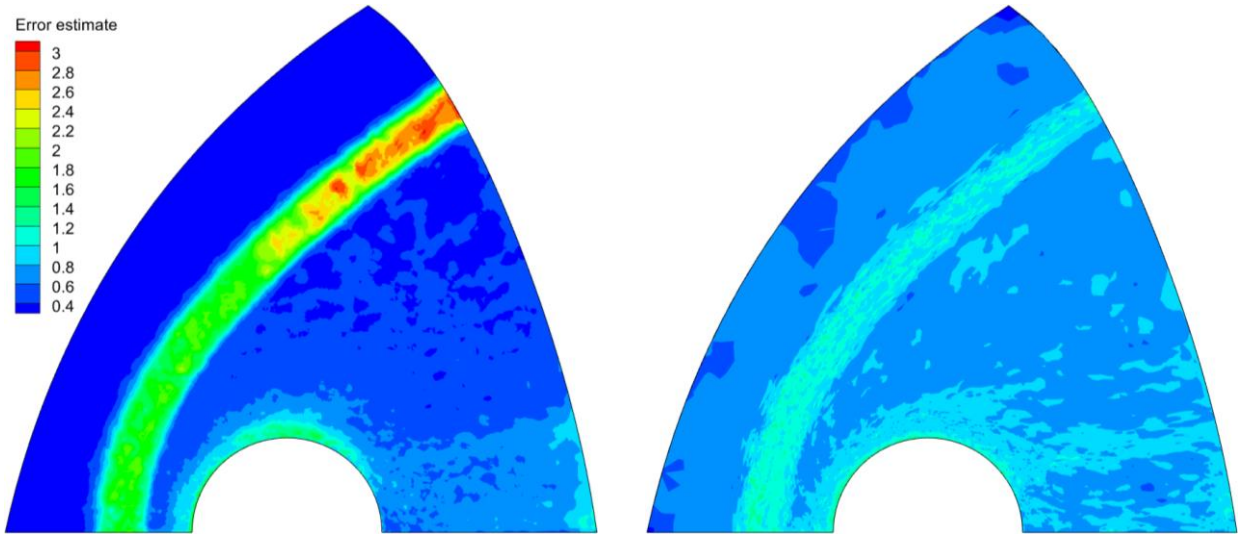

Fig. 3.123 Contours of the error estimate for the initial (left) and adapted (right) meshes for the flow of Argon over a 2D cylinder (case A). (Mach 10, Knudsen 0.01)

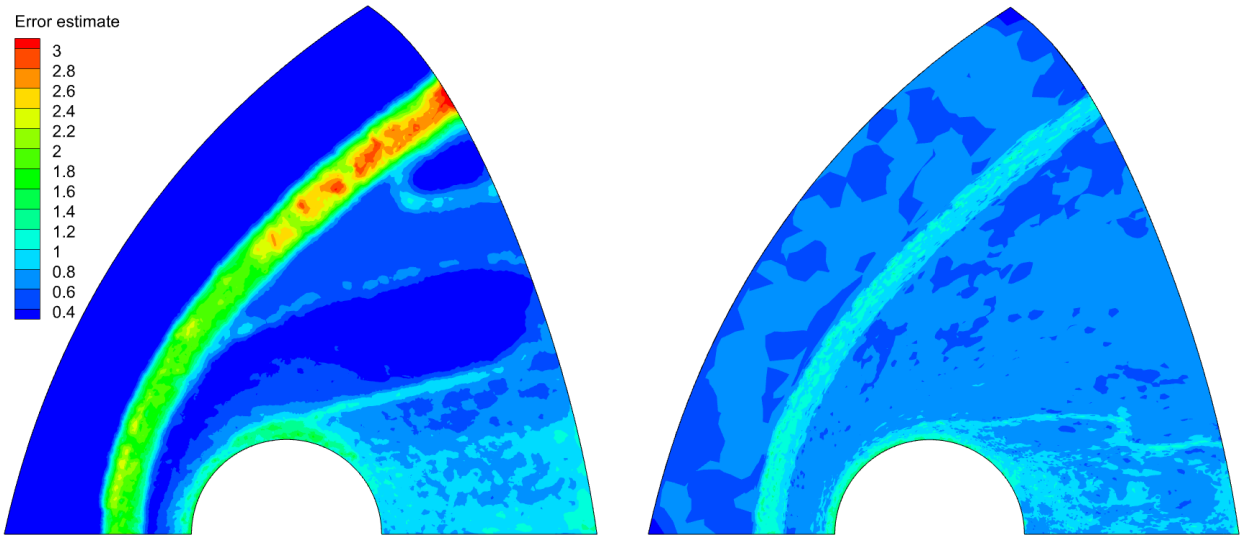

Fig. 3.124 Contours of the error estimate for the initial (left) and adapted (right) meshes for the flow of Argon over a 2D cylinder (case B). (Mach 10, Knudsen 0.01)

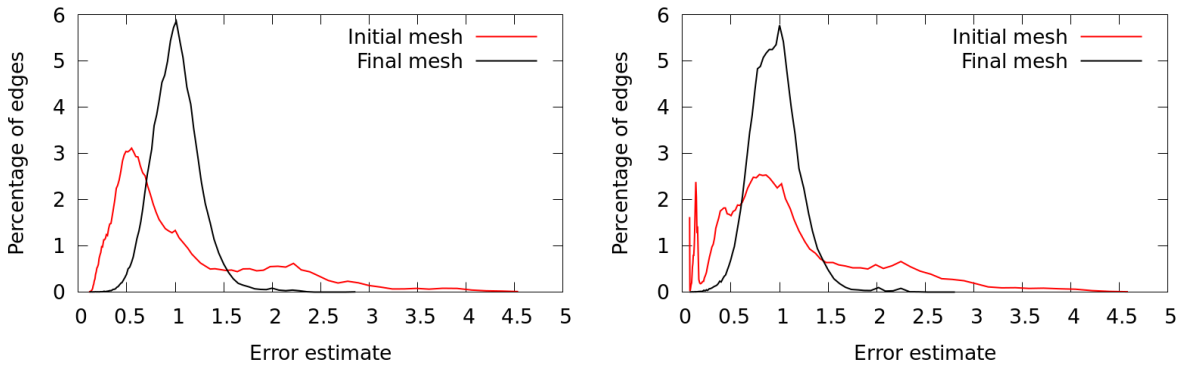

Fig. 3.125 Edge distributions for the initial and adapted meshes of case A (left) and case B (right) for the flow of Argon over a 2D cylinder. (Mach 10, Knudsen 0.01)

3.3.3 Reacting Nitrogen Mixture Flow over 2D Cylinder (Mach 8.34, Knudsen 0.026)

This test case considers the full DSMC flow of a reacting mixture of N_2 and N over a 0.3048 m diameter cylinder to explore the use of species mass fractions as adaptation scalars. The domain geometry and boundary conditions are similar to the illustration in Fig. 3.114. Hybrid simulations are not considered here due to the lack of consistent thermal non-equilibrium models. The freestream pressure, temperature, and x-velocity are 0.58635 N/m^2, 200 K, and 2883 m/s. The freestream mole fractions are 0.5 for both N_2 and N, and the diffuse wall temperature is 500 K. The freestream Mach and Knudsen (based on the cylinder diameter) numbers are 8.34 and 0.026,

respectively, and the time step is 1×10^{-7} seconds. The reactions and reaction parameters are provided in Appendix B. Two adapted meshes are generated with these two adaptation scalar sets: case A with $\{ X_{\mathrm{N}}, X_{\mathrm{N}_2} \}$ and case B with $\{ \rho, U_{\mathrm{x}}, U_{\mathrm{y}}, T_{\mathrm{t}}, T_{\mathrm{r}}, p, Ma, X_{\mathrm{N}}, X_{\mathrm{N}_2} \}$ where X is the species mole fraction. Vibrational temperature is not considered as an adaptation scalar because it causes an extraneous refinement of the freestream, as will become clear in the flow field contours that follow. The mesh adaptation constraints for both case A and B are: (i) a minimum edge length of 0.002 m (equal to ~6 times the minimum mfp) (ii) a maximum edge length of 0.0467 m (equal to ~6 times the freestream mfp) and (iii) a target cell count of 113000. Around 3.3 million particles are present at steady-state for each mesh iteration for both adaptation scalar sets. The convergence of the mesh adaptation algorithm for case B is given in Table 3.7, and the two adapted meshes are shown in Fig. 3.126 and 3.127. When mole fractions are used as adaptation scalars, the shock, boundary layer, and wake regions undergo refinement. The refined shock and boundary layer regions are thinner for case A than for case B. For case A, the mesh is refined only in those areas of the shock and boundary layer where a change in either species' concentration occurs. In case B, the thicker shock region is attributed to multiple adaptation scalars that reinforce the shock and boundary layer regions to capture these flow features fully. None of the adaptation scalars in Section 3.3.2 caused the refinement of the wake, rather, some coarsening of the wake was seen, which along with Fig. 3.126, leads to the conclusion that any refinement of the wake region in Fig. 3.127 is solely due to the addition of mole fractions as adaptation scalars. When Fig. 3.126 and 3.127 are compared, it can be deduced that the use of multiple scalars that reinforce the same region, in this case the shock, causes the optimization algorithm to preferentially refine the shock region over lesser reinforced regions such as the wake.

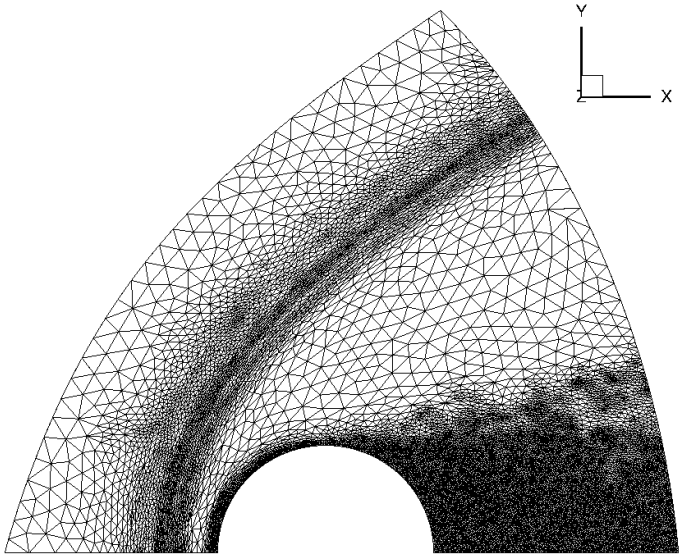

Fig. 3.126 Final adapted mesh for case A, where $\{ X_{\mathrm{N}}, X_{\mathrm{N_2}} \}$ is the adaptation scalar set for the flow of a Nitrogen mixture over a 2D cylinder. (Mach 8.34, Knudsen 0.026)

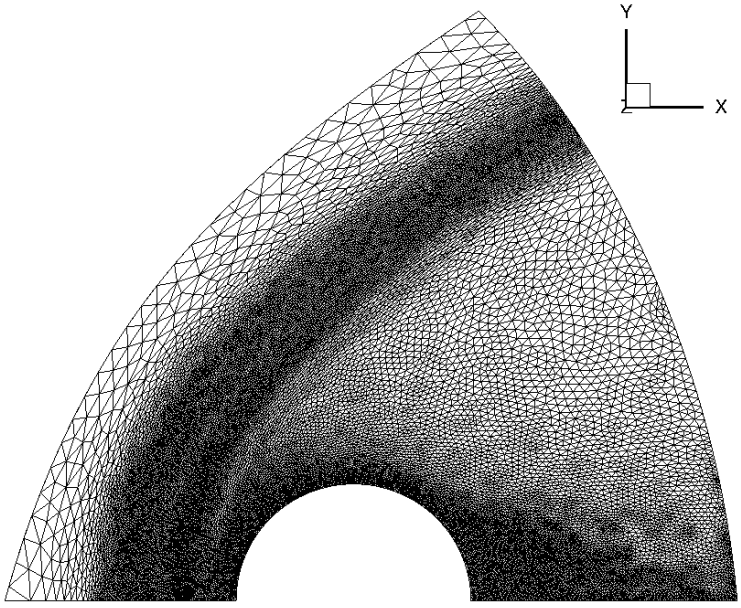

Fig. 3.127 Final adapted mesh for case B, where $\{ \rho, U_{\mathrm{x}}, U_{\mathrm{y}}, T_{\mathrm{t}}, T_{\mathrm{r}}, p, Ma, X_{\mathrm{N}}, X_{\mathrm{N_2}} \}$ is the adaptation scalar set for the flow of a Nitrogen mixture over a 2D cylinder. (Mach 8.34, Knudsen 0.026)

Table 3.7 Convergence of the mesh adaptation algorithm for case B involving the flow of a Nitrogen mixture over a 2D cylinder

	Node count	Facet count	Cell count
Unstructured adapted mesh			
cycle 1 (initial mesh)	38,462	76,920	113,646
cycle 2	35,965	70,982	108,104
cycle 3	37,666	74,554	112,843
cycle 4	38,518	76,426	115,213
cycle 5	38,898	77,150	116,438
cycle 6	39,167	77,710	117,198
cycle 7	39,232	77,880	117,380
cycle 8 (Fig. 3.127)	**39,330**	**77,994**	**117,724**

Contours of Mach number, vibrational temperature, and species mass fractions of case B are provided in Fig. 3.128 and 3.129. The Mach contours feature a shock thicker than for Section. 3.3.2 due to the larger freestream Knudsen number. Flow field variables such as density, pressure, velocities, and temperatures are better captured on the adapted mesh, with smooth contours being visualized for these variables. Some statistical scatter is found in the wake region, and this is attributed to the low particle counts in this region coupled with a refined mesh in the wake that generally demands more particles. The vibrational temperature field also shows statistical scatter in the freestream, which has been noted before in the literature [107]. This scatter, like the one in the wake, registers as increased error and prompts the mesh optimizer to refine these regions. For this reason, the vibrational temperature is not used as an adaptation scalar. Contours of mcs/mfp for the initial and adapted meshes of case B are presented in Fig. 3.130 where refinement in the shock results in a decreased mcs/mfp in this region. Again, the freestream mcs/mfp for adapted mesh is ~1, while that at the stagnation point is ~5.6. Plots of heat flux and shear stress obtained on the adapted mesh of case B are shown in Fig. 3.131 where lesser scatter than in Section 3.3.2 can be observed thanks to the freestream Knudsen number being larger, which is less punishing in terms of particle count.

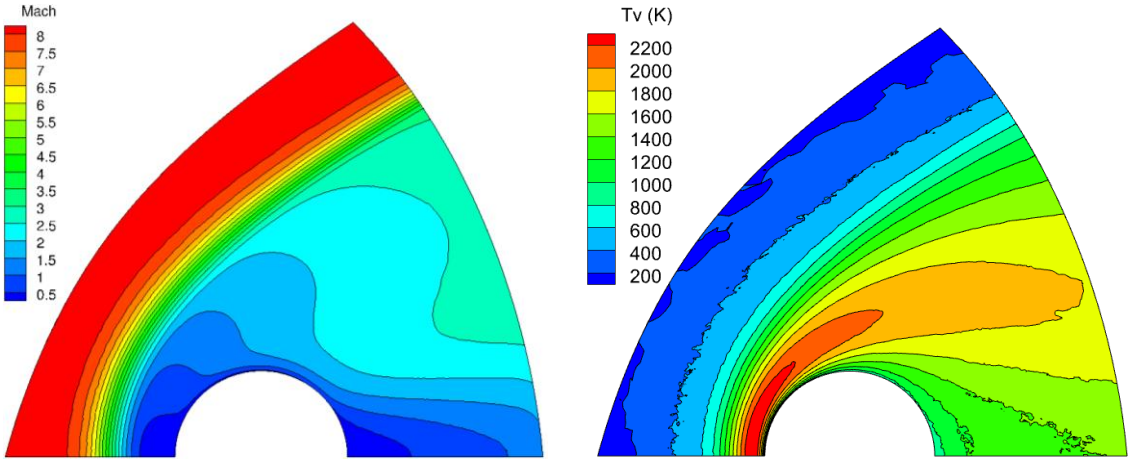

Fig. 3.128 Mach number (left) and vibrational temperature (right) contours of the adapted mesh (case B) for the flow of a Nitrogen mixture over a 2D cylinder. (Mach 8.34, Knudsen 0.026)

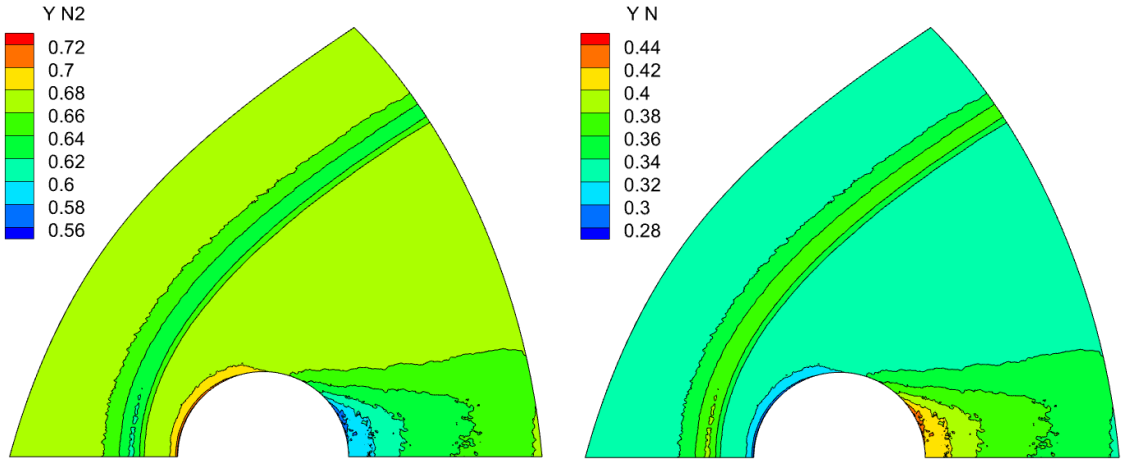

Fig. 3.129 N2 (left) and N (right) mass fraction contours of the adapted mesh (case B) for the flow of a Nitrogen mixture over a 2D cylinder. (Mach 8.34, Knudsen 0.026)

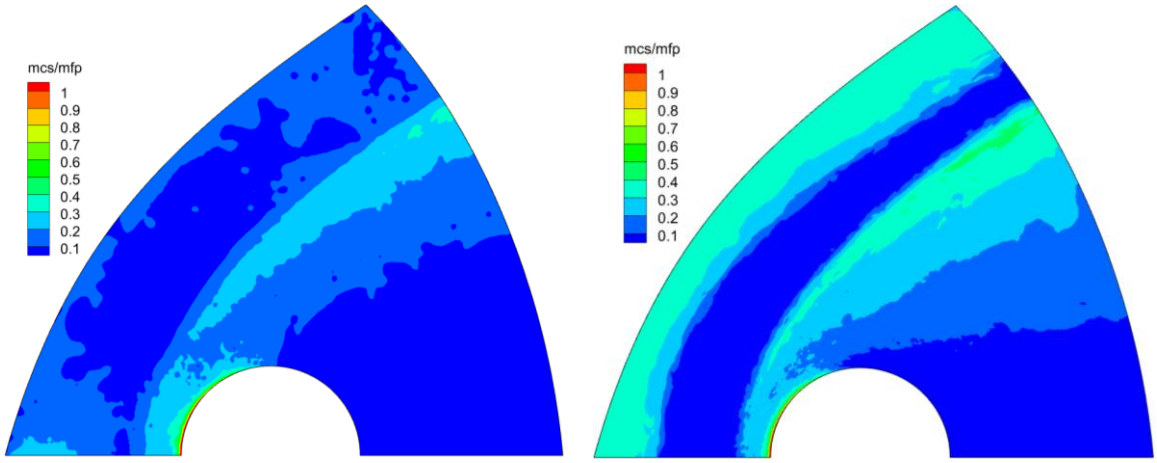

Fig. 3.130 mcs/mfp for the initial (left) and adapted (right) meshes (case B) for the flow of a Nitrogen mixture over a 2D cylinder. (Mach 8.34, Knudsen 0.026)

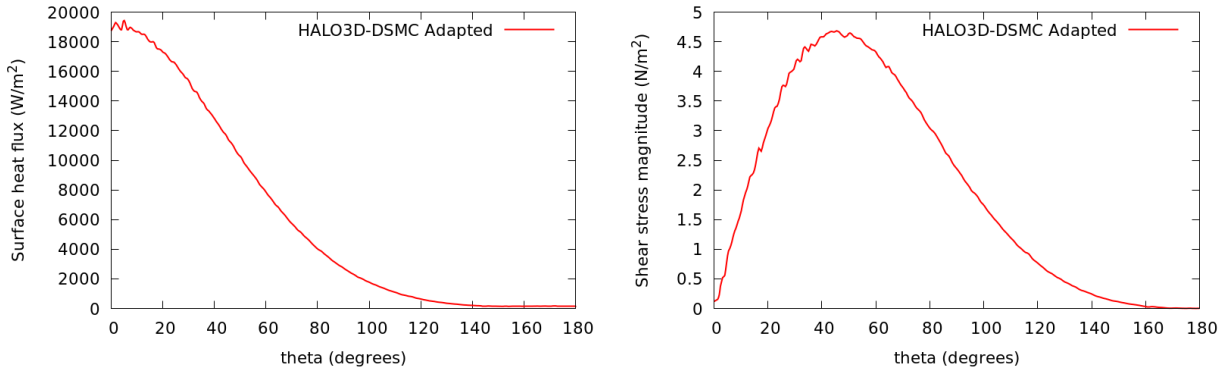

Fig. 3.131 Surface heat flux (left) and shear stress (right) of the adapted mesh (case B) for the flow of a Nitrogen mixture over a 2D cylinder. (Mach 8.34, Knudsen 0.026)

Contour plots of the error estimate for both cases A and B are presented in Fig. 3.132 and 3.133 In both cases, the initial mesh displays large errors in the shock region, which are rectified through mesh adaptation. The error estimate contours also showcase the equi-distribution of the error estimate throughout the domain. This is also seen in the line plots of edge distribution shown in Fig. 3.134, where a sharp singular peak exists for the adapted meshes of both cases A and B. Some noise exists in the error contours for the adapted meshes in the wake regions. This is because of the wake's refinement and the already low particle count usually found in this region. While a better resolution of the wake is possible by employing much larger particle counts for each mesh iteration, the goal of the present study is to employ as few particles as possible for the intermediate mesh iterations. The final adapted mesh is reserved for large particle count runs as necessary.

Therefore, it is advocated to use the several adaptation scalars already established instead of the mass fractions. Since the mass fractions bring about the refinement of the shock and wake region, and there already exist several other variables that reinforce the shock, and the refinement of the wake is not wanted, the mass fractions need not be considered as adaptation scalars.

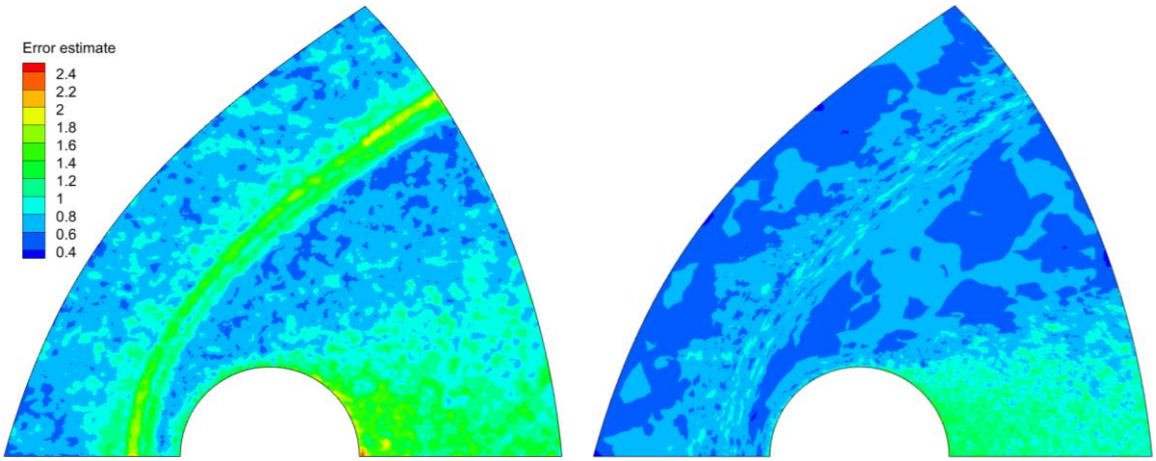

Fig. 3.132 Error estimate on the initial (left) and adapted (right) meshes for the flow of a Nitrogen mixture over a 2D cylinder (case A). (Mach 8.34, Knudsen 0.026)

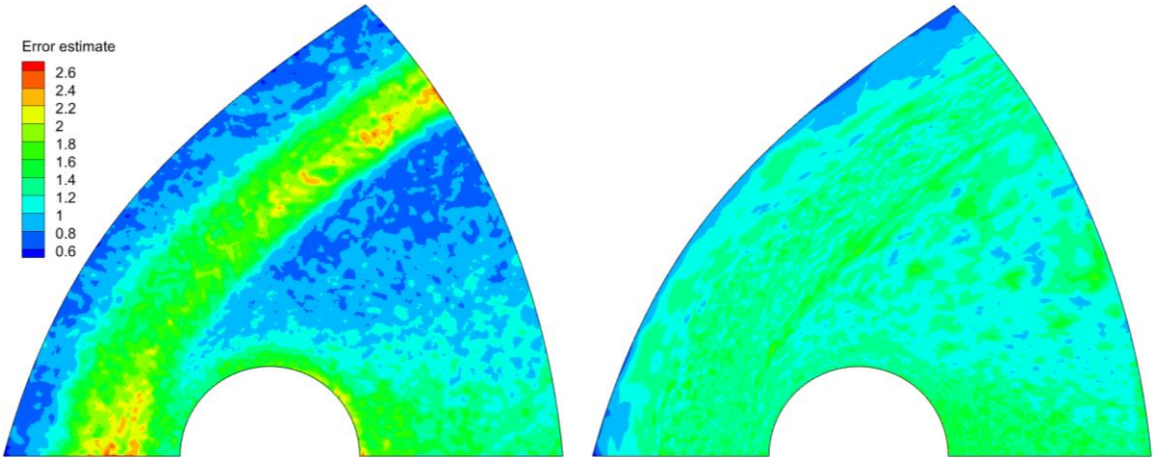

Fig. 3.133 Error estimate on the initial (left) and adapted (right) meshes for the flow of a Nitrogen mixture over a 2D cylinder (case B). (Mach 8.34, Knudsen 0.026)

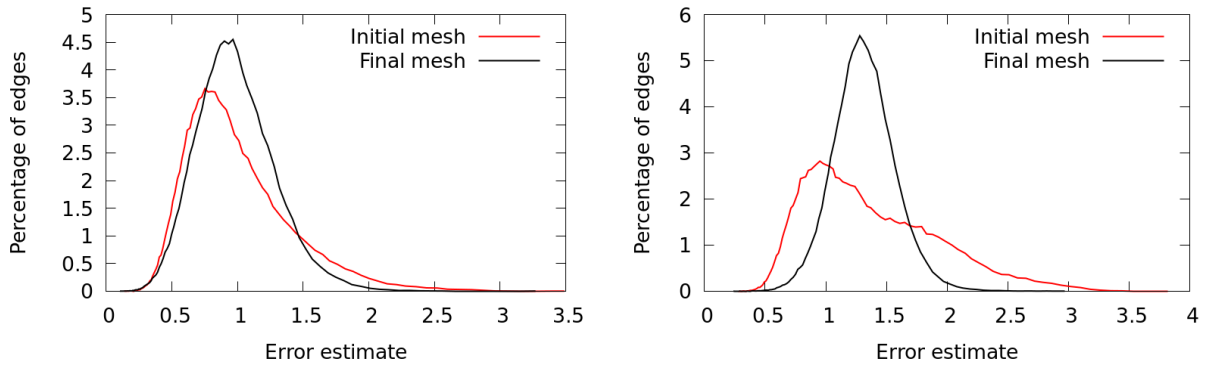

Fig. 3.134 Edge distributions for the initial and adapted meshes for case A (left) and case B (right) for the flow of a Nitrogen mixture over a 2D cylinder. (Mach 8.34, Knudsen 0.026)

3.3.4 Argon Flow over 3D Flat-Nosed Cylinder (Mach 5.37, Knudsen 0.047)

A 2D axisymmetric flow of Argon over a 0.02 m diameter flat-nosed cylinder has been simulated by Bird [9] and later modeled in the form of a 3D quarter-symmetry problem by Scanlon *et al.* [108]. This quarter-symmetry domain is used in this test case and is shown along with the boundary conditions in Fig. 3.135. The freestream conditions for Mach number, Knudsen number, pressure, temperature, and the *x*-component of velocity equal 5.37, 0.047, 1.381 Pa, 100 K, and 1000 m/s, respectively. Full DSMC mesh optimization is performed here since the Knudsen number is quite large for hybrid simulations. The diffuse wall temperature is 300 K, and the initial uniform mesh shown in Fig. 3.136a has cells sized to the freestream mfp. The equivalent number of simulated particles is 1.24×10^{10}, and the time step is 1.87×10^{-7} s. The set of adaptation scalars used for this problem is $\{ \rho, T_t, p, U_x, U_y, U_z, Ma \}$, and the optimization constraints given to OptiGrid are as follows: (i) a minimum edge length of 3.6×10^{-4} m (equal to 3 times the minimum mfp), (ii) a maximum edge length of 0.01 (equal to 3 times the maximum mfp), and (iii) a target cell count equal to 250,000. Fig. 3.136b shows the final adapted mesh, while the contours of Mach number for that mesh are presented in Fig. 3.137. Since the minimum edge length constraint is set based on the minimum mfp, the background mesh acts more as a collisional-sampling mesh with fewer sub-cells created per collision cell on average compared with the approach of Section 3.3.2. The convergence of the mesh adaptation algorithm is provided in Table 3.8.

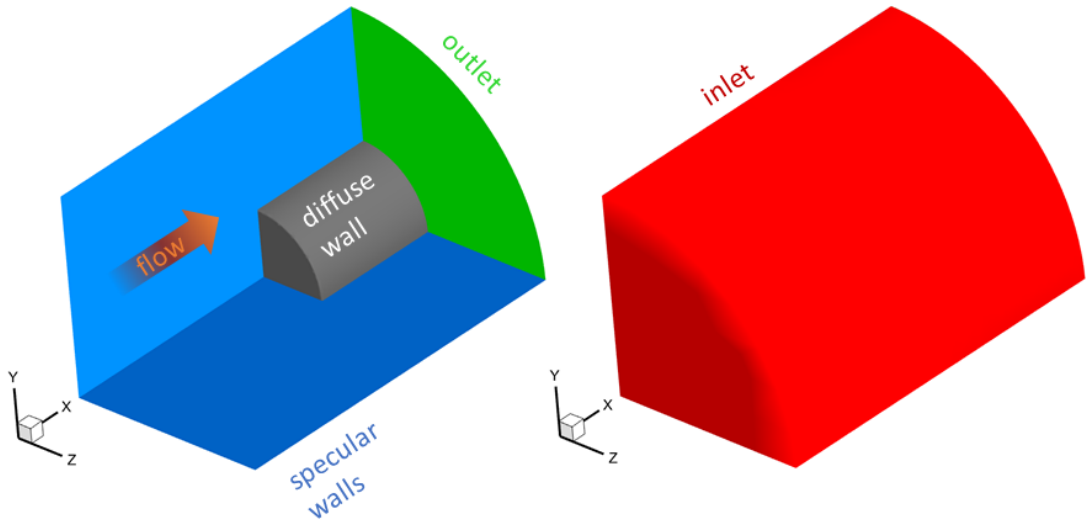

Fig. 3.135 Domain and boundary conditions for the hypersonic flow over a 3D flat-nosed cylinder

Table 3.8 Convergence of the mesh adaptation algorithm for the flow of Argon over a 3D flat-nosed cylinder

	Node count	Facet count	Cell count
Bird's 2D axisymmetric mesh [9]			4,800
Scanlon *et al.* [108]			275,000
Unstructured adapted mesh			
cycle 1 (initial mesh)	31,363	18,248	156,216
cycle 2	47,130	13,550	253,239
cycle 3	44,935	11,938	246,050
cycle 4	45,857	11,890	251,111
cycle 5	45,947	11,888	251,805
cycle 6 (Fig. 3.136b)	**46,002**	**11,908**	**252,061**

OptiGrid captures the relatively weaker gradients characteristic of larger Knudsen number flows, with mesh nodes in the near-wall region being better distributed when compared to the initial mesh, while the freestream region and area downstream near the outflow boundary are coarsened accordingly. Contours of non-dimensional density and temperature are presented in Fig. 3.138 and 3.139. Optimized mesh results show that fields are better resolved in the vicinity of the front face of the cylinder and in the shock layer, compared to initial mesh results. In addition, the final

adapted mesh contours are in good agreement with Bird's 2D axisymmetric results, whether that is in the stagnation region or around the corner.

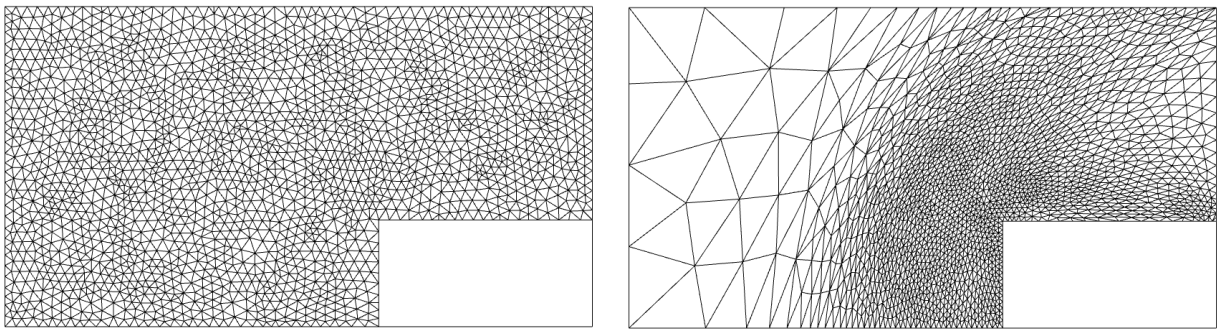

(a) Initial mesh

(b) Final adapted mesh after 6 optimization cycles

Fig. 3.136 Automatic mesh optimization for the flow of Argon over a 3D flat-nosed cylinder. (Mach 5.37, Knudsen 0.047)

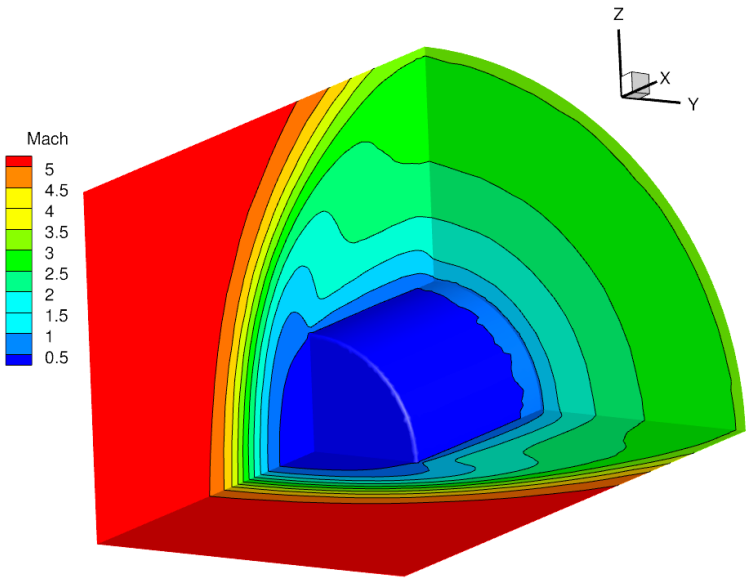

Fig. 3.137 Contours of Mach number for the flow of Argon over a 3D flat-nosed cylinder. (Mach 5.37, Knudsen 0.047)

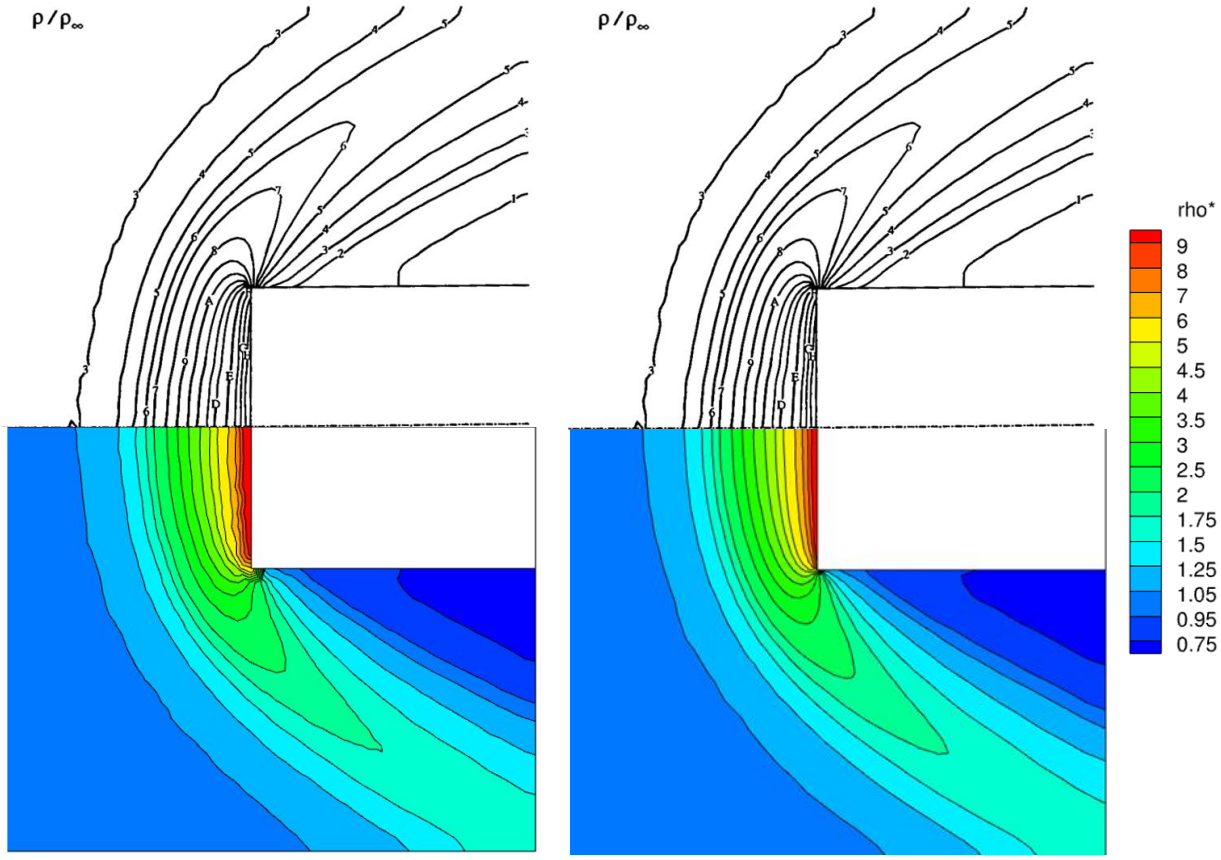

Fig. 3.138 Non-dimensional density contours for the initial (bottom-left) and optimized (bottom-right) meshes compared to Bird's solution (top) for the flow of Argon over a 3D flat-nosed cylinder. (Mach 5.37, Knudsen 0.047)

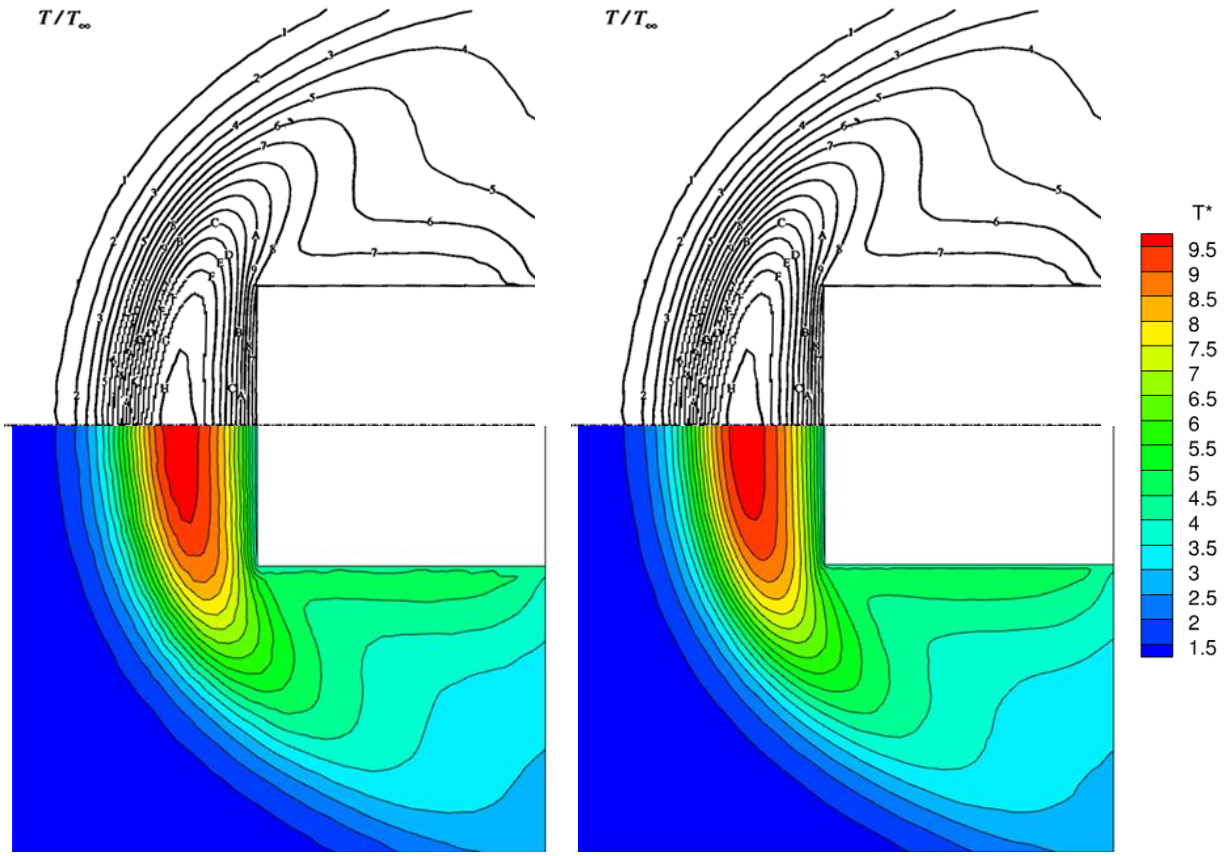

Fig. 3.139 Non-dimensional translational temperature contours for the initial (bottom-left) and optimized (bottom-right) meshes compared to Bird's solution (top) for the flow of Argon over a 3D flat-nosed cylinder. (Mach 5.37, Knudsen 0.047)

Fig. 3.140 illustrates the ratio of mcs to mfp for the initial mesh and the final adapted mesh. The maximum value of this ratio is 1.4 for the initial mesh and 0.6 for the adapted mesh, indicating that the mesh adaptation process generates a mesh better suited for DSMC. The region of large mcs/mfp at the front face of the cylinder seen in the results for the initial mesh is treated by mesh adaptation to produce a region of smoothly varying mcs/mfp. Also, the low mcs/mfp region in the bow shock is expanded and the shock is delineated because of the difference in cell size between the freestream and the rest of the domain.

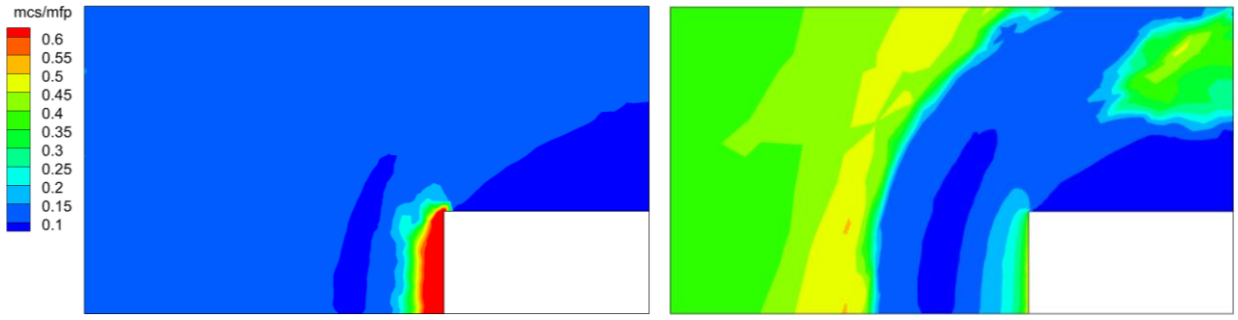

Fig. 3.140 Contours of mcs/mfp for the initial (left) and optimized (right) meshes for the flow of Argon over a 3D flat-nosed cylinder. (Mach 5.37, Knudsen 0.047)

The contours of the error estimate for the initial and adapted mesh are illustrated in Fig. 3.141. A thick, diffuse shock region can be discerned in the contours of the initial mesh indicating that errors are high in the shock. Since regions of the domain with a higher error are refined while regions with a lower error are coarsened, the resulting adapted mesh is refined near the front face, bow shock, and wall regions and coarsened in the freestream and wake regions. The contours of error for the adapted mesh are starkly different from those of the initial mesh and showcase OptiGrid's method of equi-distributing the error estimate well. This can also be observed in the plots of edge distribution shown in Fig. 3.142 where edges are collected under a single peak, irrespective of their size. Further, the plots indicate that a significant fraction of edges at higher error levels in the initial mesh have been treated through mesh adaptation.

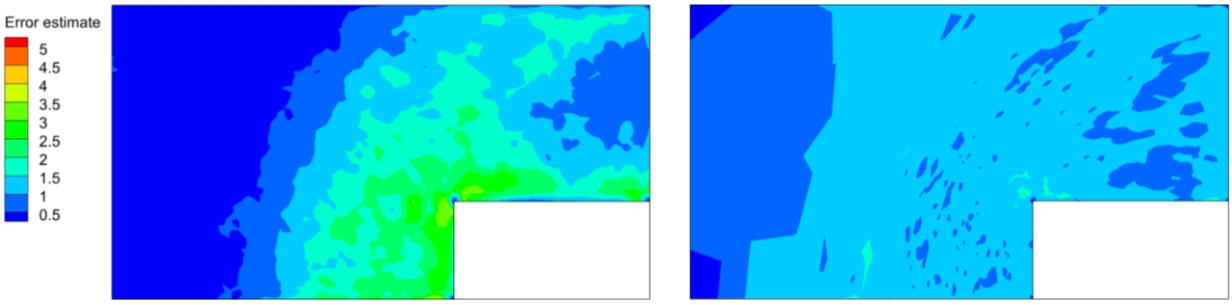

Fig. 3.141 Contours of error estimate for initial (left) and adapted (right) meshes for the flow of Argon over a 3D flat-nosed cylinder. (Mach 5.37, Knudsen 0.047)

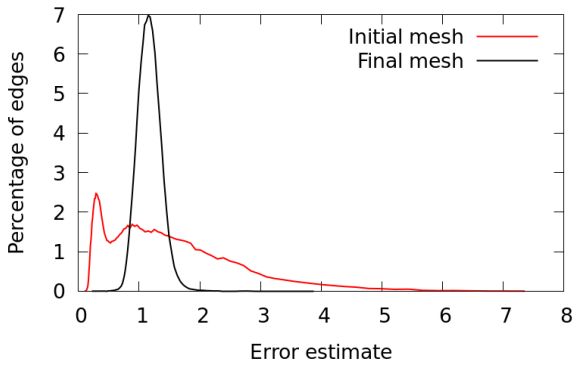

Fig. 3.142 Edge distributions of the initial and adapted meshes for the flow of Argon over a 3D flat-nosed cylinder. (Mach 5.37, Knudsen 0.047)

Chapter 4

Conclusions and Future Work

As part of the HALO3D project to build a multidisciplinary simulation tool for the design of hypersonic aircraft, rarefied flow modules and mesh optimization strategies are required to account for high altitude flow conditions, capture multiscale flow features, and better represent the flow solution. The HALO3D ensemble consists of an edge-based Finite Element NS hypersonic flow solver, HALO3D-NS, ablation and surface chemistry modules, magnetohydrodynamics modules, and the in-house solution-driven mesh optimizer, OptiGrid. The current work extends the domain of applicability of HALO3D to the rarefied regime through the development of a DSMC solver, HALO3D-DSMC, and a hybrid NS-DSMC framework, HALO3D-HYBRID. The thesis showcases the development and testing of the DSMC and hybrid solvers and their coupling with OptiGrid through several 2D/3D flow problems of varying thermochemical complexity.

Verification simulations conducted for the hypersonic corner, leading-edge, flat-plate and a reacting five-species air mixture flow over a 2D cylinder show that the modules comprising HALO3D-DSMC function effectively and produce accurate results. Surface quantities such as the heat transfer and shear stress coefficients and flow field contours are used for verification purposes where good agreement is observed between HALO3D-DSMC and reference solutions from DS2V, DS3V, MONACO, DAC, and dsmcFoam. The inverse distance-weighted interpolation is found to work well for converting the cell-based DSMC macroscopic data to a set of node-based fields for use in the hybrid algorithm and coupling with OptiGrid. The use of Finite Element shape functions to generate random positions for particles during initialization and at inlets is found to produce a good quality freestream in the full DSMC simulations and a good quality DSMC region in the hybrid simulations.

HALO3D-HYBRID employs HALO3D-NS and HALO3D-DSMC in appropriate areas of the domain, and full solutions from all three solvers are compared where the DSMC solution is taken as the reference. Verification simulations conducted for the leading-edge flows and 2D cylinders with Knudsen numbers ranging from 0.006 to 0.018 confirm the accuracy of HALO3D-HYBRID

and showcase the cost benefits obtained from the use of hybrid solvers as compared to full DSMC solvers. This loosely coupled approach is robust and can handle poor quality meshes and hybrid masks that are usually found in the initial stages of mesh adaptation. It is also less expensive than tightly coupled formulations. Consistent modeling of thermal non-equilibrium between the NS and DSMC solvers is necessary to obtain continuous and smooth temperature fields when strong vibrational non-equilibrium is present in the flow. Surface quantities such as shear stress, heat flux, surface density, and pressure agree well between the hybrid and DSMC codes, even in the presence of inconsistent thermal non-equilibrium modeling. Flow field contour plots also compare well between hybrid and DSMC solvers. These results show that the Finite Element Method can be effectively coupled with DSMC to tackle hypersonic flow problems at varying degrees of rarefaction.

The applications of OptiGrid with matrix-equation-based continuum flow solvers have been well documented, and this thesis provides, for the first time, an extension of its use to the rarefied regime. As such, the present work

- Contributes to the scarce body of unstructured mesh hybrid NS-DSMC and DSMC literature by investigating the generation of an unstructured not only adapted but optimized mesh obtained by the equi-distribution of the error estimate of a solution scalar throughout the domain.
- Shows the effects of different initial meshes, adaptation scalars, and optimization constraints on the final adapted mesh.
- Evaluates the effectiveness of OptiGrid in manipulating a collisional-sampling mesh to provide a good quality background mesh for DSMC.
- Showcases the merits of a single unstructured optimized mesh for hybrid NS-DSMC simulations.

Mesh adaptation computations have been carried out for flows with freestream Knudsen numbers ranging from 0.01 to 0.047. The leading-edge flow is used to investigate the effects of different adaptation scalars on the final adapted mesh. It is shown that density alone as an adaptation scalar generates a mesh that does not capture surface quantities such as heat flux and shear stress. The addition of velocity components in the scalar set greatly improves surface quantity predictions and mesh node distribution in the boundary layer, while a scalar set consisting of density, velocity

components, modal temperatures, pressure, and Mach number shines best for detached bow shock problems. Indeed, they are found to each reinforce salient flow features such as the shock, wake, and boundary layer, thus yielding a mesh that is better defined in these regions. Adapted meshes represent flow field variables better than the initial meshes for the 2D/3D cylinder simulations. OptiGrid's capability to capture the relatively weaker gradients in the rarefied regime is best portrayed at the largest Knudsen number for the Kn 0.047 Argon flow over a 3D flat-nosed cylinder. Observables such as surface heat flux, non-dimensional density, and temperature compare well against the literature. The adapted hybrid meshes are very similar to the adapted DSMC meshes, hence showcasing the solver-independence aspect of OptiGrid and indicating that the hybrid solver produces the same solution as the DSMC solver. The hybrid masks are very smooth for the adapted unstructured meshes in contrast with the structured mesh hybrid simulations where castellated patterns can be observed in the masks. It was also found that through mesh adaptation, a single unstructured mesh can be used to optimally discretize both NS and DSMC solutions where the NS region is composed of larger cells near the shock and boundary layer.

For the optimization constraints, different rules have been used to define the minimum and maximum edge lengths as a function of the mean free path. The best compromise is found when they are directly proportional to the minimum and maximum local mean free paths obtained on the initial grid, respectively. Two metrics are used to evaluate the mesh adaptation: the mcs/mfp (mean collision separation over the mean free path) and an edge-based error estimate computed from the Hessian of the adaptation scalars. Regions of high mcs/mfp did not affect the surface quantity measurements nor the flowfield comparisons for the leading-edge case, and when combined with a sub-celling technique, all three cylinder cases produced meshes that conform to good DSMC practice as indicated by the mcs/mfp field. The meshes in the DSMC regions of the hybrid mesh adaptation simulations are also of good quality since the mcs/mfp in these regions is lower than 1. Plots of the error estimate showed that adapted meshes can be generated with a global error equi-distributed over the domain, and the local error in salient flow features considerably lowered. The equi-distribution of error is observed for NS and DSMC regions as well during hybrid mesh adaptation. Consequently, these results show that OptiGrid is a user-independent, mesh-independent, solver-independent, and now, regime-independent mesh optimization tool.

Future work on the hybrid solver should focus on the development of adaptive hybrid interfaces, particle initialization routines that employ generalized Chapman-Enskog distribution functions, consistent thermal non-equilibrium modeling between the NS and DSMC solvers, tuned collision-specific collisional parameters, and code parallelization. Additionally, acceleration techniques for NS solver such as LU-SGS can be accommodated within the hybrid framework thanks to the loose coupling of the NS and DSMC modules.

For parallel computations, the hybrid masks can be used to ensure that the inter-processor boundaries overlay the NS-DSMC boundaries. In this manner, all hired processors can be made to work on the NS and DSMC zones sequentially with low idle times. Currently there is limited information on the principles to follow to distribute mesh elements between NS and DSMC zones for efficient parallel computations. The DSMC simulation time heavily depends on the number of particles, while the NS solution time depends on the mesh count. Nevertheless, minimizing the number of elements leads to a faster computation for both NS and DSMC solvers. With a sequential parallel strategy, the NS and DSMC region meshes could be decomposed for parallelization independently, according to separate criteria. The present work offers a way to distribute nodes/cells between NS and DSMC regions for a single unstructured mesh by equi-distributing an error estimate, thus ensuring accuracy. Code parallelization with such a mesh can be investigated since the NS and DSMC region meshes are already distinct from each other.

The use of multiple meshes is not uncommon in the DSMC and hybrid literature. Hence, future work for meshing could investigate the benefits of multiple unstructured meshes compared to a single unstructured adapted mesh. Independent meshes for the collision and sampling routines of DSMC as well as for NS can be considered because such a setup presents the most freedom for the mesh adaptation of hybrid simulations since the three meshes can be adapted with independent constraints and even adaptation scalars. These benefits come with increased computational and memory costs when compared to a method employing a single adapted mesh.

Development of the hybrid algorithm for unsteady flow simulations can also be considered. There exists an unsteady version of the NS solver within HALO3D that obtains time-accuracy with an implicit Euler scheme. The DSMC solver is already time-accurate but would require the construction of an ensemble-averaging setup similar to the one used to parallelize the sampling stage. Several ensembles would need to be run with the resulting transient hybrid solver expected

to be much more expensive than the steady-state algorithm. The NS-DSMC interface could be recalculated based on the new $Kn_{\max}$ distribution at every outer step.

References

[1] P.J. Erbland, “Current and Near-Term RLV/Hypersonic Vehicle Programs,” RTO-AVT Lecture Series, RTO-EN-AVT-116, 2004.

[2] Zhang, W., Habashi, W. G., Baruzzi, G. S., and Salah, N. B., “Edge-Based Finite Element Formulation of Magnetohydrodynamics at High Mach Numbers,” *International Journal of Computational Fluid Dynamics*, Vol. 35, No. 5, 2021, pp. 349–372.
doi: 10.1080/10618562.2021.1929938

[3] Liu, C., Zhu, Y., and Xu, K., “Unified Gas-Kinetic Wave-Particle Methods I: Continuum and Rarefied Gas Flow,” *Journal of Computational Physics*, Vol. 401, 2020, p. 108977.
doi: 10.1016/j.jcp.2019.108977

[4] Chen, S., Xu, K., Lee, C., and Cai, Q., “A Unified Gas Kinetic Scheme with Moving Mesh and Velocity Space Adaptation,” *Journal of Computational Physics*, Vol. 231, No. 20, 2012, pp. 6643-6664.
doi: 10.1016/j.jcp.2012.05.019

[5] Li, W., Liu, C., Zhu, Y., Zhang, J., and Xu, K., “Unified Gas-Kinetic Wave-Particle Methods III: Multiscale Photon Transport,” *Journal of Computational Physics*, Vol. 408, 2020, p. 109280.
doi: 10.1016/j.jcp.2020.109280

[6] Liu, C., and Xu, K., “Unified Gas-Kinetic Wave-Particle Methods IV: Multi-Species Gas Mixture and Plasma Transport,” *Advances in Aerodynamics*, Vol. 3, No. 1, 2021, pp. 1-31.
doi: 10.1186/s42774-021-00062-1

[7] Bird, G. A., “Approach to Translational Equilibrium in a Rigid Sphere Gas,” *Physics of Fluids*, Vol. 6, No. 10, 1963, pp. 1518-1519.
doi: 10.1063/1.1710976

[8] Bird, G. A., *Molecular Gas Dynamics*, Clarendon Press, Oxford, UK, 1976.

[9] Bird, G. A., *Molecular Gas Dynamics and the Direct Simulation of Gas Flows*, Clarendon Press, Oxford, UK, 1994.

[10] Tumuklu, O., Theofilis, V., and Levin, D. A., "On the Unsteadiness of Shock–Laminar Boundary Layer Interactions of Hypersonic Flows over a Double Cone," *Physics of Fluids*, Vol. 30, No. 10, 2018, p. 106111
doi: 10.1063/1.5047791

[11] Mahdavi, A. M., and Roohi, E., "Investigation of Cold-to-Hot Transfer and Thermal Separation Zone Through Nano Step Geometries," *Physics of Fluids*, Vol. 27, No. 7, 2015, p. 072002.
doi: 10.1063/1.4927069

[12] Wang, P., Su, W., and Zhang, Y., "Oscillatory Rarefied Gas Flow Inside a Three Dimensional Rectangular Cavity," *Physics of Fluids*, Vol. 30, No. 10, 2018, p. 102002.
doi: 10.1063/1.5052253

[13] Gallis, M. A., Koehler, T. P., Torczynski, J. R., and Plimpton, S. J., "Direct Simulation Monte Carlo Investigation of the Richtmyer-Meshkov Instability," *Physics of Fluids*, Vol. 27, No. 8, 2015, p. 084105.
doi: 10.1063/1.4928338

[14] Gallis, M. A., Bitter, N. P., Koehler, T. P., Torczynski, J. R., Plimpton, S. J., and Papadakis, G., "Molecular-Level Simulations of Turbulence and its Decay," *Physical Review Letters*, Vol. 118, No. 6, 2017, p. 064501.
doi: 10.1103/PhysRevLett.118.064501

[15] Wagner, W., "A Convergence Proof for Bird's Direct Simulation Monte Carlo Method for the Boltzmann Equation," *Journal of Statistical Physics*, Vol. 66, No. 3, 1992, pp. 1011-1044.
doi: 10.1007/BF01055714

[16] Bird, G. A., "Sophisticated DSMC," *DSMC 07 Workshop*, Santa Fe, USA, 2007

[17] Wu, J. S., Tseng, K. C., and Wu, F. Y., "Parallel Three-Dimensional DSMC Method Using Mesh Refinement and Variable Time Step Scheme," *Computer Physics Communications*, Vol. 162, No. 3, 2004, pp. 166-187.
doi: 10.1016/j.cpc.2004.07.004

[18] Myong, R. S., Karchani, A., and Ejtehadi, O., "A Review and Perspective on a Convergence Analysis of the Direct Simulation Monte Carlo and Solution Verification," *Physics of Fluids*, Vol. 31, No. 6, 2019, p. 066101.
doi: 10.1063/1.5093746

[19] Karchani, A., and Myong, R. S., "Convergence Analysis of the Direct Simulation Monte Carlo Based on the Physical Laws of Conservation," *Computers and Fluids,* Vol. 115, No. 1, 2015, pp. 98-114.
doi: 10.1016/j.compfluid.2015.03.022

[20] Alexander, F. J., Garcia, A. L., and Alder, B. J., "Cell Size Dependence of Transport Coefficients in Stochastic Particle Algorithms," *Physics of Fluids*, Vol. 10, No. 6, 1998, pp. 1540-1542.
doi: 10.1063/1.869674

[21] Boyd, I. D., Chen, G., and Candler, G. V., "Predicting Failure of the Continuum Fluid Equations in Transitional Hypersonic Flows," *Physics of Fluids*, Vol. 7, No. 1, 1995, pp. 210-219.
doi: 10.1063/1.868720

[22] Lofthouse, A., Scalabrin, L., and Boyd, I., "Hypersonic Aerothermodynamics Analysis Across Nonequilibrium Regimes Using Continuum and Particle Methods," AIAA Paper 2007-3903, 2007.
doi: 10.2514/6.2007-3903

[23] Lofthouse, A., Scalabrin, L., and Boyd, I., "Velocity Slip and Temperature Jump in Hypersonic Aerothermodynamics," AIAA Paper 2007-0208, 2007.
doi: 10.2514/1.31280

[24] Holman, T. D., and Boyd, I. D., "Effects of Continuum Breakdown on Hypersonic Aerothermodynamics for Reacting Flow," *Physics of Fluids,* Vol. 23, No. 2, 2011, p. 027101.
doi: 10.1063/1.3541816

[25] Wang, W. L., and Boyd, I. D., "Predicting Continuum Breakdown in Hypersonic Viscous Flows," *Physics of Fluids,* Vol. 15, No. 1, 2003, pp. 91-100.

doi: 10.1063/1.1524183

[26] Deschenes, T. R., Holman, T. D., and Boyd, I. D., "Effects of Rotational Energy Relaxation in a Modular Particle-Continuum Method," *Journal of Thermophysics and Heat Transfer*, Vol. 25, No. 2, 2011, pp. 218-227.
doi: 10.2514/1.50720

[27] Wu, J. S., Lian, Y. Y., Cheng, G., Koomullil, R. P., and Tseng, K. C., "Development and Verification of a Coupled DSMC–NS Scheme Using Unstructured Mesh," *Journal of Computational Physics*, Vol. 219, No. 2, 2006, pp. 579-607.
doi: 10.1016/j.jcp.2006.04.013

[28] Hash, D., and Hassan, H., "A Decoupled DSMC/Navier–Stokes Analysis of a Transitional Flow Experiment," AIAA Paper 1996-0353, 1996.
doi: 10.2514/6.1996-353

[29] Garcia, A. L., Bell, J. B., Crutchfield, W. Y., and Alder, B. J., "Adaptive Mesh and Algorithm Refinement Using Direct Simulation Monte Carlo," *Journal of Computational Physics*, Vol. 154, No. 1, 1999, pp. 134-155.
doi: 10.1006/jcph.1999.6305

[30] Stephani, K., Goldstein, D., and Varghese, P., "Generation of a Hybrid DSMC/CFD Solution for Gas Mixtures with Internal Degrees of Freedom," AIAA Paper 2012-648, 2012.
doi: 10.2514/6.2012-648

[31] Schwartzentruber, T. E., Scalabrin, L. C., and Boyd, I. D., "Modular Implementation of a Hybrid DSMC-NS Algorithm for Hypersonic Non-Equilibrium Flows," AIAA Paper 2007-613, 2007.
doi: 10.2514/6.2007-613

[32] Espinoza, D. E. R., Casseau, V., Scanlon, T. J., and Brown, R. E., "An Open-Source Hybrid CFD-DSMC Solver for High Speed Flows," *In AIP Conference Proceedings*, Vol. 1786, No. 1, 2016, p. 050007.
doi: 10.1063/1.4967557

[33] Gupta, R. N., Yos, J. M., Thompson, R. A., and Lee, K. P., "A Review of Reaction Rates and Thermodynamic and Transport Properties for an 11 Species Air Model for Chemical and Thermal Nonequilibrium Calculations to 30,000K," Technical report, NASA RP-1232, 1990

[34] Park, C., "Review of Chemical-Kinetic Problems of Future NASA Missions. I-Earth Entries," *Journal of Thermophysics and Heat transfer*, Vol. 7, No. 3, 1993, pp. 385-398.
doi: 10.2514/3.431

[35] Millikan, R. C., and White, D. R., "Systematics of Vibrational Relaxation," *Journal of Chemical Physics*, Vol. 39, No. 12, 1963, pp. 3209-3213.
doi: 10.1063/1.1734182

[36] Evans, J. S., Schexnayder Jr, C. J., and Grose, W. L., "Effects of Nonequilibrium Ablation Chemistry on Viking Radio Blackout," *Journal of Spacecraft and Rockets*, Vol. 11, No. 2, 1974, pp. 84-88.
doi: 10.2514/3.62013

[37] Parker, J. G., "Rotational and Vibrational Relaxation in Diatomic Gases," *Physics of Fluids*, Vol. 2, No. 4, 1959, pp. 449-462.
doi: 10.1063/1.1724417

[38] Koomullil, R. P., and Soni, B. K., "Flow Simulation Using Generalized Static and Dynamic Grids," *AIAA Journal*, Vol. 37, No. 12, 1999, pp. 1551-1557.
doi: 10.2514/2.655

[39] Wu, J. S., and Lian, Y. Y., "Parallel Three-Dimensional Direct Simulation Monte Carlo Method and its Applications," *Computers and Fluids*, Vol. 32, No. 8, 2003, pp. 1133-1160.
doi: 10.1016/S0045-7930(02)00083-X

[40] Scalabrin, L. C., and Boyd, I. D., "Development of an Unstructured Navier-Stokes Solver for Hypersonic Nonequilibrium Aerothermodynamics," AIAA Paper 2005-5203, 2005.
doi: 10.2514/6.2005-5203

[41] Dietrich, S., and Boyd, I. D., "Scalar and Parallel Optimized Implementation of the Direct Simulation Monte Carlo Method," *Journal of Computational Physics*, Vol. 126, No. 2, 1996, pp. 328-342.
doi: 10.1006/jcph.1996.0141

[42] Schwartzentruber, T. E., and Boyd, I. D., "Progress and Future Prospects for Particle-Based Simulation of Hypersonic Flow," *Progress in Aerospace Sciences*, Vol. 72, No. 1, 2015, pp. 66-79.
doi: 10.1016/j.paerosci.2014.09.003

[43] Park, C., "Problems of Rate Chemistry in the Flight Regimes of Aeroassisted Orbital Transfer Vehicles," AIAA Paper 1984-1730, 1984.
doi: 10.2514/6.1984-1730

[44] Deschenes, T. R., and Boyd, I. D., "Extension of a Modular Particle-Continuum Method to Vibrationally Excited, Hypersonic Flows," *AIAA Journal*, Vol. 49, No. 9, 2011, pp. 1951-1959.
doi: 10.2514/1.J050908

[45] Verhoff, A. M., and Boyd, I. D., "Extension of a Hybrid Particle-Continuum Method for a Mixture of Chemical Species," *In AIP Conference Proceedings*, Vol. 1501, No. 1, 2012, pp. 342-349.
doi: 10.1063/1.4769538

[46] Schwartzentruber, T. E., Scalabrin, L. C., and Boyd, I. D., "Hybrid Particle-Continuum Simulations of Nonequilibrium Hypersonic Blunt-Body Flowfields," *Journal of Thermophysics and Heat transfer*, Vol. 22, No. 1, 2008, pp. 29-37.
doi: 10.2514/1.30216

[47] Schwartzentruber, T. E., Scalabrin, L. C., and Boyd, I. D., "Multiscale Particle-Continuum Simulations of Hypersonic Flow over a Planetary Probe," *Journal of Spacecraft and Rockets*, Vol. 45, No. 6, 2008, pp. 1196-1206.
doi: 10.2514/1.30216

[48] Schwartzentruber, T. E., and Boyd, I. D., "A Hybrid Particle-Continuum Method Applied to Shock Waves," *Journal of Computational Physics*, Vol. 215, No. 2, 2006, pp. 402-416.
doi: 10.1016/j.jcp.2005.10.023

[49] Sun, Q., and Boyd, I. D., "Evaluation of Macroscopic Properties in the Direct Simulation Monte Carlo Method," *Journal of Thermophysics and Heat transfer*, Vol. 19, No. 3, 2005, pp. 329-335.
doi: 10.2514/1.12542

[50] Verhoff, A. M., and Boyd, I. D., "Consistent Modeling of Rotational Nonequilibrium in a Hybrid Particle-Continuum Method," AIAA Paper 2013-3145, 2013.
doi: 10.2514/6.2013-3145

[51] LeBeau, G. J., and Lumpkin III, F. E., "Application Highlights of the DSMC Analysis Code (DAC) Software for Simulating Rarefied Flows," *Computer Methods in Applied Mechanics and Engineering*, Vol. 191, No. 6, 2001, pp. 595-609.
doi: 10.1016/S0045-7825(01)00304-8

[52] Wright, M. J., Candler, G. V., and Bose, D., "Data-Parallel Line Relaxation Method for the Navier-Stokes Equations," *AIAA Journal*, Vol. 36, No. 9, 1998, pp. 1603-1609.
doi: 10.2514/2.586

[53] Stephani, K., Goldstein, D., and Varghese, P., "Development of a Hybrid DSMC/Navier-Stokes Solver with Application to the STS-119 Boundary Layer Transition Flight Experiments," AIAA Paper 2011-534, 2011.
doi: 10.2514/6.2011-534

[54] Ramshaw, J. D., and Chang, C. H., "Friction-Weighted Self-Consistent Effective Binary Diffusion Approximation," *Journal of Non-Equilibrium Thermodynamics*, Vol. 21, No. 1, 1996, pp. 223-232.
doi: 10.1515/jnet.1996.21.3.223

[55] Lagarias, J. C., Reeds, J. A., Wright, M. H., and Wright, P. E., "Convergence Properties of the Nelder-Mead Simplex Method in Low Dimensions," *SIAM Journal on Optimization*, Vol. 9, No. 1, 1998, pp. 112-147.

doi: 10.1137/S1052623496303470

[56] Vincenti, W. G., and Kruger, C. H., *Introduction to Physical Gas Dynamics*, Krieger, Malabar, USA, 1967.

[57] Gimelshein, N. E., Gimelshein, S. F., and Levin, D. A., "Vibrational Relaxation Rates in the Direct Simulation Monte Carlo Method," *Physics of Fluids*, Vol. 14, No. 12, 2002, pp. 4452-4455.
doi: 10.1063/1.1517297

[58] Casseau, V., Scanlon, T. J., and Brown, R. E., "Development of a Two-Temperature Open-Source CFD Model for Hypersonic Reacting Flows," AIAA Paper 2015-3637, 2015.
doi: 10.2514/6.2015-3637

[59] White, C., "Adaptive Mesh Refinement for an Open Source DSMC Solver," AIAA Paper 2015-3632, 2015.
doi: 10.2514/6.2015-3632

[60] Espinoza, D. E. R., "An Open-Source Hybrid CFD-DSMC Solver for High Speed Flows," Ph.D Dissertation, Department of Mechanical and Aerospace Engineering, University of Strathclyde, Glasgow, Scotland, 2018.

[61] Gnoffo, P. A., Gupta, R. N., and Shinn, J. L., "Conservation Equations and Physical Models for Hypersonic Air Flows in Thermal and Chemical Nonequilibrium," NASA TP-2867, 1989.

[62] Park, C., *Nonequilibrium Hypersonic Aerothermodynamics*, John Wiley and Sons, New York, 1990.

[63] Scanlon, T. J., White, C., Borg, M. K., Palharini, R. C., Farbar, E., Boyd, I. D., Reese, J. M., and Brown, R. E., "Open-Source Direct Simulation Monte Carlo Chemistry Modeling for Hypersonic Flows," *AIAA Journal*, Vol. 53, No. 6, 2015, pp. 1670-1680.
doi: 10.2514/1.J053370

[64] Wilke, C. R., "A Viscosity Equation for Gas Mixtures," *Journal of Chemical Physics*, Vol. 18, No. 4, 1950, pp. 517-519.
doi: 10.1063/1.1747673

[65] Nompelis, I., and Schwartzentruber T. E., “Strategies for Parallelization of the DSMC Method,” AIAA Paper 2013-1204, 2013.

[66] Gao, D., Zhang, C., and Schwartzentruber, T. E., “Particle Simulations of Planetary Probe Flows Employing Automated Mesh Refinement,” *Journal of Spacecraft and Rockets*, Vol. 48, No. 3, 2011, pp. 397-405.
doi: 10.2514/1.52129

[67] Sawant, S. S., Tumuklu, O., Jambunathan, R., and Levin, D. A., “Application of Adaptively Refined Unstructured Grids in DSMC to Shock Wave Simulations,” *Computers and Fluids*, Vol. 170, No. 1, 2018, pp. 197-212.
doi: 10.1016/j.compfluid.2018.04.026

[68] Ivanov, M. S., Kashkovsky, A. V., Gimelshein, S. F., Markelov, G. N., Alexeenko, A. A., Bondar, Y. A., Zhukova, G. A., Nikiforov, S. B., and Vaschenkov, P. V., “SMILE System for 2D/3D DSMC Computations,” *Proceedings of 25th International Symposium on Rarefied Gas Dynamics*, St. Petersburg, Russia, 2006, pp. 21-28.

[69] Arslanbekov, R., Kolobov, V., Burt, J., and Josyula, E., “Direct Simulation Monte Carlo with Octree Cartesian Mesh,” AIAA Paper 2012-2990, 2012.
doi: 10.2514/6.2012-2990

[70] Klothakis, A. G., Nikolos, I. K., Koehler, T. P., Gallis, M. A., and Plimpton, S. J., “Validation Simulations of the DSMC Code SPARTA,” *AIP Conference Proceedings*, Vol. 1786, No. 1, 2016, p. 050016.
doi: 10.1063/1.4967566

[71] Wu, J. S., Tseng, K. C., and Kuo, C. H., “The Direct Simulation Monte Carlo Method Using Unstructured Adaptive Mesh and its Application,” *International Journal for Numerical Methods in Fluids*, Vol. 38, No. 4, 2002, pp. 351-375.
doi: 10.1002/fld.229

[72] Kim, M. G., Kim, H. S., and Kwon, O. J., “A Parallel Cell-Based DSMC Method on Unstructured Adaptive Meshes,” *International Journal for Numerical Methods in Fluids*, Vol. 44, No. 12, 2004, pp. 1317-1335.

doi: 10.1002/fld.644

[73] Su, C. C., Tseng, K. C., Wu, J. S., Cave, H. M., Jermy, M. C., and Lian, Y. Y., "Two-Level Virtual Mesh Refinement Algorithm in a Parallelized DSMC Code Using Unstructured Grids," *Computers and Fluids*, Vol. 48, No. 1, 2011, pp. 113-124.
doi: 10.1016/j.compfluid.2011.04.002

[74] Ivanov, M. S., Markelov, G. N., and Gimelshein, S. F., "Statistical Simulation of Reactive Rarefied Flows: Numerical Approach and Applications," AIAA Paper 1998-2669, 1998.
doi: 10.2514/6.1998-2669

[75] Bird, G. A., *The DSMC Method*, CreateSpace Independent Publishing Platform, California, USA, 2013.

[76] Dietrich, S., and Boyd, I., "A Scalar Optimized Parallel Implementation of the DSMC Method," AIAA Paper 1994-355, 1994.
doi: 10.2514/6.1994-355

[77] Padilla, J., and Boyd, I., "Assessment of Gas-Surface Interaction Models in DSMC Analysis of Rarefied Hypersonic Flow," AIAA Paper 2007-3891, 2007.
doi: 10.2514/6.2007-3891

[78] Boyd, I. D., "Computation of Hypersonic Flows Using the Direct Simulation Monte Carlo Method," *Journal of Spacecraft and Rockets*, Vol. 52, No. 1, 2015, pp. 38-53.
doi: 10.2514/1.A32767

[79] Seguin, J., Gao, S., Habashi, W. G., Isola, D., and Baruzzi, G. "A Finite Element Solver for Hypersonic Flows in Thermo-Chemical Non-Equilibrium, Part I," *International Journal of Numerical Methods for Heat and Fluid Flow*, Vol. 29, No. 7, 2019, pp. 2352–2388.
doi: 10.1108/HFF-09-2018-0498

[80] Gao, S., Seguin, J., Habashi, W. G., Isola, D., and Baruzzi, G., "A Finite Element Solver for Hypersonic Flows in Thermo-Chemical Non-Equilibrium, Part II," *International Journal of Numerical Methods for Heat and Fluid Flow*, Vol. 30, No. 2, 2020, pp. 575–606.
doi: 10.1108/HFF-12-2018-0725

[81] Gao, S., Habashi, W. G., Isola, D., Baruzzi, G. S., and Fossati, M., "A Jacobian-Free Edge-Based Galerkin Formulation for Compressible Flows," *Computers and Fluids*, Vol. 143, No. 1, 2016, pp. 141–156.
doi: 10.1016/j.compfluid.2016.10.026

[82] McBride, B. J., Gordon, S., and Reno, M. A., "Coefficients for Calculating Thermodynamic and Transport Properties of Individual Species", NASA TM-4513, 1993.

[83] Law, C. K., *Combustion Physics*, Cambridge University Press, Cambridge, UK, 2006.

[84] Mason, E., and Saxena, S., "Approximate Formula for the Thermal Conductivity of Gas Mixtures," *Physics of Fluids*, Vol. 1, No. 5, 1958, pp. 361-369.
doi: 10.1063/1.1724352

[85] Dumas, M.-E., Habashi, W. G., Baruzzi, G. S., Isola, D., and Fossati, M., "Finite Element Modeling of Non-Equilibrium Fluid-Wall Interaction at High-Mach Regime," *AIAA Journal of Aircraft*, Vol. 54, No. 6, 2017, pp. 2231-2339.
doi: 10.2514/1.C034211

[86] Hutton, D., *Fundamentals of Finite Element Analysis*, McGraw-Hill, New York, 2004.

[87] Fletcher, C., "A Comparison of Finite Element and Finite Difference Solutions of the One- and Two-dimensional Burgers' Equations," *Journal of Computational Physics*, Vol. 51, No. 1, 1983, pp. 159-188.
doi: 10.1016/0021-9991(83)90085-2

[88] Löhner, R., and Galle, M., "Minimization of Indirect Addressing for Edge-based Field Solvers," *Communications in Numerical Methods in Engineering*, Vol. 18, No. 5, 2002, pp. 335-343.
doi: 10.1002/cnm.494

[89] Selmin, V., and Formaggia, L., "Simulation of Hypersonic Flows on Unstructured Grids," *International Journal for Numerical Methods in Engineering*, Vol. 34, No. 2, 1992, pp. 569-606.
doi: 10.1002/nme.1620340212

[90] Selmin, V., "The Node-centred Finite Volume Approach: Bridge Between Finite Differences and Finite Elements," *Computer Methods in Applied Mechanics and Engineering*, Vol. 102, No. 1, 1993, pp. 107-138.
doi: 10.1016/0045-7825(93)90143-L

[91] Gao, S., "An Edge-Based Galerkin Formulation for Thermochemical Non-Equilibrium Flows," Ph.D. Dissertation, Department of Mechanical Engineering, McGill University, Montréal, Canada, 2018.

[92] Nanthaamornphong, A., Carver, J., Morris, K., and Filippone, S., "Extracting UML Class Diagrams from Object-Oriented Fortran: ForUML," *Scientific Programming*, Vol. 2015, No. 1, 2015, pp. 1–15.
doi: 10.1145/2532352.2532354

[93] Macpherson, G. B., Nordin, N., and Weller, H. G., "Particle Tracking in Unstructured, Arbitrary Polyhedral Meshes for Use in CFD and Molecular Dynamics," *Communications in Numerical Methods in Engineering*, Vol. 25, No. 1, 2009, pp. 263-273.
doi: 10.1002/cnm.1128

[94] Bird, G. A., "Perception of Numerical Methods in Rarefied Gasdynamics," *Rarefied Gas Dynamics: Theoretical and Computational Techniques*, AIAA, Washington, DC, 1989, pp. 211-226.

[95] Roohi, E., and Stefanov, S., "Collision Partner Selection Schemes in DSMC: From Micro/Nano Flows to Hypersonic Flows," *Physics Reports*, Vol. 656, No.1, 2016, pp. 1-38.
doi: 10.1016/j.physrep.2016.08.002

[96] Boyd, I. D., and Schwartzentruber, T. E., *Non-Equilibrium Gas Dynamics and Molecular Simulation*, Cambridge University Press, Cambridge, UK, 2017.
doi: 10.1017/9781139683494

[97] Borgnakke, C. and Larsen, P. S., "Statistical Collision Model for Monte Carlo Simulation of Polyatomic Gas Mixture," *Journal of Computational Physics*, Vol. 18, No. 4, 1975, pp. 405-420.
doi: 10.1016/0021-9991(75)90094-7

[98] Su, C. C., Tseng, K. C., Cave, H. M., Wu, J. S., Lian, Y. Y., Kuo, T. C., and Jermy, M. C., "Implementation of a Transient Adaptive Sub-cell Module for the Parallel-DSMC Code Using Unstructured Grids," *Computers and Fluids*, Vol. 39, No. 7, 2010, pp. 1136-1145. doi: 10.1016/j.compfluid.2010.02.003

[99] Habashi, W. G., Dompierre, J., Bourgault, Y., Fortin, M., and Vallet, M.-G., "Certifiable Computational Fluid Dynamics Through Mesh Optimization," *Special Issue on Credible Computational Fluid Dynamics Simulation, AIAA Journal*, Vol. 36, No. 5, 1998, pp. 703-711.
doi: 10.2514/2.458

[100] Habashi, W. G., Dompierre, J., Bourgault, Y., Ait-Ali-Yahia, D., Fortin, M., and Vallet, M.-G., "Anisotropic Mesh Adaptation: Towards User-Independent, Mesh-Independent and Solver-Independent CFD. Part I: General Principles," *International Journal for Numerical Methods in Fluids*, Vol. 32, No. 6, 2000, pp. 725-744.
doi: 10.1002/(SICI)1097-0363(20000330)32:6<725::AID-FLD935>3.0.CO;2-4

[101] Zhang, W., Habashi, W. G., Salah, N. B., Isola, D., and Baruzzi, G. S., "Edge-Based Finite Element Formulation of Hypersonic Flows Under an Imposed Magnetic Field," *AIAA Journal*, Vol. 56, No. 7, 2018, pp. 2756-2768.
doi: 10.2514/1.J056368

[102] Allegre, J., Raffin, M., Chpoun, A., and Gottesdiener, L., "Rarefied Hypersonic Flow over a Flat Plate with Truncated Leading Edge," *Progress in Astronautics and Aeronautics*, Vol. 160, No. 1, 1994, pp. 285-295.
doi: 10.2514/5.9781600866326.0285.0295

[103] Padilla, J. F., "Comparison of DAC and MONACO DSMC Codes with Flat Plate Simulation," NASA TM-2010-216835, 2010.

[104] Bird, G. A., "Chemical Reactions in DSMC," *In AIP Conference Proceedings*, Vol. 1333, No. 1, 2011, pp. 1195-1202.
doi: 10.1063/1.3562806

[105] Liechty, D. S., "State-to-State Internal Energy Relaxation Following the Quantum-Kinetic Model in DSMC," AIAA Paper 2013-2901, 2013.
doi: 10.2514/6.2013-2901

[106] Myong, R. S., "A computational method for Eu's generalized hydrodynamic equations of rarefied and microscale gasdynamics," *Journal of Computational Physics*, Vol. 168, No. 1, 2001, pp. 47-72.
doi: 10.1006/jcph.2000.6678

[107] Lofthouse, A. J, "Non-Equilibrium Hypersonic Aerothermodynamics using the Direct Simulation Monte Carlo and Navier-Stokes Models," Ph.D. Dissertation, Department of Aerospace Engineering, University of Michigan, Ann Arbor, USA, 2018.

[108] Scanlon, T. J., Roohi, E., White, C., Darbandi, M., and Reese, J. M., "An Open Source, Parallel DSMC Code for Rarefied Gas Flows in Arbitrary Geometries," *Computers and Fluids*, Vol. 39, No. 10, 2010, pp. 2078-2089.
doi: 10.1016/j.compfluid.2010.07.014

Appendix A: Species Data

This Section provides data concerning the different chemical species modeled in the present work. Table A.1 lists the species molecular weight, heat of formation and characteristic vibrational temperatures common to all the test cases. Table A.2 provides the VHS parameters for the different species used in the test cases.

Table A.1 Species parameters

Species	m (g/mol)	e_f^0 (J/kg)	θ_v (K)
N_2	28.01348	0	3395
O_2	31.99880	0	2239
NO	30.00614	3.00E+06	2817
N	14.00674	3.36E+07	0
O	15.99940	1.54E+07	0

Table A.2 VHS parameters for all species considered

Species	ω	T_{ref} (K)	d_{ref} (m)
Ar (Sections 3.1.1 / 3.2.1.1 / 3.3.4)	0.81	273	4.17×10^{-10}
N_2 (Sections 3.1.2 / 3.1.3 / 3.2.1.2 / 3.2.1.3 / 3.2.1.4 / 3.2.2.2 / 3.3.1 / 3.3.3)	0.74	273	4.17×10^{-10}
O_2 (Section 3.1.3)	0.77	273	4.07×10^{-10}
NO (Section 3.1.3)	0.79	273	4.20×10^{-10}
N (Sections 3.1.3 / 3.2.1.4 / 3.3.3)	0.8	273	3.00×10^{-10}
O (Section 3.1.3)	0.8	273	3.00×10^{-10}
Ar (Sections 3.2.2.1 / 3.3.2)	0.734	1000	3.595×10^{-10}
O_2 (Section 3.2.2.3)	0.7	288	3.96×10^{-10}
O (Section 3.2.2.3)	0.7	288	3.00×10^{-10}

Appendix B: Reaction Coefficients

This Section details the chemical reactions and provides reaction data for the test cases simulated in the present work. Tables are presented for each Section considering reacting mixtures and parameters for exchange reactions are provided as well.

Table B.1 Reactions and reaction coefficients for Section 3.1.3

Reactions	A^f	η^f	E_a x10^{-19} J	h_r x10^{-19} J
$N_2 + N \rightarrow 3N$	1.0×10^{-11}	-0.68	15.67	15.67
$N_2 + N_2 \rightarrow 2N + N_2$	4.1×10^{-12}	-0.62	15.67	15.67
$N_2 + NO \rightarrow 2N + NO$	1.5×10^{-11}	-0.68	15.67	15.67
$N_2 + O_2 \rightarrow 2N + O_2$	1.5×10^{-11}	-0.68	15.67	15.67
$N_2 + O \rightarrow 2N + O$	4.0×10^{-12}	-0.54	15.67	15.67
$O_2 + O \rightarrow 3O$	1.5×10^{-10}	-1.05	8.197	8.197
$O_2 + O_2 \rightarrow 2O + O_2$	5.33×10^{-11}	-1.0	8.197	8.197
$O_2 + N_2 \rightarrow 2O + N_2$	1.3×10^{-10}	-1.0	8.197	8.197
$O_2 + NO \rightarrow 2O + NO$	1.1×10^{-10}	-1.0	8.197	8.197
$O_2 + N \rightarrow 2O + N$	1.1×10^{-10}	-1.0	8.197	8.197
$NO + N_2 \rightarrow N + O + N_2$	2.1×10^{-10}	-1.0	10.43	10.43
$NO + O_2 \rightarrow N + O + O_2$	2.0×10^{-10}	-1.0	10.43	10.43
$NO + NO \rightarrow N + O + NO$	1.0×10^{-10}	-1.0	10.43	10.43
$NO + O \rightarrow N + O + O$	4.0×10^{-10}	-1.1	10.43	10.43
$NO + N \rightarrow N + O + N$	4.0×10^{-10}	-1.1	10.43	10.43
$N_2 + O \rightarrow NO + N$	0.8×10^{-16}	0.0	5.175	5.175
$NO + O \rightarrow O_2 + N$	2.3×10^{-19}	0.5	2.719	2.719
$NO + N \rightarrow N_2 + O$	5.0×10^{-16}	-0.35	0.2	-5.175
$O_2 + N \rightarrow NO + O$	4.0×10^{-15}	-0.39	0.2	-2.719

Table B.2 Parameters a and b used to the adjust activation energies of exchange reactions in Section 3.1.3

Exchange reactions	*a*		*b*	
	Bird 2013	**Scanlon *et al.* 2015**	**Bird 2013**	**Scanlon *et al.* 2015**
$N_2 + O \rightarrow NO + N$	0.15	0.15	0	0.15
$NO + O \rightarrow O_2 + N$	0.1	0.085	0.68	0.65
$NO + N \rightarrow N_2 + O$	0.033	0.033	0.8	0.8
$O_2 + N \rightarrow NO + O$	0.1	0.1	0.48	0.1

Table B.3 Reactions and reaction coefficients for Section 3.2.2.3

Reactions	A^f	η^f	E_a x10^{-19} J	h_r x10^{-19} J
$O_2 + O_2 \rightarrow 2O + O_2$	4.58×10^{-11}	-1.0	8.197	8.197
$O_2 + O \rightarrow 3O$	1.375×10^{-10}	-1.0	8.197	8.197

Table B.4 Reactions and reaction coefficients for Section 3.3.3

Reactions	A^f	η^f	E_a x10^{-19} J	h_r x10^{-19} J
$N_2 + N \rightarrow 3N$	1.0×10^{-11}	-1.6	15.67	15.67
$N_2 + N_2 \rightarrow 2N + N_2$	4.1×10^{-12}	-1.6	15.67	15.67